The University Of Sheffield.

Magnetically Geared Electrical Drives

Glynn Cooke

A thesis submitted for the degree of

Doctor of Philosophy

Department of Electrical and Electronic Engineering

May 2018

Abstract

Considerable research efforts are being carried out worldwide to develop technologies which meet the increasing demand for the efficient utilisation of energy resources. Modern applications, such as renewable energy and electrical vehicles, place a premium on electro-mechanical energy conversion in a power dense and high efficiency manner. Magnetic gears (MG) and magnetically geared machines, offer an attractive alternative to existing systems which may favour the combination of a high speed electrical machine with a mechanical gearbox.

This has led to the opportunity to use Pseudo Direct Drives (PDDs) and MGs to be developed for use on an industrial scale. Therefore, in this thesis techniques for facilitating the manufacture and robustness of PDDs are presented, for both radial and axial field topologies. This includes use of alternative windings and soft magnetic composites.

PDDs and MGs has so far mainly been developed in the radial topology and little attention has been given to axial topologies. The pole piece (PP) rotor required for MG operation, represents the main difference between PDD/MG and a conventional electrical machine. As such the PP shape and supporting structures have been investigated both in terms of electromagnetic and mechanical performance.

Furthermore, detailed electromagnetic and thermal design and analysis of an axial field PDD (AFPDD) with improved robustness was undertaken, and a prototype was manufactured to demonstrate the operation of the AFPDD and validate the predictions.

List of Publications

Journal Papers from the Thesis

- G. Cooke; K. Atallah, "'Pseudo' Direct Drive Electrical machines with alternative winding configurations," in IEEE Transactions on Magnetics, vol. 53, no. 11, pp. 1-8, Nov. 2017

- G. Cooke; K. Atallah, "Axial field 'Pseudo' Direct Drive electrical machines," To be submitted to IEEE Transactions on Energy Conversion

Other Journal Papers

- A. Penzkofer, G. Cooke, M. Odavic and K. Atallah, "Coil Excited Pseudo Direct Drive Electrical Machines," in IEEE Transactions on Magnetics, vol. 53, no. 1, pp. 1-11, Jan. 2017

- H. Harrison, G. Cooke, D. A. Hewitt, D. A. Stone, J. E. Green, "Magnetic Tomography for Lead Acid Batteries," in Journal of Energy Storage, vol. 12, pp. 1-10, Aug. 2017

Acknowledgements

I would like to express my sincere thanks to Professor Kais Atallah for his continuous guidance, encouragement and advice during the course of this research. I would also like to thank my colleagues in the Electrical Machines and Drives group for their knowledge, advice and friendship.

I gratefully acknowledge the financial support provided by Electrical and Electronic Engineering department and by the INNWIND.EU project, carried out under the European Union's Seventh Framework Programme. I would also like to thank Magnomatics Ltd for their sponsorship and technical support during the course of this PhD. Additionally I would like to thank Radu Stefan Dragan for his insight and assistance. Special thanks are also due to the technical staff of the Electrical Machines and Drives group for their help during the manufacture of a prototype electrical machine.

I am grateful to my Mum, Dad, Brother and family for their unquestioning love and support throughout my life. Finally, I would like to thank my wife Kelly for her love, support and understanding in the course of writing this thesis.

Table of Contents

Figure and Table List

Nomenclature

Symbol	Definition	Units
(A,C,L)MG	(Axial, Co-axial, Linear) Magnetic Gear	
A	Area	[m^2]
A_s	Slot Area	[m^2]
AFMM	Axial Flux-Modulated Motor	
AFPDD	Axial Field Pseudo Direct Drive	
AF	Axial Field	
AlNiCo	Aluminium Nickel Cobalt	
BLAC	Brushless AC	
B (B_{max} , B_{min})	Flux Density (maximum, minimum)	[T]
B_x , B_y , B_z	Flux Density Component (x, y, z)	[T]
B_r , B_θ	Flux Density Component (radial, circumferential)	[T]
B_1	Fundamental Flux Density	[T]
C	Bearing Load Rating	[N]
C_f	Cogging Torque Factor	
CFD	Computational Fluid Dynamics	
d	Lamination Thickness	[m]
D_{av}	Average Diameter	[m]
D_i , D_o	Tooth Diameter (inner, outer)	[m]
D_{iw} , D_{ow}	Diametric Limit of Winding (inner, outer)	[m]
E-CVT	Electric-Continuously Variable Transmission	
EM	Electro-Magnetic	
E	Young's Modulus	[Pa]
f_h , f_n	Bearing Factor (fatigue life, speed)	
F_c	Centripetal force	[N]
F_{min}	Force (minimum)	[N]
F_a , F_r	Bearing loading force (axial, radial)	[N]
F_f	Fitting force (axial)	[N]
F_s	Nut axial clamping force (minimum)	[N]
f	Electrical Frequency	[Hz]
f_{sh}	Mechanical Cycle Frequency	[Hz]
f_{pp}	Pole Piece Frequency	[Hz]
F (F_z)	Force (axial)	[N]
FeCo	Iron-Cobalt	
FEA	Finite Element Analysis	
g	Air gap thickness	[m]
$G_{A,B,C,D}$	Pre-set bearing preload	[N]
G_r	Gear Ratio	
GCD	Greatest Common Divisor	
h , h_{gap} , h_s	Heat Transfer Coefficient (surface, air gap, shaft)	[W / (m^2.ºC)]
HSR	High Speed Rotor	

I_{rms}	Current (rms)	[A]
I_{area}	Second moment of area	[m^4]
k (k_a , k_c , k_r)	Thermal Conductivity (axial, circumferential, radial)	[W / (m.ºC)]
k_{con}	Number of Consecutive Magnets	
k_d	Distribution Factor	
k_{ex}	Classical Eddy Current Loss constant	
k_h	Hysteresis Loss constant	
k_p	Pitch Factor	
k_{pf}	Packing Factor	
k_w	Winding Factor	
K	Thread tightening factor	
K_e	Back EMF Constant	[$V.s.rad^{-1}$]
l_i , l_o	Length of arc (inner, outer)	[m]
L_{ap} , L_{cp} , L_{rp}	Thermal Path Length (axial, circumferential, radial)	[m]
L_{AA} , L_s	Inductance (Self, Synchronous)	[H]
L_{end_i} ,L_{end_o}	End winding Length (inner, outer)	[m]
L_{slot} , L_w	Length (conductor in the slot, total winding)	[m]
l_r	HSR outer ring length	[m]
L_{10}	Bearing lifetime de-rating	
L_a	Active Length	[m]
L_{sh}	Shaft Length	[m]
LCM	Lowest Common Multiple	
LSR	Low Speed Rotor	
LPM	Lumped Parameter Model	
m_m , m_r , m_s	Mass (magnet, rotor, shaft)	[kg]
M	Frictional moment on bearing	[N.mm]
M_{AB}	Inductance (Mutual)	[H]
n	Harmonic Order	
n_s	Number of Pole Pieces	
N_l	Number of Minor Loops	
N	Number of conductor turns	
Nu	Nusselt Number	
N_{cp}	Number of bearing of same orientation	
N_R	Bearing loss (due to friction)	[W]
NdFeB	Neodymium Iron Boron	
p (p_h, p_l)	Pole pairs on rotor (high-speed, low-speed)	
p_f	Power Factor	
P_r	Radial Pressure	[Pa]
P_{iron} (P_{hyst} , P_{eddy} , P_{ex})	Iron Loss (Hysteresis, Classical Eddy, Excess)	[W]
P_{cu}	Copper Loss	[W]
PDD®	Pseudo-Direct Drive	
PM	Permanent Magnet	
PMSM	Permanent Magnet Synchronous Motor	
PP	Pole Piece	

PPR	Pole Piece Rotor	
P_o , P_{loss}	Power (Output, Total Loss)	[W]
q	Number of phases	
q_{ph}	Number of spokes per phase	
Q_{rms}	Electrical Loading (rms)	[Am^{-1}]
Q_t	Number of Slots	
r (r_i , r_m , r_o)	Radius (inner, mean, outer)	[m]
r_1 , r_2	Arc segment radii (inner, outer)	
R_a , R_c , R_r	Thermal Resistance (Axial, Circumferential, Radial)	[ºC/W]
R_c , R_{ph}	Resistance (per coil, per phase)	[Ω]
R_{conv} , R_{cond}	Thermal Resistance (Convection, Conduction)	[ºC/W]
R_s	Stator Bore Radius	[m]
R_o	Machine Outer Radius	[m]
Re	Reynolds Number	
RFMM	Radial Flux-Modulated Motor	
RF	Radial Field	
RNA	Reluctance Network Analysis	
SMC	Soft Magnetic Composite	
SmCo	Samarium Cobalt	
SmFeN	Samarium Iron Nitride	
SPM	Somaloy Prototyping Material	
t	Machine Periodicity	
t_r	HSR outer ring thickness	[m]
t_{pp}	Nominal Pole Piece axial thickness	[mm]
T (T_{ax} , T_r)	Torque (Axial machine, Radial machine)	[N.m]
T	Time Period	[s]
Ta	Taylor Number	
T_e	Electromagnetic Torque	[Nm]
T_h	AFPDD Torque (High Speed Rotor)	[Nm]
T_o	AFPDD Torque (Pole Piece Rotor)	[Nm]
T_{op} , T_{ref}	Temperature (operating, reference)	[ºC]
TEFC	Totally Enclosed, Fan Cooled	
T/AV	Torque per Active Volume	[$N.m^{-2}$]
T/MV	Torque per Magnet Volume	[$N.m^{-2}$]
TRS	Tensile Rupture Strength	
V	Volume	[m^3]
V_{DC}	DC Link Voltage	[V]
w_{pp}	Mean width of PP	[m]
X , Y	Bearing Load Factor (radial, axial)	
y_q	Slot Pitch (in number of slots)	

α	Slot opening proportion	
α_{as}	Angle of arc segment	[degrees]
α_{cu}	Temperature coefficient (copper resistivity)	
α_{ph}	Electrical angle between star of slots	[degrees]
α_{pp}	Ratio of Air to Ferromagnetic Material	

α_s	Slot pitch	[degrees]
α_{TB}	Tooth body to slot pitch ratio	
α_{TP}	Tooth pitch to slot pitch ratio	
β	Hysteresis Loss constant	
β_1	Half Tooth Slot Pitch	[degrees]
δ	Beam deflection	[m]
δ_s , δ_l	Shaft deflection (due to shaft, due to load)	[m]
ε	Back EMF	[V]
η	Efficiency	
θ	Angular Position	[radians]
θ_t	HSR Tilt angle	[degrees]
λ	Ratio of Inner to Outer Diameter	
λ_{air}	Thermal conductivity of air	[W / (m.ºC)]
μ_o	Permeability of free space	[H/m]
ν_d	Kinematic viscosity of air	[$m^2.s^{-1}$]
ν_{pp}	Linear velocity (PPR)	[$m.s^{-1}$]
ρ_T , ρ_{ref}	Resistivity of Copper (Operating Temperature, reference)	[Ω.m]
σ	Electrical Conductivity	[$\Omega^{-1}.m^{-1}$]
σ_{ax} , σ_{rad}	Shear Stress (axial, radial)	[Pa]
σ_h	Hoop Stress	[Pa]
σ_{max}	Beam Stress	[Pa]
σ_w	Coil Span Angle	[degrees]
ω_b	Relative speed between bearing races	[r/min]
ω_c	Critical speed	[rpm]
ω_h , ω_l , ω_{pp}	Rotor Speed (HSR, LSR, PPR)	[$rad.s^{-1}$]
ω_{rel}	Rotor Speed (Relative)	[$rad.s^{-1}$]
ω_{sh}	Relative speed (between HSR and LSR)	[$rad.s^{-1}$]

Chapter 1

Introduction

1.1. Motivation

Substantial research is being carried out worldwide to develop technologies which meet the increasing demand and utilisation of energy resources. Modern applications, such as renewable energy and electrical vehicles, place a premium on electro-mechanical energy conversion in a power dense and high efficiency manner. These applications often employ mechanical gearbox components when high-torque low-speed operation is required in a low cost and lightweight format. The high-speed low-torque input of the gearbox is transferred to a low-speed high-torque output via mechanical contact between gear sets. This mechanical interaction of gearbox components results in several associated issues such as the requirement for lubrication and maintenance, generation of acoustic noise, vibration transmission and damage in over-load conditions [1.1]. This can result in a low system utilisation, requiring labour intensive maintenance and replacement of components after a gearbox becomes unserviceable [1.2]. Due to these inherent challenges for drivetrains with mechanical gear boxes it is desirable to reduce the number of gear stages or remove the mechanical gearbox entirely.

Magnetic gears (MG) and magnetically geared machines, which physically and magnetically integrate a magnetic gear within a synchronous AC electrical machine, offer an attractive alternative to the mechanical gearbox [1.3] [1.4]. Due to the lack of physically connecting components the requirement for periodic maintenance and lubrication are essentially eliminated. During an over-load condition the magnetic gear

‘pole-slips’, during which additional acoustic noise and vibrations may be caused but no lasting damage should occur within the drivetrain [1.5]. The compliance of the magnetic gear significantly reduces the transmission of torsional vibrations which is particularly beneficial in certain applications [1.6]. Furthermore, magnetically geared electrical machines are capable of achieving larger torque densities than those of equivalent conventional permanent magnet (PM) machines. The resulting drivetrain may offer a competitive alternative to a conventional machine-gearbox arrangement and are a good candidate for use in the automotive and wind turbine sectors [1.7].

As MGs and MG integrated PM machines advance from technology demonstrators and prototypes, research is focusing on cost reductions and improved manufacturability. With the technology maturing and finding applications in a variety of fields from down-well oil and gas, automotive traction motors, aerospace actuators and marine propulsion, the ease of manufacture and mechanical robustness become important considerations, in addition to the electromagnetic performance. Several aspects of the technology are yet to be investigated and present potential opportunities in which the advantages of the MG technology can be exploited in a more robust and simple to manufacture manner.

1.2. Trends in AC Machines and Materials

AC electrical machines are typically categorised between two fundamental types, those being synchronous or asynchronous. The most extensively employed asynchronous machines are AC induction motors whereas synchronous machines include brushless PM machines, variable reluctance, switched reluctance and hysteresis[1.8]. When supplied with sinusoidal current and voltage, brushless machines are known as Permanent Magnet Synchronous Motor (PMSM) or Brushless AC (BLAC).

PMSMs are extensively utilised in applications where torque density and efficiency are primary requirements. Both radial field (RF) and axial field (AF) topologies exist with RF PMSMs more commonly utilised due to being inherently balanced along their axial length. This makes the manufacture of smaller air gaps generally more achievable [1.9]. AF PMSMs become favourable when the length is the prevailing constraint for applications such as automotive 'in-wheel' drives [1.10] [1.11]. RF and AF machine topologies have historically been compared using the value of air gap shear stress as given by σ_{rad} for the radial machine and σ_{ax} for the axial machine given by:

$$\sigma_{rad} = \frac{T}{2\pi r_m^2 L_a} \tag{1.1}$$

$$\sigma_{ax} = \frac{2T}{\pi(r_o^2 - r_i^2)(r_o + r_i)} \tag{1.2}$$

where T is the value of torque, r_m is the mean airgap radius of the radial machine, L_a is the active length of the radial machine. r_i and r_o are the inner and outer radii of the axial topology respectively as shown in Figure 1.1(a) and (b).

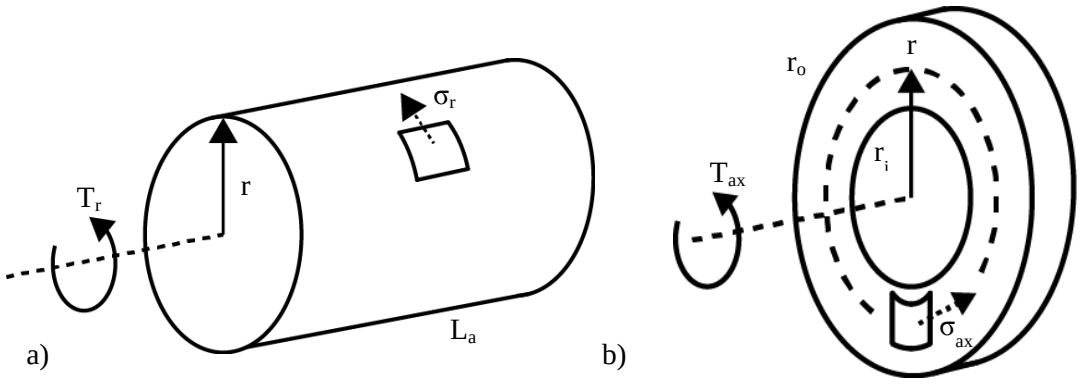

Figure 1.1 *Electromagnetic shear stress definition in a) Radial machine and b) Axial machine*

When considering the continuous rating of an electrical machine, typical values of shear stress for industrial machines >1kW, air-cooled aerospace machines and larger liquid-

cooled machines as 4-15kPa, 20-35kPa and 70-100kPa respectively in [1.8][1.12]. In the past these values were unobtainable due to the poor magnetic field strength and coercivity of Ferrite or Aluminium Nickel Cobalt (AlNiCo) based materials [1.13].

The prevalence of applications which demand high efficiency and high power density in has increased alongside the global recognition that industries should limit their impact on the earth's resources. As such the increasing global demand for rare-earth Neodymium Iron Boron (NdFeB) and Samarium Cobalt (SmCo) can drive large fluctuations in the global prices of PM material [1.14][1.15]. As a consequence ongoing research aims to reduce the quantity of rare-earth PM for high-volume, cost sensitive applications. This is done by means of optimal use of PM material, new magnet configurations and in some applications utilising the flux focusing effect [1.16][1.17]. The increasing interest amongst researchers is aptly seen in the volume of published work concerned with PM machines, as shown in Figure 1.2 [1.18].

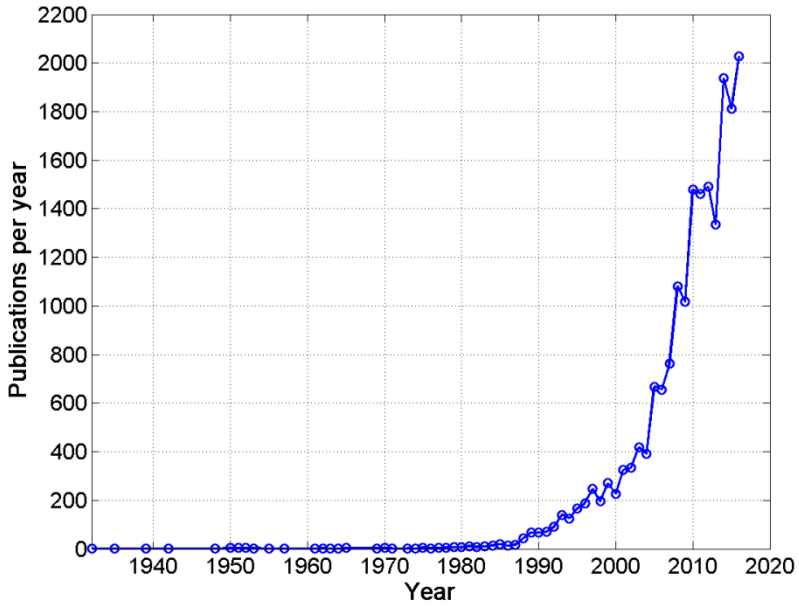

Figure 1.2 *Variation of interest in PM machines with time*

Historically an improvement in the maximum energy product of PM materials corresponds to the development of new material with a higher maximum energy product as seen in Figure 1.3 [1.19][1.20][1.21]. PMs such as Samarium Iron Nitride (SmFeN) have the future potential to exceed the properties of NdFeB but requires further development due to the difficulties associated with its manufacture [1.22].

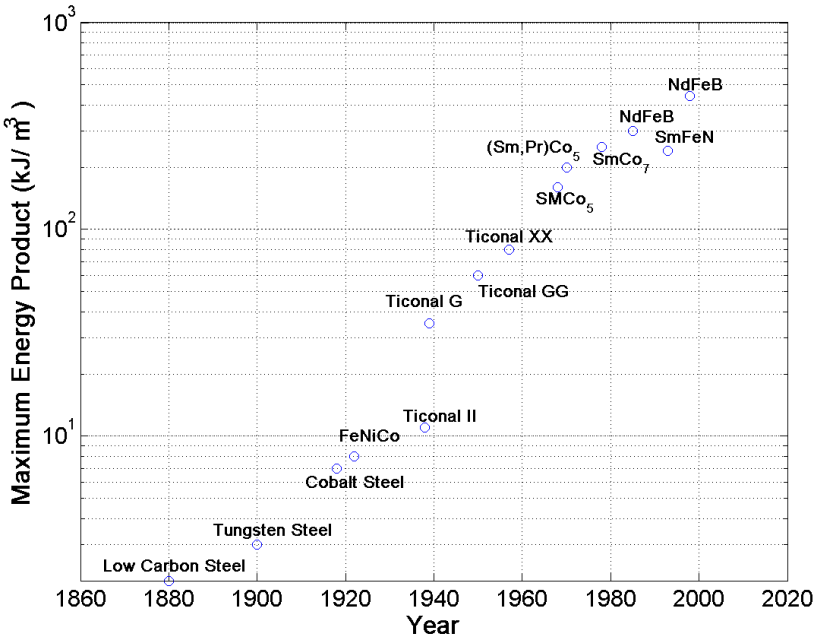

Figure 1.3 *Variation of magnetic materials energy product with time*

The use of high energy PMs in volume restricted applications can lead to saturation of the soft magnetic materials, necessitating the development of specialist steels such as the commonly used Low Carbon Steel or less used Iron-Cobalt (FeCo) [1.23]. FeCo has been limited to applications such as aerospace in which the reduced mass of the device is the principle target and the increased saturation limit overrides the higher material cost.

The soft magnetic material used in the construction of stator cores are predominately thin laminations of electrical steel, typically stacked or wound in the case of RF and AF machines respectively [1.24]. An alternative stator core material is Soft Magnetic

Composite (SMC), which is a sintered ferromagnetic powder used to form complex three-dimensional components and is particularly useful in AF machines [1.25] [1.26]. Table 1.1 shows a comparison of the soft magnetic materials with their non-linear B-H characteristics shown in Figure 1.4.

Material	***Saturation Magnetization (T)***	***Resistivity (μΩm)***	***Permeability (μ_{max})***	***Coercivity (Am^{-1})***	***Tensile Strength (MPa)***
Low Carbon Steel (e.g. M270-35A) [1.27]	2.0	0.4	5000	55	586
Cobalt Iron[1.28]	2.4	0.4	15000	32	1344
Soft Magnetic Composite[1.29]	1.63	70	850	217	64

Table 1.1 *Comparison of soft magnetic materials*

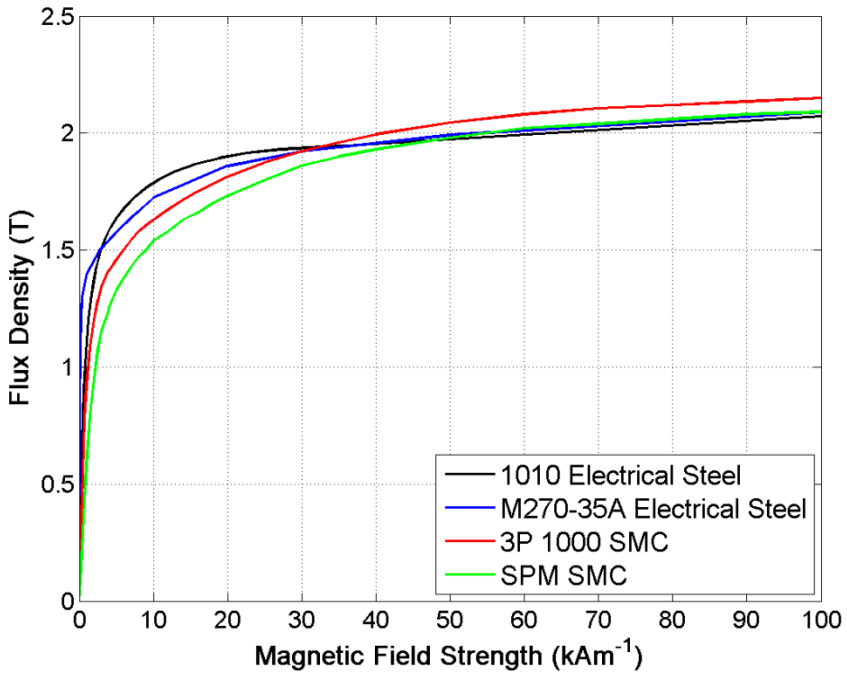

Figure 1.4 *Variation of flux density with magnetic field strength (soft magnetic materials)*

Halbach arrays are used to further exploit rare-earth PMs and prevent the need for large yokes [1.30]. A resultant 'one-sided' magnetic field is produced as the poles support

magnetic field in one direction while cancelling the field in the opposite direction as shown in Figure 1.5.

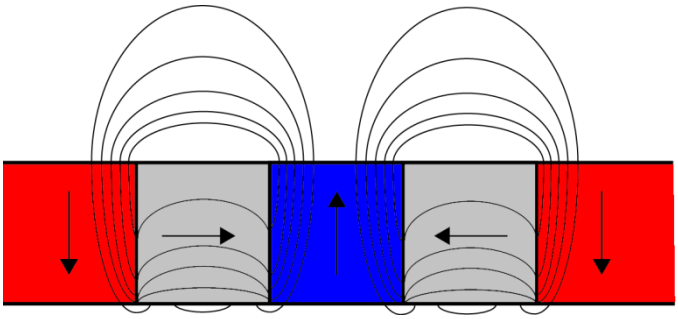

Figure 1.5 *Halbach oriented magnet array*

1.3. Magnetic Gears and Magnetically Geared Machines

In the past the transmission of torque has primarily relied upon two physically contacting bodies, with the exception of fluid type couplings found in torque converters. The earliest source found regarding MGs relates to an electromagnetic gear from 1901 [1.31] [1.32]. The device consists of two rotors which transmit force in a non-contact manner, via the field produced from a coil excited rotor interacting with ferromagnetic teeth of a second rotor. Following this several magnetic type gears have been proposed, mainly resembling their non-magnetic variants such as spur and worm, rack and pinion, bevel gear, internal and external spur gears and planetary gears [1.32] [1.33] [1.34] [1.35]. The special case in which the gear ratio (G_r) is 1:1 is often referred to as magnetic couplings. Both radial and axial magnetic couplings have been employed to provide over-load protection with the structures shown in Figure 1.6 (a) and (b) respectively [1.36].

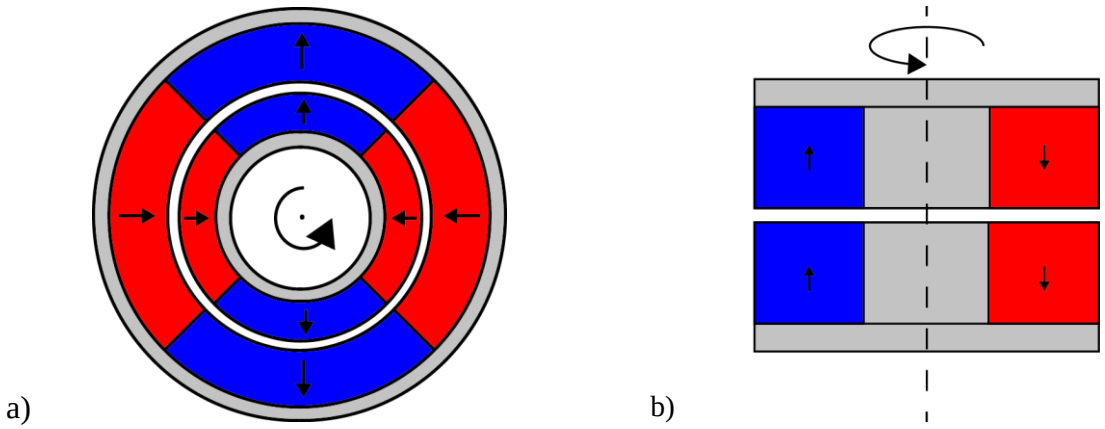

Figure 1.6 *Magnetic Coupling structure a) Radial coupling and b) Axial coupling*

For several decades a lack of interest in this technology persisted due to the poor torque density which is mainly attributed to the available PM materials and their poor topological utilisation [1.36]. In most cases only a single pair of magnets contribute to torque transmission. An exception to this is the magnetic planetary gearbox, a kin to its mechanical counterpart, in which each planet aids torque transmission and have been shown to achieve torque densities of ~100kN/m^3 [1.37]. However, these required a high number of planetary gears and as such the resulting structure is mechanically complex.

Another subset of mechanical gearboxes are known as strain wave or harmonic gears [1.38]. These comprise of three components, one of which is a high-speed wave generator with an appropriate profile which rotates within a flexible low-speed rotor. This produces an advancing waveform on the flexible component. Rotation of this component within a fixed circular spline results with the engagement of teeth at multiple points at the limit of the profile. Due to a different number of teeth on the low-speed and fixed circular splines, gear ratios above 150:1 can be achieved [1.39]. A radial field harmonic MG equivalent was proposed in 2010 and achieved ripple-free torque transmission of up to ~150kN/m^3 with a 360:1 gear ratio [1.40]. The issue with this MG arrangement remains the complex mechanical arrangements and need to couple

an eccentric or flexible rotor with a concentric output. This can be overcome using a 2 stage arrangement but somewhat compromises the torque density of the gearbox. Axial MG variants offer limited advantages in reducing bearing loads and operating at higher speeds [1.41].

1.1.1 Coaxial Magnetic Gear

The notion of a coaxial magnet gear (CMG) is indicated present in a US patent from 1967 [1.42]. The employment of three distinct components with radially directed flux and the use of an arrangement of pole rings is suggested in [1.43] [1.44]. However, no further mention of the operating principle, including how the gearing effect is realised, can be found until 1995 in which the necessary number of pole number and modulators is given [1.45]. In 2001 a paper by K. Atallah and D. Howe presented an analysis of the spatial flux density distributions required for a torque dense CMG [1.46]. The topology of such a magnetic gear is shown in Figure 1.7.

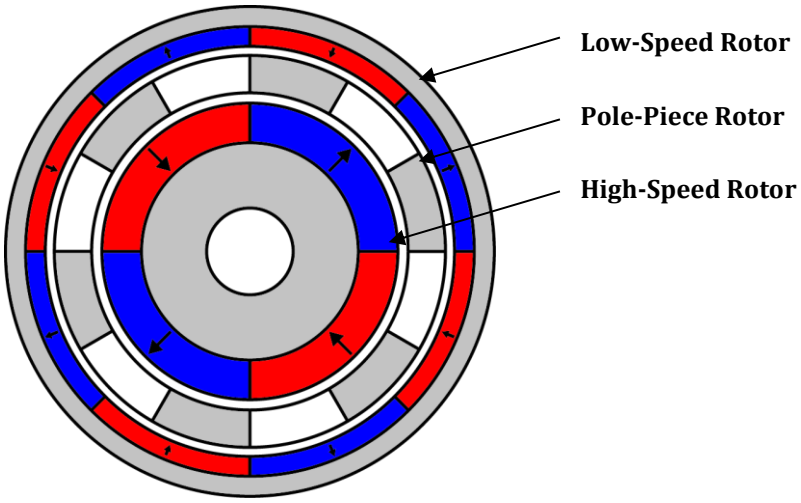

Figure 1.7 *Coaxial magnetic gear topology*

The magnetic gear topology proposed the use of high energy PM material to contribute to the transmission of torque via field modulation using pole pieces (PP). The ferromagnetic pole pieces are arranged onto a rotor and separated by non-ferrous, non-

magnetic segments. Accordingly this rotor structure is known as the pole-piece rotor (PPR). The high-speed rotor (HSR) and low speed rotor (LSR) comprise of PM arrays with alternating polarity segments of different pole number as shown in Figure 1.7. A fixed-ratio radial flux MG achieved torque densities exceeding 100kNm/m^3 and demonstrated performance close to that of mechanical gears.

Several attempts have since been made to further investigate the technology. Flux focusing using tangentially magnetised PMs to exceed the airgap flux density of surface mounted arrays have been analysed but at the detriment to the torque ripple [1.47]. Furthermore, the mechanisms and influences of end effects in radial magnetic gears were identified [1.48].

The reduction of torque ripple has received some attention with the use of interior PMs, magnet skewing and so called 'pole pairing' in which a proportion of the magnet arc is reduced for part of the axial length [1.49] [1.50] [1.51].

1.1.2 Linear Magnetic Gear

Linear motion drives have in the past been implemented using hydraulic or pneumatics actuators. Both of these systems require lubrication, regular maintenance and can suffer from seizing or jamming. Alternatively this motion can be achieved via electrically powered linear actuators or by coupling a motor with a lead-screw and nut style gearbox. However, a compromise is often seen between the thrust-force density and reliability of the system [1.52] [1.53]. By employing the same working principle as CMGs the Linear Magnetic Gear (LMG) has been developed to achieve a high reliability, high thrust force system. The suggested topology of an LMG consists of the same three essential components as CMGs but in a linearized topology as shown in Figure 1.8. The possibility to eliminate these issues and benefit from increased force

densities compared to liquid cooled linear motors makes LMGs particularly suitable for aerospace applications in which compact, force dense actuators are preferred [1.54].

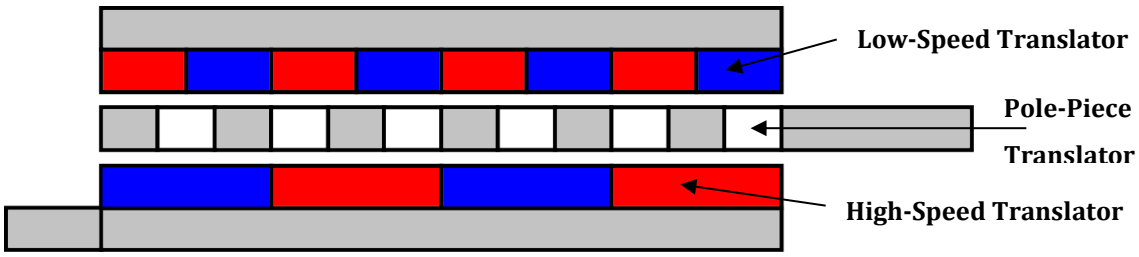

Figure 1.8 *Linear magnetic gear topology*

Two key aspects of the LMGs were identified upon the completion of a prototype [1.55]. The volumetric force density could be optimised for low axial length high-speed armatures and large air gaps. The compressive modulus of the non-ferrous, non-magnetic components of the PPR proved to be a critical design consideration as variation in the spacing between PPs of ~5% resulted in a reduction of the transmitted force by ~30%.

1.1.3 Axial Magnetic Gear

Furthermore, an Axial Magnetic Gear (AMG) presents yet another variant on the CMG principle of operation. The potential to provide physical isolation is of benefit in applications such as the food and pharmaceutical sectors whilst the form factor means AMGs may find use in in-wheel automotive, aerospace and renewable energy applications [1.56]. Torque densities in excess of 70kNm/m^3 have been realised though significant challenges still remain relating to the strong axial forces within the device [1.57]. The topology of an AMG is shown in Figure 1.9. As with CMG's attempts have been made to develop the AMG including using flux focusing methods and reducing cogging torque [1.58][1.59][1.60].

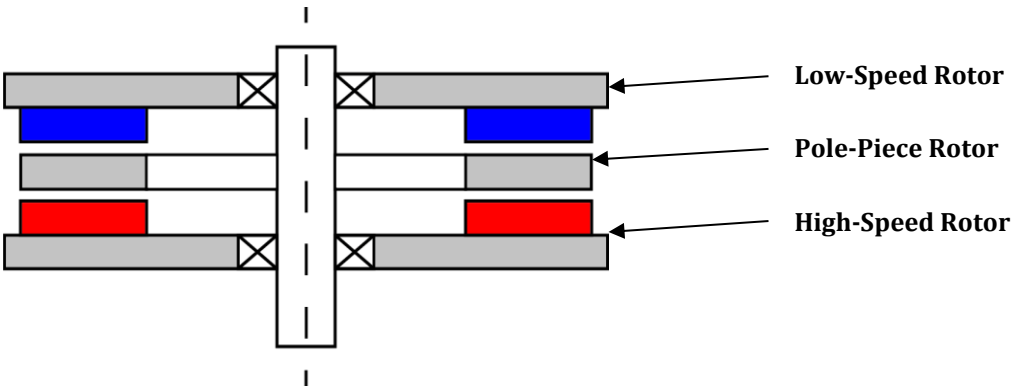

Figure 1.9 *Axial magnetic gear topology*

A number of hybrid magnetic gears have been proposed in which the PPs are removed from between the PM arrays [1.61][1.62][1.63][1.64]. This is achieved by modification of the PPs to permit the transference of flux in a direction that is not aligned with the magnetisation direction. These topologies can further benefit by reducing the leakage flux at the edge of the PM arrays. However, construction of such devices remains physically challenging.

1.1.4 Magnetically Geared Machines

The development of an electrical machine topology in which a PMSM is mechanically and magnetically integrated with a magnetic gear gave rise to a 'pseudo' direct-drive (PDD®) which offers the potential operational advantages of a MG within an electrical machine. In 2008 the operating characteristics, electromechanical modelling and realisation of the radial topology shown in Figure 1.10 were achieved [1.4] [1.65]. A demonstrated torque density in excess of 60kNm/m^3 surpassed other technologies such as radial and transverse field force cooled PM machines which exhibit torque densities of ~30kNm/m^3 and ~50kNm/m^3 respectively [1.66]. Furthermore, through the inclusion of an additional rotor the device has also been proposed as a variable gear ratio, power split device [1.67].

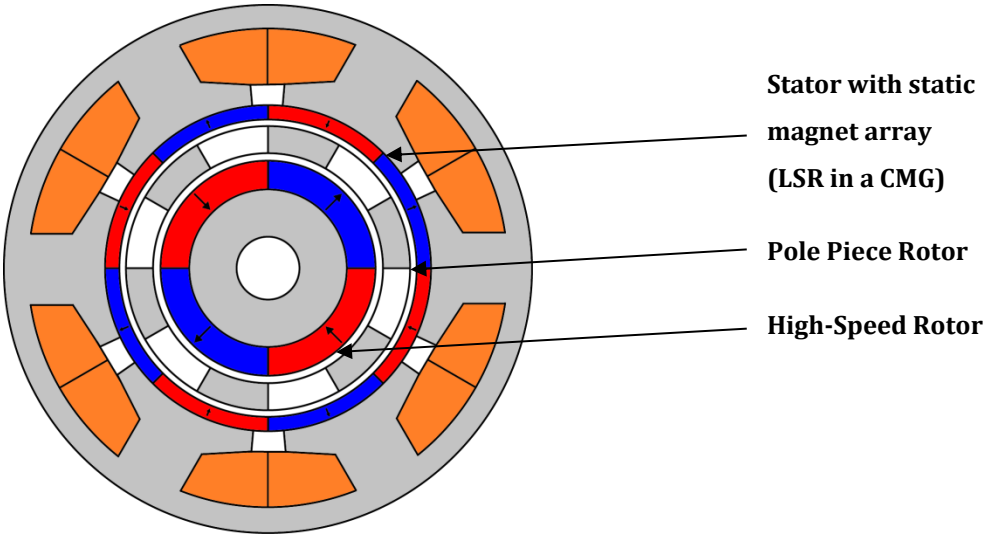

Figure 1.10 '*Pseudo' direct-drive topology*

Torque transmission via magnetic fields results in a low mechanical stiffness between input and output rotors, compromising the speed and position control using conventional control methods. In 2009 the limitations of conventional field oriented control of a PDD were demonstrated [1.68]. The effects of inherent compliance of the magnetic gear element can be addressed, with a full state feedback control employed to suppress the oscillatory nature and improve the controllability of the PDD.

The lack of physical connection between the magnetic gear prime mover and output requires an understanding of the dynamic aspects such as inertia and compliance for accurate motion control [1.69]. Using position sensing from a single rotor a reduced order observer control scheme for a PDD was implemented and allowed for an improvement in the PDD mechanical structure and ease of integration within existing systems [1.70] [1.71].

1.4. Magnetic Gears Principle of Operation

The MG principle relies on the coupling of two magnetic arrays via ferromagnetic pole pieces. The PPs act to modulate the field of the PM arrays in such a way that an interaction is caused between them and a resultant transmission of torque occurs. The resulting asynchronous harmonic of one PM array set of pole-pairs is modulated to the harmonic number which relates to the number of pole-pairs on the second PM array. It was shown that the spatial harmonic flux density distribution resulting from the interaction of either PM rotors is given by [1.3]:

$$p(m,k) = |mp + kn_s| \tag{1.7}$$

where p is the number of pole pairs on the PM array, n_s is the number of PPs, $m \in \{1,3,5,\dots,\infty\}$, $k \in \mathbb{Z}$. The highest asynchronous space component is found at $m = 1$ and $k = -1$ and gives:

$$n_\mathrm{s} = p_h + p_l \tag{1.8}$$

where p_h and p_l are the number of pole pairs on the high-speed and low-speed rotors respectively. The velocity of the flux density space harmonic rotation is given by:

$$\omega_{h,\mathrm{l}}(m,k) = \frac{mp_{h,\mathrm{l}}}{mp_{h,\mathrm{l}} + kn_s}\omega_{h,l} + \frac{kn_s}{mp_{h,\mathrm{l}} + kn_s}\omega_{pp} \tag{1.9}$$

where ω_h , ω_l , ω_pp are the rotational velocities of the HSR, LSR and PPR respectively. The gear ratio G_r is determined by the stationary component in a comparable manner to that of planetary gears. For a stationary PPR G_r is given respectively by:

$$G_\mathrm{r} = \frac{n_\mathrm{s} - p_h}{p_h} \tag{1.10}$$

and for a stationary low speed PM rotor G_{r} is given respectively by:

$$G_{\mathrm{r}} = \frac{n_{\mathrm{s}}}{p_h} \tag{1.11}$$

As p_l relates to the PM array which is usually static and in the case of PDDs secured to the stator, it will from this point be known as the stationary PM array.

1.5. Modelling Techniques

The principle methods for investigating magnetic problems are analytical modelling, Lumped Parameter Modelling (LPM) and Finite Element Analysis (FEA). The use of FEA is a commonly used tool for the analysis of electric machines [1.72] [1.73]. FEA predictions are generally accepted to deliver accurate results for magnetic field problems. This is only entirely true as elements tend toward being infinitely small and if the problem is defined correctly [1.74]. Where possible FEA can be simplified using geometric symmetry and is conducted in two dimensions (2D). The analysis of MGs pose a challenge to FEA due to the dual air gaps, possibility of two moving components and lack of periodicity [1.75]. This necessitates the use of multiple layers of elements within air gap regions and appropriate modelling of the motion. One such method is the moving band technique to achieve accurate results without a large investment of computational resource.

The use of LPM (also known as Reluctance Network Analysis, RNA) offers a computationally efficient alternative to the finite element analysis of MGs. The accuracy of LPM is dependent on the number of basic elements (sources and passives) used to represent the physical aspects of a device. In a complex model a large number of elements will be required but it is likely that each element will require few

interconnections with neighbouring elements. This technique has been employed to analyse the CMG which exhibited a high accuracy and required low computational effort [1.76]. Furthermore, a study of the LMG showed good agreement between LPM and FEA and incorporated the effects of non-linear steel [1.53]. Furthermore, when 3D geometry is to be analysed the model complexity of LPM scales less severely than FEA [1.77].

Analytical models provide the least computational resources by providing the solution to Maxwell's equations, given the correct boundary information and material characteristics. An early example of this for magnetic couplings relates the stiffness and force between the two PM arrays [1.36]. Further to this closed form expressions have been developed which model the PM of a magnetic coupling as magnetic charge distributions and then relate the force and torque between the two charge distributions [1.78] [1.79] [1.80]. These analytical methods represent effective design tools when compared to FEA. A quasi-analytical model of the AMG was developed with a high accuracy for predicting flux density but a 30% over estimate of output torque in [1.81].

The optimisation of large magnetic gears using analytical models was carried out by A. Penzkofer in [1.82][1.83][1.84]. The analytical model showed good agreement with FEA and enabled the design of MG for wind turbines having efficiencies of ~99%.

1.6. Thesis Outline

The thesis structure shown in Figure 1.11 outlines the work in this thesis and contains the following:

Chapter 2 - PDD machines with alternative winding configurations that simplify manufacture are presented. Comparisons between the conventional and proposed topology are made in terms of shear stress and efficiency. Furthermore, the pole piece rotor forces of the proposed topology are examined.

Chapter 3 – The modelling and scaling of an AMG are explored. Magnetic 3D FEA is employed to analyse essential characteristics including the inner to outer diameter ratio, λ. Modifications to the conventional PP shape are investigated with the effects analysed, particularly considering the output torque and magnetic forces.

Chapter 4 – An investigation of the forces incurred by the PPs of an AMG during assembly and normal operation are considered. Models of the mechanical structure are employed, with various PP shapes and structures, to develop a more robust AMG.

Chapter 5 – The electromagnetic design of an axial field PDD (AFPDD) is investigated and optimised toward development of a prototype. Furthermore, the thermal performance is examined with the influence on the choice of materials and operating conditions of the AFPDD considered.

Chapter 6 – The challenges associated with the manufacturing process of an AFPDD are examined. To simplify construction the choice of materials, shaft and bearing arrangements and stator designs are analysed. The testing of a prototype AFPDD showed good agreement with FEA predictions although careful design of the HSR and PPR supporting structures and materials are required.

Chapter 7 – Conclusions are drawn regarding the presented work and its contribution to the state of the art implementation of MGs and PDDs.

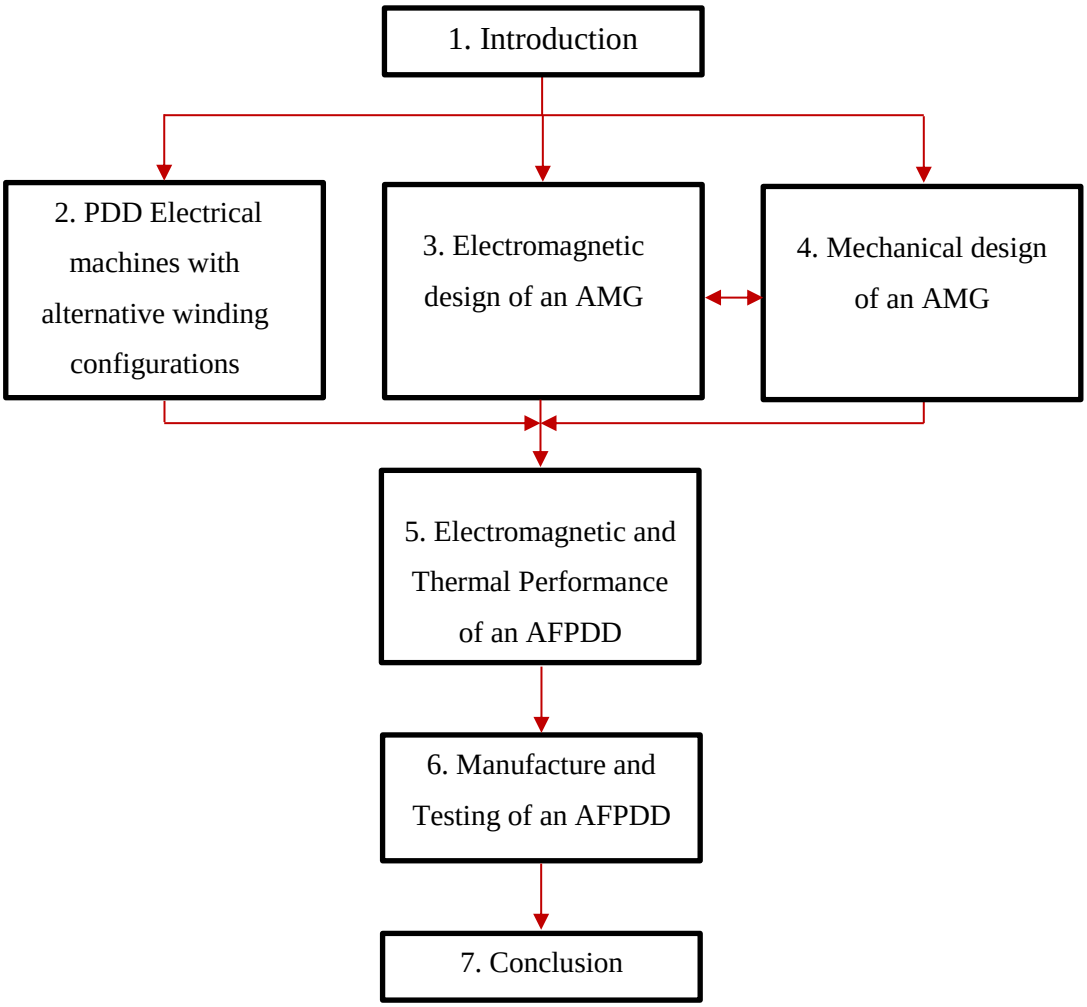

Figure 1.11 *Thesis structure*

1.7. References

[1.1] J. D. Smith, *Gear Noise and Vibration*. 2003.

[1.2] J. Ribrant and L. M. Bertling, “Survey of Failures in Wind Power Systems With Focus on Swedish Wind Power Plants During 1997–2005,” *IEEE Trans. Energy Convers.*, vol. 22, no. 1, pp. 167–173, Mar. 2007.

[1.3] K. Atallah, S. D. Calverley, and D. Howe, “Design , analysis and realisation of a high- performance magnetic gear,” *IEE Proc.-Electr Power Appl.*, vol. 151, no. 2, pp. 135–143, 2004.

[1.4] K. Atallah, J. Rens, S. Mezani, and D. Howe, “A Novel ‘Pseudo ’ Direct-Drive Brushless Permanent Magnet Machine,” *IEEE Trans. Magn.*, vol. 44, no. 11, pp. 4349–4352, 2008.

[1.5] R. G. Montague, C. . Bingham, and K. Atallah, “Characterisation and Modelling of Magnetic Couplings and Gears for Servo Control Systems,” in *5th IET International Conference on Power Electronics, Machines and Drives (PEMD 2010)*, 2010, p. 1,6.

[1.6] D. J. Powell, S. D. Calverley, F. De Wildt, and K. Daffey, “Design and Analysis of a Pseudo Direct-Drive Propulsion Motor,” *Power Electron. Mach. Drives (PEMD 2010)*, p. 1,2, 2010.

[1.7] H. Polinder, J. A. Ferreira, B. B. Jensen, A. B. Abrahamsen, K. Atallah, and R. a. McMahon, “Trends in Wind Turbine Generator Systems,” *IEEE J. Emerg. Sel. Top. Power Electron.*, vol. 1, no. 3, pp. 174–185, 2013.

[1.8] T. J. E. Miller, *Brushless Permanent-Magnet and Reluctance Motor Drives*, no. 1st. 1989.

[1.9] K. Sitapati and R. Krishnan, “Performance Comparisons of Radial and Axial Field , Permanent Magnet , Brushless Machines,” in *Industry Applications Conference*, 2000, no. ii, p. 228,234.

[1.10] P. Campbell, “Principles of a permanent-magnet axial-field d.c. machine,” *Proc. Inst. Electr. Eng.*, vol. 121, no. 12, p. 1489, 1974.

[1.11] Z. Zhang, F. Profumo, and A. Tenconi, “Axial Flux Wheel Machines for Electric Vehicles,” *Electr. Mach. Power Syst.*, vol. 24, no. 8, pp. 883–896, 1996.

[1.12] C. Lewis, “The Advanced Induction Motor,” *IEEE Power Eng. Soc. Summer Meet.*, vol. 1, pp. 250–253, 2002.

[1.13] U. S. Deshpande, “Recent Advances in Materials for use in Permanent Magnet Machines - A Review,” *Electr. Mach. Drives Conf. 2003. IEMDC’03. IEEE Int.*, vol. 1, pp. 509–515, 2003.

[1.14] S. R. Trout, “Rare earth magnet industry in the USA : Current status and future trends,” 2002.

[1.15] W. Rodewald and M. Katter, “Properties and applications of high performance magnets,” 2004.

[1.16] W. Zhao, T. a. Lipo, and B.-I. Kwon, “Material-Efficient Permanent Magnet Shape

for Torque Pulsation Minimization in SPM Motors for Automotive Applications," *IEEE Trans. Ind. Electron.*, vol. 46, no. c, pp. 1–1, 2014.

[1.17] K. Atallah and J. Wang, "A Rotor With Axially and Circumferentially Magnetized Permanent Magnets," *IEEE Trans. Magn.*, vol. 48, no. 11, pp. 3230–3233, Nov. 2012.

[1.18] IEEE, "IEEE Xplore," 2017. [Online]. Available: http://ieeexplore.ieee.org/search/searchresult.jsp?newsearch=true&queryText=permanent magnet machines.

[1.19] P.R.Bardell, "Permanent Magnet Materials," in *Magnetic Materials in the Electrical Industry*, 1st ed., London: MacDonald, 1955, pp. 44–53.

[1.20] E. P. Wohlfarth, K. H. J. Buschow, and U. Enz, "Magnetism and magnetic materials: Historical developments and present role in industry and technology," in *Ferromagnetic Materials*, 1st ed., E. P. Wohlfarth, Ed. 1988, pp. 1–36.

[1.21] O. Gutfleisch, M. a. Willard, E. Brück, C. H. Chen, S. G. Sankar, and J. P. Liu, "Magnetic materials and devices for the 21st century: Stronger, lighter, and more energy efficient," *Adv. Mater.*, vol. 23, no. 7, pp. 821–842, 2011.

[1.22] S. Sugimoto, "Current status and recent topics of rare-earth permanent magnets," *J. Phys. D. Appl. Phys.*, vol. 44, no. 6, p. 64001, 2011.

[1.23] F. Bloch, T. Waeckerle, and H. Fraisse, "The use of iron-nickel and iron-cobalt alloys in electrical engineering, and especially for electrical motors," in *Electrical Insulation Conference and Electrical Manufacturing Expo*, 2007, pp. 394–401.

[1.24] D. J. Patterson, J. L. Colton, B. Mularcik, B. J. Kennedy, S. Camilleri, and R. Rohoza, "A comparison of radial and axial flux structures in electrical machines," *2009 IEEE Int. Electr. Mach. Drives Conf.*, pp. 1029–1035, May 2009.

[1.25] Y. Chen and P. Pillay, "Axial-flux PM Wind Generator with A Soft Magnetic Composite Core," in *Conference Record of the 2005 Industry Applications Conference*, 2005, vol. 1, pp. 231–237.

[1.26] R. Kobler, D. Andessner, J. Passenbrunner, and W. Amrhein, "Modeling, simulation and design of an axial flux machine using soft magnetic composite," in *2011 IEEE Vehicle Power and Propulsion Conference (VPPC)*, 2011, pp. 1–6.

[1.27] Carpenter Technology Corporation, "Carpenter Silicon Core Iron B-FM," 2015.

[1.28] Carpenter Technology Corporation, "Hiperco 50A Alloy," 2005.

[1.29] Hoganas AB Ltd., "Somaloy 1000 3P," 2015.

[1.30] J. Ofori-Tenkorang and J. H. Lang, "A Comparative Analysis of Torque Production in Halbach and Conventional Surface-Mounted Permanent-Magnet Synchronous Motors," *Ind. Appl. Conf. IAS '95*, vol. 1, p. 657,663, 1995.

[1.31] C. Armstrong, "Power-transmitting device," in *US Patent 687292A*, 1901.

[1.32] P. M. Tlali, R. Wang, and S. Gerber, "Magnetic Gear Technologies: A Review," in *International Conference on Electrical Machines (ICEM '14)*, 2014, pp. 544–550.

[1.33] D. E. Hesmondhalgh and D. Tipping, "A multielement magnetic gear," *IEE Proc.*, vol. 127, no. 3, pp. 129–138, 1980.

[1.34] K. Tsurumoto and S. Kikuchi, “A New Magnetic Gear Using Permanent Magnet,” *IEEE Trans. Magn.*, vol. M, no. 5, pp. 3622–3624, 1987.

[1.35] Y. D. Yao, R. Huang, and Y. Chiang, “The Radial Magnetic Coupling Studies of Perpendicular Magnetic Gears,” *IEEE Trans. Magn.*, vol. 32, no. 5, pp. 0–2, 1996.

[1.36] J. Yonnet, “Permanent Magnet Bearings and Couplings,” *IEEE Trans. Magn.*, vol. MAG-17, no. 1, pp. 1169–1173, 1981.

[1.37] Cheng-Chi Huang, Mi-Ching Tsai, David G. Dorrell, and Bor-Jeng Lin, “Development of a Magnetic Planetary Gearbox,” *IEEE Trans. Magn.*, vol. 44, no. 3, pp. 403–412, 2008.

[1.38] C. W. Musser, “Strain wave gearing,” in *US Patent 2906143 A*, 2015.

[1.39] Harmonic Drive LLC, “Harmonic Drive Catalogue.” pp. 3–7, 2017.

[1.40] J. Rens, K. Atallah, S. D. Calverley, and D. Howe, “A Novel Magnetic Harmonic Gear,” *IEEE Trans. Ind. Appl.*, vol. 46, no. 1, pp. 206–212, 2010.

[1.41] K. Davey, L. Mcdonald, and T. Hutson, “Axial Flux Cycloidal Magnetic Gears,” *IEEE Trans. Magn.*, vol. 50, no. 4, pp. 1–7, 2014.

[1.42] N. Laing, “Device for the magnetic transmission of torque,” in *US Patent 3354833 A*, 1967.

[1.43] T. Martin, “Magnetic transmission,” in *US Patent 3378710 A*, 1968.

[1.44] T. Martin, “Magnetic transmission,” in *US Patent 3645650 A*, 1972.

[1.45] B. Ackermann and L. Honds, “Magnetic drive arrangement comprising a plurality of magnetically cooperating parts which are movable relative to one another,” in *US Patent 5633555 A*, 1997.

[1.46] K. Atallah and D. Howe, “A novel high-performance magnetic gear,” *IEEE Trans. Magn.*, vol. 37, no. 4, pp. 2844–2846, Jul. 2001.

[1.47] H. Kong, X. Li, K. T. Chau, M. Cheng, W. Hua, and Y. Du, “An Improved Coaxial Magnetic Gear Using Flux Focusing,” in *International Conference on Electrical Machines and Systems (ICEMS)*, 2011, no. d, pp. 2–5.

[1.48] S. Gerber and R. Wang, “Analysis of the End-Effects in Magnetic Gears and Magnetically Geared Machines,” in *International Conference on Electrical Machines (ICEM)*, 2014, pp. 396–402.

[1.49] N. W. Frank and H. A. Toliyat, “Gearing ratios of a magnetic gear for wind turbines,” in *IEEE International Electric Machines and Drives Conference (IEMDC ’09)*, 2009, pp. 1224–1230.

[1.50] G. Jungmayr, J. Loeffler, B. Winter, F. Jeske, and W. Amrhein, “Magnetic gear: Radial force, cogging torque, skewing and optimization,” *IEEE Energy Convers. Congr. Expo. ECCE 2015*, no. 99, pp. 1–9, 2015.

[1.51] H. Zaytoon, A. S. Abdel-Khalik, A. Massoud, S. Ahmed, and I. Elarabawy, “Torque Ripple Reduction of Radial Magnetic Gearbox Using Axial Pole Pairing,” in *7th IET International Conference on Power Electronics, Machines and Drives (PEMD 2014)*, 2014, pp. 1–6.

[1.52] K. Atallah, J. Wang, and D. Howe, “A high-performance linear magnetic gear,” *J.*

Appl. Phys., vol. 97, no. 10, 2005.

[1.53] R. C. Holehouse, K. Atallah, and J. Wang, "A linear magnetic gear," *2012 XXth Int. Conf. Electr. Mach.*, pp. 563–569, Sep. 2012.

[1.54] A. Garcia, I. Cusid, J. A. Rosero, J. A. Ortega, and L. Romeral, "Reliable Electro-Mechanical Actuators in Aircraft," 2008.

[1.55] R. C. Holehouse, K. Atallah, and J. Wang, "Design and Realization of a Linear Magnetic Gear," *IEEE Trans. Magn.*, vol. 47, no. 10, pp. 4171–4174, Oct. 2011.

[1.56] S. Mezani, K. Atallah, and D. Howe, "A high-performance axial-field magnetic gear," *J. Appl. Phys.*, vol. 99, no. 8, p. 08R303, 2006.

[1.57] M. Johnson, M. Post, and H. A. Toliyat, "Analysis and Development of an Axial Flux Magnetic Gear," in *Energy Conversion Congress and Exposition (ECCE)*, 2014, pp. 5893–5900.

[1.58] V. M. Acharya, J. Z. Bird, and M. Calvin, "A Flux Focusing Axial Magnetic Gear," *IEEE Trans. Magn.*, vol. 49, no. 7, pp. 4092–4095, 2013.

[1.59] S. A. Afsari, H. Heydari, and B. Dianati, "Cogging Torque Minimization in Double sided Axial Flux Magnetic Gear," in *The 6th International Power Electronics Drive Systems and Technologies Conference (PEDSTC2015)*, 2015, vol. 2, no. February, pp. 3–4.

[1.60] S. A. Afsari, H. Heydari, and B. Dianati, "Cogging Torque Mitigation in Axial Flux Magnetic Gear System Based on Skew Effects Using an Improved Quasi 3-D Analytical Method," *IEEE Trans. Magn.*, vol. 51, no. 9, pp. 1–11, 2015.

[1.61] X. Yin, P.-D. Pfister, and Y. Fang, "A Novel Magnetic Gear: Towards a Higher Torque Density," in *IEEE Magnetics Conference (INTERMAG '15)*, 2015, pp. 1–1.

[1.62] S. Peng, W. N. Fu, and S. L. Ho, "A Novel Triple-Permanent-Magnet-Excited Hybrid-Flux Magnetic Gear and Its Design Method Using 3-D Finite Element Method," *IEEE Trans. Magn.*, vol. 50, no. 11, pp. 1–4, 2014.

[1.63] W. Bomela, J. Z. Bird, and V. M. Acharya, "The Performance of a Transverse Flux Magnetic Gear," *IEEE Trans. Magn.*, vol. 50, no. 1, pp. 1–4, 2014.

[1.64] Y. Chen, W. N. Fu, S. L. Ho, and H. Liu, "A Quantitative Comparison Analysis of Radial-Flux , Transverse-Flux , and Axial-Flux Magnetic Gears," *IEEE Trans. Magn.*, vol. 50, no. 11, pp. 1–4, 2014.

[1.65] K. Atallah, S. Calverley, R. Clark, J. Rens, and D. Howe, "A New PM Machine Topology for Low-Speed, High-Torque Drives," in *International Conference on Electrical Machines (ICEM)*, 2008, pp. 5–8.

[1.66] D. Bucherl, R. Nuscheler, W. Meyer, and H. Herzog, "Comparison of Electrical Machine Types in Hybrid Drive Trains: Induction Machine vs. Permanent Magnet Synchronous Machine," in *Proceedings of the 2008 International Conference on Electrical Machines*, 2008, pp. 1–6.

[1.67] K. Atallah, J. Wang, S. D. Calverley, and S. Duggan, "Design and Operation of a Magnetic Continuously Variable Transmission," *IEEE Trans. Ind. Appl.*, vol. 48, no. 4, pp. 1288–1295, 2012.

[1.68] J. Wang and K. Atallah, "Modeling and control of 'pseudo' direct-drive brushless

permanent magnet machines," *2009 IEEE Int. Electr. Mach. Drives Conf.*, pp. 870–875, May 2009.

[1.69] R. G. Montague, C. M. B. Member, and K. Atallah, "Magnetic Gear Dynamics for Servo Control," in *15th IEEE Mediterranean Electrotechnical Conference (MELECON 2010)*, 2010, pp. 1192–1197.

[1.70] M. Bouheraoua, J. Wang, and K. Atallah, "Observer Based State Feedback Controller Design for Psuedo Direct Drive using Genetic Algorithm," *Power Electron. Mach. Drives (PEMD 2012)*, vol. 6, p. 1,6, 2012.

[1.71] M. Bouheraoua, J. Wang, and K. Atallah, "Speed control for a Pseudo Direct Drive permanent magnet machine with one position sensor on low-speed rotor," *2013 Int. Electr. Mach. Drives Conf.*, pp. 986–992, May 2013.

[1.72] T. W. Preston and J. P. Sturgess, "Implementation of The Finite-Element Method Into Machine Design Procedures," in *Sixth International Conference on Electrical Machines and Drives*, 1993, p. 312,317.

[1.73] M. Aydin, S. Huang, and T. A. Lipo, "Design and 3D electromagnetic field analysis of non-slotted and slotted TORUS type axial flux surface mounted permanent magnet disc machines," in *IEMDC 2001 - IEEE International Electric Machines and Drives Conference*, 2001, pp. 645–651.

[1.74] M. Yilmaz and P. T. Krein, "Capabilities of finite element analysis and magnetic equivalent circuits for electrical machine analysis and design," in *IEEE Power Electronics Specialists Conference (PESC '08)*, 2008, pp. 4027–4033.

[1.75] S. Gerber and R.-J. Wang, "Evaluation of Movement Facilitating Techniques for Finite Element Analysis of Magnetically Geared Electrical Machines," *IEEE Trans. Magn.*, vol. 9464, no. 1, pp. 1–1, 2014.

[1.76] M. Fukuoka, K. Nakamura, and O. Ichinokura, "Dynamic Analysis of Planetary-Type Magnetic Gear Based on Reluctance Network Analysis," *IEEE Trans. Magn.*, vol. 47, no. 10, pp. 2414–2417, 2011.

[1.77] K. Hoang, L. Vido, M. Gabsi, and F. Gillon, "3D Modeling of Double Excitation Synchronous Motor with Reluctance Network," in *2014 International Conference on Electrical Machines (ICEM)*, 2014, pp. 2598–2604.

[1.78] E. P. Furlani, "Formulas for the Force and Torque of Axial Couplings," *IEEE Trans. Magn.*, vol. 29, no. 5, pp. 2295–2301, 1993.

[1.79] E. P. Furlani, "Analysis and optimization of synchronous magnetic couplings," *J. Appl. Phys.*, vol. 79, no. 8, p. 4692, 1996.

[1.80] T. Lubin, S. Mezani, and A. Rezzoug, "Simple Analytical Expressions for the Force and Torque of Axial Magnetic Couplings," *IEEE Trans. Energy Convers.*, vol. 27, no. 2, pp. 536–546, 2012.

[1.81] T. Lubin, S. Mezani, and A. Rezzoug, "Development of a 2D Analytical Model for the Electromagnetic Computation of Axial-Field Magnetic Gears," *IEEE Trans. Magn.*, vol. 49, no. 11, pp. 5507–5521, 2013.

[1.82] A. Penzkofer and K. Atallah, "Magnetic Gears for High Torque Applications," *IEEE Trans. Magn.*, vol. 50, no. 5, pp. 1–4, 2014.

[1.83] A. Penzkofer and K. Atallah, “Optimisation of magnetic gears for large wind turbines,” in *2015 IEEE 15th International Conference on Environment and Electrical Engineering, EEEIC 2015 - Conference Proceedings*, 2015, pp. 962–967.

[1.84] A. Penzkofer and K. Atallah, “Analytical Modeling and Optimization of Pseudo-Direct Drive Permanent Magnet Machines for Large Wind Turbines,” *IEEE Trans. Magn.*, vol. 51, no. 12, pp. 1–14, 2015.

Chapter 2

'Pseudo' Direct Drive Electrical machines with alternative winding configurations

As magnetically geared machines advance from technology demonstrators and prototypes, research is focusing on cost reductions and improved manufacturability. With the technology maturing and finding applications in a variety of fields from down-well oil and gas, automotive traction motors, aerospace actuators and marine propulsion the ease of manufacture and mechanical robustness are becoming key considerations, in addition to the electromagnetic performance.

The mechanical and magnetic integration of a magnetic gear and permanent magnet brushless machine gave rise to the so called 'Pseudo' Direct Drive (PDD®)[2.1]. As it develops toward volume manufacture for several applications many design decisions have already been considered. For example, in order to improve the mechanical integrity early prototypes are superseded by closed structures in which the high-speed rotor (HSR) is completely enclosed within the pole-piece rotor (PPR). This, however, makes position sensing for commutation purposes more challenging, requiring advanced control methods to be developed [2.2][2.3].

As can be seen in Figure 2.1, concentrated windings have been extensively employed in the design of PDDs, as this effectively decouples the selection of the number of poles on the stationary magnet array and the number of stator slots [2.1][2.4][2.5]. Therefore, this chapter describes a method which significantly facilitates the realisation of the stationary permanent magnet array, while coupling the process of winding and pole-pair

selections. This approach should facilitate the use of automated winding processes employed in low cost industrial induction machines, for example.

As can be seen in Figure 2.2, in the proposed technique, a stationary permanent magnet is fixed on a stator tooth. This provides a significantly more robust fixing method and avoids the possibility of poles having to be mounted on the slot opening, Figure 2.1. However, in addition to linking the selection of the number poles and the number of slots, in this topology, the magnetic fluxes produced by the stationary permanent magnet array, will also exhibit a significantly stronger coupling with the windings as they return through the teeth and the back-iron.

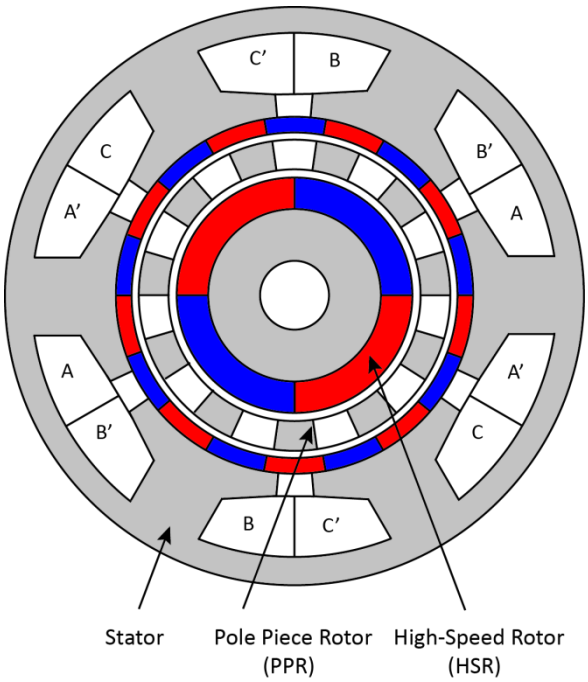

Figure 2.1 *Conventional concentrated winding and stationary magnet array*

2.1. Proposed 'Pseudo' Direct Drive Machine

2.1.1. Gear Ratio Selection

The principle of operation of the proposed machine topologies remain consistent with those outlined in [2.1]. The realisation of the magnetic gear component should yield high airgap shear stress whilst maintaining low cogging torque. In turn the stator should strongly couple the fluxes associated with the fundamental component of the flux density waveform produced by HSR PMs and the winding. Selecting a single tooth per stator magnet pole couples the pole number to the winding configuration and the number of stator teeth. Intrinsic to this is the number of electrical phases and in order to achieve a viable machine, the following conditions must be satisfied:

$$Q_t = nq \tag{2.1}$$

where $n = 1,2,3, \ldots$

$$p_l = \frac{Q_t}{k_{con}} \tag{2.2}$$

$$n_s = p_h + p_l \tag{2.3}$$

$$G_r = \frac{n_s}{p_h} \tag{2.4}$$

$$\mathrm{C}_f = \frac{2p_h n_s}{LCM(p_h, n_s)} = 1 \tag{2.5}$$

where q is the number of phases, Q_t is the number of stator slots, k_{con} is the number of consecutive stator PMs per pole, p_h and p_l are the number of pole pairs on the HSR and

stationary PM arrays, respectively. n_s is the number of modulating pole-pieces, G_r is the gear ratio and C_f is the Cogging Torque Factor [2.6].

Figure 2.2 (a) shows an example of a PDD, where each stator PM pole is mounted on a stator tooth. However, the use of multiple teeth per stator pole is made possible by selecting the appropriate number of consecutive magnets of the same polarity ($k_{con} > 1$). This can result in a different winding configuration as shown in Figure 2.2(b).

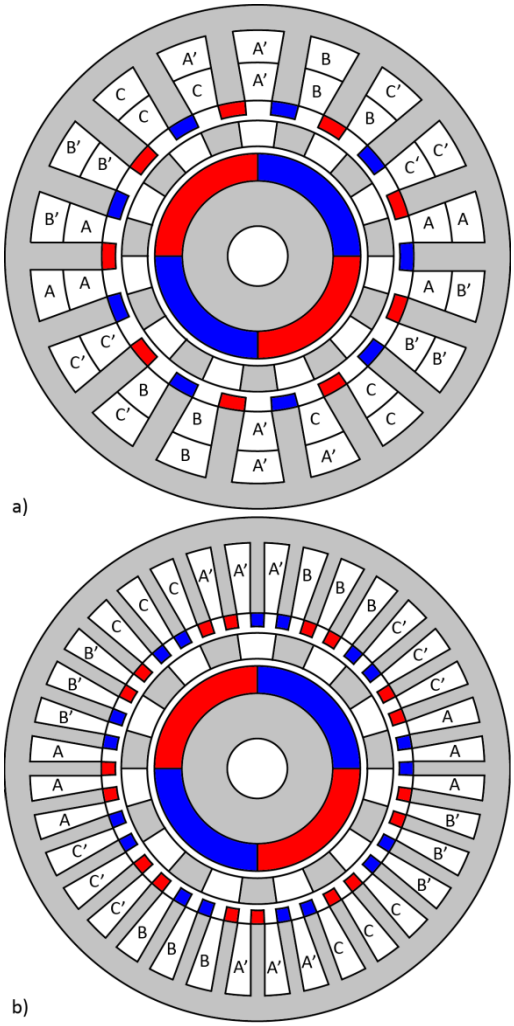

Figure 2.2 *Proposed realisation of PM magnet array and alternative winding with a) k_{con} = 1 and b) k_{con} = 2*

2.1.2. Winding Configurations

To analyse key electrical characteristics of the proposed machine configuration, parameters including winding factor are required. The winding configuration is determined using the method outlined in [2.7]. For no rotor or stator skewing the winding factor for the fundamental component k_w is given by:

$$k_w = k_d k_p \tag{2.6}$$

where, k_d is the distribution factor is given:

$$k_d = \frac{\sin(q_{ph}\alpha_{ph}/4)}{(q_{ph}/2)\sin(\alpha_{ph}/2)} \quad \text{for even } q_{ph} \tag{2.7}$$

$$k_d = \frac{\sin(q_{ph}\alpha_{ph}/4)}{q_{ph}\sin(\alpha_{ph}/4)} \quad \text{for odd } q_{ph} \tag{2.8}$$

where,

$$\alpha_{ph} = \alpha_s t \tag{2.9}$$

$$q_{ph} = \frac{Q}{qt} \tag{2.10}$$

where α_s is the slot pitch and t is the greatest common divisor (GCD) of Q and p_h. The pitch factor k_p is given by:

$$k_p = \sin\left(\frac{\sigma_w}{2}\right) \tag{2.11}$$

where the coil span σ_w is given by:

$$\sigma_w = \frac{2\pi p_h y_q}{Q} \tag{2.12}$$

where y_q is the number of whole slots per pole. An example of such a winding is shown in Figure 2.3.

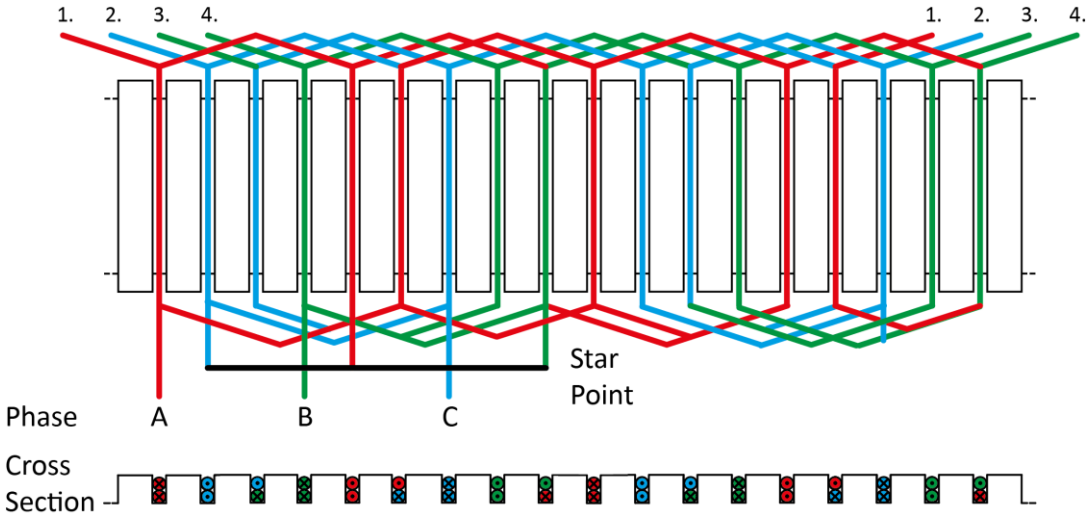

Figure 2.3 *Possible winding for machine with p_h = 2, n_S =11, p_l = 9 (shown in Figure 2.2(a))*

2.1.3. Finite Element Analysis

Analysis of the proposed PDD structures required the use of 2D FEA. This was accomplished using magneto-static simulations of the PDDs, positioned in the pull-out torque position. To find this position a scan of the PPR position with respect to the HSR and stator magnet arrays was conducted. From this aspects of the geometry shown in Figure 2.4(a) could be parametrically varied. Meshing, as seen in Figure 2.4(b), was implemented and the mesh density verified using mesh invariance testing. The physical aspects of the PDD as defined using the material properties, mechanical sets and magnetisation directions assigned as shown in Figure 2.4(c). Furthermore, an outer air region surrounding the PDD was defined with a tangential magnetic field condition. Solving the now defined FEA gave the values of torque per region and along with magnetic field plots such as those seen plot Figure 2.4(d). Additionally, transient magnetic analysis was employed to ascertain values of iron loss, eddy current loss, PP

and PPR forces. The same procedures were applied to 3D analysis, albeit with increased meshing and solving times.

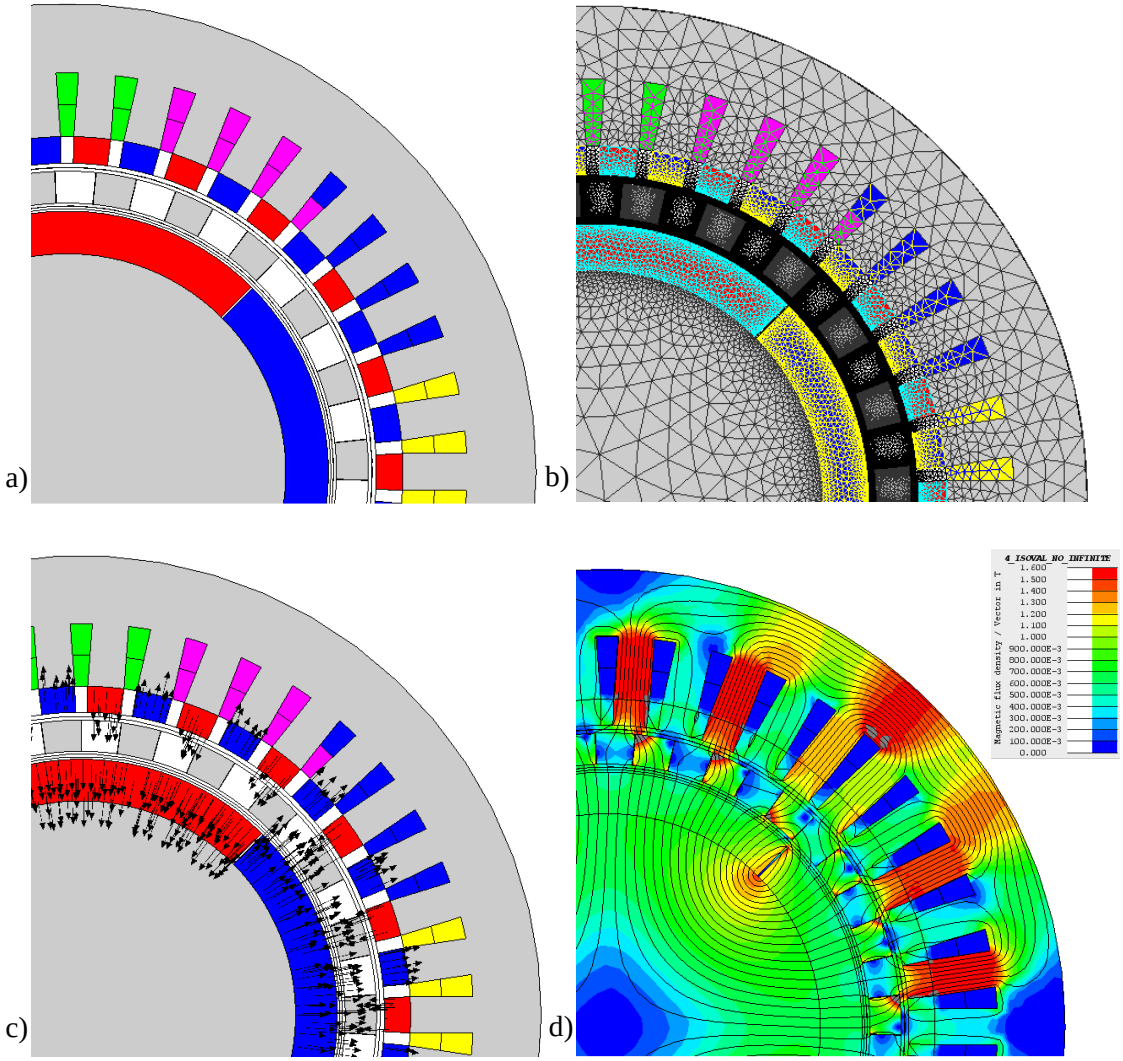

Figure 2.4 *FEA procedure a) Geometry b) Meshing c) Physics d) Solving*

Due to the two moving elements (HSR and PPR) two sliding mesh interfaces are required. In Flux 2D this is achieved by separating the air gap into three layers, the first layer being rotational, the second layer being static and the third layer being either rotational or static. The typical air gap mesh of a PDD with alternative windings is shown in Figure 2.5.

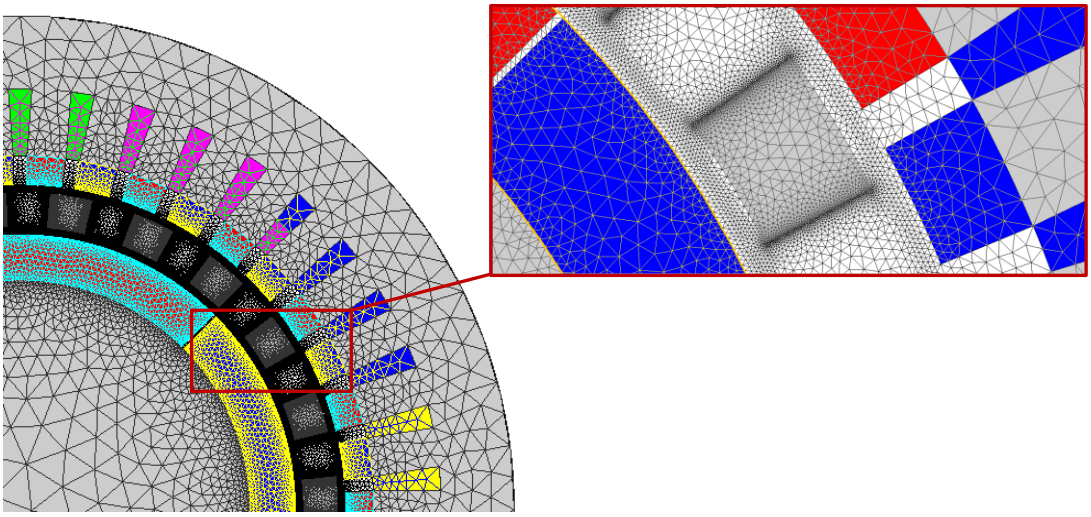

Figure 2.5 *PDD Meshing procedure*

2.2. Simulation Studies

Finite element analysis enabled the determination of the key parameters, including the fundamental airgap flux density, transmitted torque and flux linkage, is used to investigate the performance of the various topologies. The parameters of machines under investigation are given in Table 2.1. Where applicable the quoted equivalent shear stress values are taken at the gear element pull-out torque. Furthermore, the rated torque of the PDD was considered as 80% of the pull-out torque value.

Quantity	***Value***
HSR Pole Pairs	2-8
Gear Ratio	4-15
Cogging Torque Factor	1
Stator Bore Diameter	126mm
Stator Outer Diameter	176mm
Number of Electrical Phases	3
Airgap length (HSR-PPR)	1.5mm
Airgap length (PPR-Fixed Array)	1.5mm
Permanent Magnet Material	N38
Permanent Magnet (PM) Remanence	1.25T
Relative recoil permeability of PM	1.044

Table 2.1 *Parameters of studied alternative winding PDDs*

A single tooth per stationary PM array pole ($k_{con} = 1$) accommodates the winding configuration but results in a reduction of the stator magnet volume, and α is defined as the ratio of slot opening to slot pitch. Common values for induction machines may vary between 0.25 and 0.6 [2.8]. For $\alpha = 0.5$, Figure 2.6 shows the variation of the pull-out torque with gear ratio. It can be seen that the transmitted torque is reduced compared to the conventional PDD, Figure 2.1, employing a concentrated winding. The change of geometry, due to the change of gear ratio, results in a reduction of torque with gear ratio. This is further illustrated in Figure 2.7 and Figure 2.8, which show the space harmonic spectra of the radial flux density waveforms in the airgap adjacent to the HSR and due to the stator PM array. It can be seen that the magnitude of the asynchronous space harmonics, responsible for torque transmission, are reduced by adopting a 1-magnet pole per tooth configuration. However, this effect is alleviated for smaller values of α and as such low values of α are preferable. Figure 2.9 shows the variation of the equivalent shear stress with α, where it can be seen that it has a significant effect, but

it can also be seen that shear stresses similar to those of the original machine can be achieved for smaller values of α.

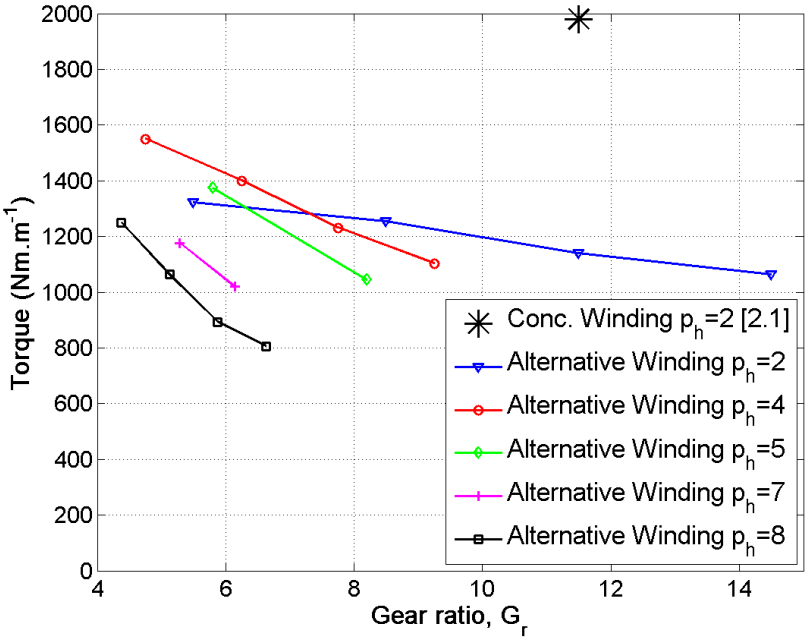

Figure 2.6 *Variation of pull-out torque with gear ratio for HSR pole numbers*

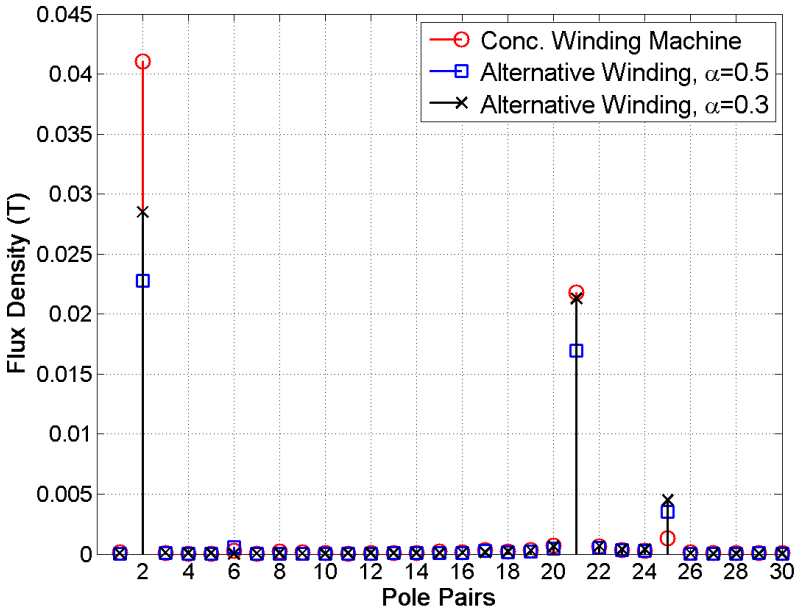

Figure 2.7 *Harmonic spectra of radial flux density resulting from the stationary magnet array, p_l=23 in the airgap adjacent to the HSR, p_h=2*

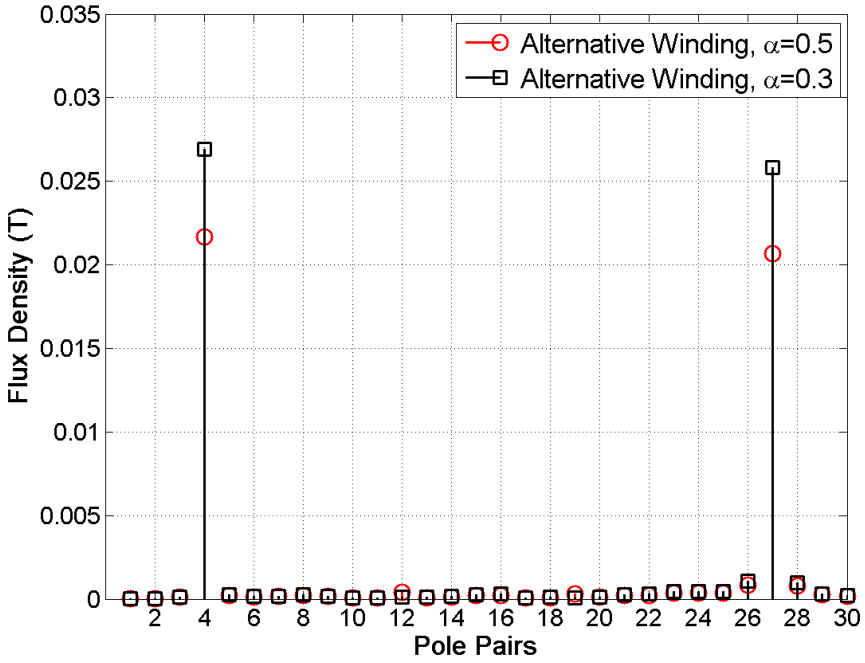

Figure 2.8 *Harmonic spectra of radial flux density resulting from the stationary magnet array, p_l=27 in the airgap adjacent to the HSR, p_h=4*

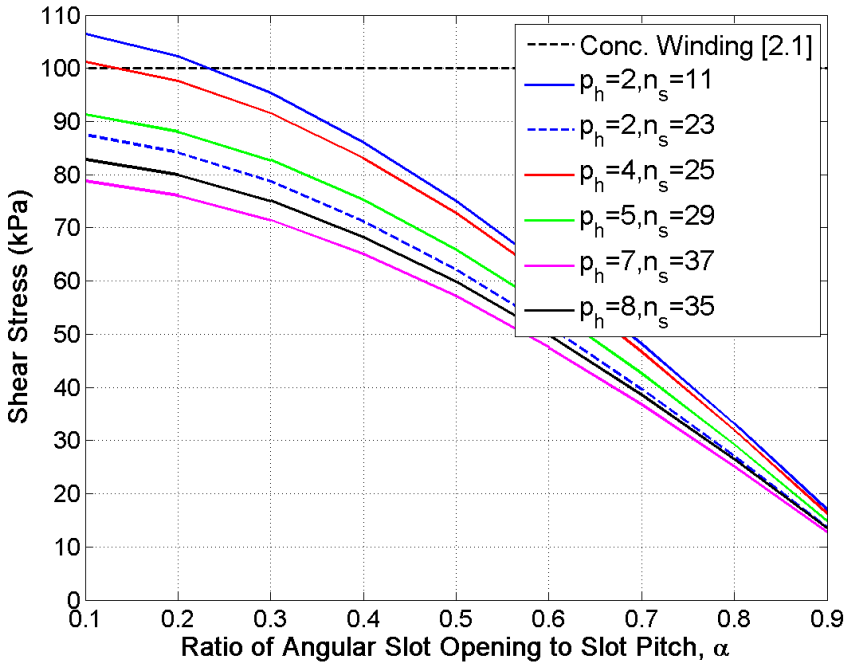

Figure 2.9 *Variation of shear stress at pull-out torque with the ratio of angular slot opening to slot pitch*

Following the case of a single pole per tooth, consecutive magnets of the same orientation, $k_{con} = 2,3, \ldots$ can be used to produce multiple teeth per stator magnet pole. This modification offers the machine designer more choice of gear ratios. However, the resulting equivalent shear stresses, as shown in Figure 2.10, are lower than those attained with a value of $k_{con} = 1$. Similarly to configurations with 1 stator pole per tooth, higher shear stresses are achieved with smaller values of α.

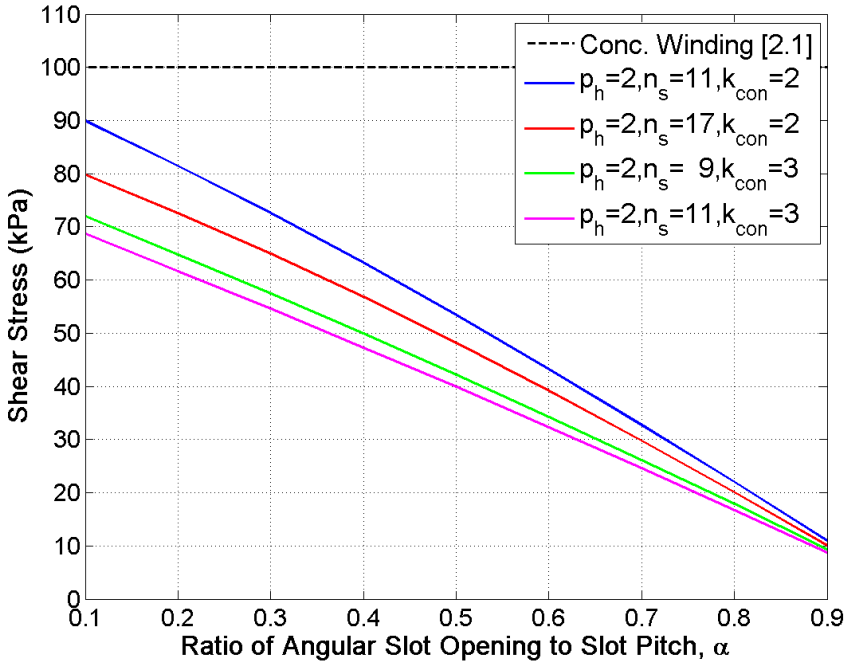

Figure 2.10 *Variation of shear stress at pull-out torque with the ratio of angular slot opening to slot pitch for $k_{con} > 1$*

Figure 2.11 and Figure 2.12 show the variation of the required active length with α, in order to achieve the rated output torque of 120Nm (equal to the machine equipped with concentrated winding [2.1]). The machines with alternative windings require greater active length than the conventional concentrated winding machine. Figure 2.13 and Figure 2.14 show the variation of efficiency at rated power, where only copper losses P_{cu} are considered. For many values of α, the alternative winding machines exceeded the efficiency of the concentrated winding machine.

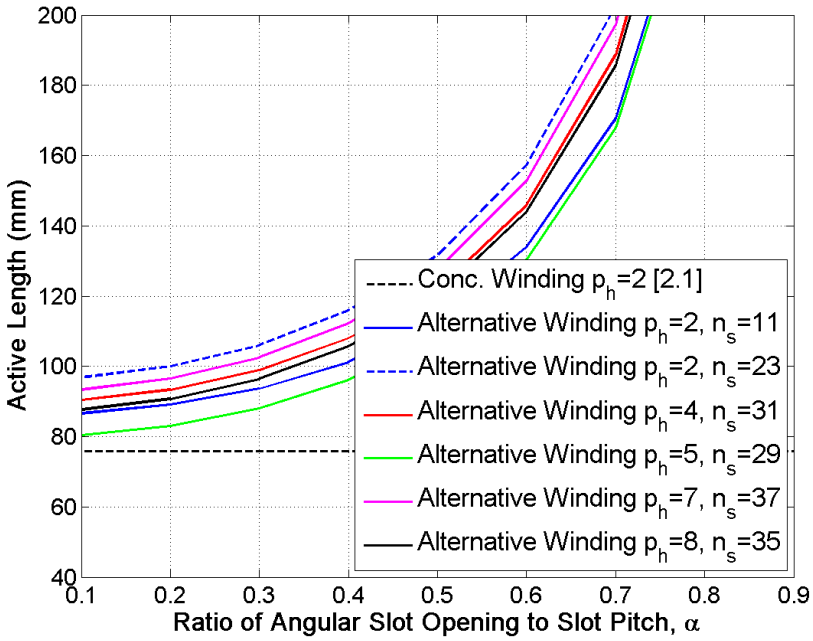

Figure 2.11 *Variation of Required active length with the ratio of angular slot opening to slot pitch when kcon =1*

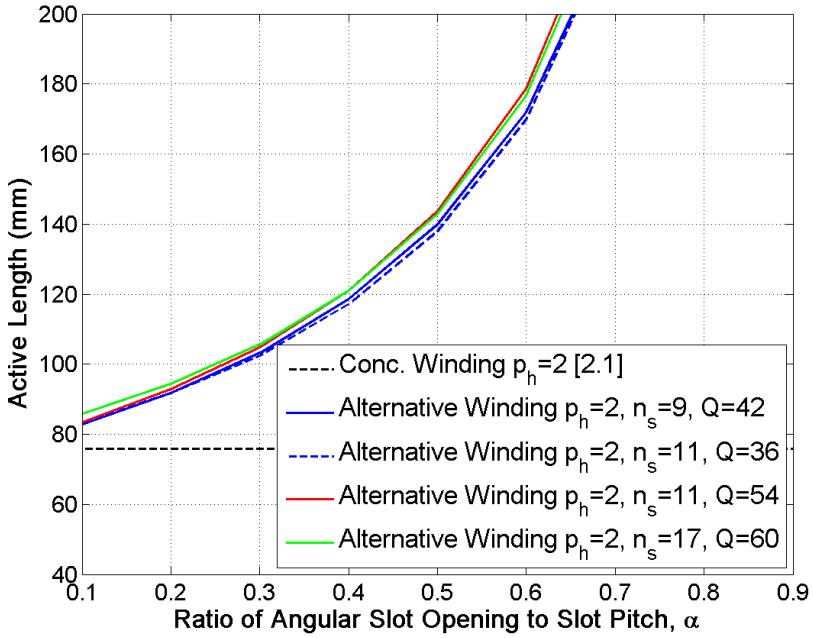

Figure 2.12 *Variation of Required active length with the ratio of angular slot opening to slot pitch when kcon >1*

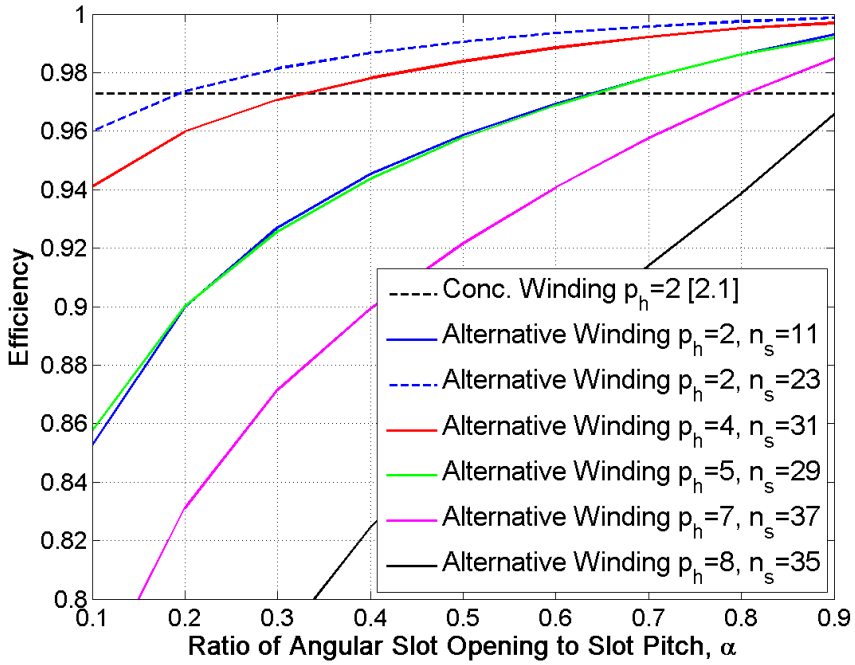

Figure 2.13 *Variation of Efficiency with the ratio of angular slot opening to slot pitch when kcon =1 at rated power, as in [2.1]*

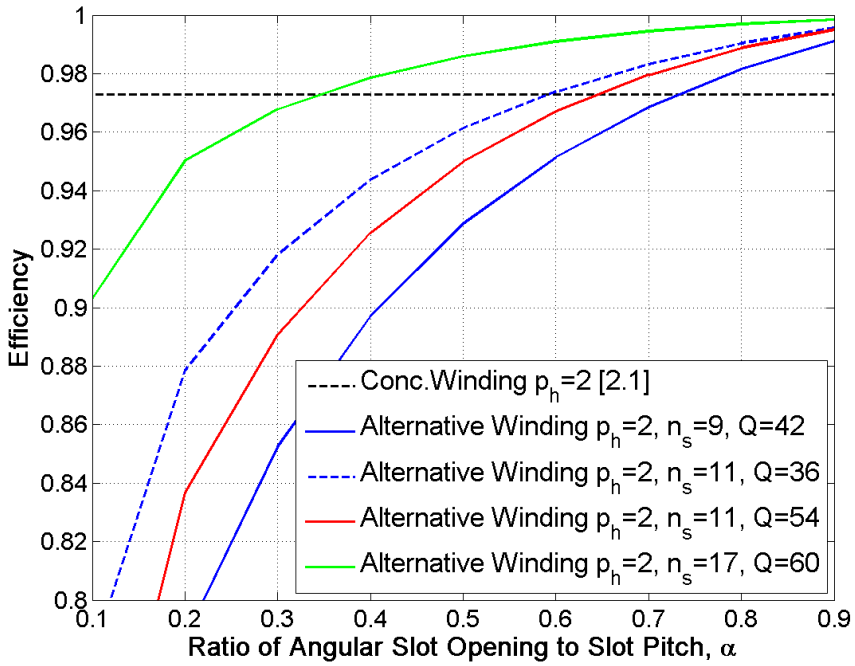

Figure 2.14 *Variation of Efficiency with the ratio of angular slot opening to slot pitch when kcon >1 at rated power, as in [2.1]*

It can be seen that efficiency increased with increased α, albeit at the expense of increased size. However, the PDDs with lower gear ratios can potentially be operated at higher speeds, as the mechanical constraints which restrict the maximum speed of the HSR are similar for all machines. The resulting maximum achievable power of those machines is shown in Figure 2.15. The machines with lower gear ratios show increased efficiencies when operated at higher speed, as seen in Figure 2.14 and Figure 2.17 which show the variations of the efficiency with α.

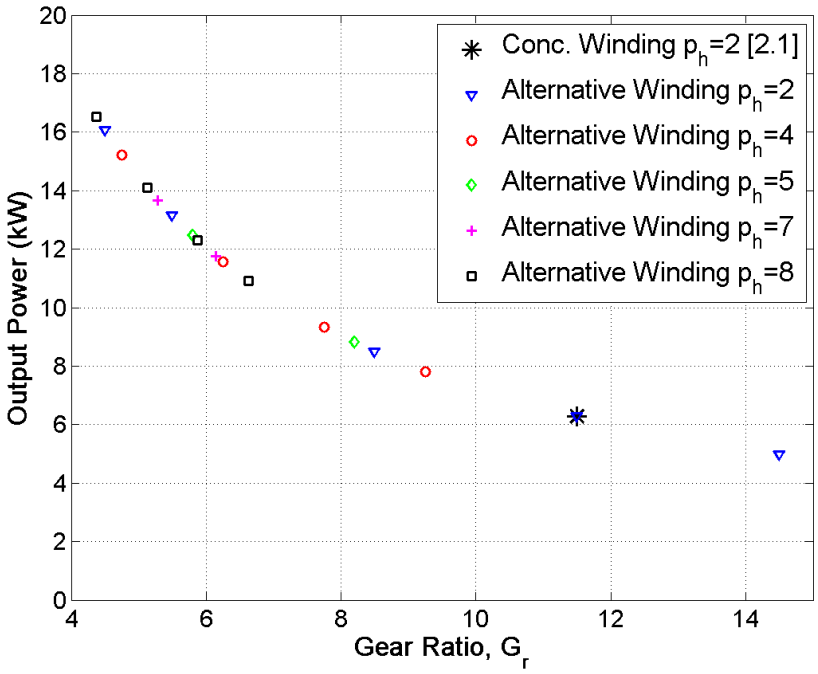

Figure 2.15 *Variation of potential output power with PPR at 500rpm, as in [2.1]*

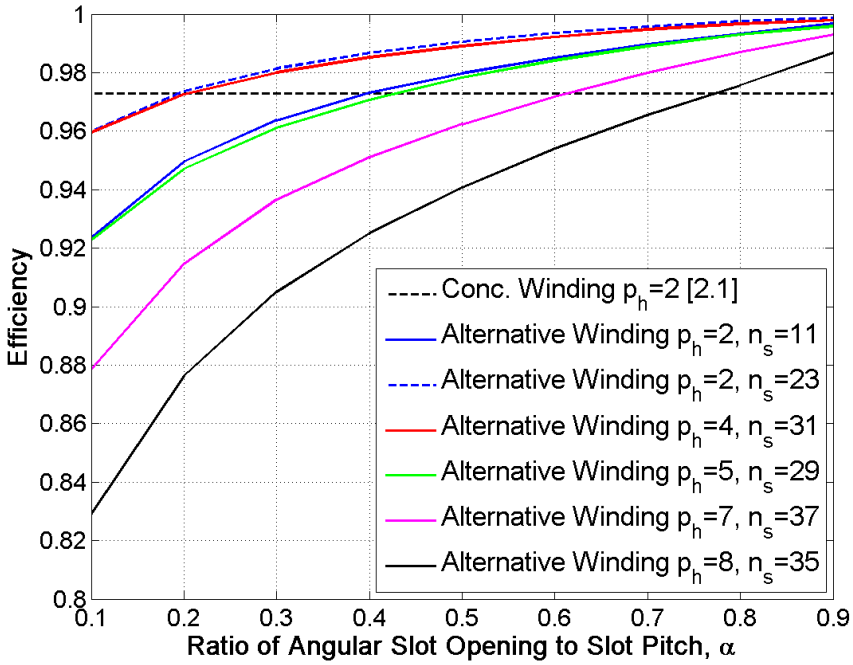

Figure 2.16 *Variation of Efficiency with the ratio of angular slot opening to slot pitch when k_{con} = 1 (Maximum output power)*

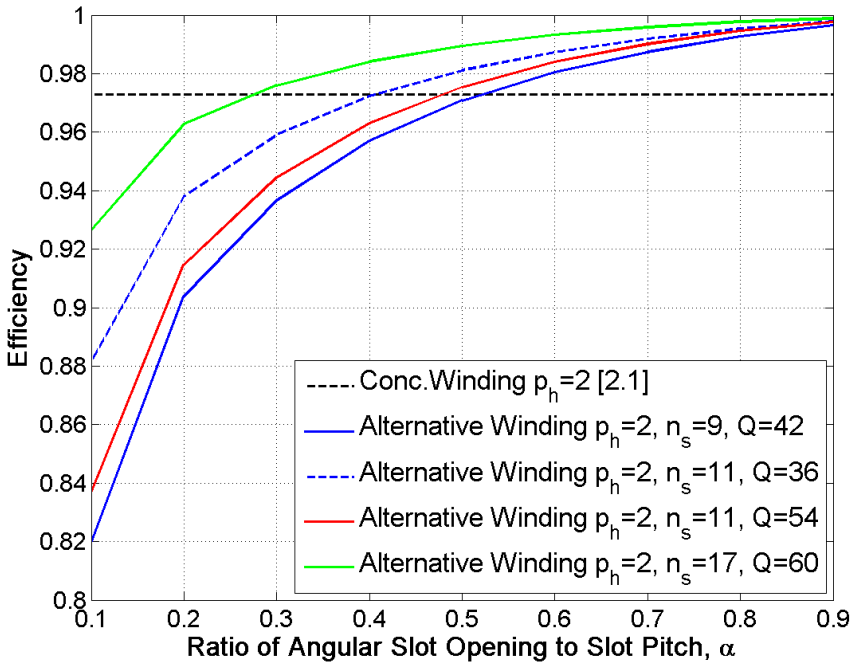

Figure 2.17 *Variation of Efficiency with the ratio of angular slot opening to slot pitch when k_{con} > 1 1 (Maximum output power)*

In the proposed machine topology a single stator magnet is bonded to a single tooth. This leads to a stator tooth carrying the flux from a stator magnet, the magnets on the high speed rotor and flux produced by the stator winding. This can lead to increased flux densities in the teeth and the back-iron. The resulting potential saturation can be alleviated by increasing the thickness of the back-iron and the teeth without increasing the width of a stator permanent magnet. Although this may also reduce the iron losses, it may result in increased copper losses due to reductions in the slot areas.

Three designs have been selected for further analysis, including the iron losses, where the hysteresis P_{hyst}, classical eddy current P_{eddy} and excess eddy current P_{ex} components are considered and given by:

$$P_{iron} = P_{hyst} + P_{eddy} + P_{ex} \tag{2.13}$$

$$P_{hyst} = k_h B_m^{\beta} f \tag{2.14}$$

$$P_{eddy} = \frac{\sigma d^2}{12T} \int_0^T \left(\frac{dB(t)}{dt} \right)^2 dt \tag{2.15}$$

$$P_{ex} = \frac{k_{ex}}{T} \int_0^T \left(\frac{dB(t)}{dt} \right)^{1.5} dt \tag{2.16}$$

where B_m is the peak magnetic flux density, f is the electrical frequency, d is the lamination thickness, σ is the electrical conductivity and k_h, β and k_e are constants determined from iron loss tests under sinusoidal flux density waveforms and covering a range of frequencies and flux densities. The FEA package was used along with the iron loss constant values given in Table 2.2 to calculate the iron loss of each design [2.9] [2.10].

Symbol	***Quantity***	***Value***	***Unit***
k_h	Hysteresis loss coefficient	17.9	$WsT^{-2}kg^{-1}$
β	Hysteresis loss exponent	2.0	
k_{ex}	Excess loss coefficient	2.0×10^{-4}	$Ws^{1.5}T^{-1.5}kg^{-1}$
d	Lamination thickness	0.35	mm
σ	Conductivity of laminations	2.22×10^{6}	$\Omega^{-1}m^{-1}$

Table 2.2 *Parameters for iron loss calculations*

For the pole-pieces the frequency is different from that of the stator and is given by:

$$f_{pp} = \frac{G_r - 1}{G_r} f \tag{2.17}$$

The strategy for selecting an optimal PDD with alternative winding involved maximising both airgap shear stress and efficiency for the rated output conditions (PPR speed 500rpm, PPR torque 120Nm) within the stator outer diameter, 178mm and stator bore diameter 126mm. To achieve the rated torque value the machine active length is allowed to vary. Due to the changes in geometry, the fundamental flux linking the HSR to the stator winding varies, thus causing a change in the required current density.

Table 2.3 summarises the parameters and performance of the selected designs. It can be seen that PDD designs with alternative windings can be achieved with high equivalent airgap shear stresses as well as high efficiencies and power factors.

Quantity	*Machine A*	*Machine B*	*Machine C*
Winding Type	Concentrated	Alternative	
HSR Pole Pairs	2	2	4
Gear Ratio	11.5	11.5	7.75
Number of slots	6	42	54
PPR speed (rpm)	500	500	500
Rated Torque (Nm)	120	120	120
Stator outer diameter (mm)	178	178	178
Machine Axial Length (mm)	75	111	99
Copper losses (W)	175	102	165
Iron losses (W)	102	124	172
Efficiency	0.958	0.965	0.949
Power factor	0.95	0.99	0.98
Magnet Mass (kg)	3.27	4.46	3.74
Current Density ($A_{rms}mm^{-2}$)	1.5	1.3	1.7
Equivalent Airgap Shear Stress (kPa)	101.4	73.2	71.0

Table 2.3 *Parameters of optimised alternative winding PDDs*

2.3. Forces on the Pole Piece Rotor

In PDDs, the stator and HSR are very similar to those of conventional permanent magnet machines, and they would essentially exhibit similar stresses. However, the PPR is relatively unique, and its manufacture may pose some challenges, since the pole-pieces must be laminated and essentially held in a non-magnetic and non-conducting structure. Therefore, the understanding of the dynamic and static forces the pole-pieces are subjected to is essential for the successful realisation of the rotor.

At rated load, Figure 2.18 and Figure 2.19, show the variation of the radial and circumferential forces exhibited by a pole-piece over a 60 degree rotation of the PPR. These forces were calculated by integrating the Maxwell stress tensor around each PP. The PPR forces were then produced by summing the component forces of each PP.

These have been presented over 60 degrees for illustration purposes, since the period for the forces depends on the gear ratio. If the gear ratio is non-integer the period is p_h rotations of the PPR and n_s rotations of HSR. If the gear ratio is integer, the period is one rotation of the PPR and G_r rotations of the high-rotor. Therefore, for machines A and B, the period is 720º rotation of the PPR, while for machine C the period is 1440º rotation of the PPR. The average radial forces for machines A, B and C are 36N, -70N and -59N, respectively.

Figure 2.20 and Figure 2.21, show the harmonic spectra of the radial and circumferential forces exhibited by a pole-piece. It is worth noting that some spectral leakage can be seen due to the samples number and finite nature of the force profile. It can be seen that for the 3 machines the first largest harmonic order is $2p_h p_l$. The corresponding frequencies of the harmonics are given by:

$$\omega_n = \frac{n}{p_h}\omega_{pp} \tag{2.18}$$

where n is the harmonic order and $\omega_{pp}$is the speed of the PPR.

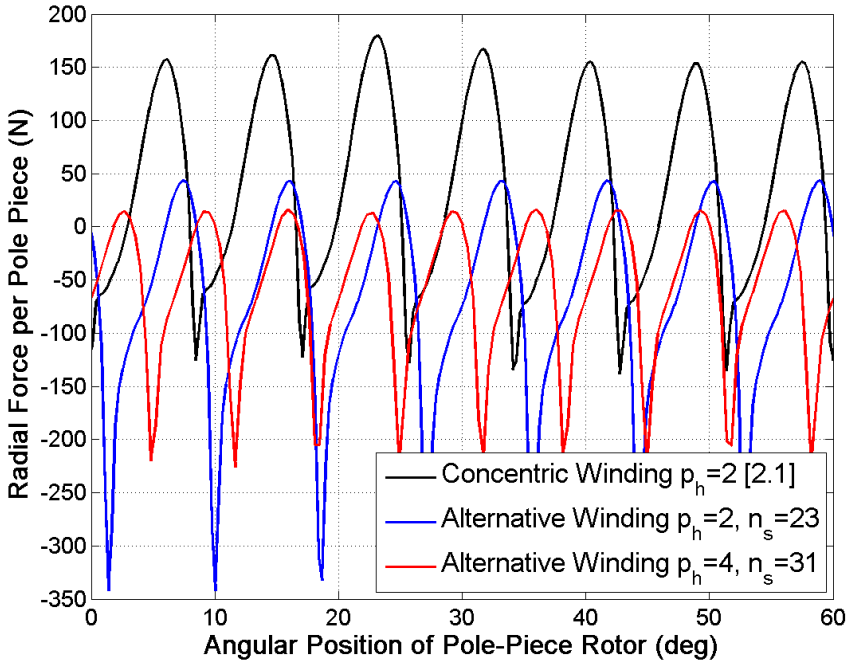

Figure 2.18 *Variation of the radial force (per pole piece) with PPR angular position at rated load*

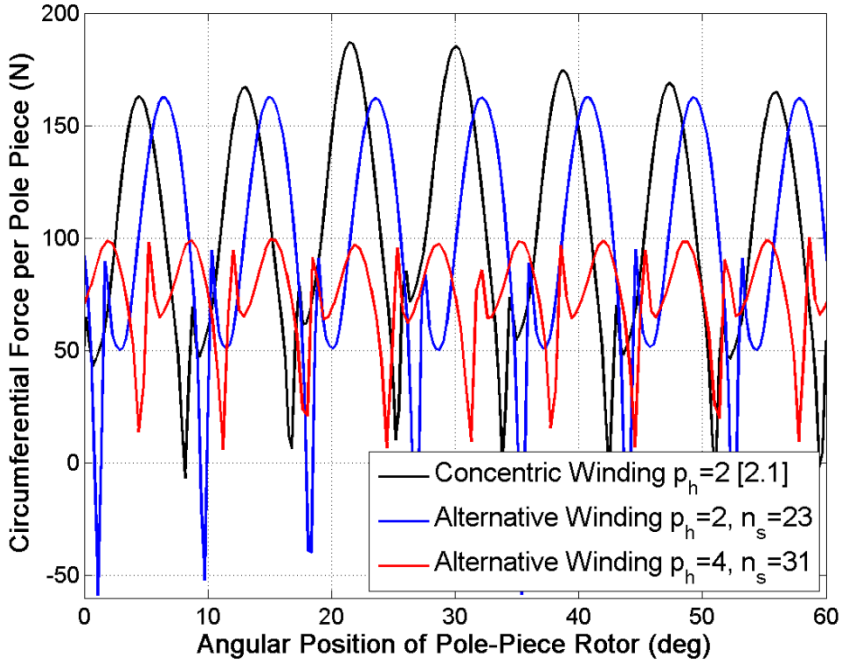

Figure 2.19 *Variation of the circumferential force (per pole piece) with PPR angular position at rated load*

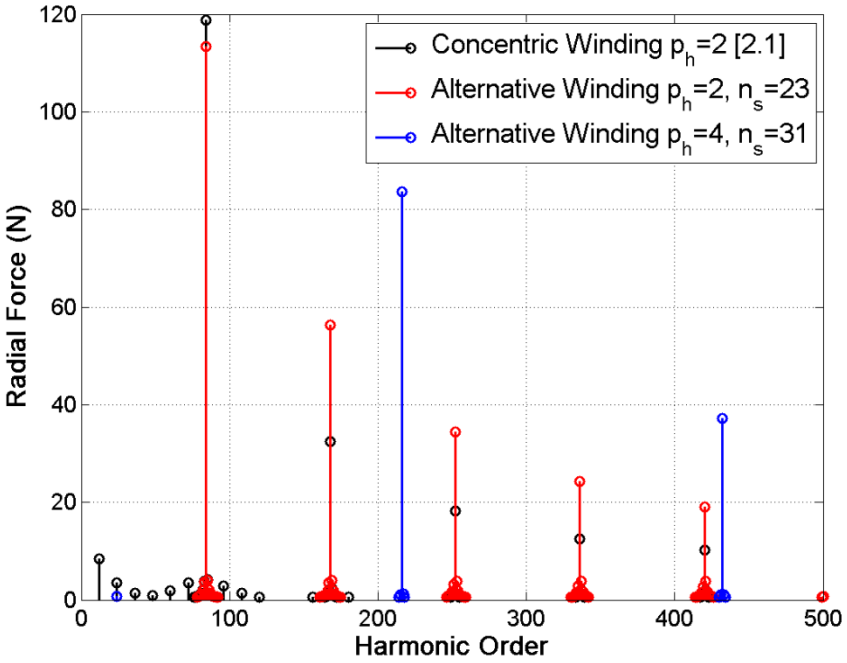

Figure 2.20 *Harmonic spectra of radial force profile (per pole piece) at rated load*

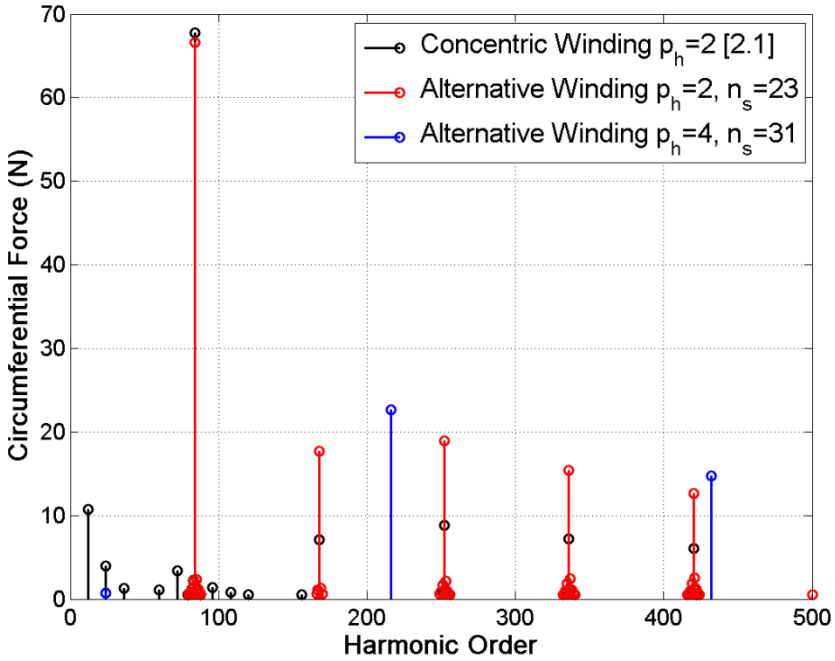

Figure 2.21 *Harmonic spectra of the circumferential force profile (per pole-piece) at rated load*

Figure 2.22 shows the contour of the total force on the PPR rotor over a 360^{o} rotation of the PPR, where it can be seen that the PPR rotor equipped with alternative windings exhibit larger unbalanced magnetic pull. At no load, Figure 2.23and Figure 2.24, show the variation of the radial and circumferential forces exhibited by a pole-piece. The average radial force during the no-load condition for machines A, B and C are 0.5N, 107N and -82N, respectively.

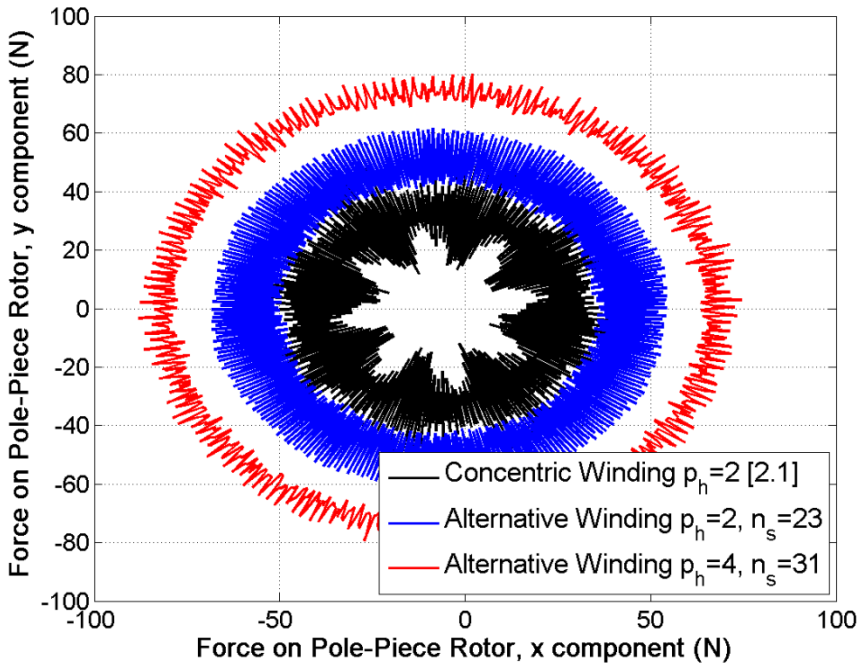

Figure 2.22 *Variation of total PPR forces at rated load*

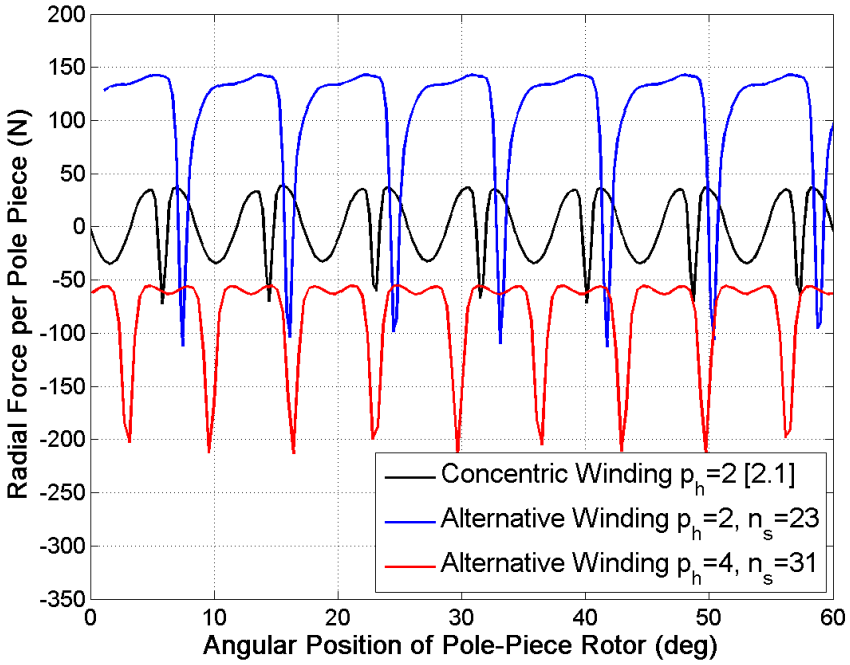

Figure 2.23 *Variation of the radial force (per pole piece) with PPR angular position at no load*

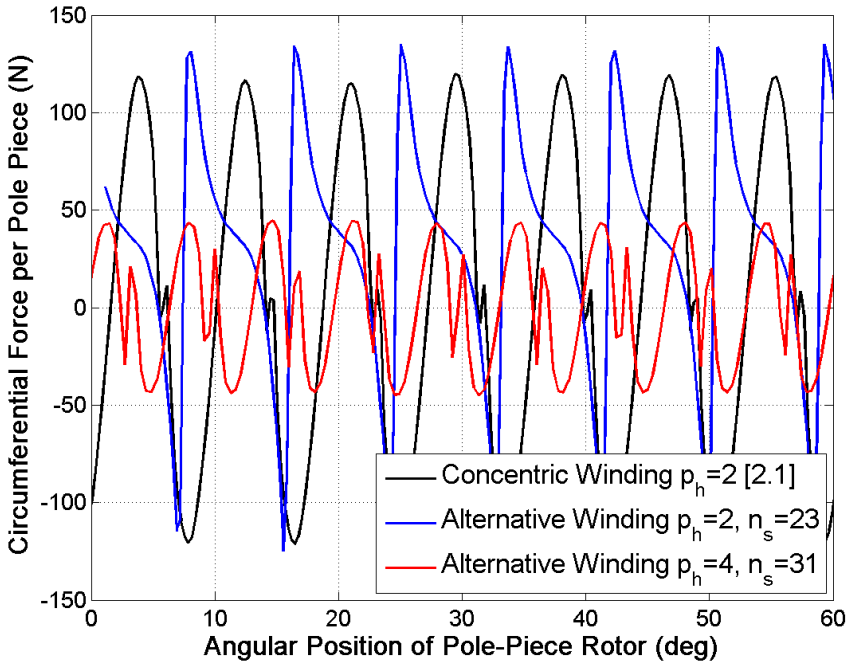

Figure 2.24 *Variation of the circumferential force (per pole piece) with PPR angular position at no load*

It can be seen that the average forces exhibited by a pole-piece are significantly affected by the load condition. Figure 2.25 and Figure 2.26, show the harmonic spectra of the radial and circumferential forces exhibited by a pole-piece. Figure 2.27 shows the contour of the total force on the PPR over a 360^{o} rotation of the PPR. It can be seen that the average unbalanced magnetic pull is similar to the rated condition.

In both the no load and rated load conditions it can be seen that the PDDs equipped with alternative windings at subjected to higher forces, both per PP and as a PPR. This is due to there no longer being a complete array of magnets, as in the concentrated winding machine, and is also influenced by the selected gear ratios

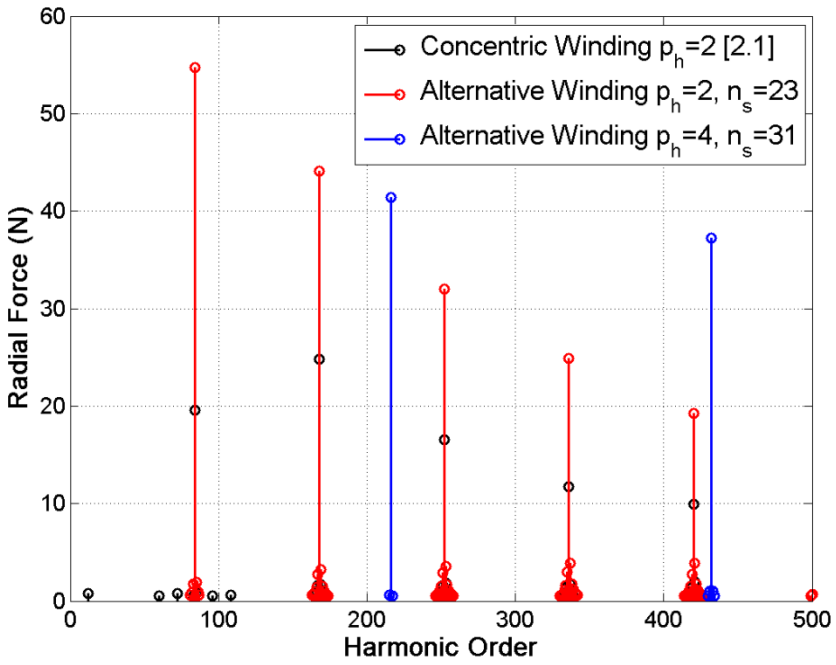

Figure 2.25 *Harmonic spectra of the radial force profile (per pole-piece) at no load*

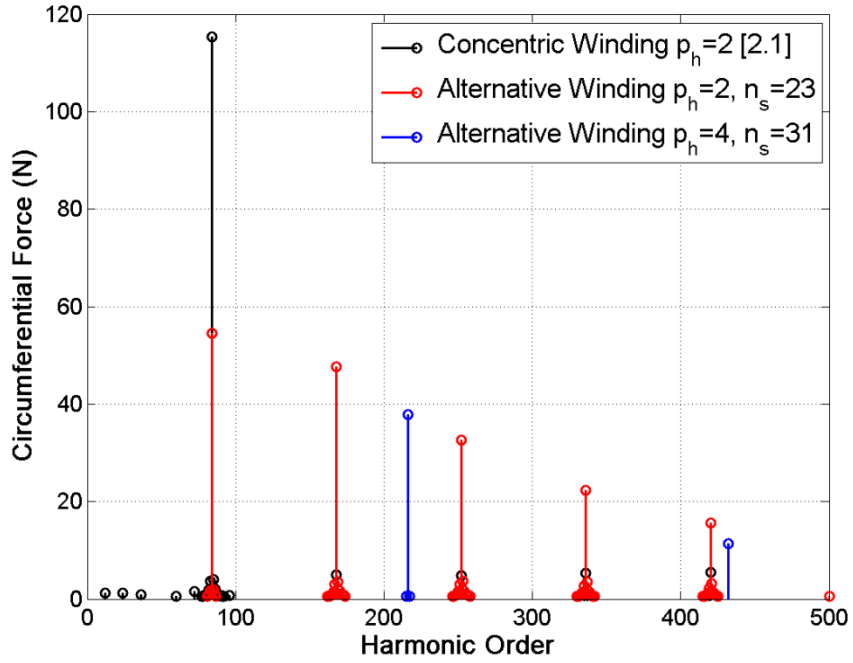

Figure 2.26 *Harmonic spectra of the circumferential force profile (per pole-piece) at no load*

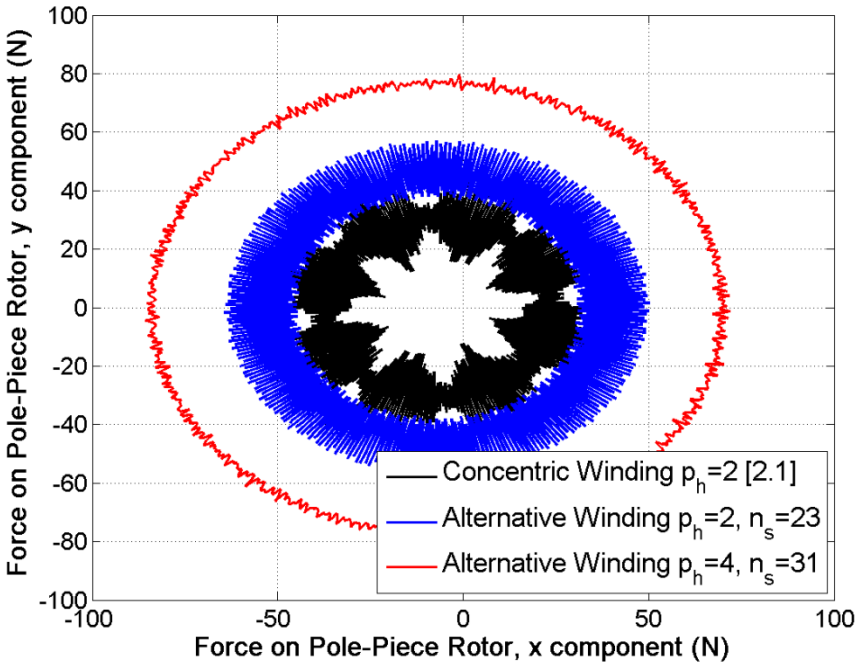

Figure 2.27 *Variation of total PPR forces at no load*

2.4. Conclusion

A technique for the selection of PDDs equipped alternative windings is presented. Simulation studies and comparisons with an existing PDD equipped with a concentrated winding are undertaken. Low values α (0.25-0.3) of are required to achieve high shear stress. It is shown that PDDs with alternative windings can be realised, albeit with reduced torque density. Special attention was given to the forces exhibited by a pole-piece, and it was shown that both the average and dynamic forces are affected by the load condition. In both the no load and rated load conditions it can be seen that the PDDs equipped with alternative windings at subjected to higher forces. Nevertheless, shear stresses and power factors in excess of 70kPa and 0.98, respectively, can still be achieved. It is shown that a significant advantage, in terms of ease of manufacture, can be achieved whilst maintaining torque densities in excess of 45kNm/m^3, under natural air cooling conditions. Furthermore, this is achieved at power factors in excess of 0.9 and with current densities below $2A_{rms}/mm^2$.

2.5. References

[2.1] K. Atallah, J. Rens, S. Mezani, and D. Howe, "A Novel 'Pseudo ' Direct-Drive Brushless Permanent Magnet Machine," *IEEE Trans. Magn.*, vol. 44, no. 11, pp. 4349–4352, 2008.

[2.2] M. Bouheraoua, J. Wang, and K. Atallah, "Observer Based State Feedback Controller Design for Pseudo Direct Drive using Genetic Algorithm," in *6th IET International Conference on Power Electronics, Machines and Drives (PEMD)*, 2012, pp. 1–6.

[2.3] M. Bouheraoua, J. Wang, and K. Atallah, "Speed control for a Pseudo Direct Drive permanent magnet machine with one position sensor on low-speed rotor," *2013 Int. Electr. Mach. Drives Conf.*, pp. 986–992, May 2013.

[2.4] S. Gerber and R. Wang, "Analysis of the End-Effects in Magnetic Gears and Magnetically Geared Machines," in *International Conference on Electrical Machines (ICEM)*, 2014, pp. 396–402.

[2.5] D. J. Evans and Z. Q. Zhu, "Optimal torque matching of a magnetic gear within a permanent magnet machine," *IEEE Int. Electr. Mach. Drives Conf.*, pp. 995–1000, 2011.

[2.6] Z. Q. Zhu and D. Howe, "Influence of design parameters on cogging torque in permanent magnet machines," *IEEE Trans. Energy Convers.*, vol. 15, no. 4, pp. 407–412, 2000.

[2.7] N. Bianchi and M. Dai Pre, "Use of the star of slots in designing fractional-slot single-layer synchronous motors," *IEE Proc. - Electr. Power Appl.*, vol. 153, no. 3, p. 459, 2006.

[2.8] E. K. Appiah, A. A. Jimoh, G. M'boungui, and J. L. Munda, "Effects of slot opening on the performance of a six phase squirrel cage induction machine using finite element and field analysis," in *IEEE AFRICON Conference*, 2013, pp. 0–4.

[2.9] K. Atallah, Z. Q. Zhu, and D. Howe, "An Improved Method For Predicting Iron Losses In Brushless Permanent Magnet DC Drives," *IEEE Trans. Magn.*, vol. 28, no. 5, pp. 2997–2999, 1992.

[2.10] D. M. Ionel, M. Popescu, S. J. Dellinger, T. J. E. Miller, R. J. Heideman, and M. I. McGilp, "On the variation with flux and frequency of the core loss coefficients in electrical machines," *IEEE Trans. Ind. Appl.*, vol. 42, no. 3, pp. 658–667, 2006.

Chapter 3

Electromagnetic design of an Axial Magnetic Gear

MG's are usually employed in applications which require a compact high performance transmission of torque. A drawback of this is the use of expensive rare-earth magnets and therefore optimisation is vital to ensure effective use of magnetic material, gear volume and overall mass.

Since the development of the CMG (Co-axial Magnetic Gear) considerable efforts have been made to develop the co-axial topology [3.1]. The AMG (Axial Magnetic Gear) has received less attention and as such parameters which remain specific to the AMG topology may require further analysis [3.2] [3.3]. Modifications to the conventional AMG include the use of Halbach arrays [3.4].

The AMG shown in Figure 3.1 has the same three components as the CMG, with the high pole number magnet array considered as fixed and consequently magnetic gearing between the HSR and the PPR. A reason for the lack of interest in the AMG may result from the pole piece structure as it undergoes significant axial forces. Therefore there is motivation to optimise the structure to be both effective at transmitting torque whilst achieving a higher level of mechanical integrity. To date limited literature has been published regarding the specifics of the pole piece rotor structure. Patents regarding the structure for radial magnetic gears exist which outline the magnetic and mechanical characteristics of novel pole piece designs [3.5][3.6]. An attempt was made to skew the trapezoidal poles to mitigate cogging torque for pole combinations which exhibit poor cogging torque factors in [3.7].

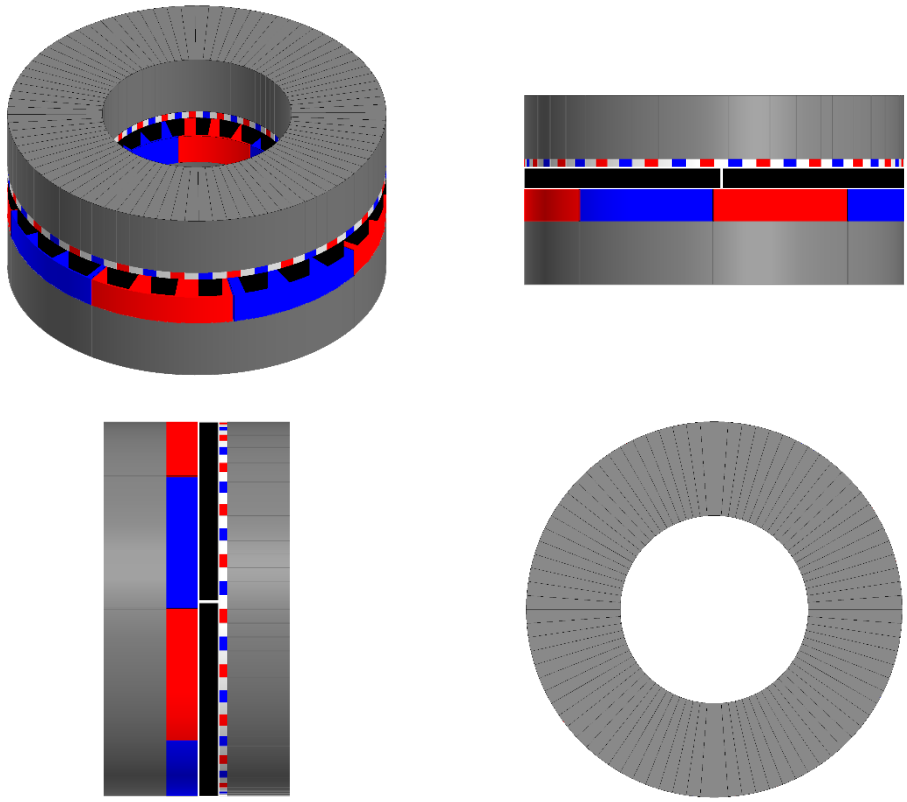

Figure 3.1 *Axial magnetic gear structure*

Section 3.1 presents key considerations when sizing an AMG and Section 3.2 examines the difficulties of modelling AMGs. A magnetic optimisation of the AMG is described in Section 3.3 with the influence of the pole piece rotor structure upon magnetic gear performance considered in Section 3.4.

3.1. Axial Magnetic Gear Sizing

The scaling of the torque T and the torque per active volume T/V of the axial magnetic gear can initially be determined by:

$$T = \sigma \int_{0}^{2\pi} \int_{\lambda r_o}^{r_o} r^2 . dr . d\theta \tag{3.1}$$

$$T = \frac{2\pi\sigma}{3} r_o^3 (1 - \lambda^3) \tag{3.2}$$

$$V = \pi r_o^2 (1 - \lambda^2) L_a \tag{3.3}$$

$$\frac{T}{V} = \frac{2\sigma}{3L_a} r_o \frac{(1 - \lambda^3)}{(1 - \lambda^2)} \tag{3.4}$$

where λ is the ratio of inner to outer diameter, σ is airgap shear stress, V is the active volume and L_a is the active length. For a constant outer radius, shear stress, air gap flux density and active length the torque and torque per magnet volume scale as shown in Figure 3.2.

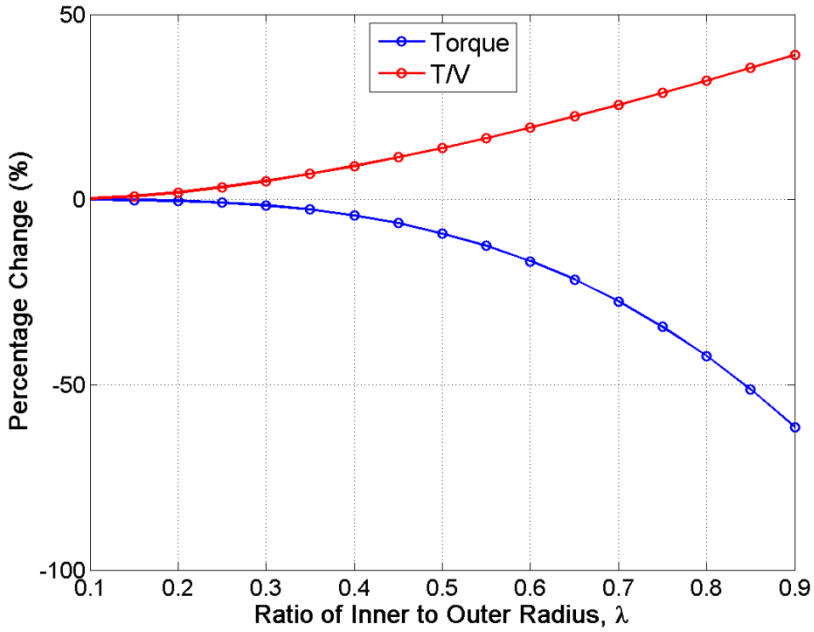

Figure 3.2 *Variation of key AMG parameters due to the ratio of inner to outer radius, λ*

3.2. Modelling Axial Magnetic Gears

Analytical solutions have been proposed as a less computational intensive alternative for investigating the performance of magnetic gears. To analyse the problem the 3D axial geometry is often simplified to a 2D representation via a rectilinear transformation about the mean radius and the PPs are usually assumed to be infinitely permeable [3.8].

These solutions have achieved accurate flux density prediction but provide limited use for considering torque output as errors as high as ~30% have been reported. The rectilinear transformation implies a constant shear stress independent of radial position and zero radial flux along the PPs toward the centre of the gear. Using FEA software (Cedrat Flux 3D) an intense flux focusing effect can be seen in the PPs toward the centre of the magnetic gear as shown in Figure 3.3 with the upper magnet array removed for clarity.

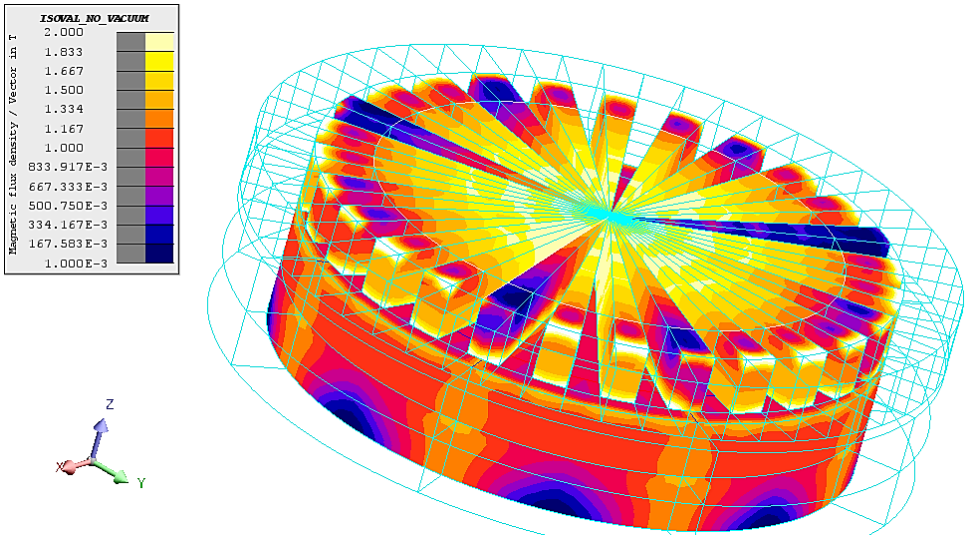

Figure 3.3 *Flux in a pole piece rotor extended to the Z-axis*

As the flux density waveforms were shown to closely represent that of the FEA model this indicates that the 2D approach of unfolding the gear about the mean radius is unsatisfactory in some instances. The mean radius should be formed from the radius at which the integrals of torque T are equal, as given by:

$$\int_{\lambda r_0}^{r_m} \sigma \mathrm{Ar}.\,\mathrm{dr} = \int_{r_m}^{r_o} \sigma \mathrm{Ar}.\,\mathrm{dr} \tag{3.5}$$

where A is the area, r is the radius and σ is the shear stress. When the shear stress is assumed to be constant the mean radius r_m is defined as:

$$r_m = \frac{r_i + r_o}{2} \tag{3.6}$$

where r_i is the inner radius. The shear stress as a function of radial position $\sigma(r)$ can be found using Maxwell's stress tensor as given by:

$$\sigma(\mathrm{r}) = \frac{1}{\mu_0} B_\theta(r) B_z(r) \tag{3.7}$$

where B_θ and B_z are the circumferential and axial flux density components which contribute to torque transmission and B_r is a flux leakage component in the radial direction. These cylindrical flux density components are given by:

$$B_r(r) = B_x(r)\cos(\theta) + B_y(r)\sin(\theta) \tag{3.8}$$

$$B_\theta(r) = -B_x(r)\sin(\theta) + B_y(r)\cos(\theta) \tag{3.9}$$

$$B_z(r) = B_z(r) \tag{3.10}$$

where θ is the angular position and the Cartesian flux density components are B_x, B_y and B_z respectively.

Figure 3.4 shows the variation of shear stress as a function of diametric positon. It is worth noting that the value of shear stress at a certain diametric position is given by the average values of the shear stresses around a circular path in the PPR-fixed array side air gap. The shear stress shows less variation for higher ratios of inner to outer radius, λ. A significant reduction in the torque producing component of shear stress is seen at the outer diameter (OD) due to the reduction in B_θ . Figure 3.5 shows the radial flux density component is greater for lower values of λ. Therefore, the discrepancy in the calculated

torque output using a rectilinear transformation would be particularly exaggerated for lower values of λ, such as the gear presented with λ=0.42 from [3.8].

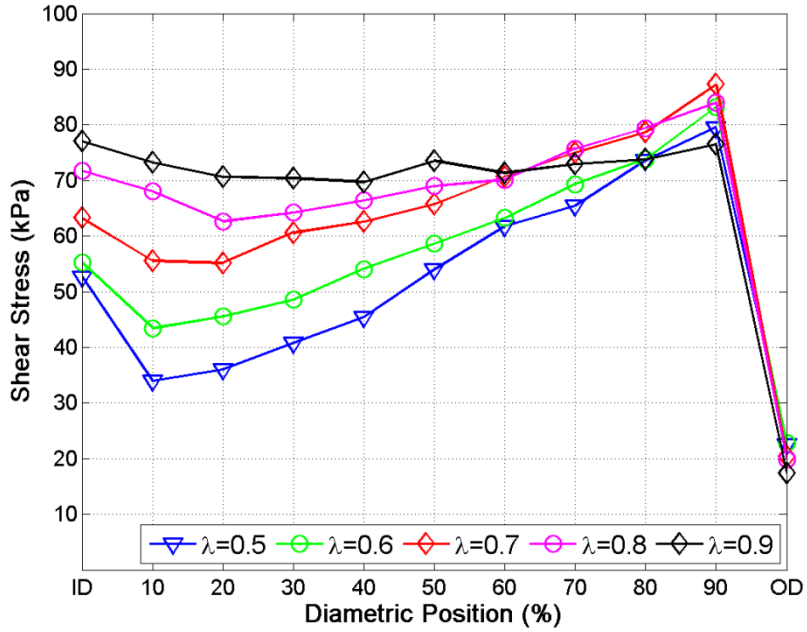

Figure 3.4 *Variation of shear stress across magnet surface of AMG*

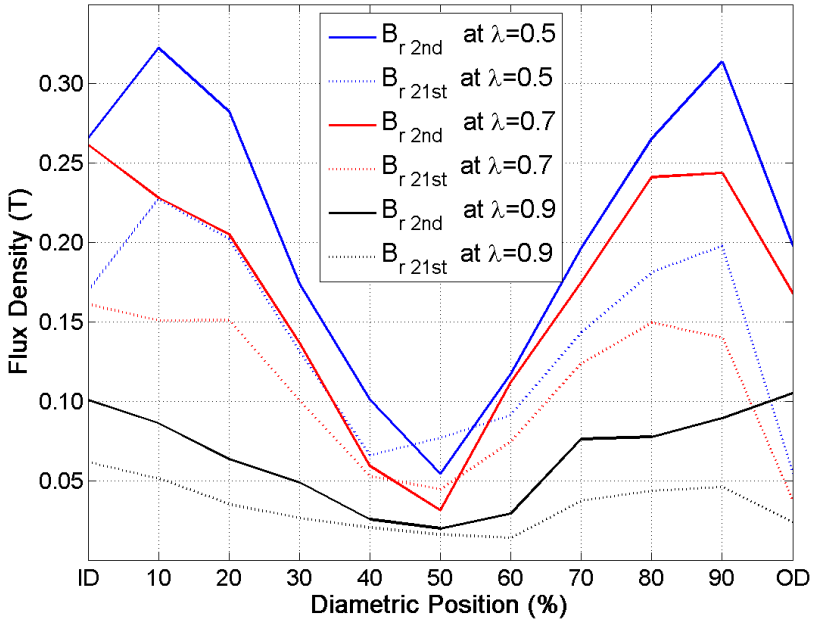

Figure 3.5 *Leakage flux density (radial) within pole pieces*

As this chapter will investigate a range of values for λ and full 3D FEA will be used, it is worth noting that a typical solution consisted of ~4million volume elements, taking ~3hours to mesh and ~3hours per step to solve.

3.3. Axial Magnetic Gear Optimisation

The design of a cost effective and torque dense AMG requires an understanding of the key parameters of the AMG including air gap lengths, the PP axial thickness, distribution of magnetic material and inner to outer diameter ratio, λ. These have to be simultaneously considered as their influence may not be independent. Key performance indicators include the torque and the axial force on the PPR which are both important for the mechanical design and realisation of an AMG. The investigation parameters outlined in Table 3.1 were conducted for several gear ratios.

Parameter under investigation / ***Fixed Parameter***	Pole Piece Thickness	Air Gap Length (per air gap)	Inner to Outer Diameter Ratio, λ	Magnetic Material Distribution	Total Magnetic Material Volume
Total Magnet Material Volume	$2x10^5 mm^3$ to	$2x10^5 mm^3$	$2x10^5 mm^3$	$2x10^5 mm^3$	
Magnet Material Distribution	50:50	50:50	50:50		
Inner to outer diameter ratio, λ	0.55	0.55			
Air Gap Length (per air gap)	2mm				
Pole Piece Thickness					

Table 3.1 *Design approach*

The parameters given in Table 3.2 were used during the computer intensive, time-consuming 3D FEA. Quoted torque values are given by the pull-out torque of the AMG and the shear stress is the equivalent shear stress at the gear pull-out torque.

Parameter	*Value*
Outer Diameter	200mm
Permanent Magnetic Material	N38
Permanent Magnet (PM) Remanence	1.25T
Relative recoil permeability of PM	1.044
Ferromagnetic Material	Somaloy® 1000 3P
HSR Magnet Array	Full pole arc, North-South
Fixed Magnet Array	Full pole arc, Halbach
Pole Piece	Trapezoidal
FEA Analysis Type	Magneto-static
Magnetic Gear Position	Pull-out torque

Table 3.2 *FEA Model parameters*

3.3.1. Effect of the Pole Piece Axial Thickness

The PP thickness is crucial to the operation of the AMG. The torque transmission capability increases rapidly with increasing PP thickness up to an optimum after which a more gradual reduction in torque transmission is found as shown in Figure 3.6. Selecting a low PP axial thickness prevents sufficient modulation of the HSR and LSR magnetic fields due to saturation within the PP, thus reducing the torque transmission capability. A large PP thickness presents a large effective air gap between magnet arrays and encourages leakage of the magnetic field, again reducing the torque transmission capability of the AMG.

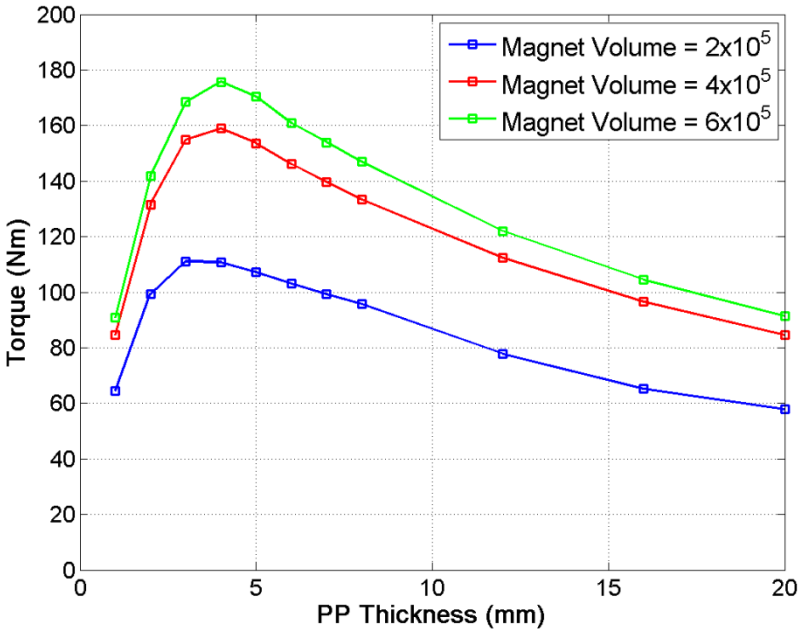

Figure 3.6 *Variation of torque with PP thickness and magnet volume*

Therefore, it was considered prudent to ensure a PP thickness to the right of the peak shown in Figure 3.6. This is done by choosing a PP axial thickness t_{pp} given by:

$$t_{pp} = \frac{\pi r_m}{n_s} \tag{3.11}$$

where n_s is the number of PPs and r_m is the mean radius of the PPR. This ratio of mean circumferential length and PP number ensures the PP shape remains essentially 'square', thus reducing the variation of torque output due to the PP thickness manufacturing tolerances and maintaining a high torque transmission capability.

3.3.2. Effect of the Air Gap Length

The desire for small air gap lengths to increase torque production has long been known in electrical machines. Usually the air gap is determined by a trade-off between machine volume and the cost of achieving improved tolerances. In the AMG reducing the size of each air gap significantly increases the transmitted torque and shear stress as seen in

Figure 3.7. However, the resulting net axial force on the PPR is also seen to increase as shown in Figure 3.8. Viable AMGs are possible with 0.5mm airgaps as forces on the PPR remain within the limits of angular contact bearings for this scale of AMG [3.9]. However, double-sided topologies should significantly reduce forces on bearings. Although the increase in torque and force with reducing air gap length is to be expected, these values are required for down selection of the gear ratio and further simulation studies within the thesis.

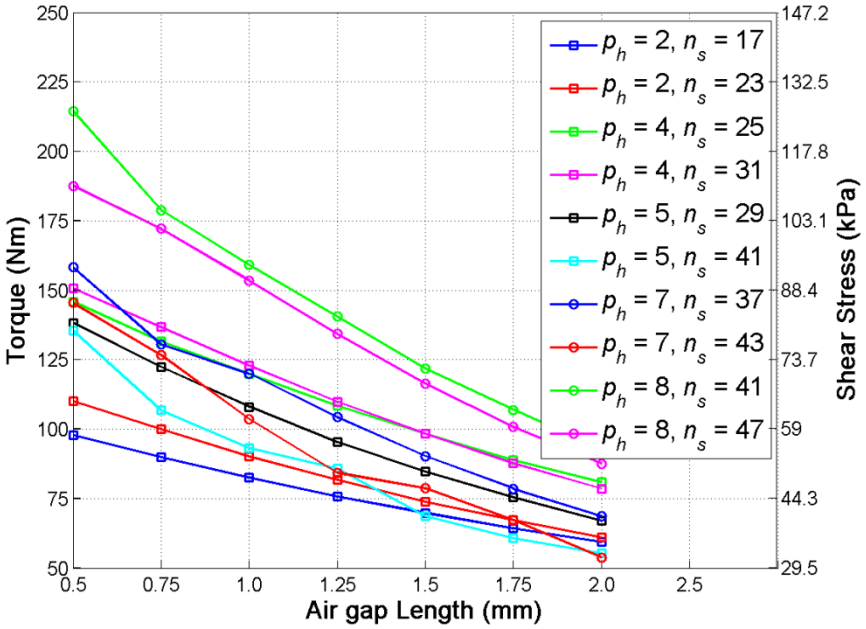

Figure 3.7 *Variation of torque and shear stress with air gap length*

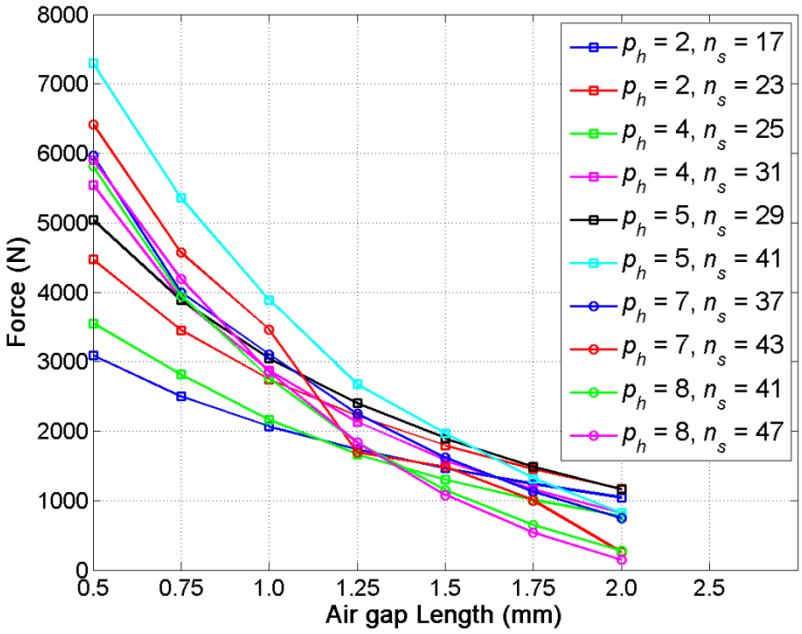

Figure 3.8 *Net force on PPR with air gap length*

A gear with $p_h = 4$ and $n_s = 25$ was selected to examine the effect of asymmetric air gaps on the torque and shear stress shown in Figure 3.9. An increase in the fixed array side air gap caused a greater reduction in torque and shear stress than the HSR side air gap. As the LSR pole number is higher, the return path of the flux is shorter and as such the same increase in air gap represents a higher proportional change in path length for the fixed array than HSR. Although output torque can be improved by minimising the fixed array side air gap, equal air gaps of 0.5mm will be used for the following optimisations. This air gap would be achievable with the facilities available if the AMG were to be prototyped whilst producing high levels of output torque for a given magnet volume. Furthermore, equal air gaps should help balance the forces on the PPR.

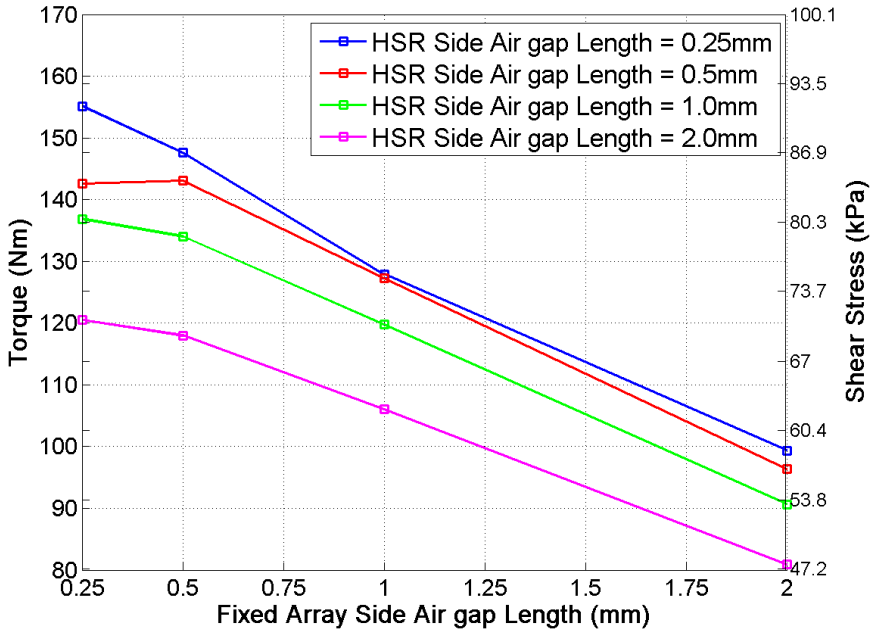

Figure 3.9 *Variation of torque and shear stress with asymmetric air gap distribution*

3.3.3. Effect of Inner to Outer Diameter Ratio

A key difference between the CMG and the AMG is the axial topology allows for variation of the inner-diameter to outer-diameter ratio λ . Figure 3.10 and Figure 3.11 show that the addition of magnet material for less than $\lambda = 0.5$ has no significant effect on the increase of torque production. This is due to the addition of lower volumes of magnet material at low values of λ and the reducing radii at which it is added.

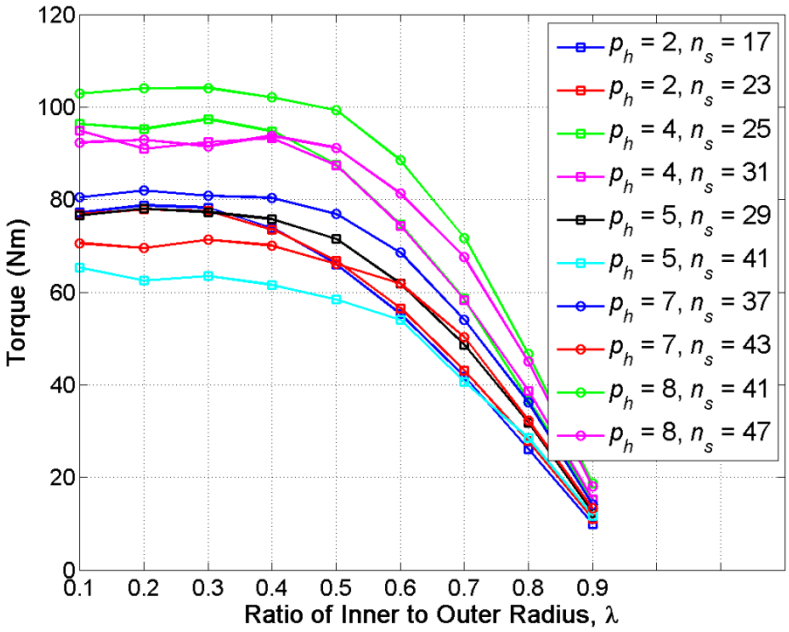

Figure 3.10 *Variation of transmitted torque with λ (Magnet Volume 2x10^{5}mm^3)*

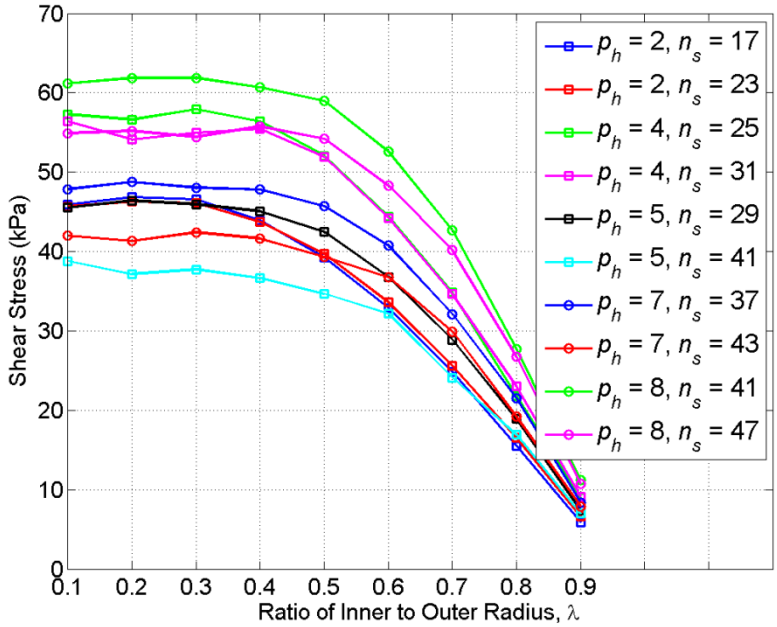

Figure 3.11 *Variation of shear stress with λ (Magnet Volume 2x10^{5}mm^3)*

3.3.4. Effect of Magnet Volume Distribution

The use of magnetic material has a high impact on the device, both in terms of performance and cost. In AMG the magnetic material is distributed between the HSR and stationary magnet array. The most effective use of magnet material was investigated by distributing a magnet volume between the HSR and fixed magnet arrays. The torque and shear stress at three magnet volumes are shown in Figure 3.12, Figure 3.13 and Figure 3.14. It is interesting to note that an optimum distribution occurs around 50:50 (HSR: Fixed) for lower magnet volumes but is biased toward the HSR for higher magnet volumes. Furthermore, Figure 3.15, Figure 3.16 and Figure 3.17 show the torque per magnet volume decreases with overall magnet volume.

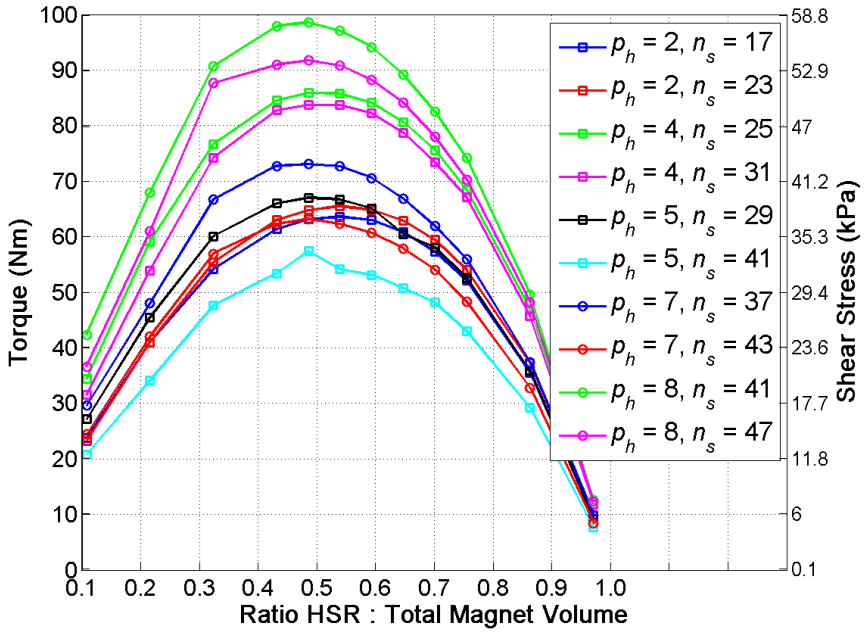

Figure 3.12 *Variation of torque and shear stress with magnet distribution (Magnet volume 2x10^{5}mm^3)*

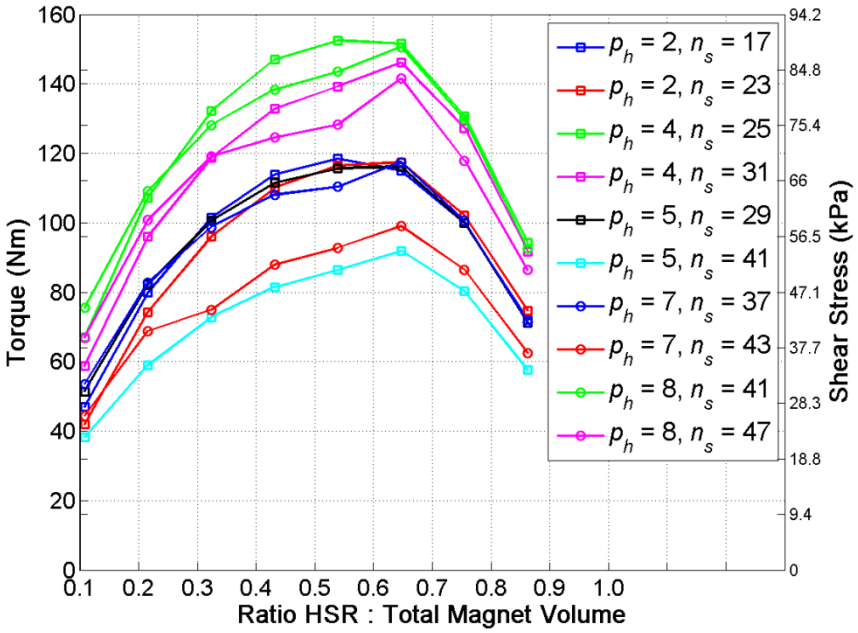

Figure 3.13 *Variation of torque and shear stress with magnet distribution (Magnet volume $4x10^5 mm^3$)*

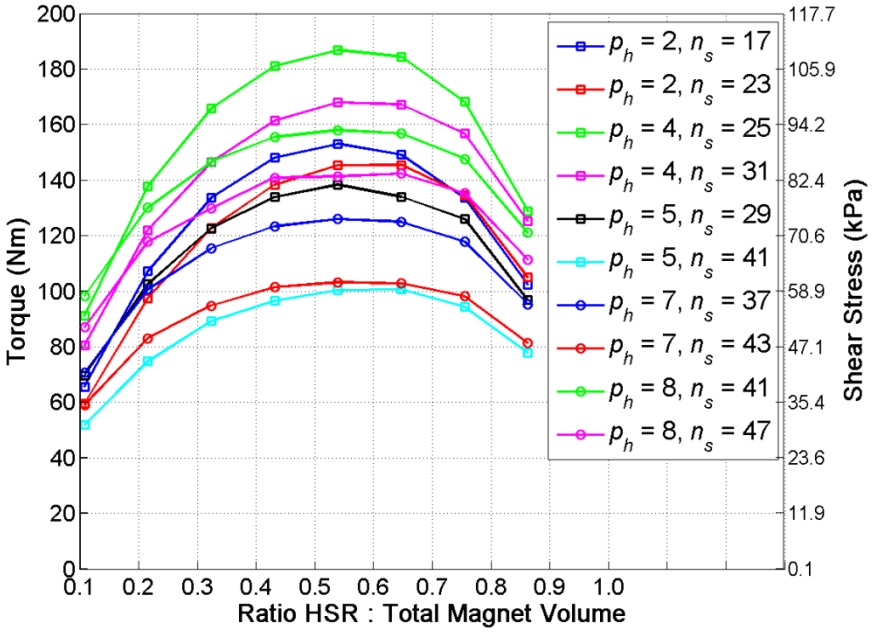

Figure 3.14 *Variation of torque and shear stress with magnet distribution (Magnet volume $6x10^5 mm^3$)*

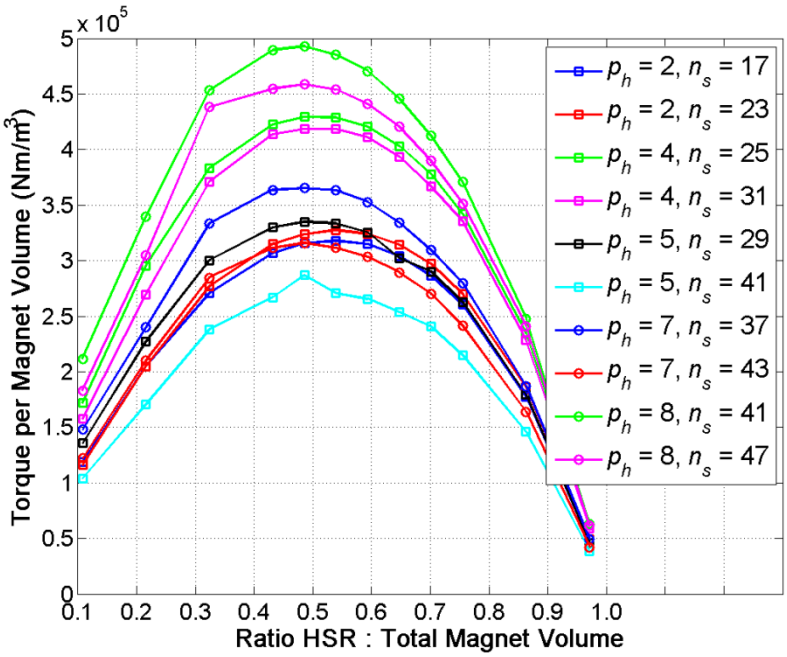

Figure 3.15 *Variation of torque per magnet volume with magnet distribution (Magnet volume $2x10^5 mm^3$)*

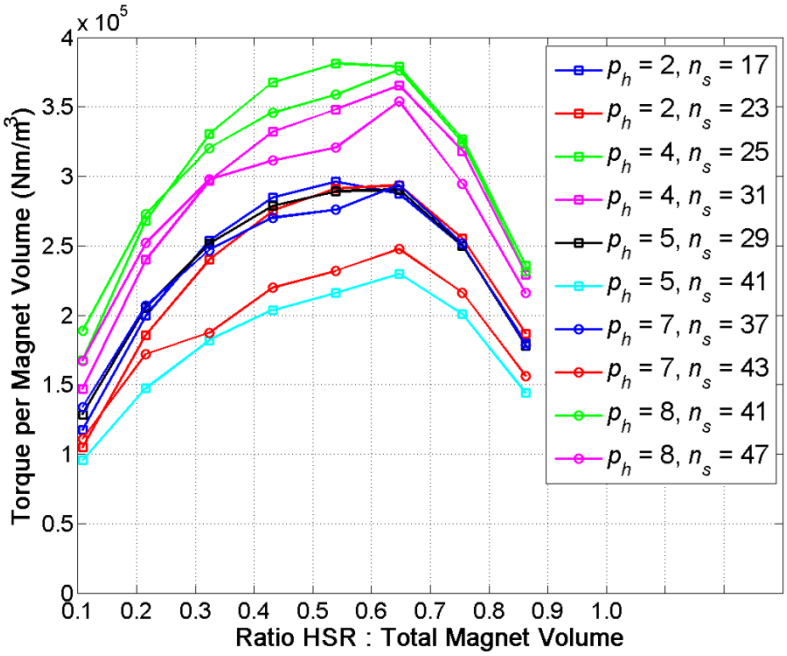

Figure 3.16 *Variation of torque per magnet volume with magnet distribution (Magnet volume $4x10^5 mm^3$)*

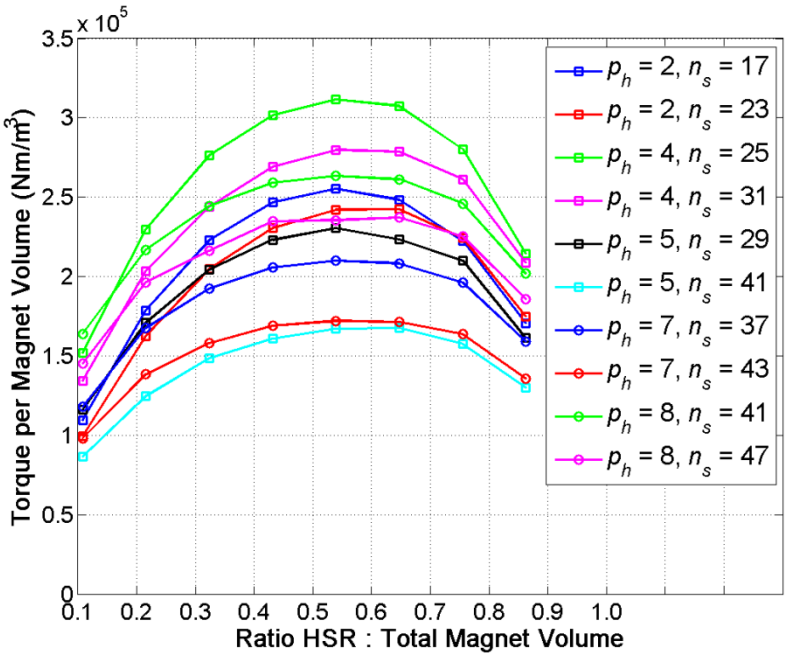

Figure 3.17 *Variation of torque per magnet volume with magnet distribution (Magnet volume $6x10^5 mm^3$)*

The torque and shear stress determined by varying the magnet volume and ratio of inner to outer radius are shown in Figure 3.18 and Figure 3.19, respectively. The AMG with 0.5mm air gap and $p_h = 4, n_s = 25$ is able to achieve shear stress values in excess of 125kPa at moderate values of λ and magnet volume. These design aspects are considered optimal and will be utilised in Section 3.4 to investigate specific aspects of the PPR design.

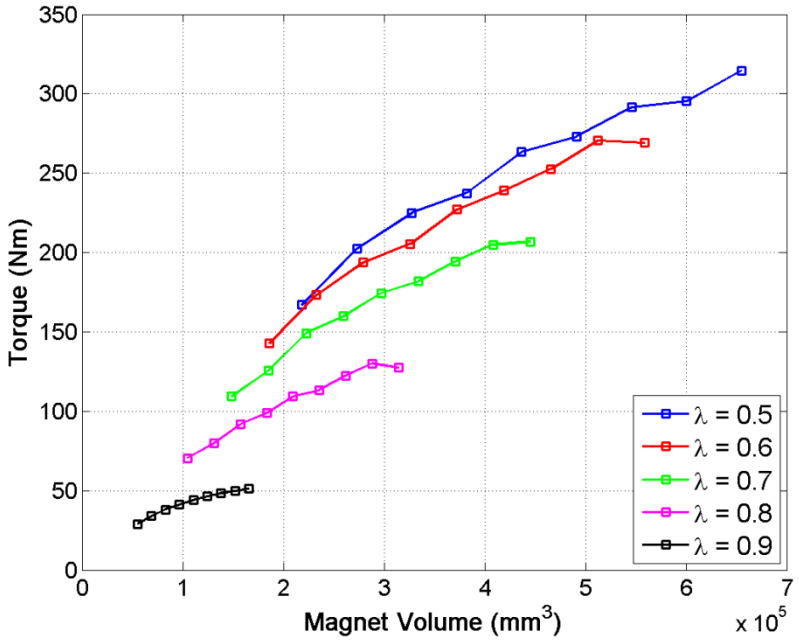

Figure 3.18 *Variation of torque with and magnet volume for different values of λ (p_h=4, n_s=25)*

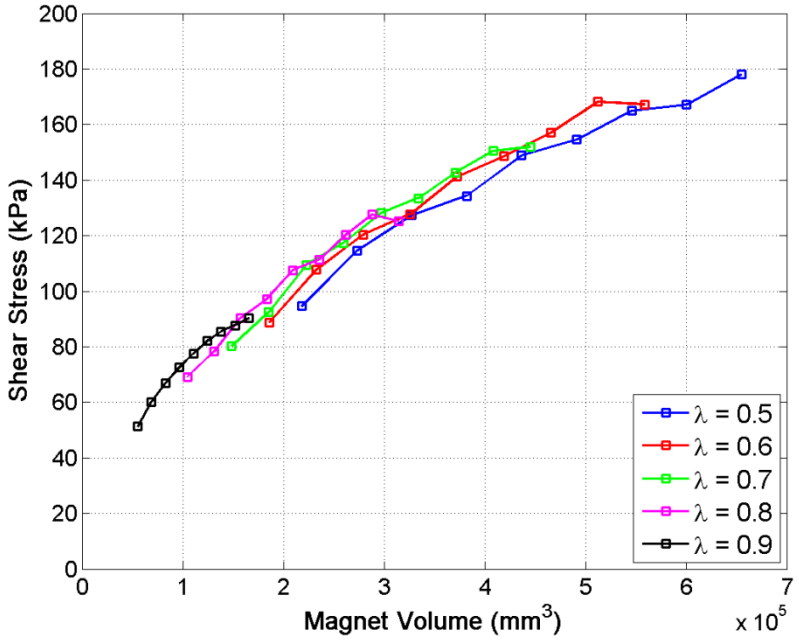

Figure 3.19 *Variation of shear stress and magnet volume for different values of λ (p_h=4, n_s=25)*

3.4. Axial Pole Piece Rotor Topology

The AMG imparts large axial forces at same air gap lengths at which torque transmission is most effective. As such the PPs require the ability to resist deflection in the axial direction and thus prevent closing of the air gap. The PPR should also be simple to manufacture and robust in its construction.

The following investigations regarding the PP design will use parameters given in Table 3.3. Soft Magnetic Composite (SMC) has lower permeability and higher resistivity than silicon iron and as such should exhibit better iron loss performance. Due to the complexity of the structures under investigation the material chosen for both the back iron and PPs was a high strength SMC.

Parameter	***Value***
Outer Diameter	200mm
Permanent Magnet Material	N38
Permanent Magnet (PM) Remanence	1.25T
Relative recoil permeability of PM	1.044
HSR Pole Pairs, p_h	4
Magnetic Material Distribution	55:45 (HSR: LSR)
Magnet Volume	$6x10^5 mm^3$
HSR Magnet Array	Full pole arc, North-South
Fixed Magnet Array	Full pole arc, Halbach
Ferromagnetic Pole Pieces, n_s	25
Ferromagnetic Material	Somaloy® 1000 3P
Air Gap Thickness	0.5mm
Inner to outer diameter ratio, λ	0.55
FEA Analysis Type	Magneto-static
Magnetic Gear Position	Pull-out torque

Table 3.3 *PPR investigation parameters*

3.4.1. Design 1

The ratio of air to ferromagnetic material in the PPR, α_{pp} has been shown to affect the transmitted torque in CMGs [3.1] [3.10]. The validation of this parameter for AMGs at a fixed PP thickness is shown in Figure 3.20. A ratio of 0 signifies the pitch is entirely occupied by the ferromagnetic material where as a value of 1 signifies the pitch is occupied by no ferromagnetic material.

When appropriate the value of $\alpha_{pp} = 0.5$ will be used in the following investigations due to this corresponding to the peak torque transmission. At $\alpha_{pp} = 0.5$ an axial force of ~250N is exists on each PP which is significant given the scale of the AMG.

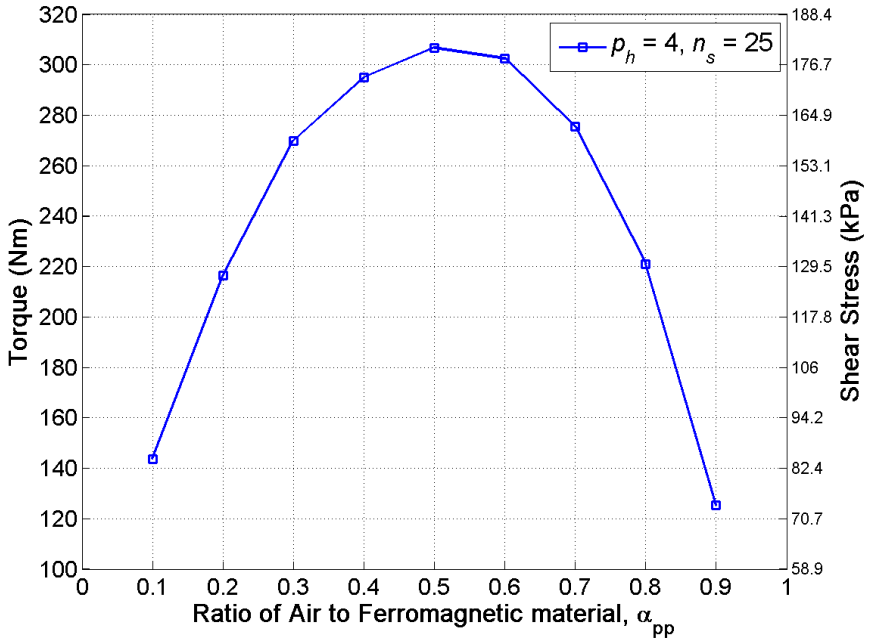

Figure 3.20 *Variation of torque and shear stress with the ratio of air to ferromagnetic material*

3.4.2. Design 2

By creating an interlocking PP shape non-ferrous, non-magnetic and mechanically stiff material can be used to support the PPs and thus reduce axial deflections. An example

of this structure is shown in Figure 3.21. The central and outer pitch of the shape can be modified which provides a greater or lesser area for the PP and supporting material to interact. Figure 3.22 shows that variation of either pitch results in a detrimental effect on the magnetic performance of the AMG.

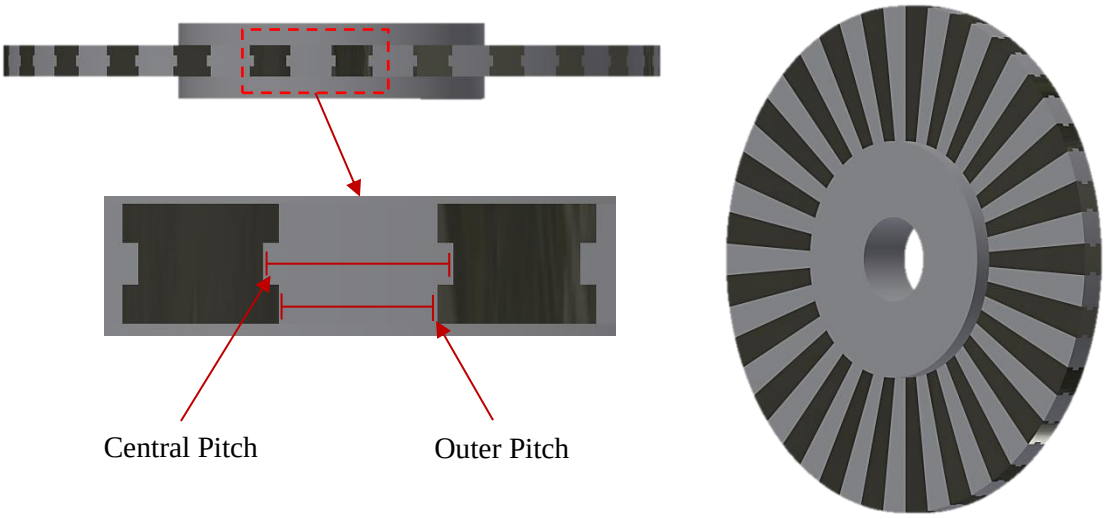

Figure 3.21 *Design 2 pole piece*

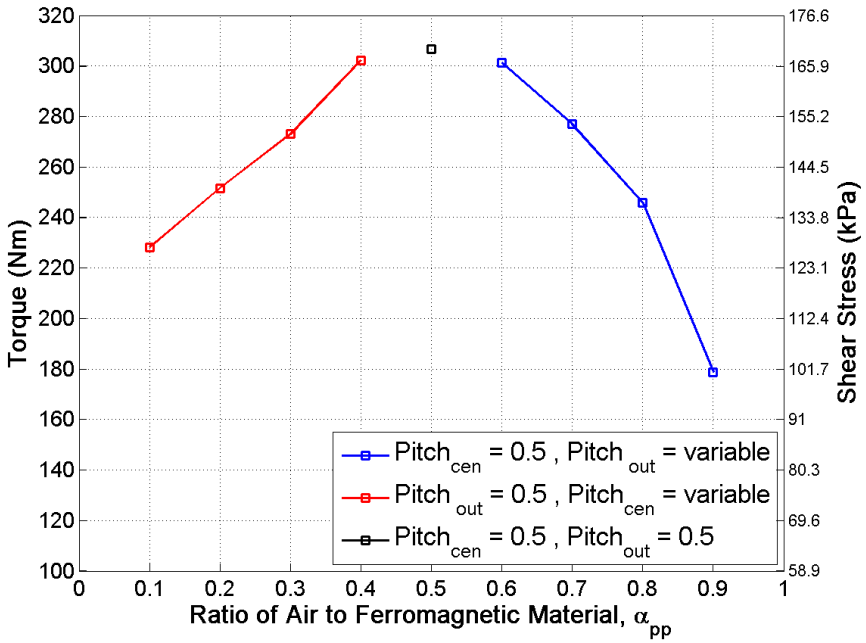

Figure 3.22 *Variation of torque and shear stress with the ratio of air to ferromagnetic material*

The reasons for decreased magnetic performance are twofold. Firstly the reduction of the central pitch causes an increase in circumferential leakage measured at the axial mid-point of the PP, as shown by the increase of the B_θ component in Figure 3.23. The highest leakage is seen to occur at the inner radii of the gear where the length of the circumferential reluctance path is shortest.

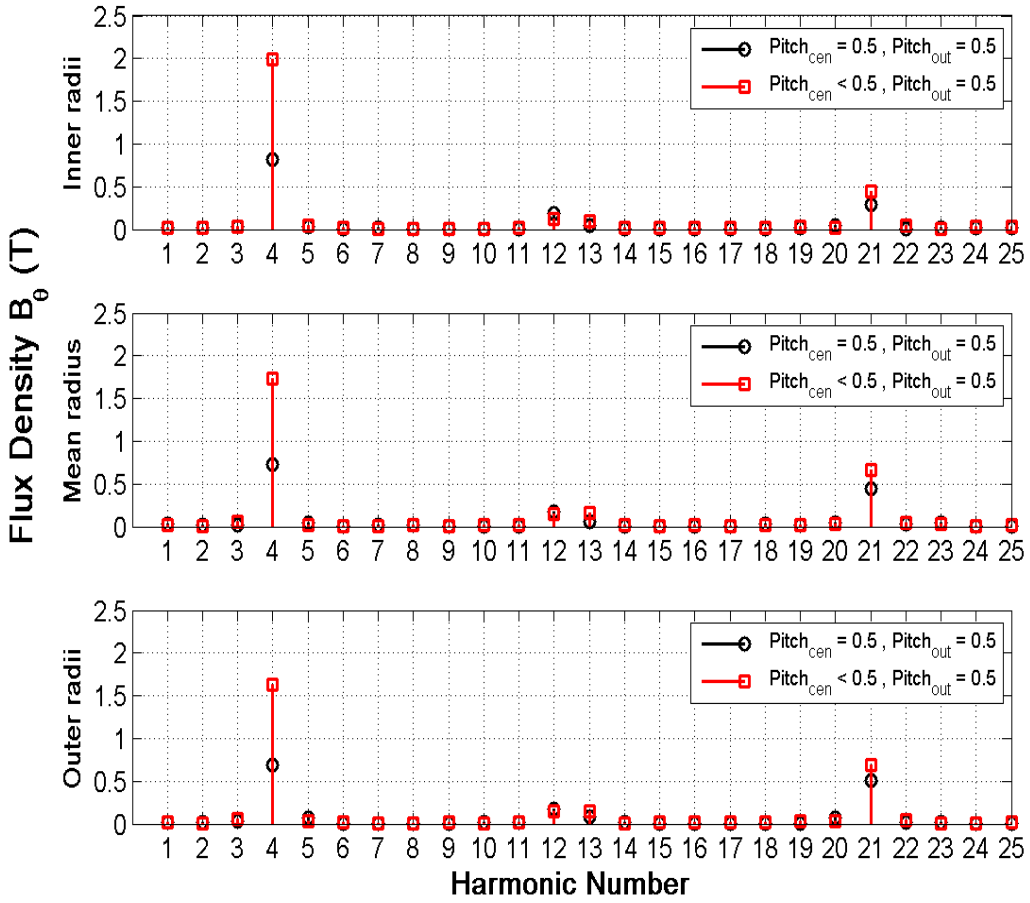

Figure 3.23 *Harmonic spectra of B_θ at different radial positions. (Design 2 PP)*

Secondly, the reduction of the outer pitch reduces the torque production due to a reduction of linkage between the magnet arrays and the PPs. This is shown in the reduction of the B_z component in Figure 3.24.

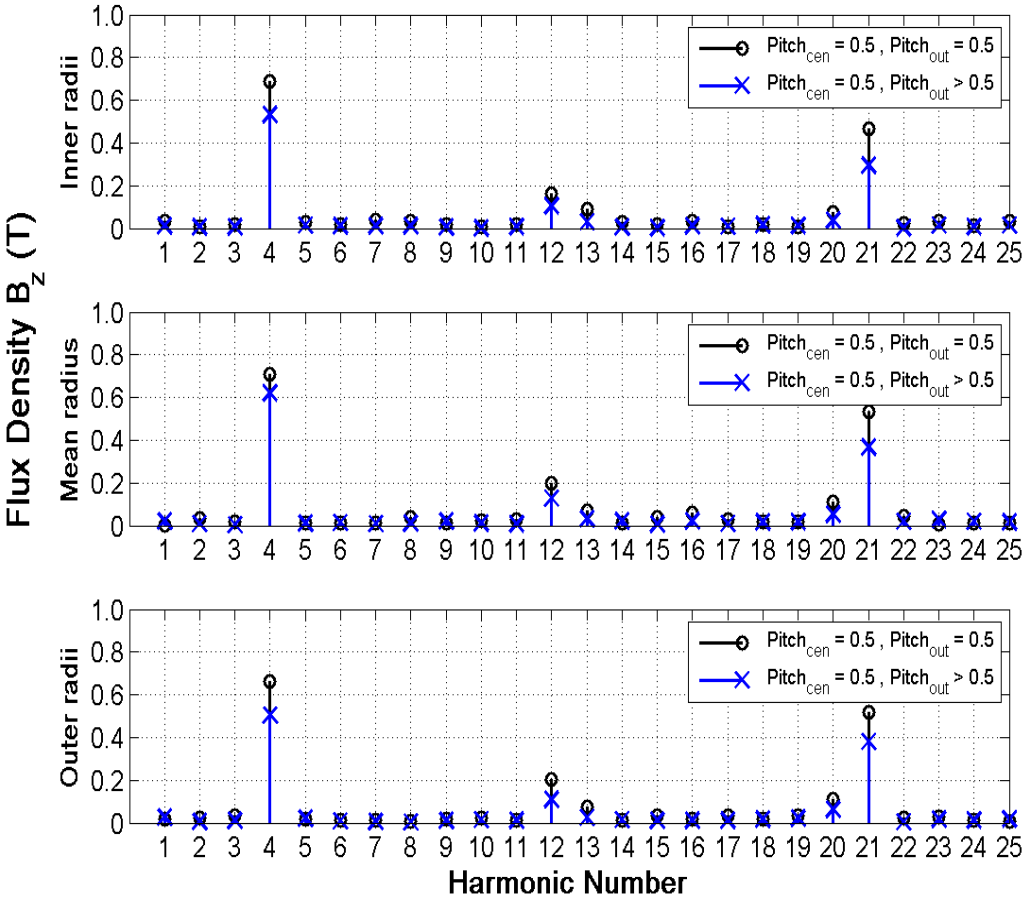

Figure 3.24 *Harmonic spectra of B_z at different radial positions. (Design 2 PP)*

The radial leakage flux density B_r is present in both variants as seen in Figure 3.25. As B_r does not contribute to the production of torque a reduction in B_r would improve the magnetic performance of the axial magnetic gear.

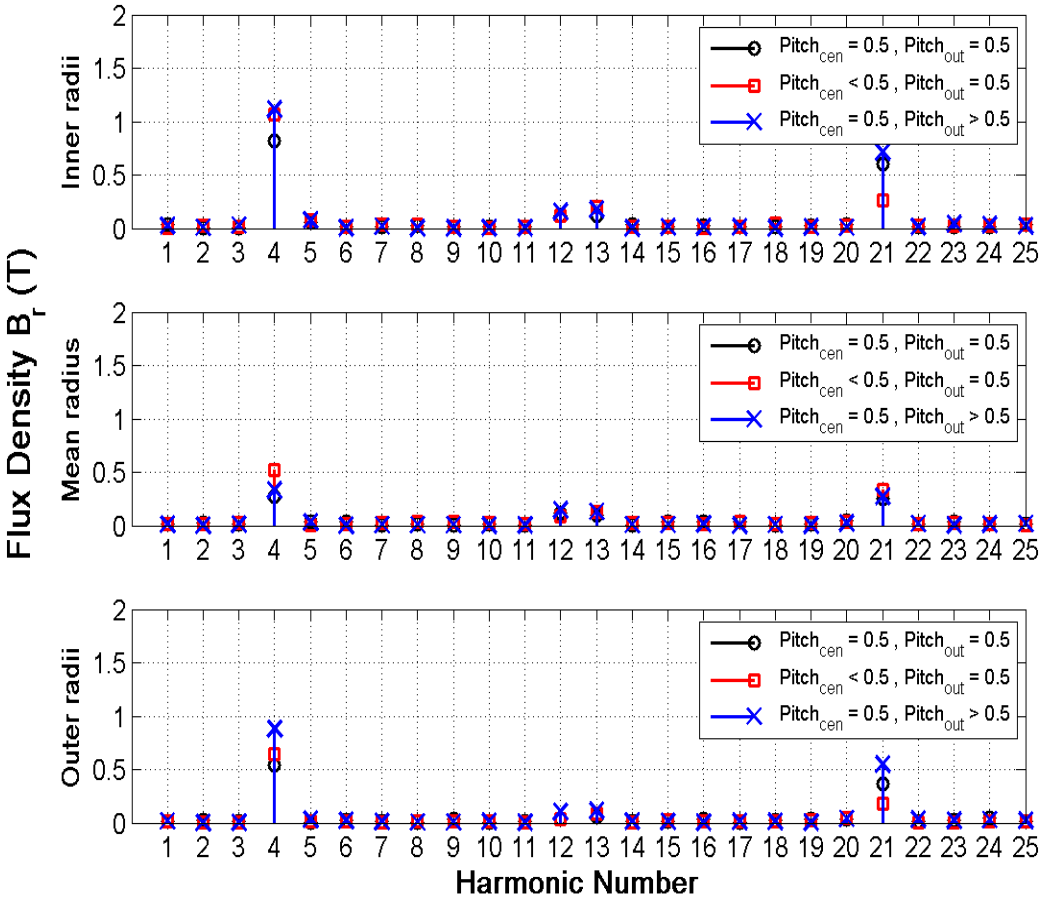

Figure 3.25 *Harmonic spectra of B_r at different radial positions. (Design 2 PP)*

3.4.3. Design 3

The traditional trapezoidal cross section is achieved when the ratio length of the inner arc l_i to the outer arc l_o is given by $l_i/l_o = \lambda$ as shown in Figure 3.26(a). A variation in the ratio of l_i/l_o results in the square cross section shown in Figure 3.26(b) at $l_i/l_o = 1$. This shape is of particular interest as the resulting PP would be simpler to manufacture. Extending $l_i/l_o > 1$ results in a trapezoid that thins toward the outer radius of the AMG as shown in Figure 3.26(c). This shape offers an opportunity to reduce the force on the PP and therefore increase the mechanical robustness of the structure.

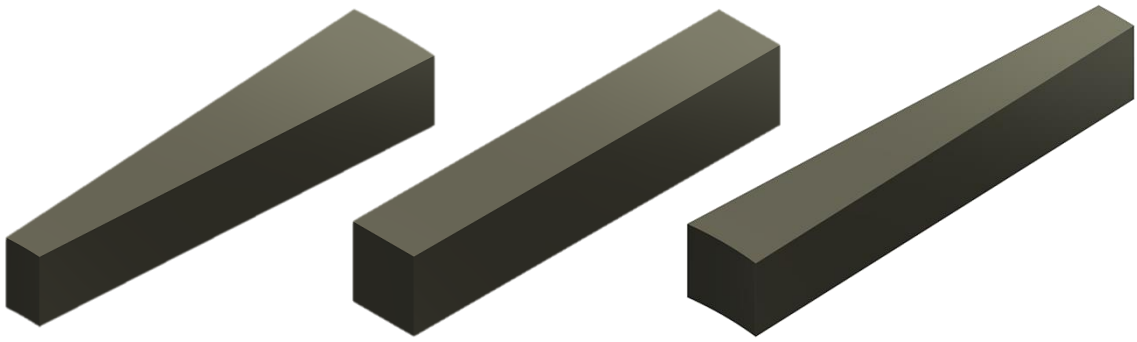

Figure 3.26 *Design 3 pole piece where l_i/l_o is a) <1, b) =1 and c) > 1*

The PP area adjacent to the airgap is fixed and a PP axial length given by t_{pp} was used for the comparison of l_i/l_o ratios. The torque, shear stress and electromagnetic force per PP are shown in Figure 3.27, Figure 3.28 and Figure 3.29 respectively. The peak force on the PPs corresponds to a value of $\lambda = 0.6$ and as such this design point should be avoided if possible.

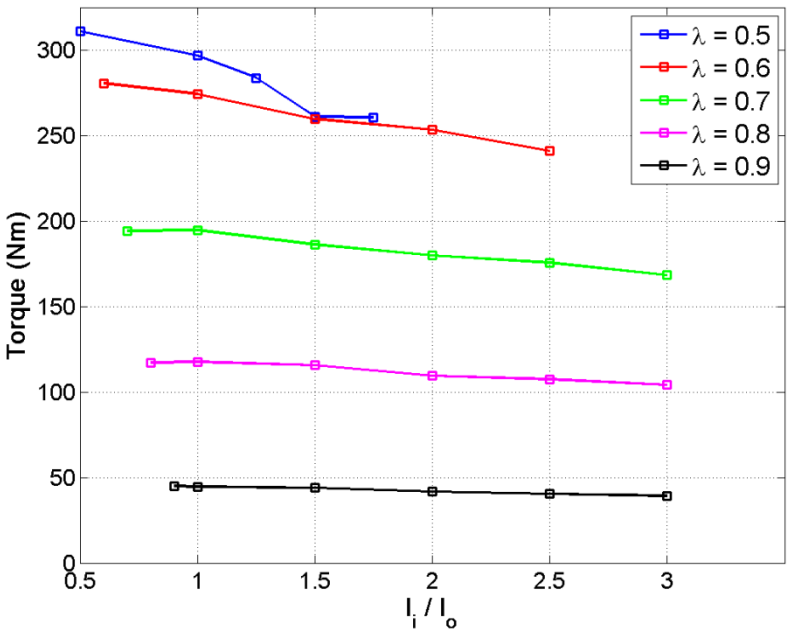

Figure 3.27 *Variation of torque with ratio l_i/l_o. (Design 3 PP)*

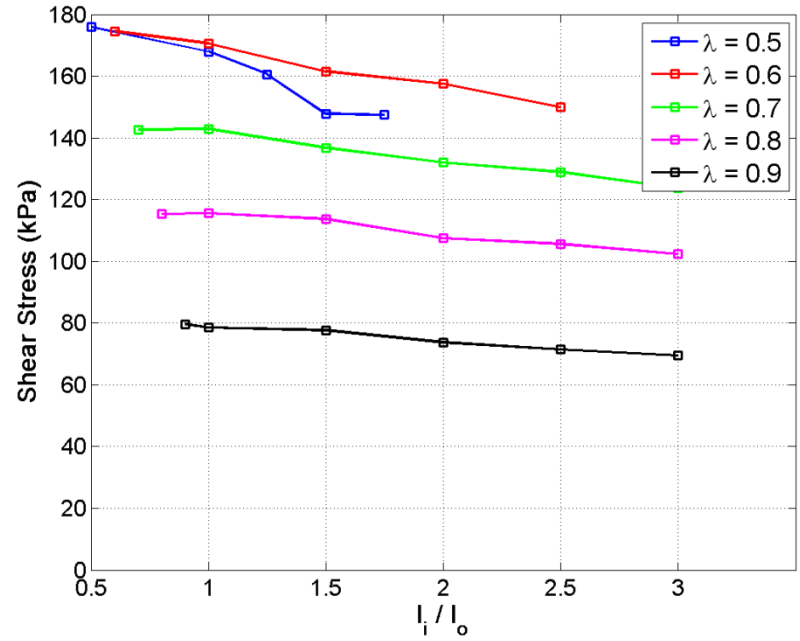

Figure 3.28 *Variation of shear stress with ratio l_i/l_o.(Design 3 PP)*

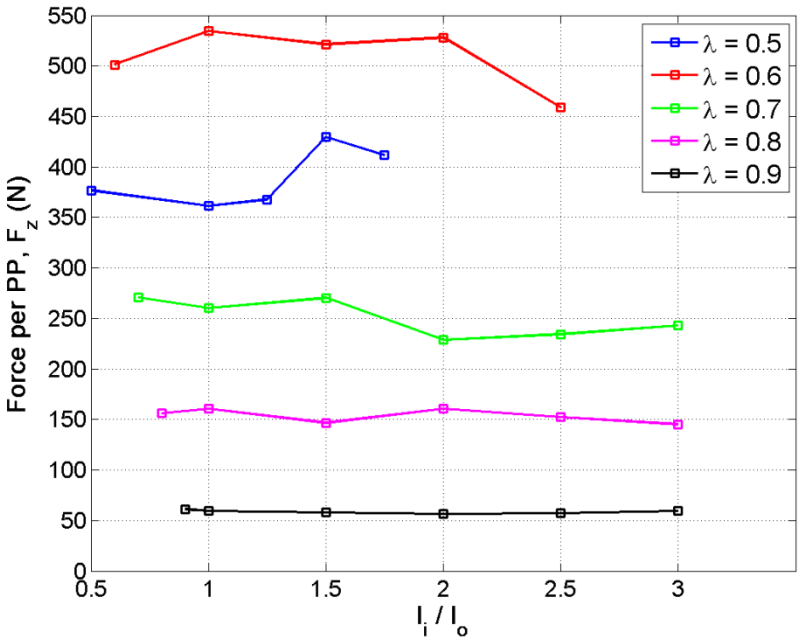

Figure 3.29 *Variation of electromagnetic force per PP, F_z with ratio l_i/l_o .(Design 3 PP)*

3.4.4. Design 4

In the topology presented in Design 2 a radial leakage component B_r was seen. This effect may be reduced by the introduction of flux barrier(s). This would take the form of a radial air gap or non-magnetic spacer in the PP as seen Figure 3.30. Figure 3.31 shows that a small barrier close to the inner radii provides the greatest reduction in B_r and thus increase in AMG output torque. A compromise must be considered between losing flux modulating PP material and introducing a sufficient flux barrier. A pole piece with no barrier had a torque value of 303Nm and shear stress of 178kPa. The reduction of the radial flux density B_r component at the inner radii can clearly be seen in Figure 3.32.

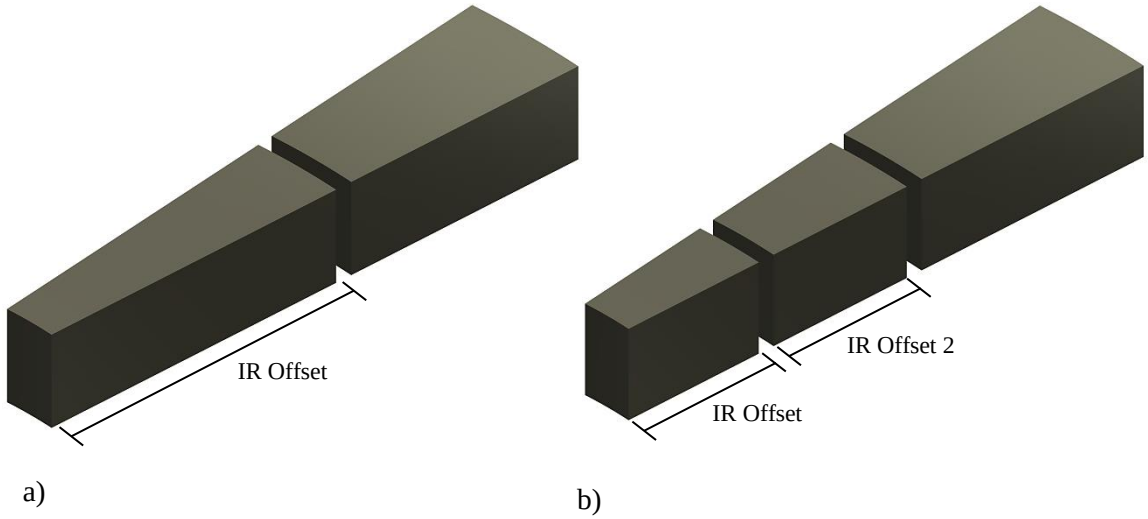

Figure 3.30 *Design 4 pole piece with a) Single Flux Barrier and b) Dual Flux Barrier*

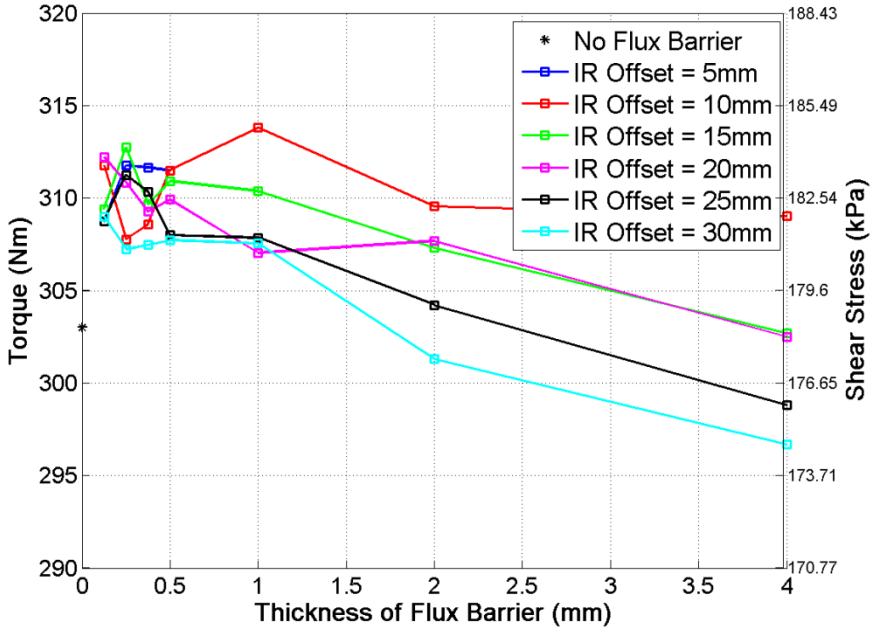

Figure 3.31 *Variation of torque and shear stress with a single flux barrier (Design 4 PP)*

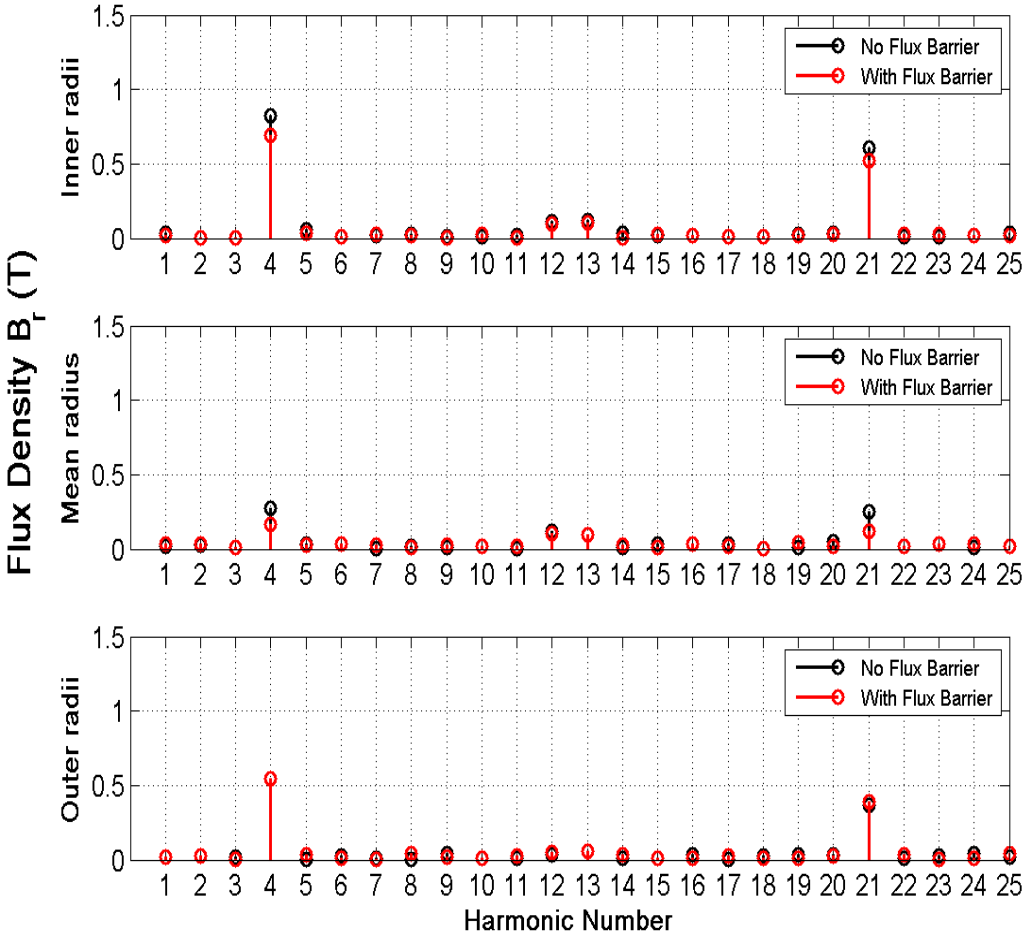

Figure 3.32 *Harmonic spectra of B_r at different radial positions. (Design 4 PP)*

There was potential for a distributed radial air gap to improve the performance of the gear. An inner radius offset of 5mm was selected with the second air gap added at a distance IR Offset 2. Three cases were considered:

1. The addition of another air gap of the same thickness (x2 1mm air gaps)
2. An equivalent length air gap that is distributed (x2 0.5mm air gaps)
3. The best case for a distributed air gap (x2 0.125mm air gaps)

The effect is a reduction in torque output and shear stress as seen in Figure 3.33. As such no advantage was seen to distributing the radial air gap in this case. It is important to note that the introduction of a flux barrier may also result in a reduction in of the PPs ability to resist deflection.

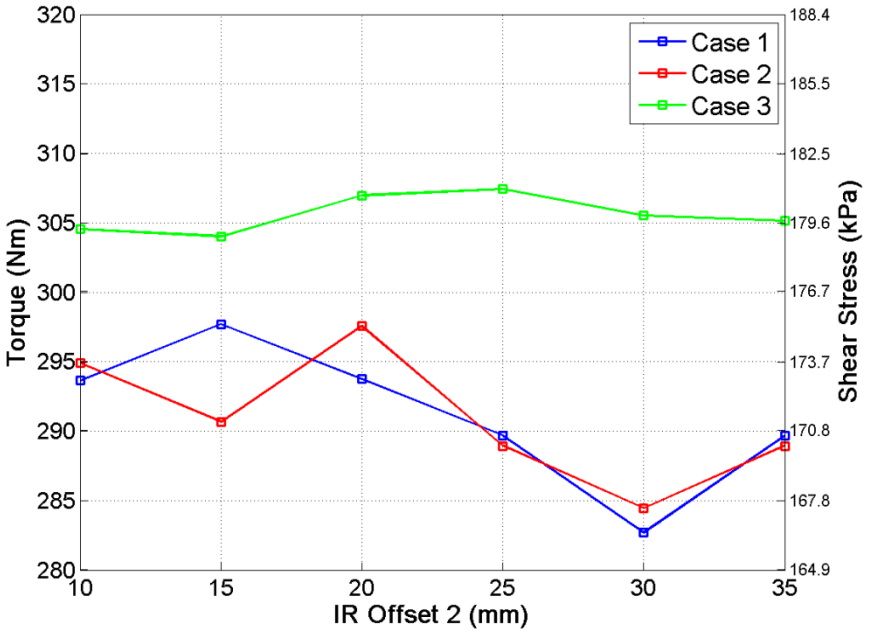

Figure 3.33 *Variation of torque and shear stress with a dual flux barrier (Design 4 PP)*

3.5. Conclusions

Optimisation of key parameters of the AMG was undertaken using 3D FEA. The reduction of the air gap gives considerable improvement in torque transmission but can only be exploited within cost and manufacturing limitations, in this case 0.5mm per air gap. The resultant magnetic force, which the PPs are subjected to, increases significantly and is limited by the mechanical strength of the PP material.

Diminishing returns are seen when reducing the inner-diameter to outer-diameter ratio, λ below 0.5. Increasing λ above 0.5 reduces both the torque and shear stress but increases torque per magnet volume, and as such a value of $\lambda = 0.7$ was considered an optimal trade-off between torque and torque per magnet volume. The magnet volume distribution between the LSR and HSR in low magnet volume applications is optimal at 50:50. It is shown that similarly to CMGs, the ferromagnetic opening to PP pitch α_{pp} is optimal at 0.5 and variation of the PP pitch gave an insight into the mechanisms which reduce magnetic performance. Ratios of $l_i/l_o > 1$ result in reduced torque transmission due to the reduction of pole area at the outer radius. Square PPs ($l_i/l_o = 1$) show a small reduction in torque/shear stress compared to that of the traditional shaped PPs and would be preferable in terms of manufacturability.

The PP has to withstand the magnetic force produced by the axial topology but also reduce the potential losses caused by the 3D flux paths seen in this topology. Although flux barriers offer potential to reduce the radial leakage flux, their implementation in a mechanically robust fashion would be challenging. A preferable solution is to use SMC PPs due to their isotropic properties and their ability to accommodate the 3D nature of the flux. However, further investigation of mechanical performance is required before a

practicable design can be developed. This, alongside other aspects which affect the realisation of the PP structure, will be discussed in Chapter 4.

3.6. References

[3.1] K. Atallah, S. D. Calverley, and D. Howe, “Design , analysis and realisation of a high- performance magnetic gear,” *IEE Proc.-Electr Power Appl.*, vol. 151, no. 2, pp. 135–143, 2004.

[3.2] S. Mezani, K. Atallah, and D. Howe, “A high-performance axial-field magnetic gear,” *J. Appl. Phys.*, vol. 99, no. 8, p. 08R303, 2006.

[3.3] M. Johnson, M. Post, and H. A. Toliyat, “Analysis and Development of an Axial Flux Magnetic Gear,” in *Energy Conversion Congress and Exposition (ECCE)*, 2014, pp. 5893–5900.

[3.4] M. Johnson, M. C. Gardner, and H. A. Toliyat, “Analysis of axial field magnetic gears with Halbach arrays,” in *Proceedings - 2015 IEEE International Electric Machines and Drives Conference, IEMDC 2015*, 2016, vol. 1, pp. 108–114.

[3.5] K. Atallah, R. E. Clark, and J. J. Rens, “Magnetic pole -piece structure,” WO 20091387252009.

[3.6] S. D. Calverley and D. J. Powell, “Magnetic pole-piece support,” WO 20091387282009.

[3.7] S. A. Afsari, H. Heydari, and B. Dianati, “Cogging Torque Mitigation in Axial Flux Magnetic Gear System Based on Skew Effects Using an Improved Quasi 3-D Analytical Method,” *IEEE Trans. Magn.*, vol. 51, no. 9, pp. 1–11, 2015.

[3.8] T. Lubin, S. Mezani, and A. Rezzoug, “Development of a 2D Analytical Model for the Electromagnetic Computation of Axial-Field Magnetic Gears,” *IEEE Trans. Magn.*, vol. 49, no. 11, pp. 5507–5521, 2013.

[3.9] NSK, “Angular Contact Ball Bearings,” no. 1. pp. 1–15, 2015.

[3.10] D. J. Evans and Z. Q. Zhu, “Influence of Design Parameters on Magnetic Gear’s Torque Capability,” pp. 1425–1430, 2011.

Chapter 4

Mechanical design of an Axial Magnetic Gear

The PPR (Pole Piece Rotor) is exclusive to magnetically geared torque transmission and its structure unique to this topology. Several challenges relate to the magnetic design of PPs (Pole Pieces) as outlined in Chapter 3, including maximising torque transmission and reducing leakage fields. This is affected by the shape of the PPs and choice of material. Since the PPs are subjected to time-varying magnetic fields, they have to be laminated or manufactured from SMC. Consequently, the PPs would generally require a support structure around them, which must be non-magnetic and ideally non-conducting. PP geometries and associated support structure arrangements have been proposed, as seen in Figure 4.1 [4.1][4.2].

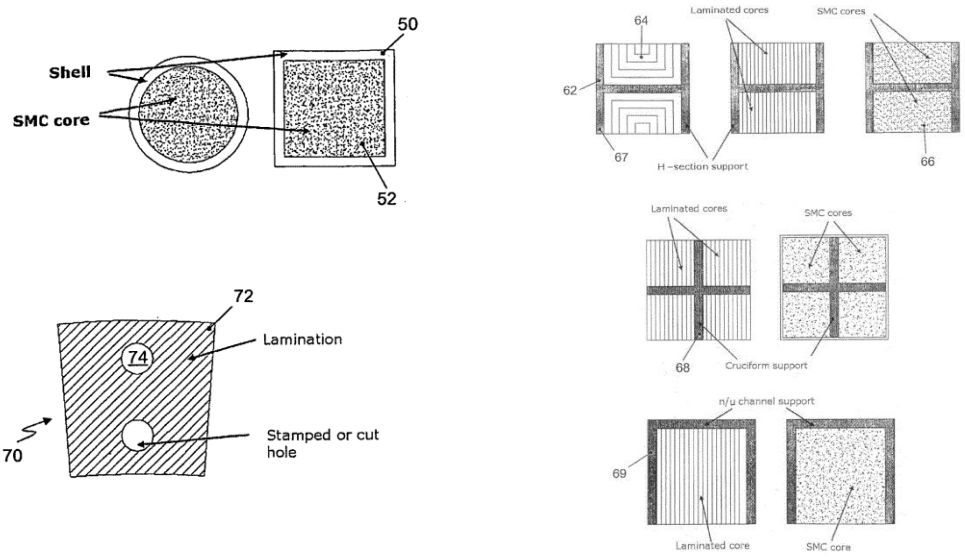

Figure 4.1 *Proposed PP shapes and associated support structures* [4.1]

Although the structures shown in Figure 4.1 may enhance the mechanical integrity of PPs, they may add further complications to their manufacture. Figure 4.2(a) shows a PP

shape which would be similar to manufacture to the unsupported PP. However, special attention must be given to the tensioned rods, which when assembled as shown in Figure 4.2(b), provide significant mechanical benefits to the CMG (Co-axial Magnetic Gear) PPR structure.

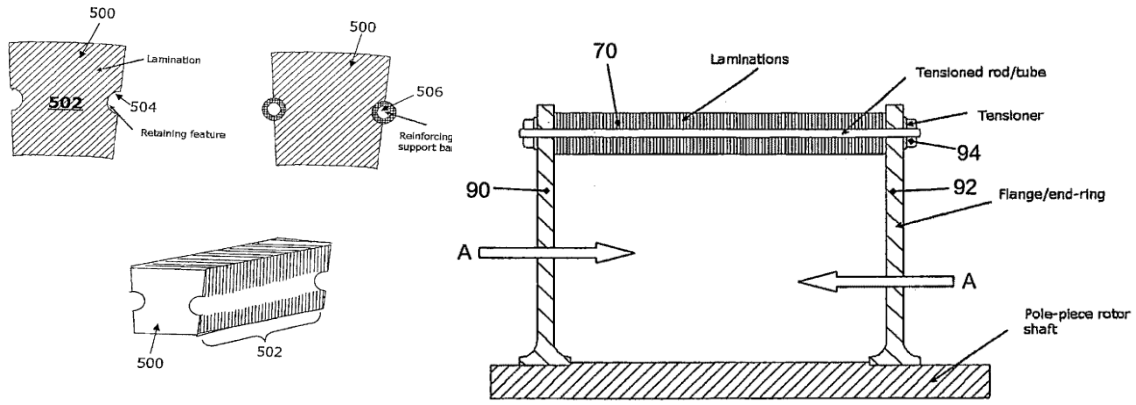

a) b)

Figure 4.2 *Proposed PP shapes and PPR structures* [4.2]

Alternative approaches relate to the reduction of the force in the active direction, such as the method for a CMG presented in [4.3]. Gear ratios which display high cogging torque but low radial force on the PPR structure can be selected, but the forces on the PPs will remain. One rotor is then skewed to reduce the high cogging torque to produce a more robust CMG.

As discussed in Chapter 3, SMC has been chosen for the PPs. This selection is beneficial as SMC exhibits isotropic magnetic and mechanical properties. Mechanically SMC is considerably weaker than silicon iron, especially the prototyping variants which have better machining characteristics. SMC comes in both machinable and non-machinable variants, such as Somaloy 1000 3P or Somaloy Prototyping Material (SPM) respectively. The Tensile Rupture Strength (TRS) of SPM (80MPa) is low compared to that of Somaloy 1000 3P (140MPa) or silicon iron which has a yeild strength in excess

of 450MPa [4.4][4.5][4.6]. Although SMC has been used for stators no previous example of its use as a PP has been reported [4.7] [4.8]. To determine an acceptable design, the analysis considered the Von Mises Stress and allowable deformation under certain load conditions. This was found from Ansys Structural FEA and represents the point at which the material will yield or crack beyond the maximum allowable yield strength or TRS of the material.

Initially in Section 4.1, the forces sustained by the PPR structure during assembly and in normal operation are investigated. In Sections 4.2 and 4.3 ways of minimising these forces on the PPs through the PP design and methods of assembly are considered.

4.1. Forces on Pole Piece Rotor

Due to the nature of the flux in the AMG, axial and circumferential forces act upon the PPs. Knowledge of these forces is necessary to determine if the structure is able to withstand both assembly and normal operation.

The outer diameter of the investigated AMGs is limited by the maximum size of SMC SPM blank (120mm) produced by Höganäs. The gear ratio chosen for the AMG is 6.25:1 ($p_h = 4, n_s = 25$) which achieves a good compromise between the achievable torque transmission, shear stress and the physical size of components. During Chapter 3 it was seen that a value of $\lambda = 0.5$, PP thickness of 5.65mm and air gap length of 0.5mm would provide an optimal gear in terms of maximum torque output. The value of axial thickness for the HSR and LSR magnets are 10mm and 2.5mm respectively. These parameters provide a basis on which the PP mechanical design process, outlined in Figure 4.3, is undertaken.

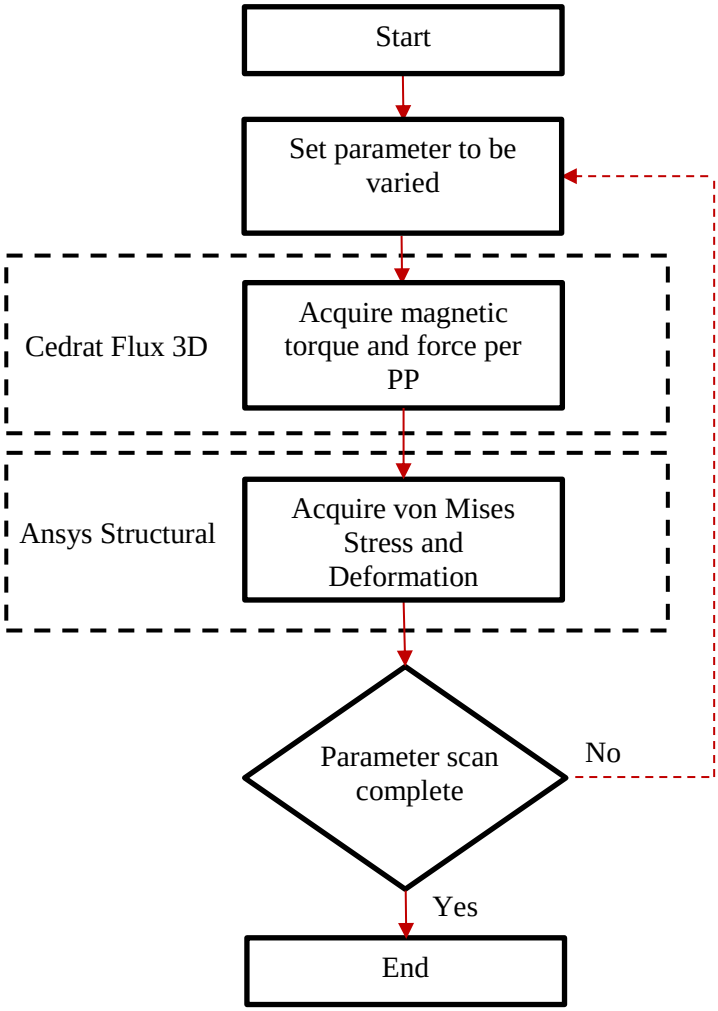

Figure 4.3 *Flowchart of PPR structure analysis*

4.1.1. Force on PPs during assembly with HSR

A method of assembly would be to reduce the axial air gap between the PPR and HSR until the required air gap is achieved. The PPs will experience a single sided force from the HSR magnets with the maximum force occurring at the required airgap. The series of steps required to perform the Ansys Static Structural analysis are shown in Figure 4.4(a)-(d). The mechanical connection shown in Figure 4.4(a) is set to 'Bonded' which represents a rigid connection between the two bodies. The mesh shown in Figure 4.4(b) is then used with the constraints shown in Figure 4.4(c). The load is applied to the PP in the axial direction (defined locally in Ansys as the x-direction) using an equivalent pressure equal to that of the electromagnetic force.

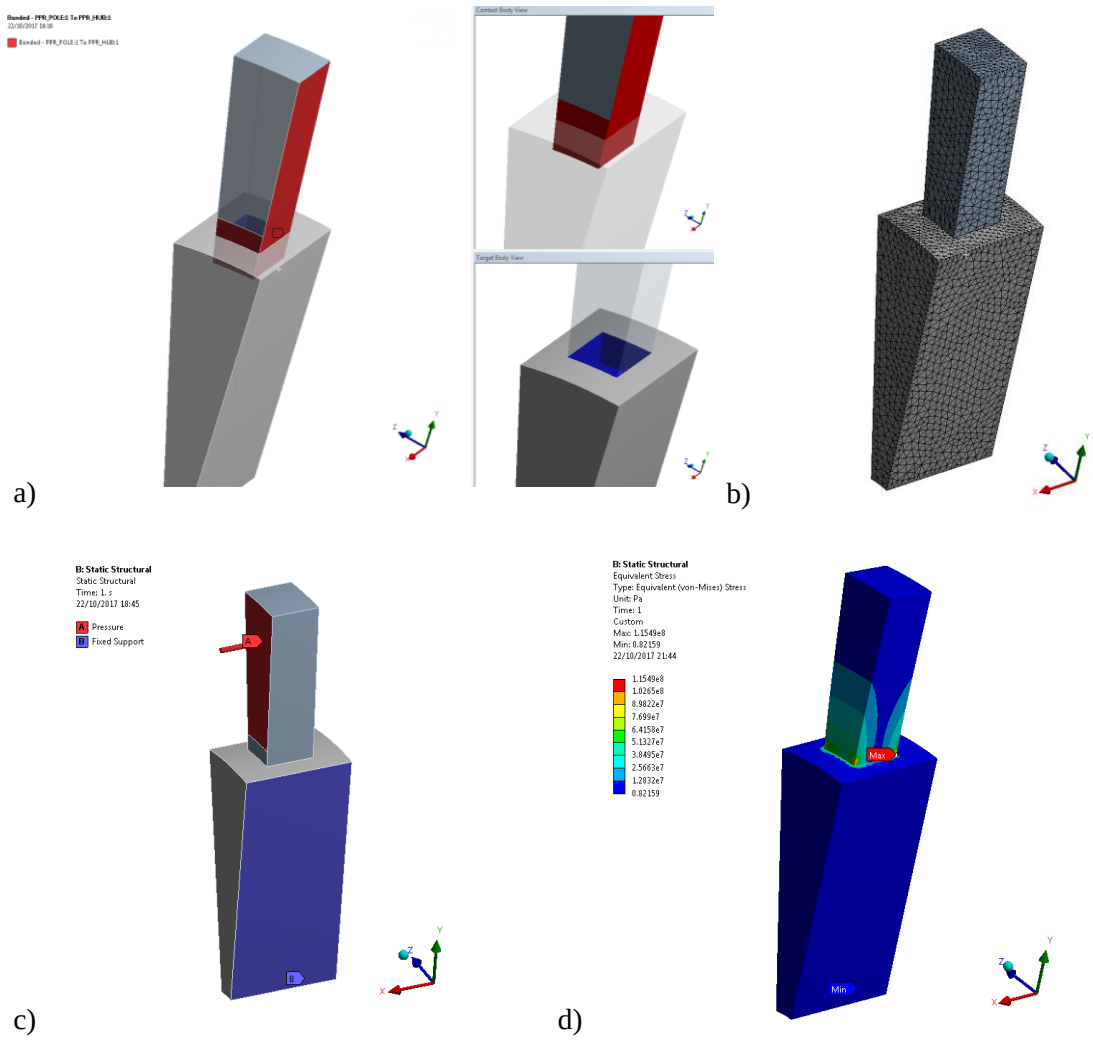

Figure 4.4 *Ansys analysis a) Geometry connection b) Mesh c) Static loading d) Solution*

Figure 4.5 shows the maximum force on the PPs with the nominal air gap being 0.5mm. Figure 4.6 shows the variation of the von Mises stress in the PPs with the airgap. It can be seen that it exceeds the TRS of SPM at low air gap lengths and low values of λ. Beyond the TRS the material would yield and then fail. Therefore values of von Mises stress and the resulting deformations beyond this point are treated as potentially erroneous, as material characteristic non-linearities are not considered. Figure 4.7 shows the deformation is significantly reduced when the von Mises stress is low.

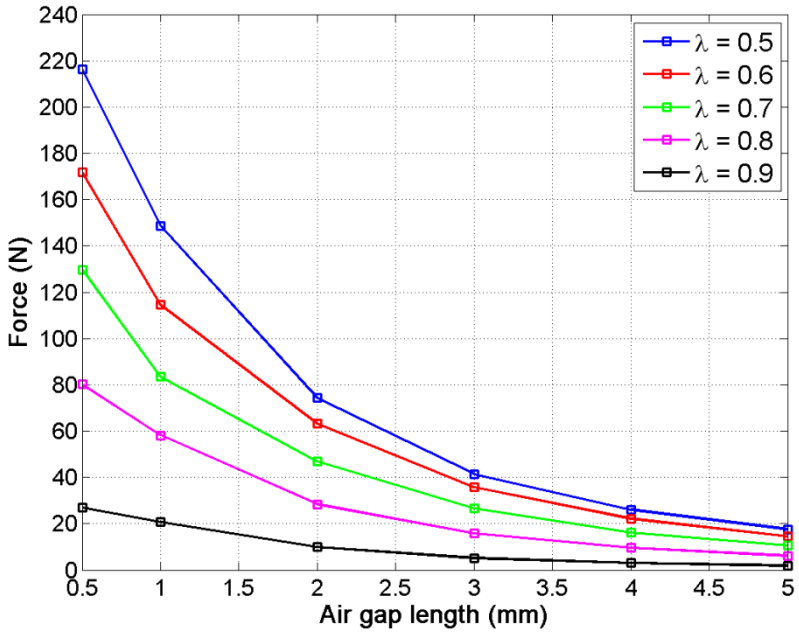

Figure 4.5 *Variation of axial force on a PP with air gap length and* $\boldsymbol{\lambda}$ *(during assembly)*

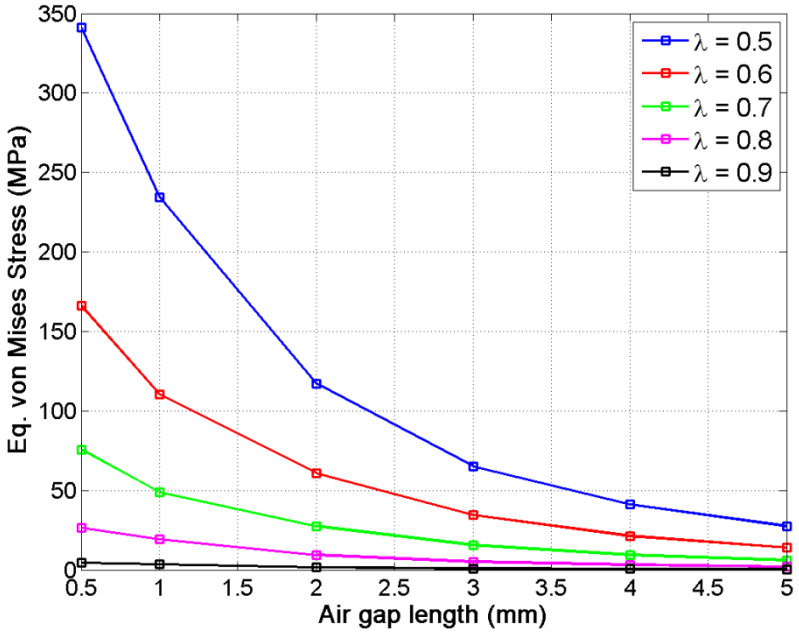

Figure 4.6 *Variation of Von Mises stress in a PP with air gap length and* $\boldsymbol{\lambda}$ *(during assembly)*

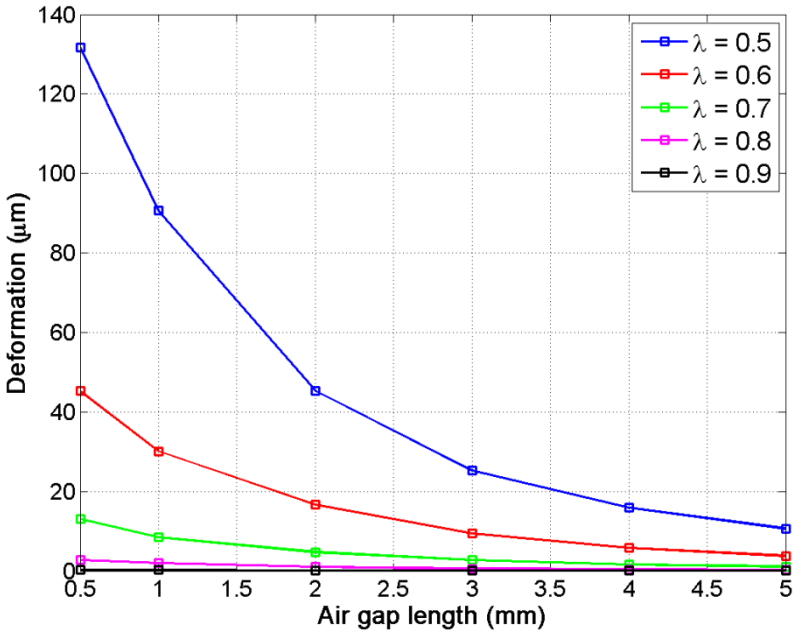

Figure 4.7 *Variation of deformation on a PP with air gap length and* $\boldsymbol{\lambda}$ *(during assembly)*

4.1.2. Force on PPs during normal operation

During normal operation of the AMG the PPs will experience a force from both the HSR and fixed magnet array. Due to this the net axial force is lower than that experienced during assembly. The PP is constrained using the 'Bonded' connection between hub and PP, with the net axial force applied using a pressure equivalent to the area of active PP as shown in Figure 4.8(a). Figure 4.8(b) shows a resultant stress analysis, with the highest stress concentrated towards the corner of the PP where it contacts the hub.

a)

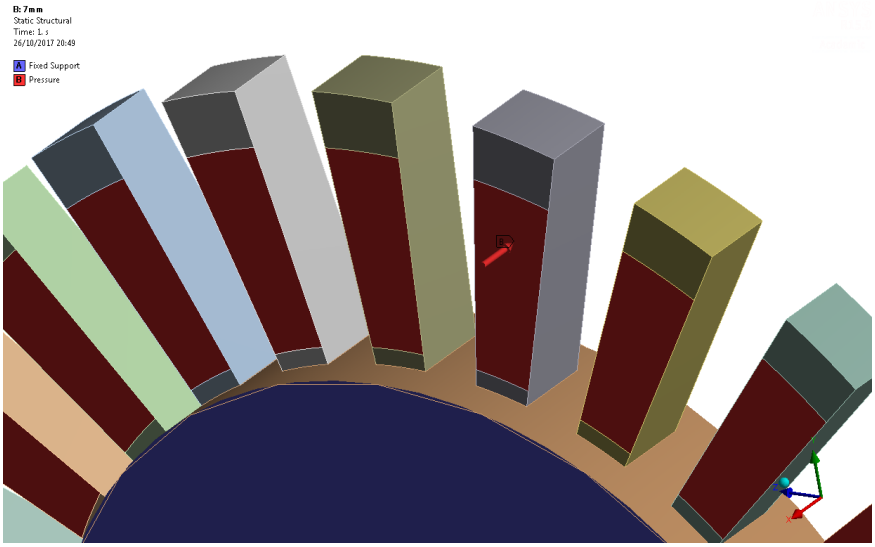

b)

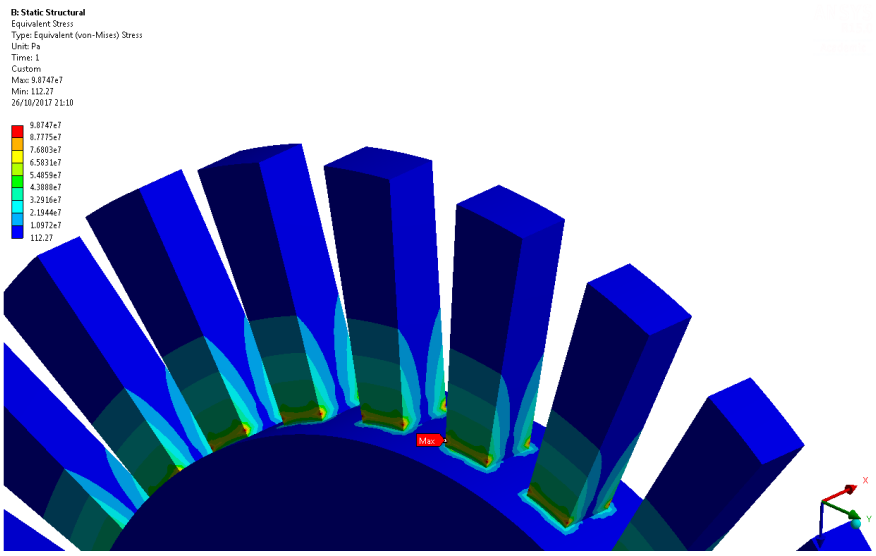

Figure 4.8 *Ansys analysis of normal operation PP forces a) Static loading b) Stress Analysis*

The ratio of inner to outer radius, λ has an impact on the AMG pull-out torque and axial force for the selected geometry as shown in Figure 4.9 and Figure 4.10. As such the resulting peak von Mises stress and deformation on the PPs are shown in Figure 4.11 and Figure 4.12, respectively.

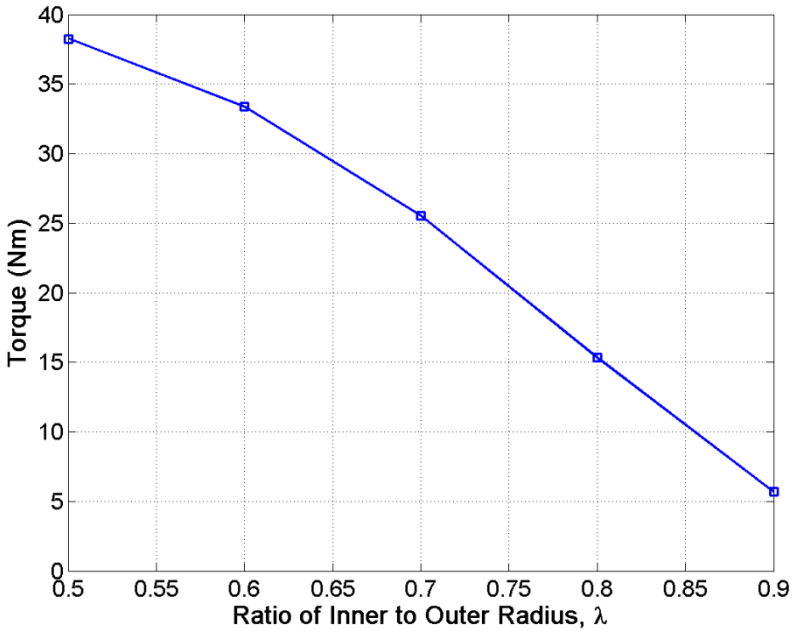

Figure 4.9 *Variation of torque with the ratio of inner to outer radius (during normal operation)*

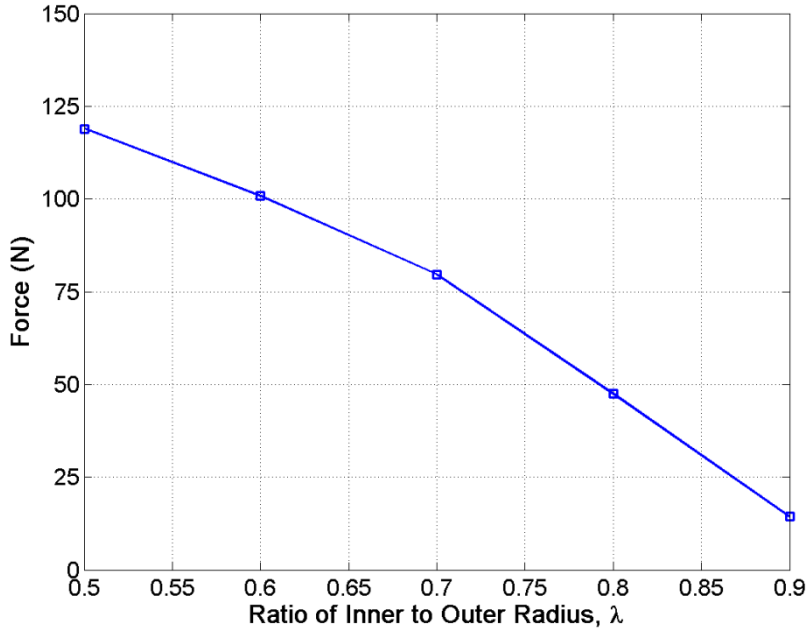

Figure 4.10 *Variation of peak EM axial force on a PP with the ratio of inner to outer radius (during normal operation)*

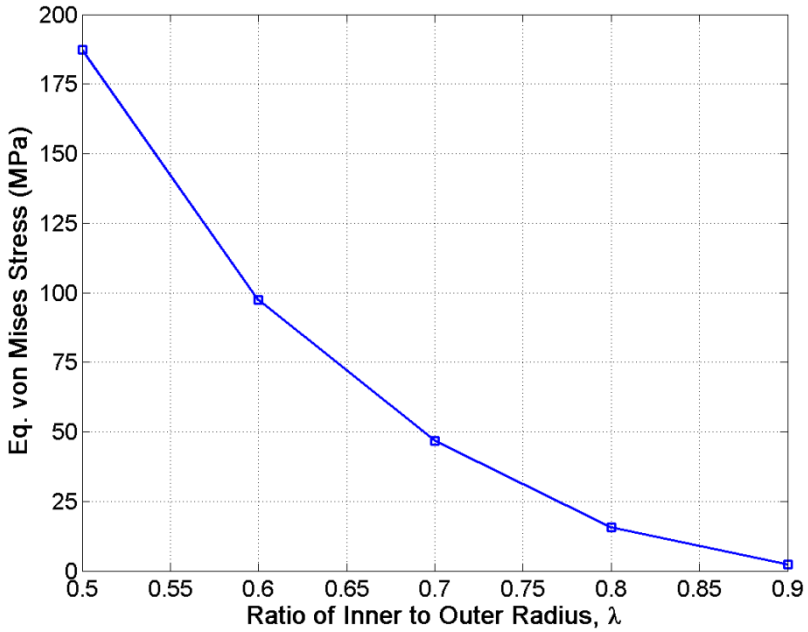

Figure 4.11 *Variation of peak Von Mises stress in a PP with the ratio of inner to outer radius (during normal operation)*

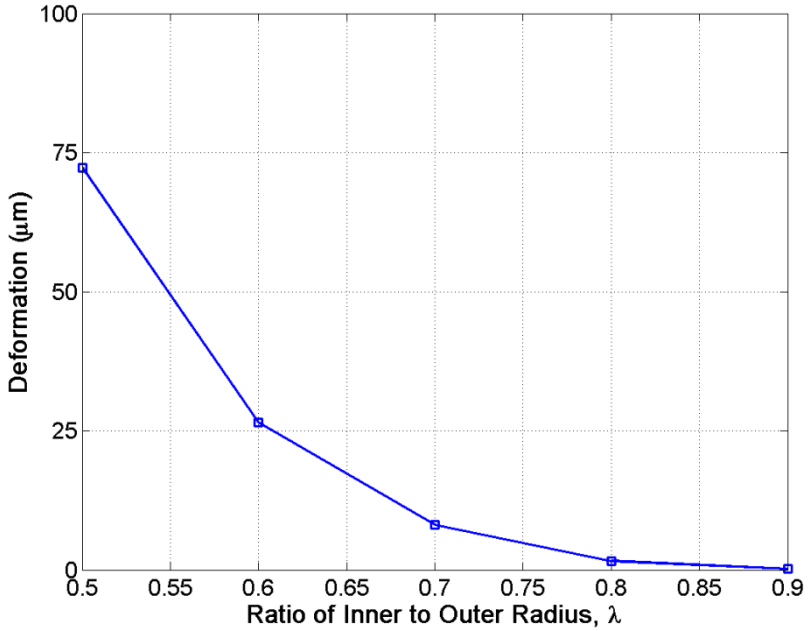

Figure 4.12 *Variation of deformation in a PP with the ratio of inner to outer radius (during normal operation)*

The frequency of the mechanical forces is derived by finding the relative speeds of each rotor as given by:

$$p_h\omega_h + p_l\omega_l - n_s\omega_{pp} = 0 \tag{4.1}$$

$$\omega_{sh} = \omega_h\left(1 - \frac{p_h}{n_s}\right) \tag{4.2}$$

$$f_{sh} = \frac{2p_h\omega_{sh}}{2\pi} \tag{4.3}$$

where ω_{sh} is the relative speed of the rotors and f_{sh} is the frequency of a mechanical cycle.

As the von Mises stress in the PPs exceeds TRS of the SMC in AMGs which exhibit high torque transmission, the prospect of reducing the axial force on the PPs whilst maintaining high torque output is inviting. By modifying the design of the PPs or by altering the assembly method this can be achieved as considered in Sections 4.2 and 4.3 respectively.

4.2. Reduction of Force via PP Design

Typically a trapezoidal PP, such as the one in Figure 4.13, is anchored at the inner radius to the PPR output. The following studies will use a nominal PP thickness of t_{pp} which corresponds to the ratio of inner to outer diameter, λ as defined in Chapter 3 by:

$$t_{pp} = \frac{\pi r_m}{n_s} \tag{4.4}$$

where n_s is the number of PPs.

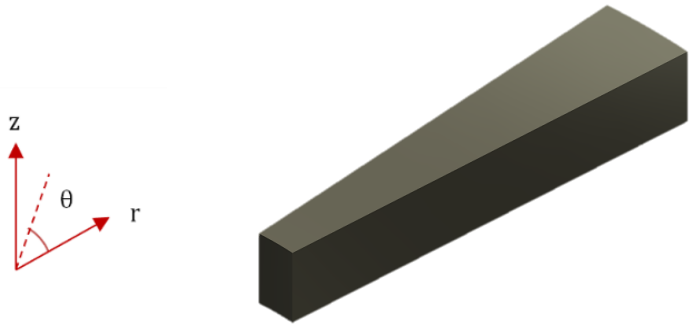

Figure 4.13 *Typical pole piece design*

4.2.1. Design 1

The first design variant (Design 1) encompasses the typical PP shape shown in Figure 4.13 with the PP axial thickness under investigation. The magnetic force on PP is shown in Figure 4.14. In Figure 4.15, it can be seen that the force is fairly independent of the axial length of the PP. However, as seen in Figure 4.16, the maximum stress is reduced significantly as the axial thickness is increased. Unfortunately, increasing the PP axial length also results in reduced torque transmission capability, as shown in Figure 4.17.

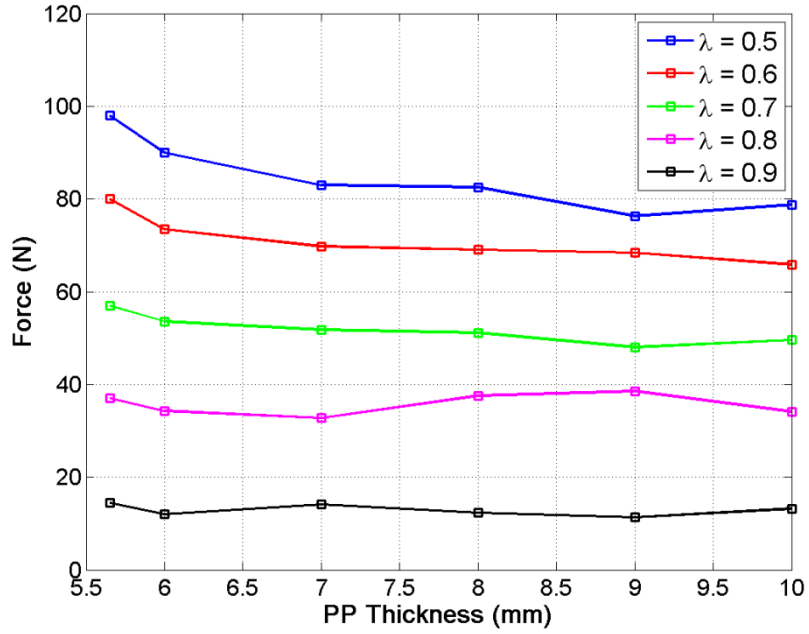

Figure 4.14 *Variation of force on a PP with its axial thickness (Design 1 PP)*

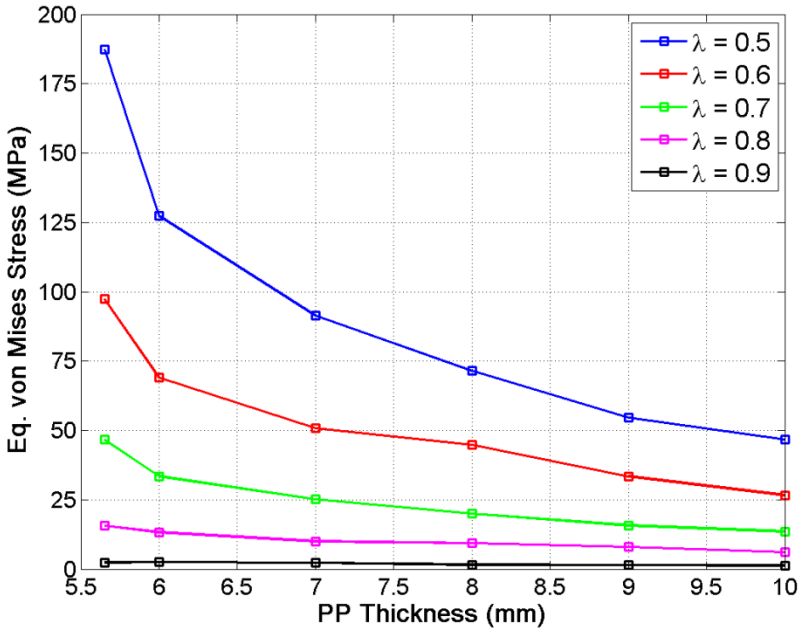

Figure 4.15 *Variation of Von Mises stress on a PP with its axial thickness (Ansys result) (Design 1 PP)*

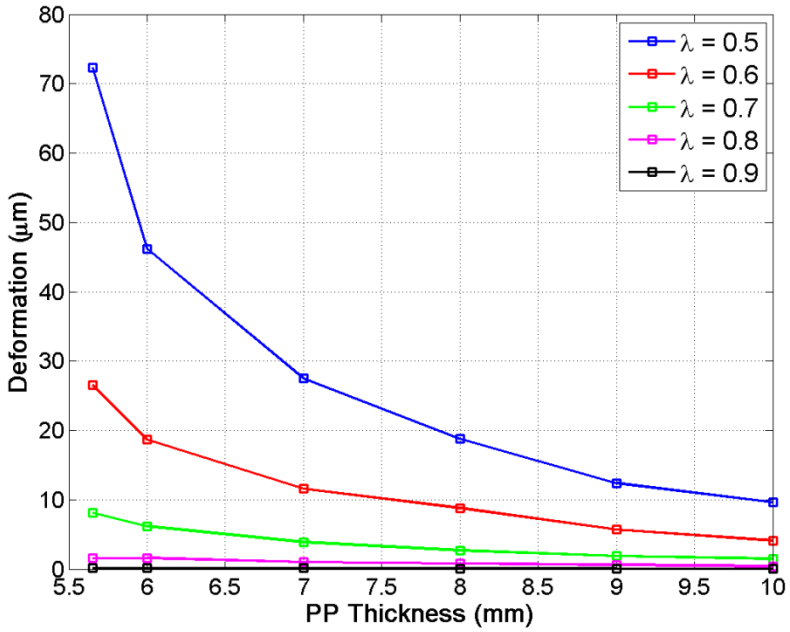

Figure 4.16 *Variation of deformation on a PP with its axial thickness (Ansys result) (Design 1 PP)*

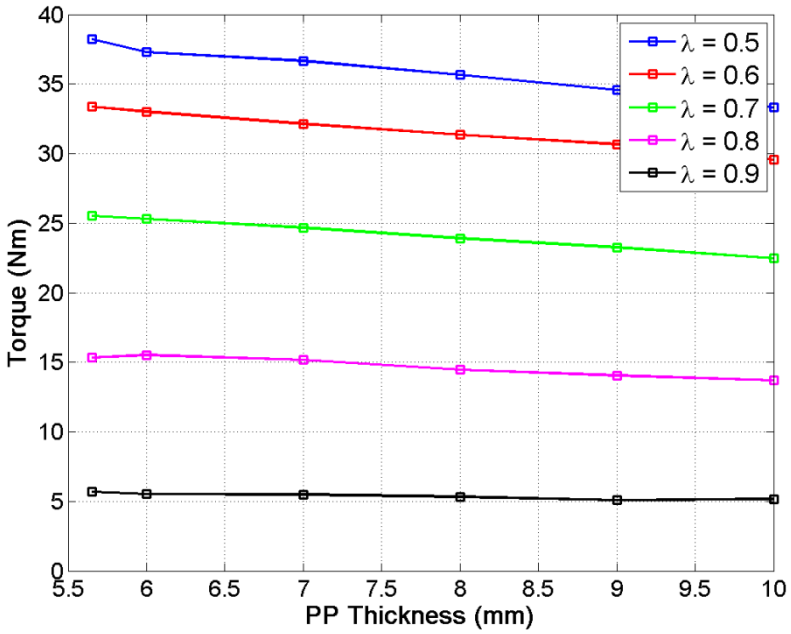

Figure 4.17 *Variation of PPR torque transmission with PP axial thickness (Design 1 PP)*

The situation resembles that of a simple beam bending problem and as such analytical expression can be used to quickly ascertain values of von Mises stress σ_{max} and deformation δ_{max} given by:

$$\delta_{max} = \frac{F(r_o - r_i)^3}{3\mathrm{EI}_x} \tag{4.5}$$

$$\sigma_{max} = \frac{F(r_o - r_i)(t_{pp}/2)}{\mathrm{I}_{area}} \tag{4.6}$$

where F is the force on the PP, r_i and r_o are the PP inner and outer radii respectively, E is the Young's Modulus, and I_{area} is the second moment of area given by:

$$\mathrm{I}_{area} = \frac{w_{pp}{t_{pp}}^3}{12} \tag{4.7}$$

where w_{pp} is the mean width of the PP.

Good correlation is seen between the analytical results in Figure 4.18 and Figure 4.19 and those attained from the Ansys model. Some variation in stress is seen due to stress concentration and numerical error at the corners of Ansys models.

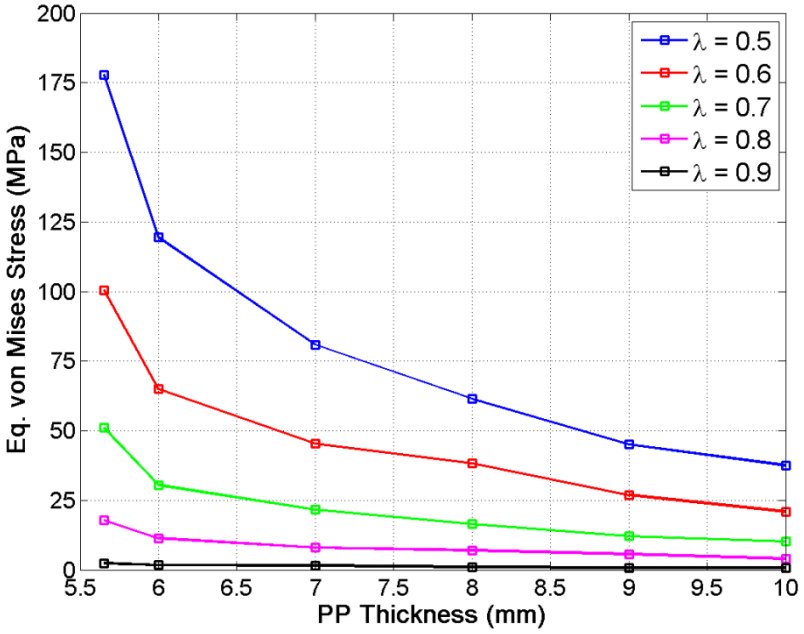

Figure 4.18 *Variation of Von Mises stress with PP axial thickness (Analytical result) (Design 1 PP)*

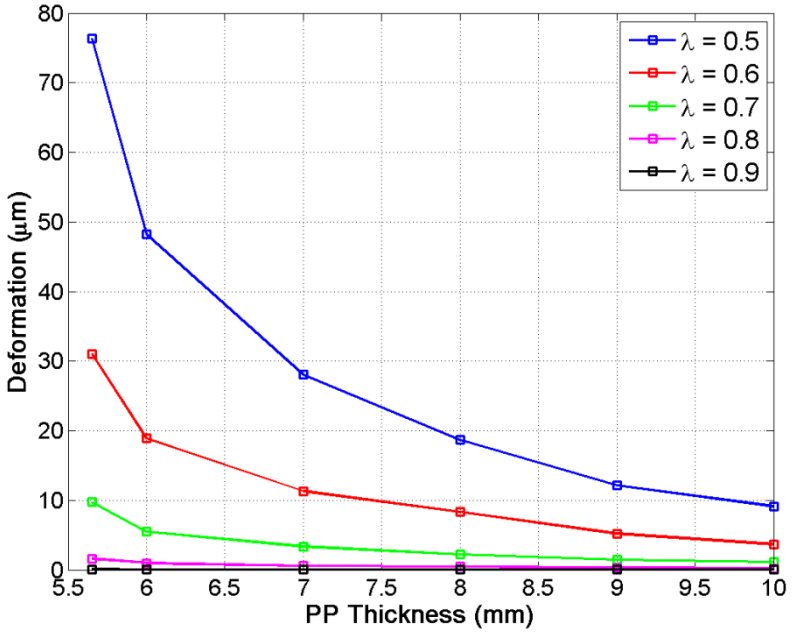

Figure 4.19 *Variation of deformation with PP axial thickness (Analytical result) (Design 1 PP)*

4.2.2. Design 2

The second design (Design 2) retains the PP shape of Design 1 and adds an outer ring made from non-magnetic, metallic material as shown in Figure 4.20. The outer ring adds the number of constraints required to define the stress analysis as shown in Figure 4.21(a). The maximum of stress distribution is seen toward the hub and not the outer ring as shown in Figure 4.21(b).

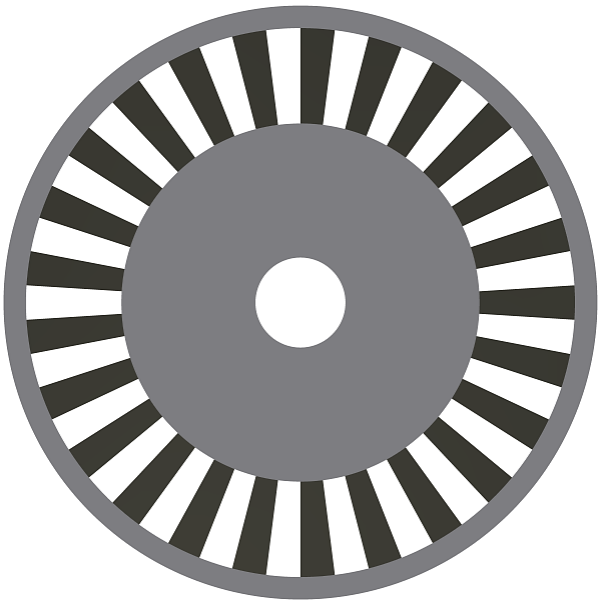

Figure 4.20 *Design 2 - PPR with outer ring*

a)

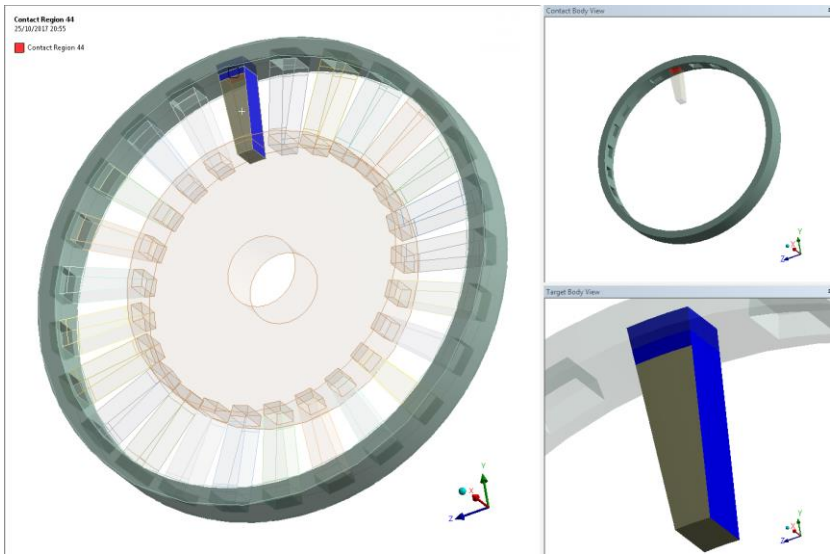

b)

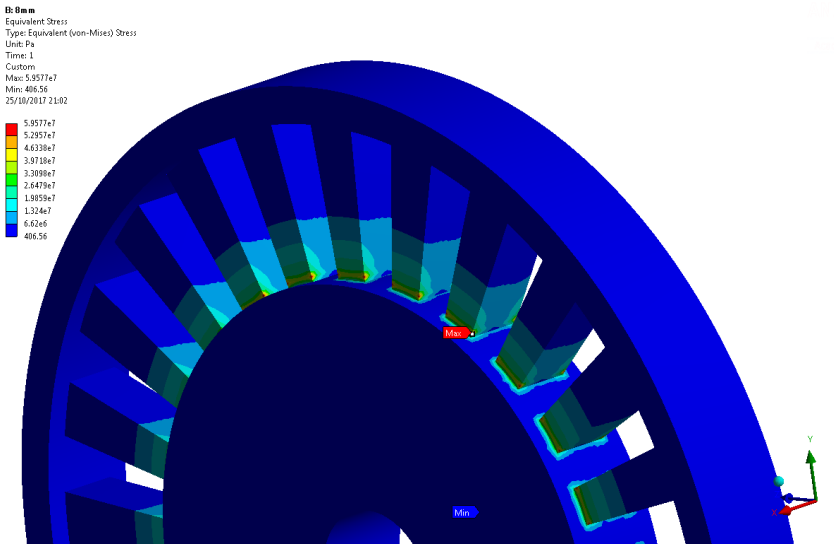

Figure 4.21 *Ansys analysis a) Constraints b) Stress analysis (Design 2 PP)*

Figure 4.22 shows the von Mises stress in the PPs is significantly reduced by the addition of the outer ring. The ability of the outer ring to resist bending improves the SMC PP's ability to resist deformation and is dependent on the PP thickness as shown in Figure 4.23.

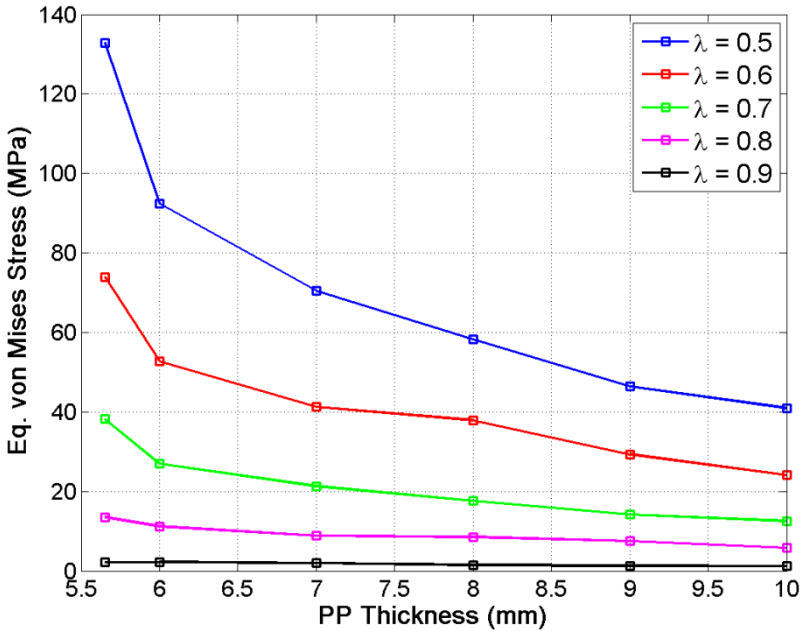

Figure 4.22 *Variation of Von Mises stress with PP thickness (Design 2 PP)*

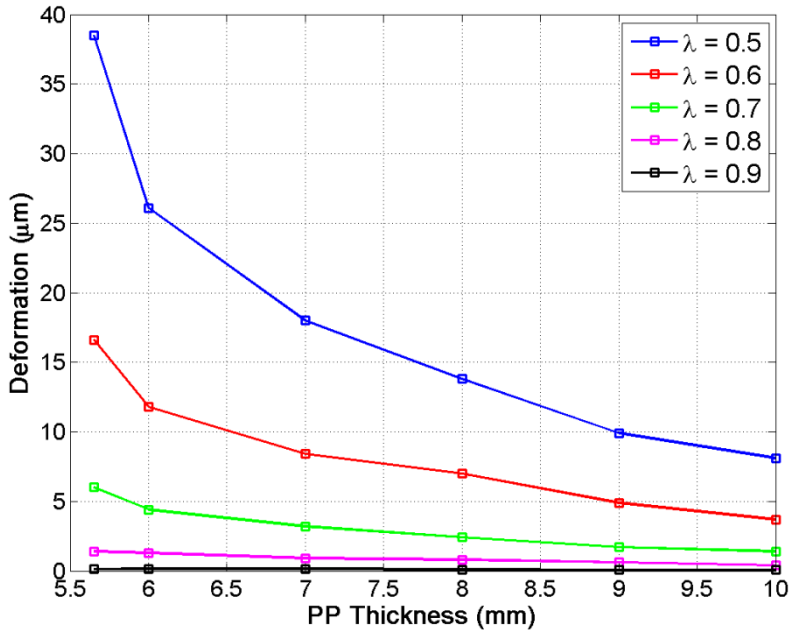

Figure 4.23 *Variation of deformation with PP thickness (Design 2 PP)*

4.2.3. Design 3

An alternative to the structure of a typical PPR shown in Figure 4.24(a) can be implemented by supporting the PPs with a non-magnetic material of the hub as shown in Figure 4.24(b). Here the red section represents the area of the hub which enters the active region of the PP within the axial length of the PP, minimising the stress on the PP.

An adhesive, with a bond thickness of 0.1mm, was modelled (Permabond ES558) as the connection between the PPs and the non-magnetic support material with a Young's modulus of 4GPa (at 25ºC) and with Poisson's ratio of 0.3. Using a PP axial thickness of 5.65mm, the reduction in equivalent von Mises stress and deformation can be seen in Figure 4.25 and Figure 4.26.

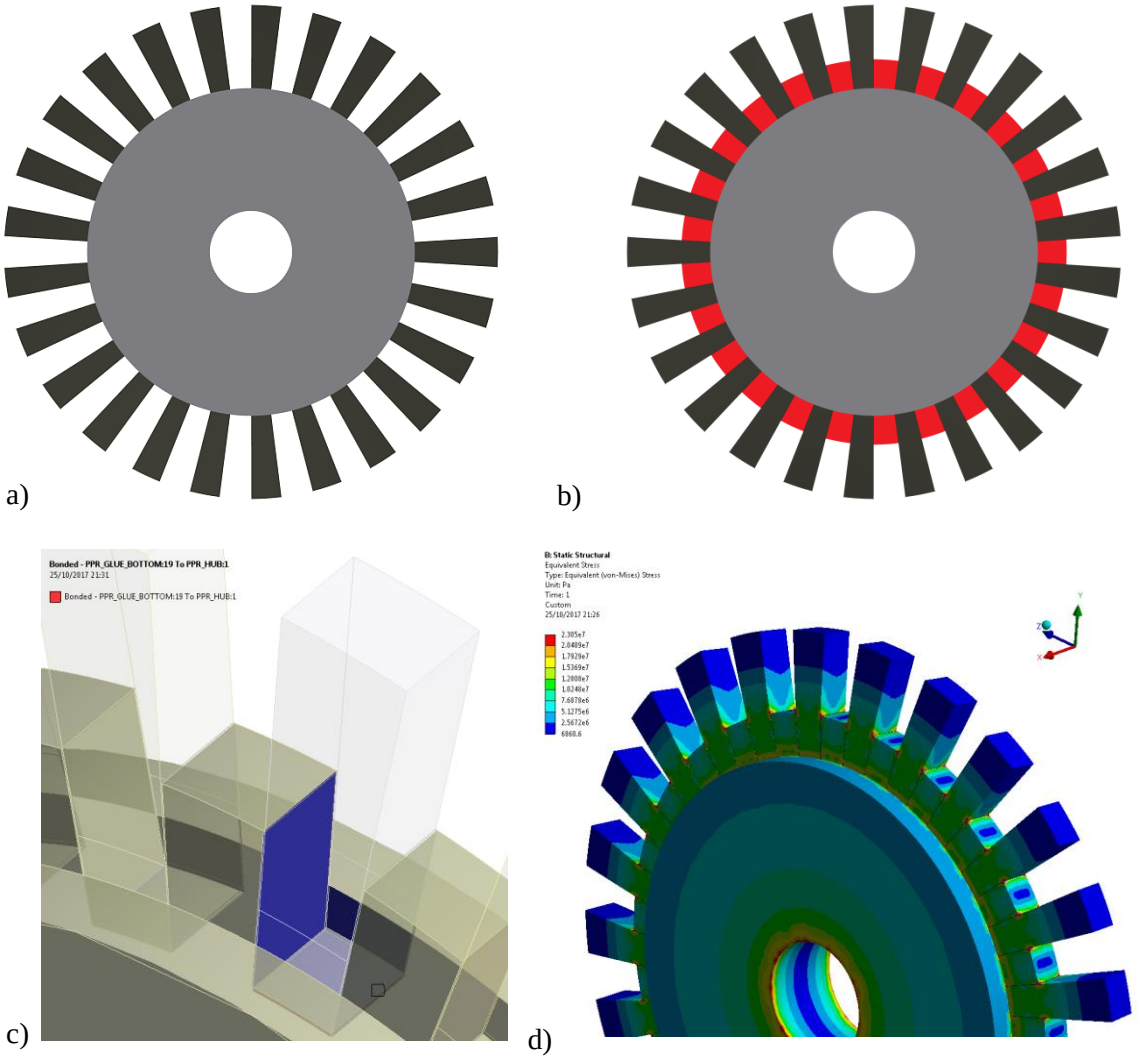

Figure 4.24 *Design 3 – a) Typical PPR and b) Supported PPs c) Ansys constraints d) Stress distribution*

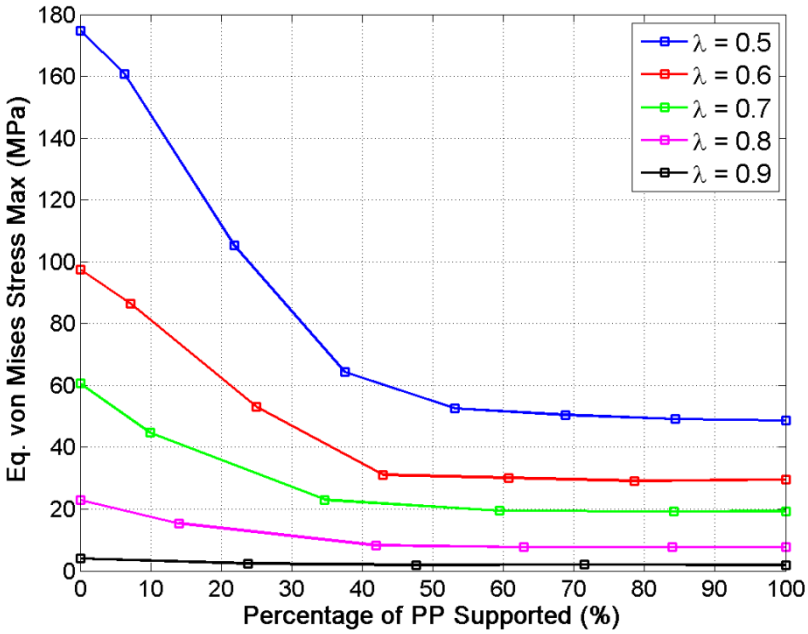

Figure 4.25 *Variation of Von Mises stress with PP support percentage (Design 3 PP)*

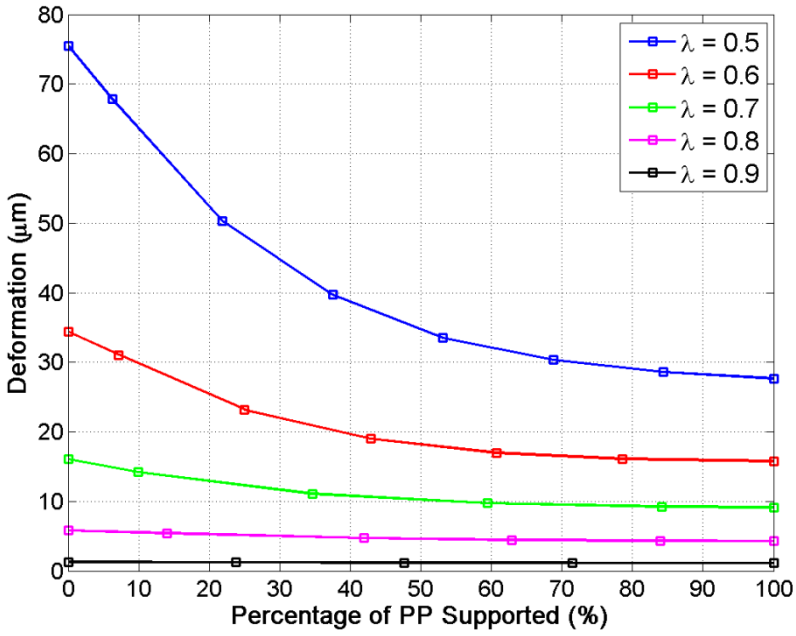

Figure 4.26 *Variation of deformation with PP support percentage (Design 3 PP)*

Two material categories may be appropriate for the PP support material. Using a non-magnetic, metallic material such as austenitic stainless steel or aluminium would be simple to manufacture but could lead significant losses due to eddy currents induced in the material during rotation of the PPR. A non-magnetic, non-conducting material such

as glass fibre may be mechanically and magnetically suitable but would pose serious challenges in terms of its construction.

It should be noted that modelling the adhesive joint between the PP and PPR rotor hub resulted in higher values of deformation and lower von Mises stress. Higher deformation results from the adhesive's lower Young's modulus. Lower von Mises stress results from a reduction in stress concentration as the corners of the PPs are no longer in direct contact with the PPR hub.

4.2.4. Design 4

The supported PPs of Design 3 and addition of an outer ring shown in Design 2 can be used together as shown in Figure 4.27. A down selected design from PPR Design 2 and Design 3 with values of $\lambda = 0.7$, $t_{pp} = 5.65mm$ and 35% PP support with an adhesive bond was chosen. The radial thickness of the ring was investigated and was shown to contribute to its ability to resist bending, with the resulting von Mises stress and deformation of the PPs shown in Figure 4.28 and Figure 4.29.

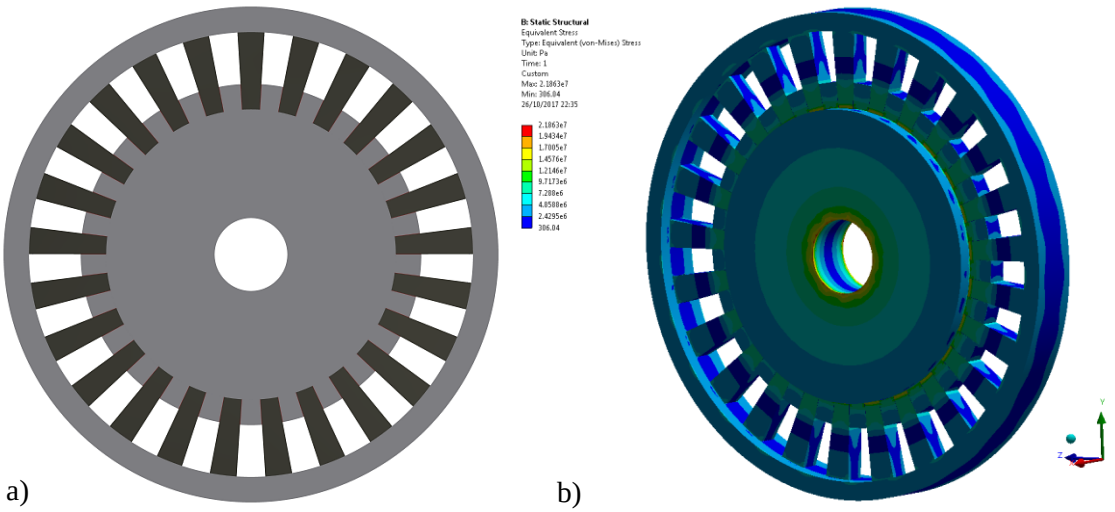

a) b)

Figure 4.27 *Design 4 a) Supported PP with outer ring b) Stress distribution*

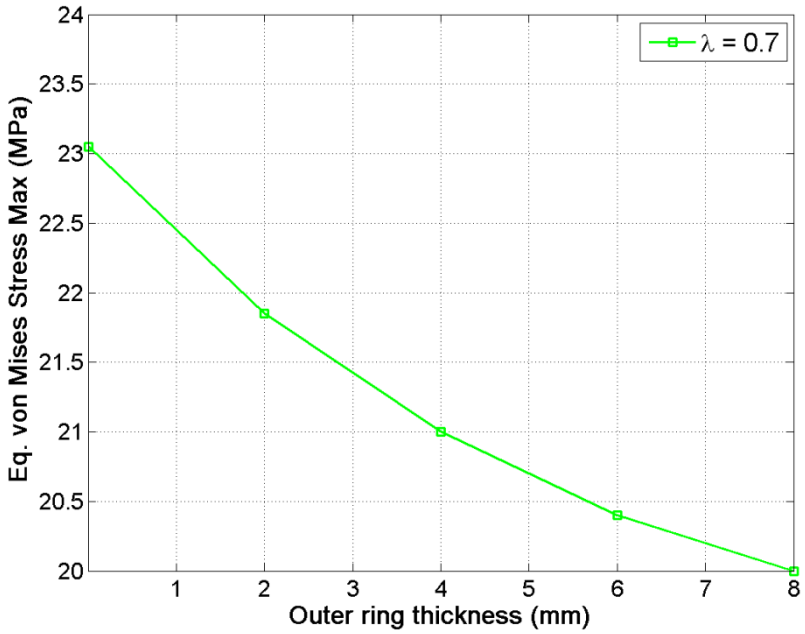

Figure 4.28 *Variation of Von Mises stress with outer ring thickness (Design 4)*

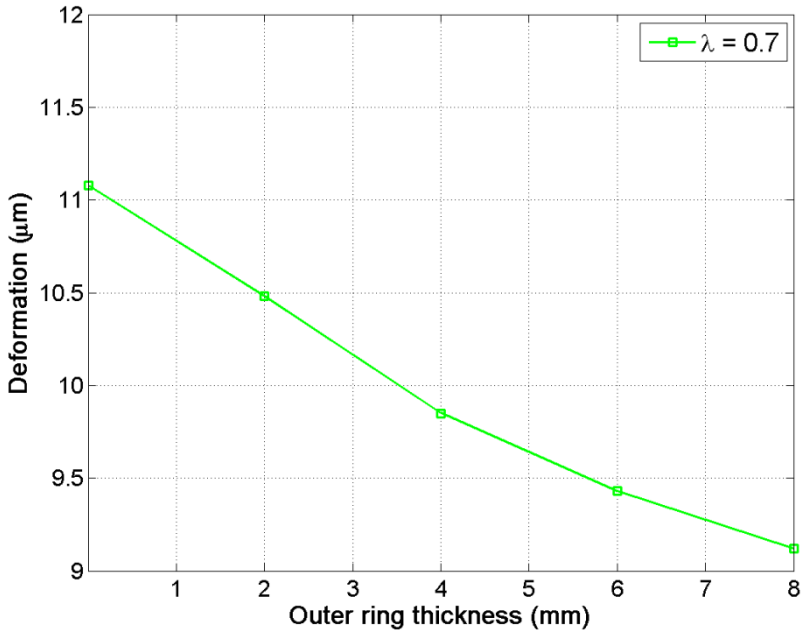

Figure 4.29 *Variation of deformation with outer ring thickness (Design 4)*

4.2.5. Design 5

The PP shape can be varied with the ratio of the length of the inner arc l_i to the length of outer arc l_o as shown in Figure 4.30. The magnetic performance discussed in Section

3.4.3 showed a deterioration of torque with increasing l_i/l_o. The Ansys analysis of the variation of l_i/l_o and stress distribution are shown in Figure 4.31.

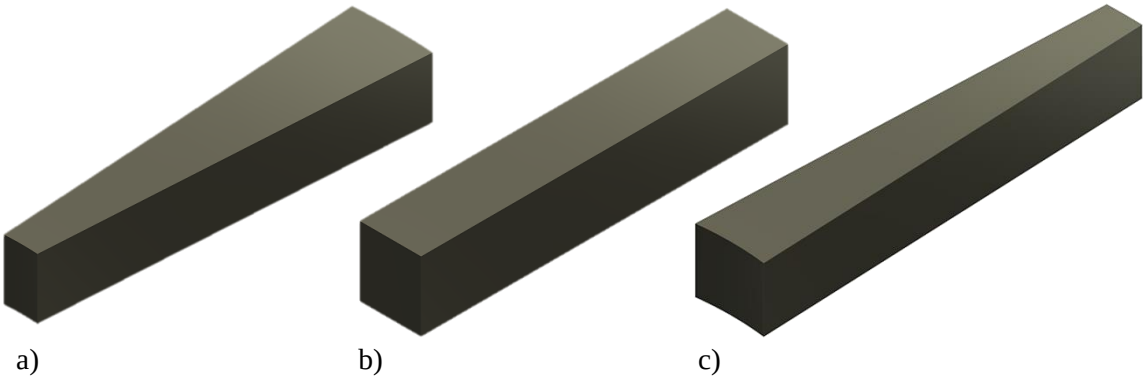

Figure 4.30 *Design 5 pole piece with l_i/l_o is a) <1, b) =1 and c) > 1*

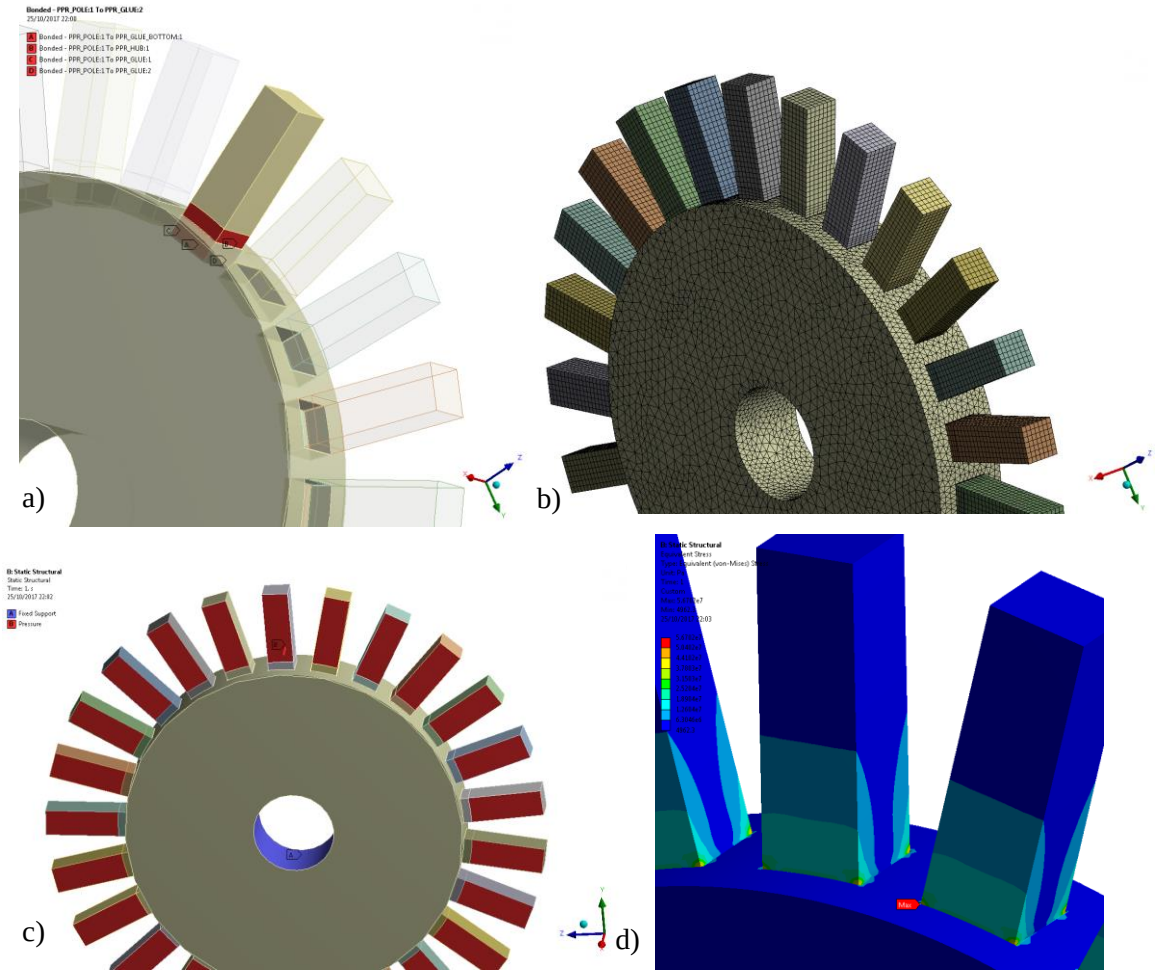

Figure 4.31 *Design 5 a) PP constraints b) Mesh c) Static loading d) Stress analysis*

An increase l_i/l_o improves the strength of the PP as the force is reduced at the outer radius. Figure 4.32 and Figure 4.33 show the torque and shear stress variation. The resulting von Mises stress and deformation show improvement beyond values of $l_i/l_o = 1$.

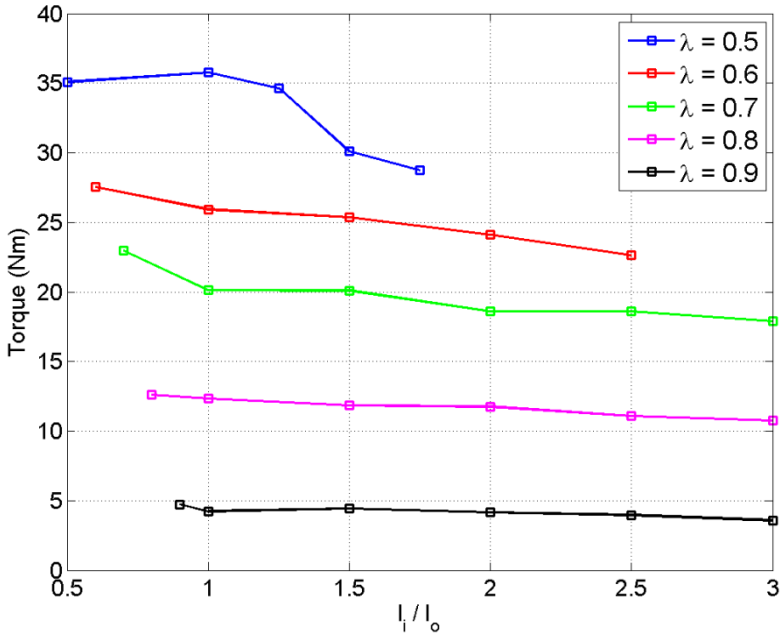

Figure 4.32 *Variation of torque with ratio l_i/l_o. (Design 5 PP)*

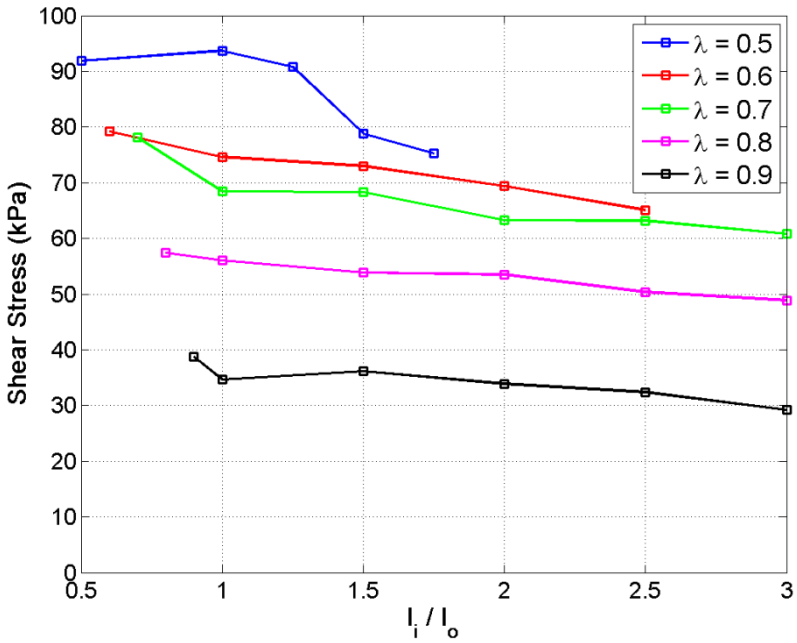

Figure 4.33 *Variation of shear stress with ratio l_i/l_o. (Design 5 PP)*

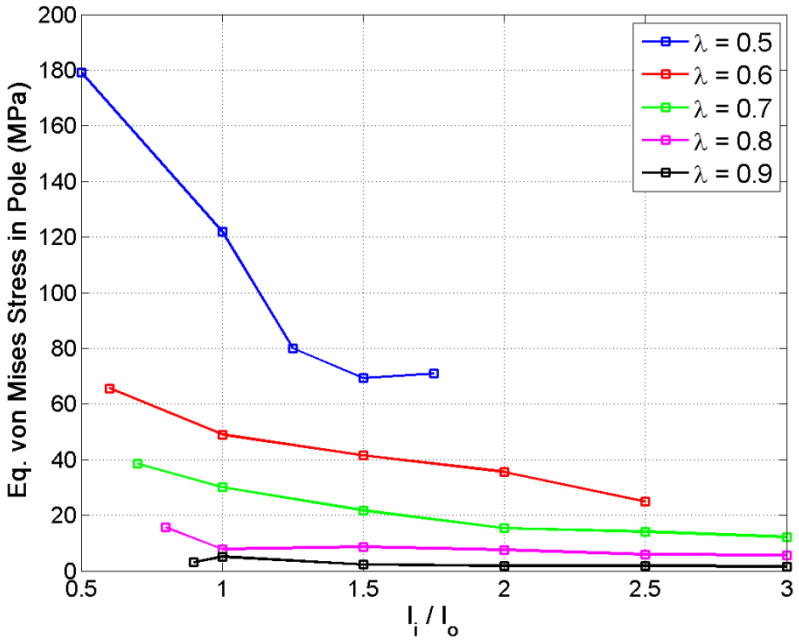

Figure 4.34 *Variation of Von Mises stress with ratio l_i/l_o. (Design 5 PP)*

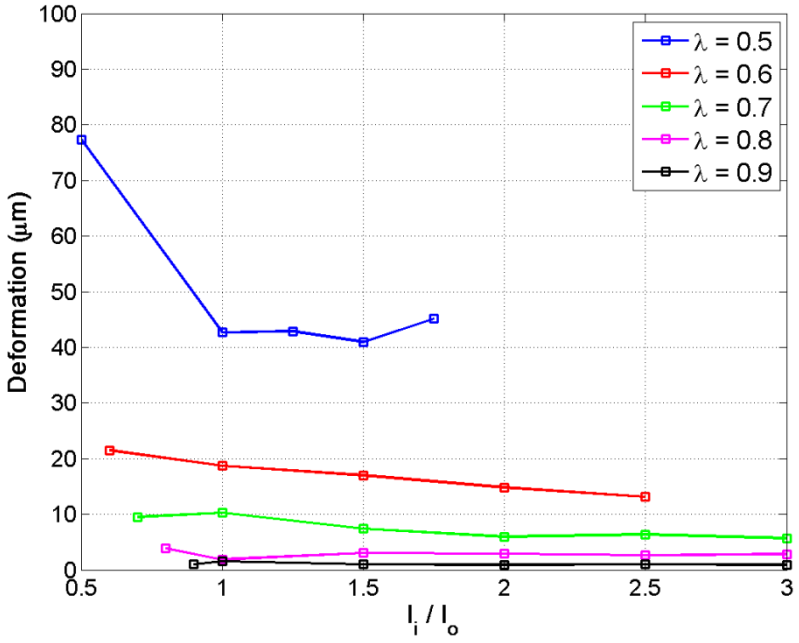

Figure 4.35 *Variation of deformation with ratio l_i/l_o. (Design 5 PP)*

4.2.6. Design 6

The trapezoidal PP thickness has to be increased to minimise the stress to acceptable levels with the resulting reduction in torque output most significant in AMG with low values of λ. As such a cylindrical PP is proposed as shown in Figure 4.36.

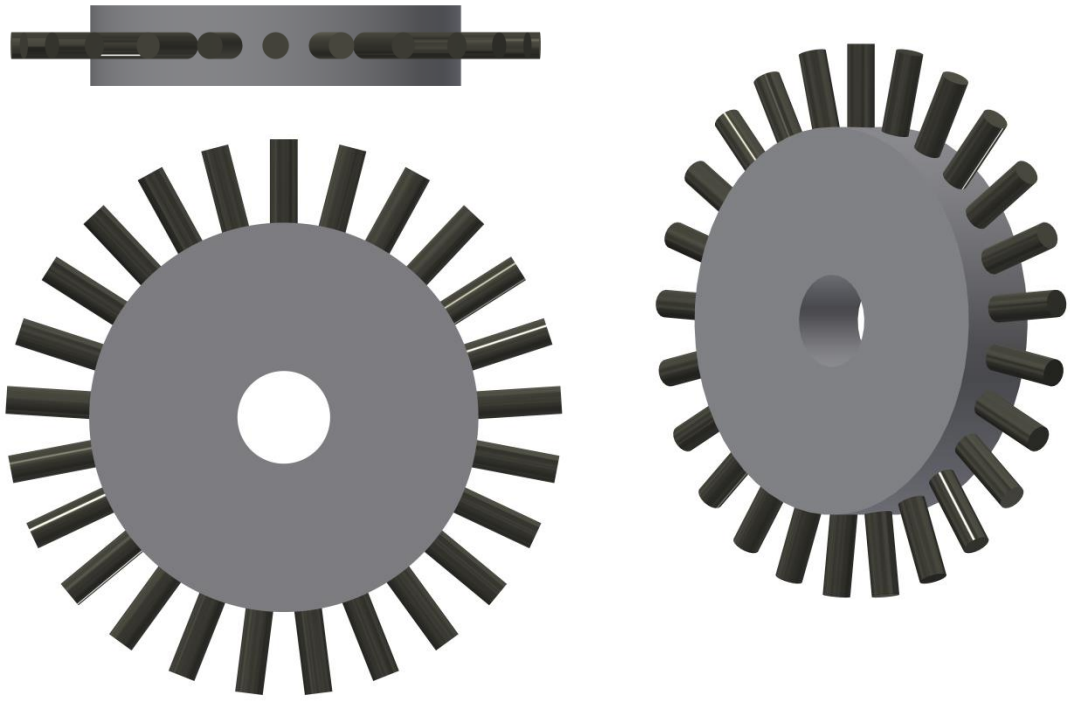

Figure 4.36 *Design 6– Cylindrical pole piece*

The cylindrical PP produces a reduced torque output but is also subjected to a lower axial force when compared to its equivalent trapezoidal PP as shown in Figure 4.37 and Figure 4.38, respectively. This is due to the round nature of the face presented to the magnet arrays which leads to lower forces and significantly lower von Mises stress and deformation as seen in Figure 4.39, Figure 4.40 and Figure 4.41. Furthermore, the cylindrical PP is advantageous in that it will not experience a moment about its own axis as the PPR rotates.

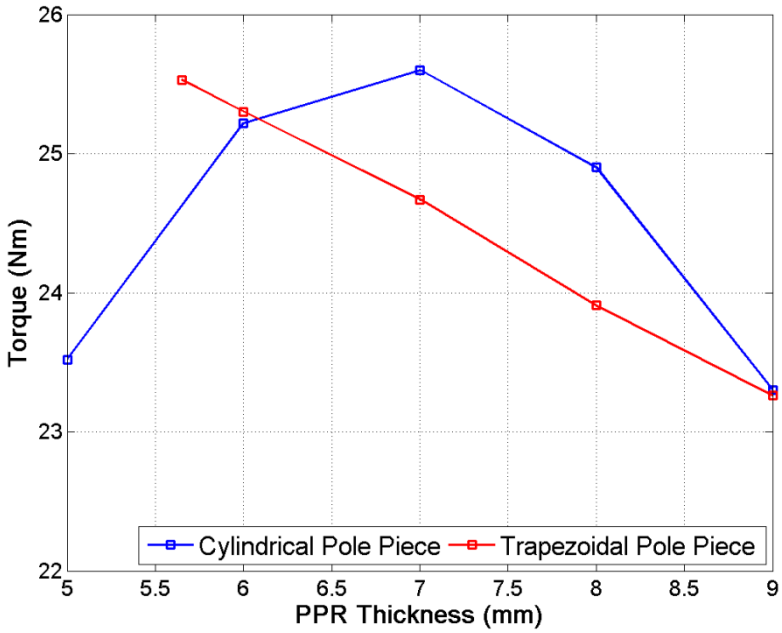

Figure 4.37 *Variation of torque with cylindrical PP axial thickness (Design 6 PP)*

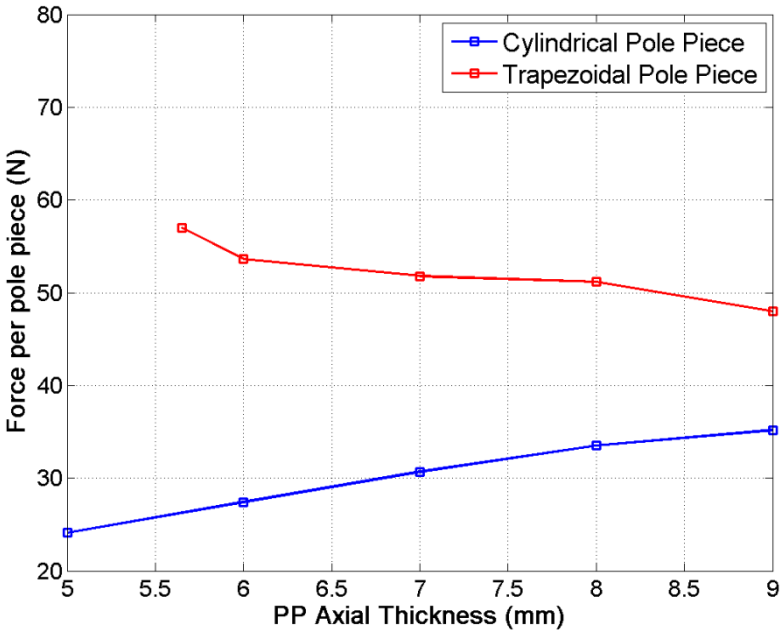

Figure 4.38 *Variation of force with cylindrical PP axial thickness (Design 6 PP)*

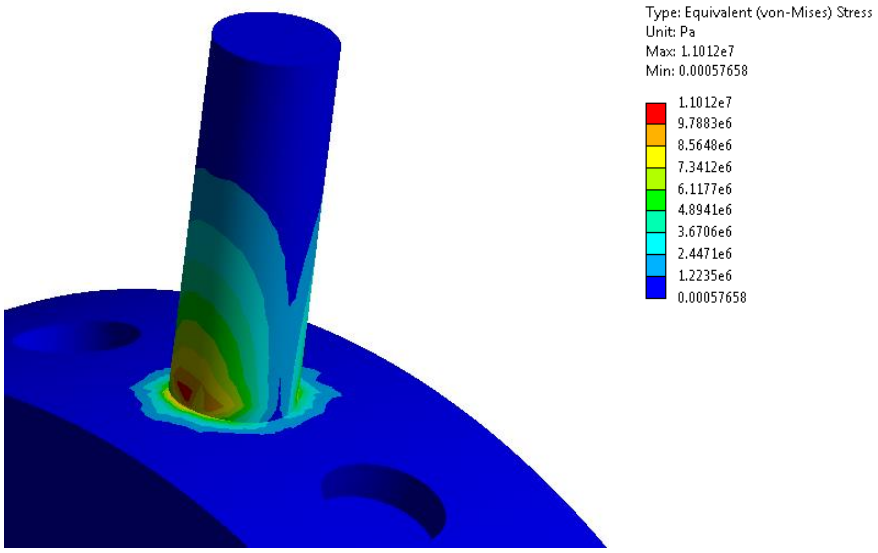

Figure 4.39 *Cylindrical PP stress analysis (Design 6 PP)*

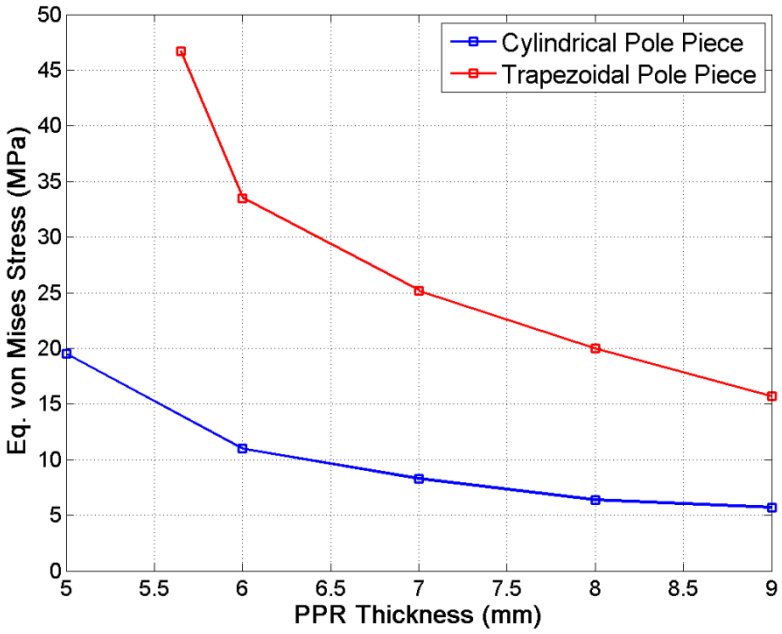

Figure 4.40 *Variation of Von Mises stress with cylindrical PP axial thickness (Design 6 PP)*

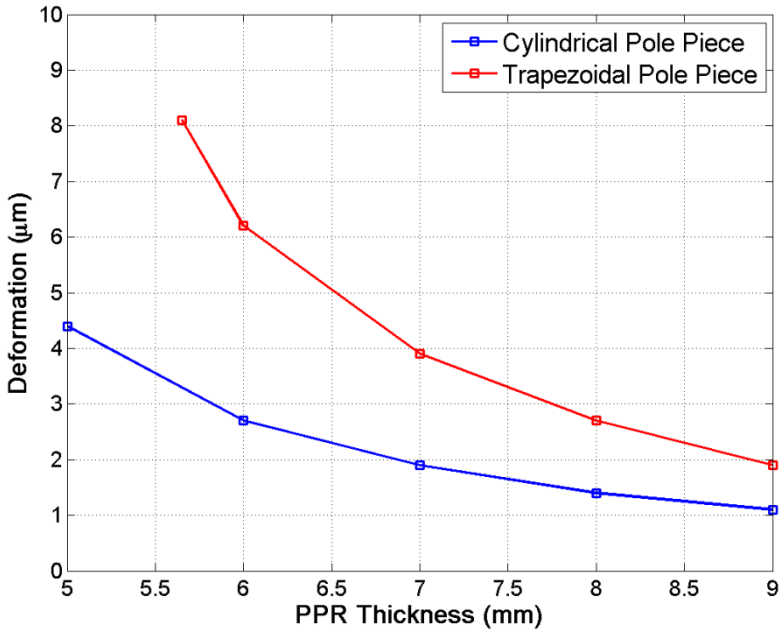

Figure 4.41 *Variation of deformation with cylindrical PP axial thickness (Design 6 PP)*

A comparison of the forces on the trapezoidal and cylindrical PPs with a hub from Design 1 and $t_{pp} = 6mm$, $\lambda = 0.7$ is shown in Figure 4.42 with a harmonic analysis shown in Figure 4.43. This is one mechanical cycle when the PPR rotates at 150rpm. Note the peaks are offset due to different PPs undergoing the maximum force at differing positions during simulation.

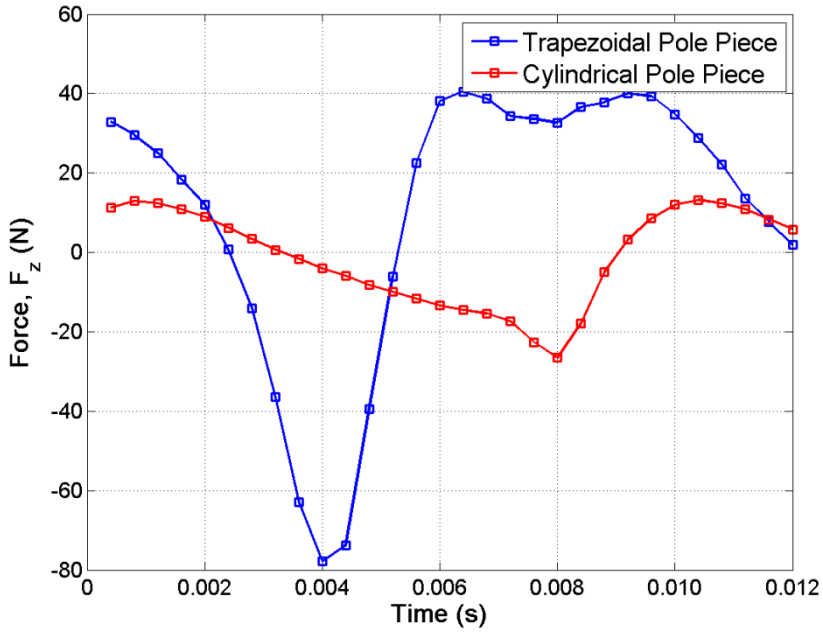

Figure 4.42 *Comparison of axial force on cylindrical and trapezoidal PP in an AMG*

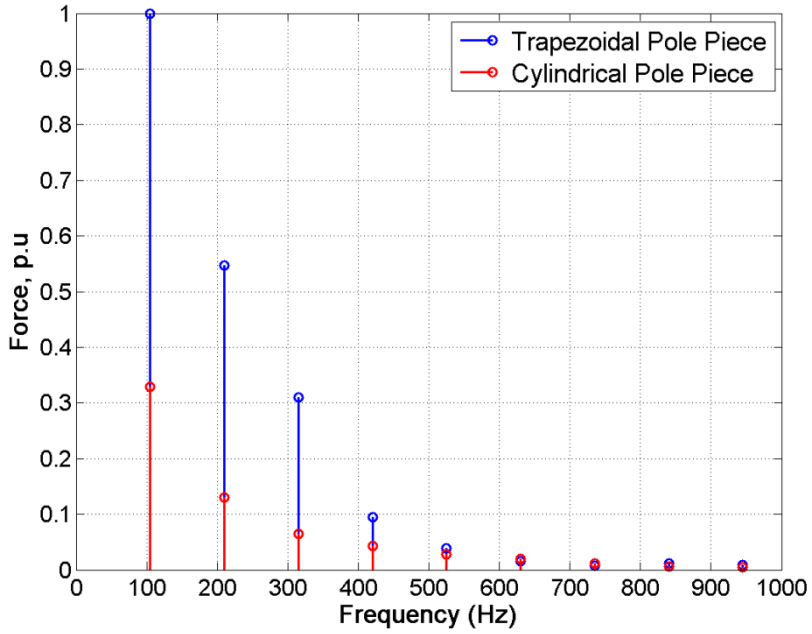

Figure 4.43 *Comparison of axial force harmonics on cylindrical and trapezoidal PP in an AMG*

A similar comparison of the radial force can also be made between the trapezoidal and cylindrical PPs in an equivalently sized CMG as shown in Figure 4.44 and Figure 4.45. To model the CMG, the AMG was 'unrolled' about the mean radius with axial

dimensions in the AMG changed to radial in the CMG. The active axial length of the CMG is then taken from the difference between outer and inner diameters of the AMG. It can be seen that the cylindrical PP in the axial topology shows the most significant reduction of force in the active direction.

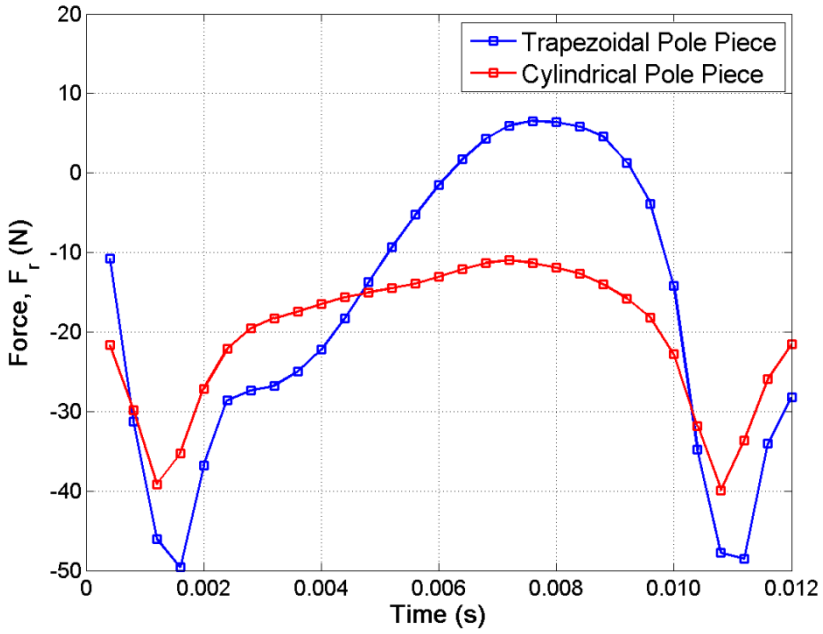

Figure 4.44 *Comparison of radial force on cylindrical and trapezoidal PP in a CMG*

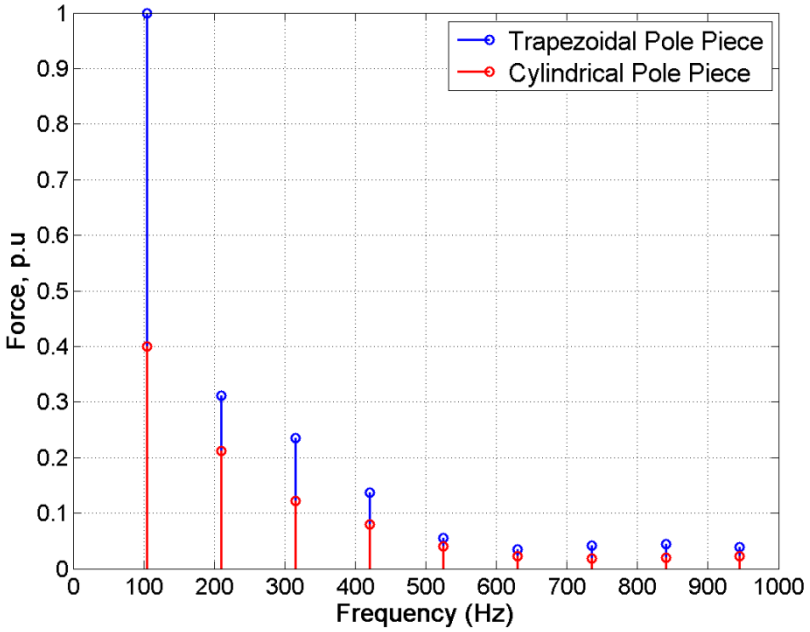

Figure 4.45 *Comparison of radial force harmonics on cylindrical and trapezoidal PP in a CMG*

4.2.7. Additional Design Variants

An additional option to improve PP mechanical performance is to use a stronger non-magnetic material to reinforce the trapezoidal or cylindrical PPs shown in Figure 4.46(a) and (b) respectively. This would provide additional strength to the SMC. A material such as Tungsten or Silicon Carbide would be appropriate due to their high Young's Modulus (400-450GPa) compared to that of SMC (160GPa) [4.9][4.4]. Construction and assembly of Silicon Carbide reinforced PPs may become difficult due to the brittle nature of Silicon Carbide which reduces the toughness of the resulting PP. Unfortunately, Tungsten is often found in niche applications making the material availability and cost prohibitive. Due to the geometric limitations this option is not suitable for a small prototype machine but is potentially more suited to larger machines.

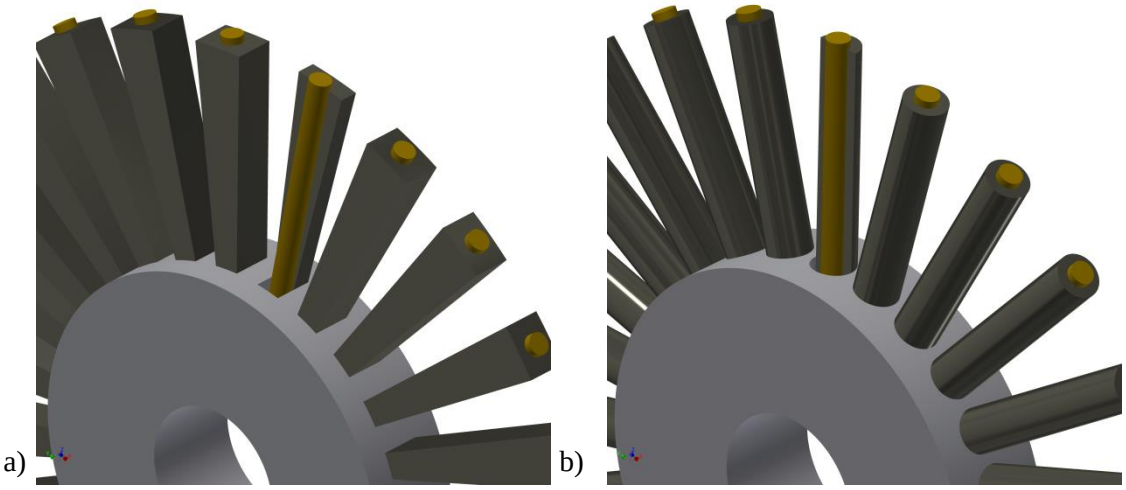

Figure 4.46 *Reinforced PP a) Trapezoidal b) Cylindrical (Design 7 PP)*

The use of a spoke type arrangement, as seen in Figure 4.47, was considered as additional strength could be provided by mechanically connecting the hub to the outer ring using tensioned spokes [4.10]. Due to the complex manufacturing involved and the difficulties posed in preventing the formation of an effective induction cage this was not considered possible on a small prototype.

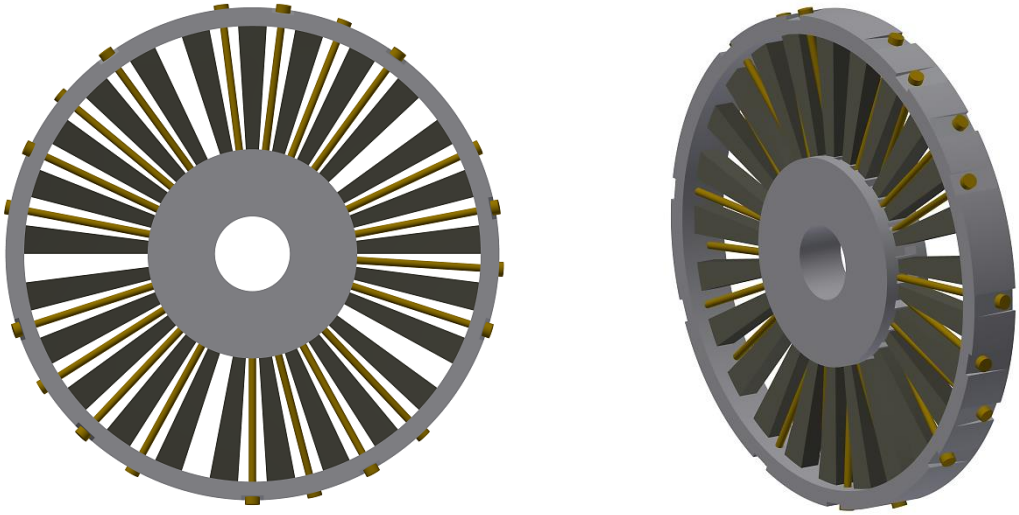

Figure 4.47 *Spoked pole piece rotor (Design 8 PP)*

4.3. Reduction of Force via Assembly Method

Efforts to reduce the force subjected to the PPs can be made by 'short circuiting' the magnets during the assembly process, as shown in Figure 4.48. An iron sheet could be placed on the surface of both magnet arrays, providing a low reluctance path for the magnetic flux.

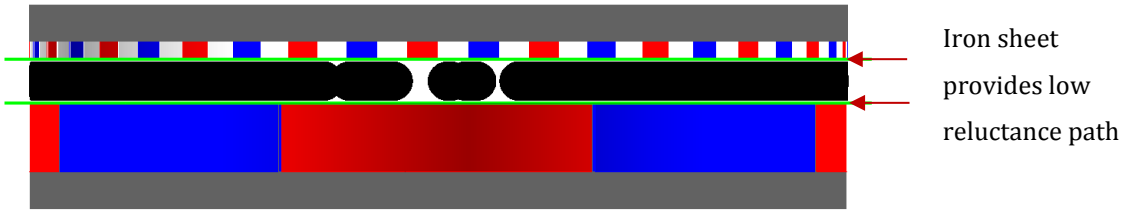

Figure 4.48 *A PP assembly method*

Using infinitely permeable iron during FEA analysis gave the force per pole effectively reduced to zero. However, when saturation of the iron sheet is considered an insignificant change in the force per pole was seen. As the airgap is 0.5mm the thickness of the iron sheet is small (<0.45mm). Due to the thin section the iron is saturated without providing a large enough path for the flux to short circuit between

magnets on the same array. This approach is therefore not applicable to a small scale prototype.

An alternative assembly method would be to add the PPs once the two magnet arrays are placed in their final position in the machine. This reduces the single-sided magnetic pull due to a cancellation of the magnetic field of the high-speed magnet array and the fixed magnet array. Using cylindrical PPs, the force upon the pole as it is inserted radially between the magnet arrays is shown in Figure 4.49. The technique is applicable to the small prototype intended and requires only limited adjustments to the overall mechanical design.

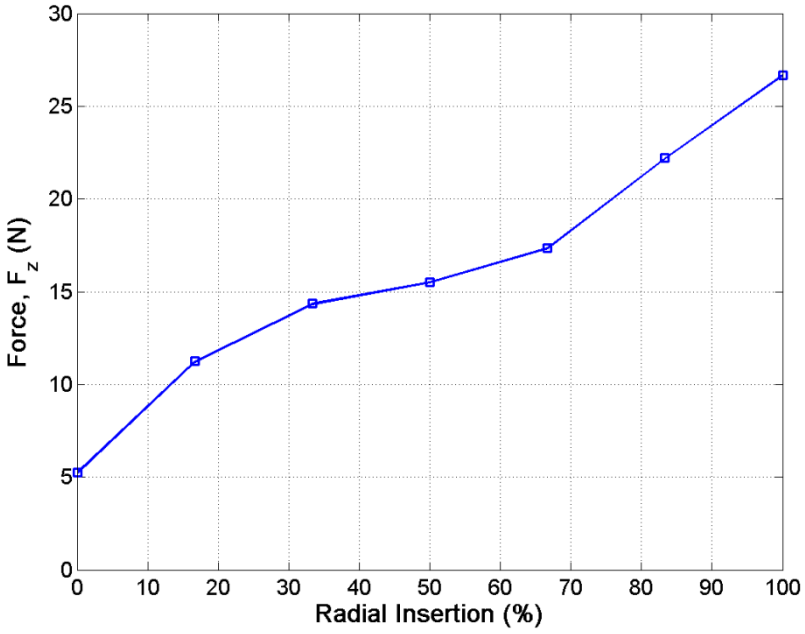

Figure 4.49 *Variation of axial force on cylindrical pole pieces (with radial insertion)*

4.4. Conclusions

The forces on PPs during assembly and under normal operating conditions have been examined. To simplify construction it was decided to use PPs assembled into a single hub with no additional supports. A ratio of $\lambda = 0.7$ was selected as a compromise

between torque transmission capability and force on the PPs. It was shown that a trapezoidal PP still required an increase in axial thickness to minimise stress to an acceptable level.

The addition of an outer ring gave a reduction in von Mises stress and deformation, in some cases ~20%. The number of parts required and inactive mass are subsequently increased. However, this method further benefits the mechanical integrity by reducing the relative oscillations of the PPs during rotation. As such it is recommended to use a structure with an outer ring.

Extending the hub into the active region reduces the Von Mises Stress within the PP but will impact the efficiency if metallic materials are used in the hub construction. Increasing the inner arc to outer arc length l_i/l_o significantly reduces the von Mises stress and deformation within the PP. Regrettably, a resultant negative impact on the torque and shear stress of the AMG is seen. The opportunity exists to investigate reinforced pin / spoke designed PPR for large machines as further work.

A cylindrical PP provides the most optimal solution in terms of reductions in von Mises stress and transmitted torques. The shape further benefits as no moment about its own axis exists and both PP and PPR hub manufacture are significantly simplified. Therefore, the cylindrical PP is selected for the design of an axial field PDD, and is further discussed in Chapter 5.

4.6. References

[4.1] K. Atallah, R. E. Clark, and J. J. Rens, "Magnetic pole -piece structure," WO 20091387252009.

[4.2] S. D. Calverley and D. J. Powell, "Magnetic pole-piece support," WO 20091387282009.

[4.3] G. Jungmayr, J. Loeffler, B. Winter, F. Jeske, and W. Amrhein, "Magnetic gear: Radial force, cogging torque, skewing and optimization," *IEEE Energy Convers. Congr. Expo. ECCE 2015*, no. 99, pp. 1–9, 2015.

[4.4] Hoganas AB Ltd., "Somaloy 1000 3P," 2015.

[4.5] Hoganas AB Ltd., "Somaloy Prototyping Material (SPM) 2015 Datasheet," 2015.

[4.6] Cogent Power Ltd., "M270-35A Datasheet," 2015.

[4.7] Y. Guo, J. G. Zhu, P. A. Watterson, and W. Wu, "Comparative Study of 3-D Flux Electrical Machines With Soft Magnetic Composite Cores," *IEEE Trans. Ind. Appl.*, vol. 39, no. 6, pp. 1696–1703, 2003.

[4.8] R. Kobler, D. Andessner, J. Passenbrunner, and W. Amrhein, "Modeling, simulation and design of an axial flux machine using soft magnetic composite," in *2011 IEEE Vehicle Power and Propulsion Conference (VPPC)*, 2011, pp. 1–6.

[4.9] The Engineering Toolbox, "Modulus of Elasticity or Young's Modulus," 2016. [Online]. Available: https://www.engineeringtoolbox.com/young-modulus-d.

[4.10] H. P. Gavin, "Bicycle-Wheel Spoke Patterns and Spoke Fatigue," *J. Eng. Mech.*, vol. 122, no. 8, pp. 736–742, 1996.

Chapter 5

Electromagnetic and Thermal Performance of an Axial Field Pseudo Direct Drive

Some literature highlights the benefits of axial electrical machines as an ideal structure for certain applications including the automotive and food industries. By incorporating a magnetic gear with this topology there is potential for compact, high torque, high efficiency electrical machines [5.1]. Previous work has largely focused on the combination of CMG and PMSM with a method of optimising this process presented in [5.2]. A single stator, dual rotor axial magnetically geared machine is analysed in [5.3]. A design study in 2011 compared an axial flux-modulated motor (AFMM) to a radial flux-modulated motor (RFMM) with the AFMM considered the simpler structure to realise [5.4].

An axial magnetically geared machine was first proposed in [5.5]. Few details are provided regarding the size and performance of the machine but it is claimed the machine can produce 40% higher torque than an equivalent radial field magnetically geared machine. An axial flux E-CVT which exhibits a similar structure to a dual stator magnetically geared machine is also analysed in [5.6].

A mechanically coupled single-sided magnetically geared axial-field machine was designed and prototyped in 2015 in [5.7]. The author incorporates the electrical machine within the centre of the axial magnetic gear and mechanically couples the two devices using the high-speed rotor, but a low torque density is reported. The difference between mechanically and magnetically coupled axial magnetically geared machines was

investigated in [5.8]. Some mechanical issues were considered and unwanted core loss examined in the single-sided topology. The machines ability to operate in motoring and generating conditions was also investigated but the analysis showed particularly low power factors.

The axial topology offers several key benefits including:

- Higher torque per mass if the outer to inner diameter ratio λ is free and large diameter to length ratios can be achieved [5.9]
- Magnet containment in radial field machines via banding increases the airgap thickness and therefore reduces the machine performance. In axial machines the magnet containment is not in the flux path and consequently the electromagnetic performance of the machine is not affected.

Variants of an integrated axial field magnetic gear and axial electrical machine structures to be evaluated are given the following acronyms - AFPDD-111 (1 Stator, 1 High-Speed Rotor, 1 Pole-Piece Rotor), AFPDD-122 (1 Stator, 2 High-Speed Rotors, 2 Pole-Piece Rotors), AFPDD-212 (2 Stators, 1 High-Speed Rotor, 2 Pole Piece Rotors).

Figure 5.1(a) shows the AFPDD-111 topology which has the advantage of the lowest number of components and bearings but the axial forces are potentially large and unbalanced. The AFPDD-122 shown in Figure 5.1(b) contains two high-speed rotors which is potentially undesirable as this doubles the number of rotors undergoing potentially unbalanced axial forces. This topology also only has a single radial heat path from the stator which could make thermal management more difficult. The machine structure of the AFPDD-212 shown in Figure 5.1(c) offers a potentially more axially balanced machine in terms of axial forces. The layout of the machine topology results in the HSR back iron not requiring lamination as it will only be subjected to a dc magnetic

field. The aforementioned structures could also be combined to form a multi-layer electrical machine with a single output shaft.

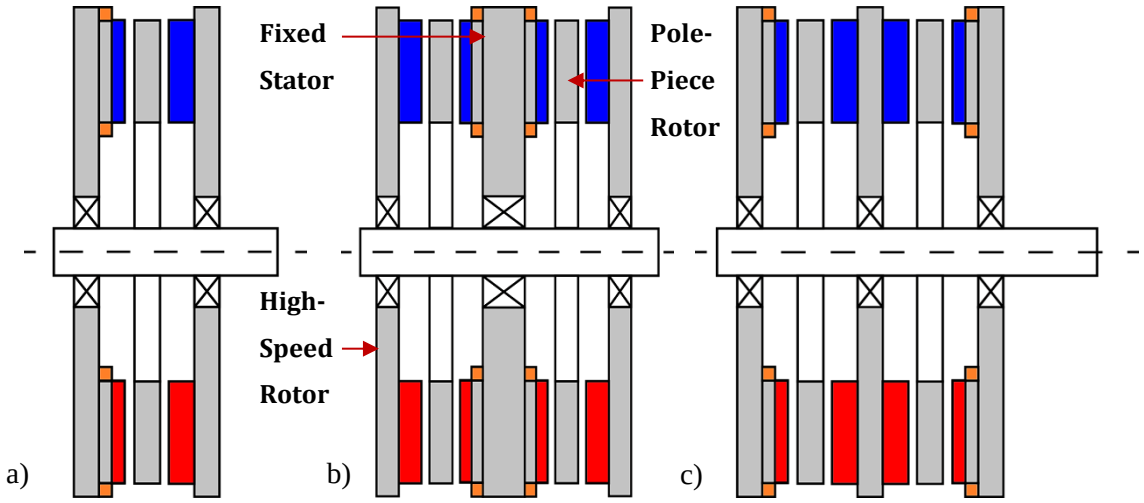

Figure 5.1 *Axial field pseudo direct drive structures (AFPDD) a) -111, b)-122 and c)-212*

In Section 5.1, the electromagnetic performance of the selected AFPDD-212 topology will be analysed. The loss mechanisms and thermal performance are then presented in Section 5.1.4 and Section 5.2.

5.1. Electromagnetic Performance

A typical 3D FEA (Cedrat Flux 3D) model of the machine including stator and magnetic gear consists of 5.4 million volume mesh elements and required ~4 hours to mesh on an Intel Xeon E5603 @ 1.60GHz with 48Gb RAM. Solving was carried out using an Intel Core-i7-3770 @3.40GHz with 16Gb RAM and required ~4hours per step, a reduction from ~10hours per step using the Xeon machine. When eddy current simulations are required the complexity increases and the Xeon machine is required due to size of the available RAM. This resulted in longer meshing times (~6 hour mesh) and a significantly longer solving time of approximately 29 hours per step.

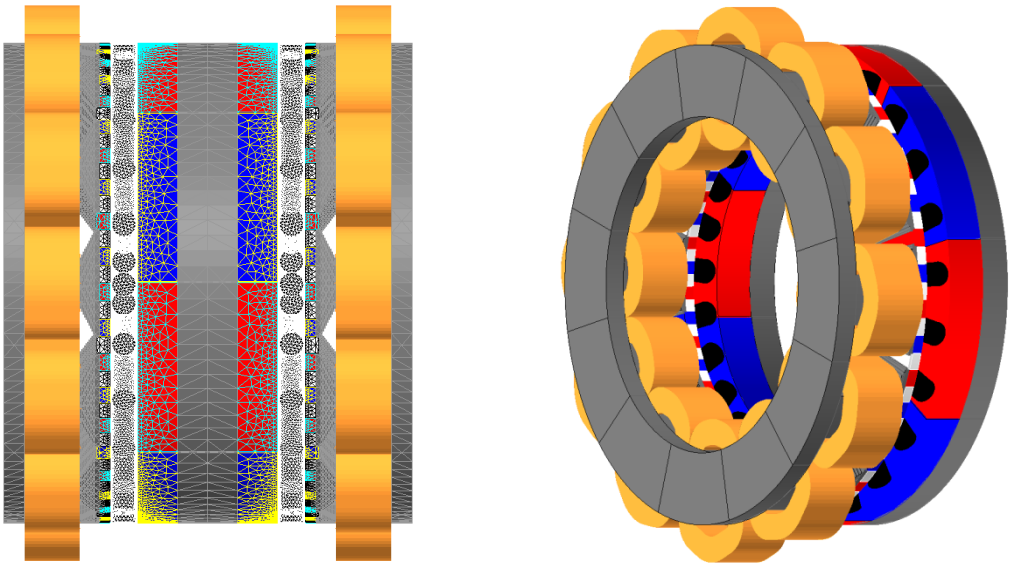

a) b)

Figure 5.2 *Modelling an axial field PDD a) FEA meshed model b) Isometric half model view*

An important aspect of moving from an AMG to an AFPDD is the fundamental flux density which links the electrical machine with the magnetic gear. Both the trapezoidal and cylindrical PPs are evaluated in terms of their effects on torque, electrical loading, torque per active volume (T/AV) and torque per magnet volume (T/MV). The outer active diameter of the machine is fixed to 120mm.

For a radial field brushless AC machine, the electromagnetic torque can be given by [5.1]:

$$T_e = \frac{\pi}{2\sqrt{2}} L_a \, R_s^2 \, B_1 \, k_w Q_{rms} \tag{5.1}$$

where L_a , R_s , k_w and Q_{rms} are the active length and the stator bore radius, the winding factor and the rms electric loading, respectively. B_1 is the fundamental component of flux density at the stator bore. Similarly, for the AFPDD at the mean radius $r_m = \frac{R_o}{2}(1+\lambda)$, the torque on the HSR can be approximated by:

$$T_h = \frac{\pi}{8\sqrt{2}} R_o^3 (1+\lambda)^2 (1-\lambda)\, B_1\, k_w Q_{rms} \tag{5.2}$$

$$T_o = G_r T_h = \frac{\pi}{8\sqrt{2}} R_o^3 (1+\lambda)^2 (1-\lambda)\, G_r\, B_1\, k_w Q_{rms} \tag{5.3}$$

where G_r is the AFPDD gear ratio and T_h and T_o are the torque on the AFPDD HSR and PPR respectively.

5.1.1. AFPDD with Trapezoidal PPs

The torque, fundamental flux density, electrical loading and torque per volume due to varying HSR and stator magnet thicknesses is investigated for the trapezoidal PP. The ratio of inner to outer radii, $\lambda = 0.7$ and air to ferromagnetic material ratio, $\alpha_{pp} = 0.5$ are down selected from the EM design optimisation conducted in Chapter 3. The PP thickness of 10mm for the trapezoidal PP is also selected for sufficient mechanical strength in an SMC PP in accordance with the findings of Chapter 4.

It can be seen in Figure 5.3 that a thicker stator magnet improves the pull-out torque of the magnetic gear. However, this significantly reduces the fundamental flux density and therefore increases the electrical loading, as can be seen in Figure 5.4 and Figure 5.5. This is due to the large effective airgap from the HSR to the stator and is further reduced due to the large thickness of the PP required for sufficient mechanical strength. Furthermore, as can be seem in Figure 5.6 and Figure 5.7, it can also be seen that both torque per magnet volume and torque per active volume increase with HSR and stator magnet thickness, albeit with diminishing returns.

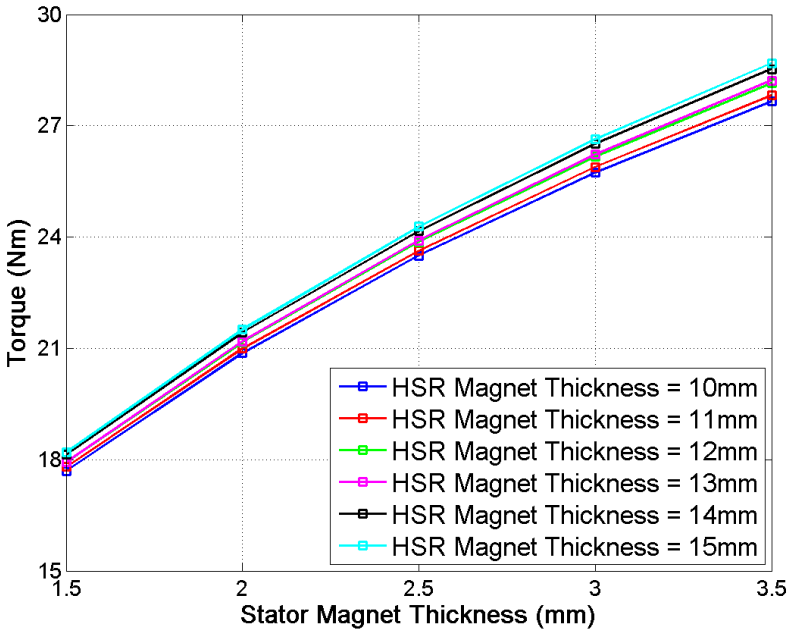

Figure 5.3 *Variation of pull-out torque with stator magnet thickness in AFPDD with trapezoidal PP and for different HSR magnet thicknesses.*

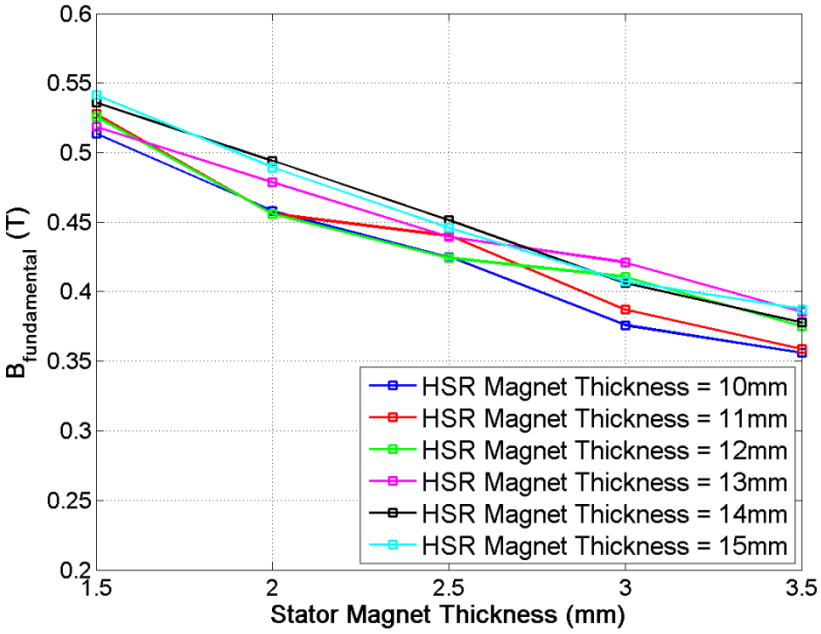

Figure 5.4 *Variation of B_1 at stator surface with stator magnet thickness in AFPDD with trapezoidal PP and for different HSR magnet thicknesses.*

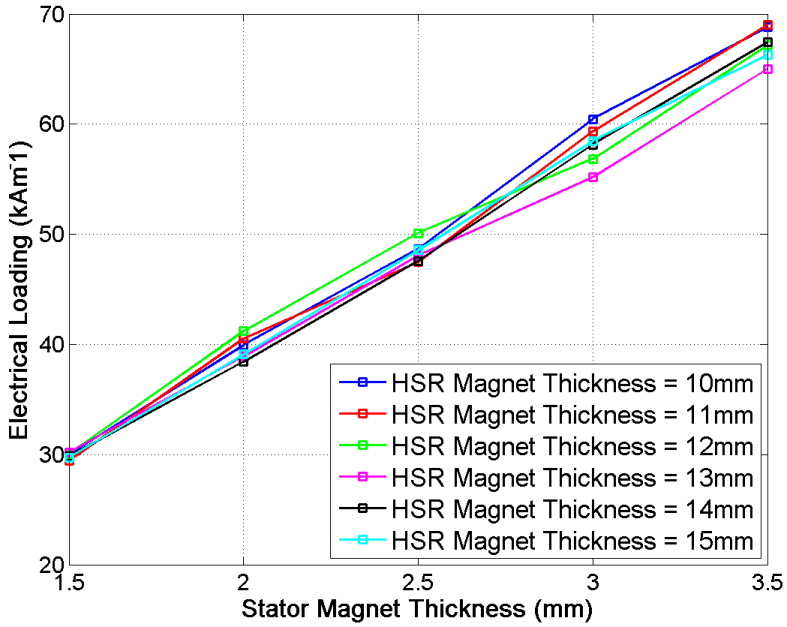

Figure 5.5 *Variation of electric loading with stator magnet thickness in AFPDD with trapezoidal PP and for different HSR magnet thicknesses.*

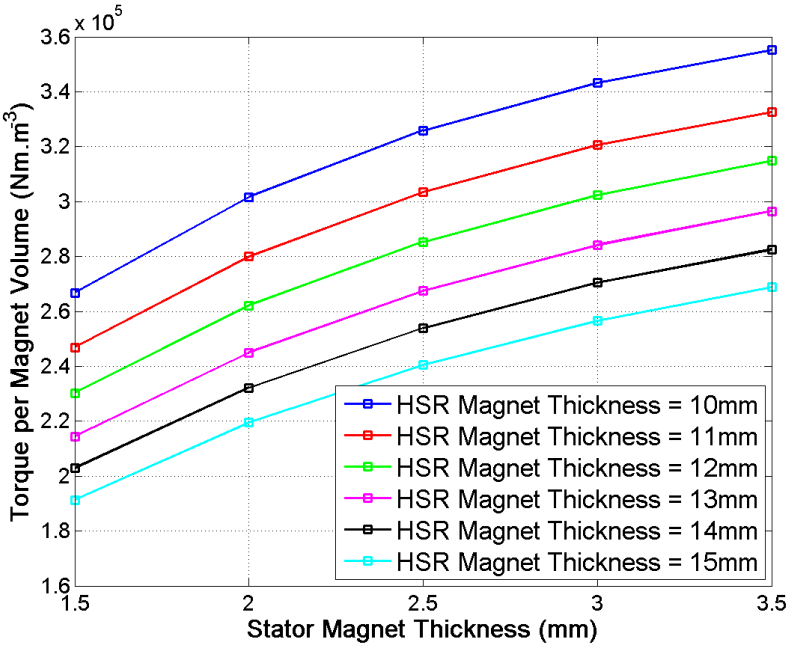

Figure 5.6 *Variation of T/MV with stator magnet thickness in AFPDD with trapezoidal PP and for different HSR magnet thicknesses.*

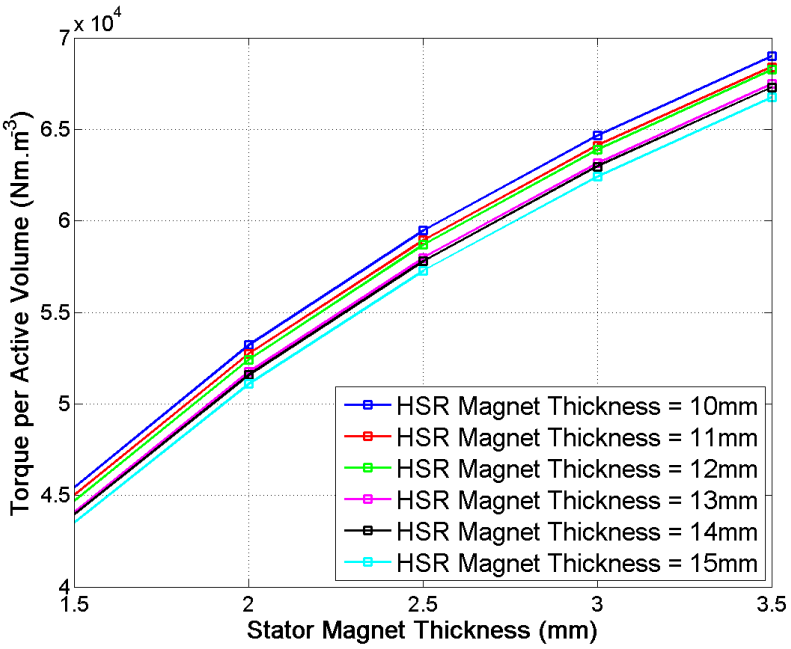

Figure 5.7 *Variation of T/AV with stator magnet thickness in AFPDD with trapezoidal PP and for different HSR magnet thicknesses.*

An optimisation to reduce the electrical loading in the trapezoidal PP AFPDD was conducted by modifying the ferromagnetic opening to pole piece pitch ratio. The large effective air gap caused by an axially thick pole piece gives rise to high circumferential leakage and is reduced by a larger ferromagnetic opening to pole piece pitch ratio. The HSR magnet thickness was fixed at 10mm. A ratio above 0.5 caused the reluctance of the circumferential leakage path to increase and gave rise to higher pull-out torque but reduced the fundamental flux density in the stator. Decreasing the ratio from 0.5 increased the fundamental flux density but also increased the circumferential leakage. As these effects were approximately equal and opposite minimal advantage was seen when trying to reduce the required electrical loading.

5.1.2. AFPDD with Cylindrical PPs

The cylindrical PPs exhibited significant advantage over their trapezoidal counterparts with respect to stress for a given PP thickness. However this was at the detriment of

magnetic gear pull-out torque. In an AFPDD it is preferable that both the output torque and fundamental of the flux density linking the HSR and stator are high. The pull-out torque of a cylindrical PP AFPDD with an inner to outer diameter ratio, $\lambda = 0.7$, is shown in Figure 5.8. A comparison is made to the trapezoidal PP with equal magnet thickness (10mm and 2.5mm for the HSR and stator magnets respectively). It can be seen that an improved torque output can be achieved for a similar fundamental flux density, as shown in Figure 5.9. As a result the required electrical loading is similar to the trapezoidal PP as shown in Figure 5.10. The higher pull-out torque also corresponds to an increase in torque per magnet volume and torque per active volume shown in Figure 5.11 and Figure 5.12.

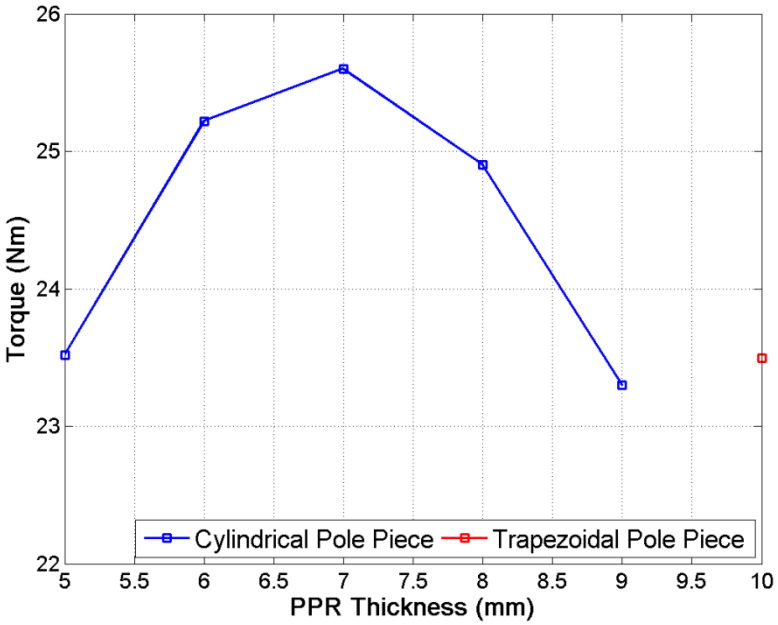

Figure 5.8 *Variation of torque with PP thickness in AFPDD with cylindrical PPs*

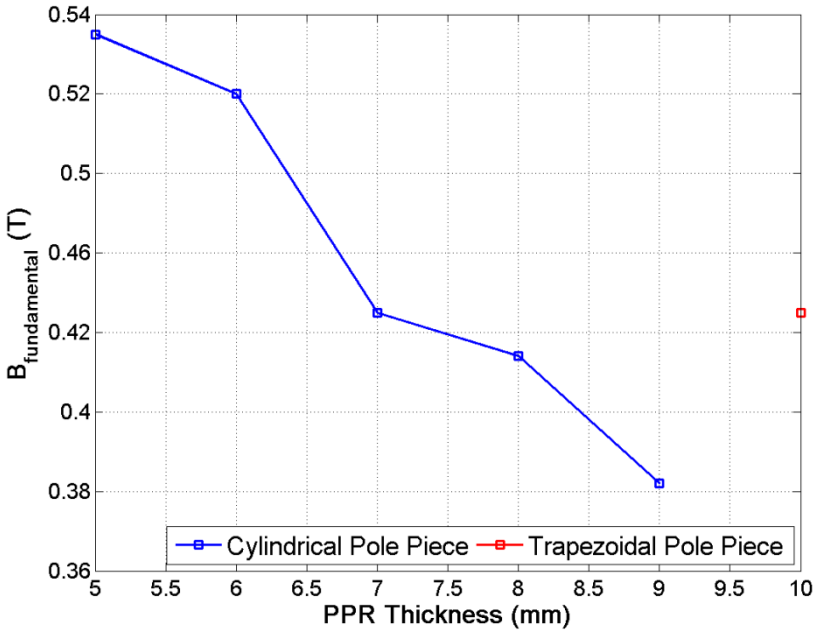

Figure 5.9 *Variation of B_{fund} with PP thickness in AFPDD with cylindrical PPs*

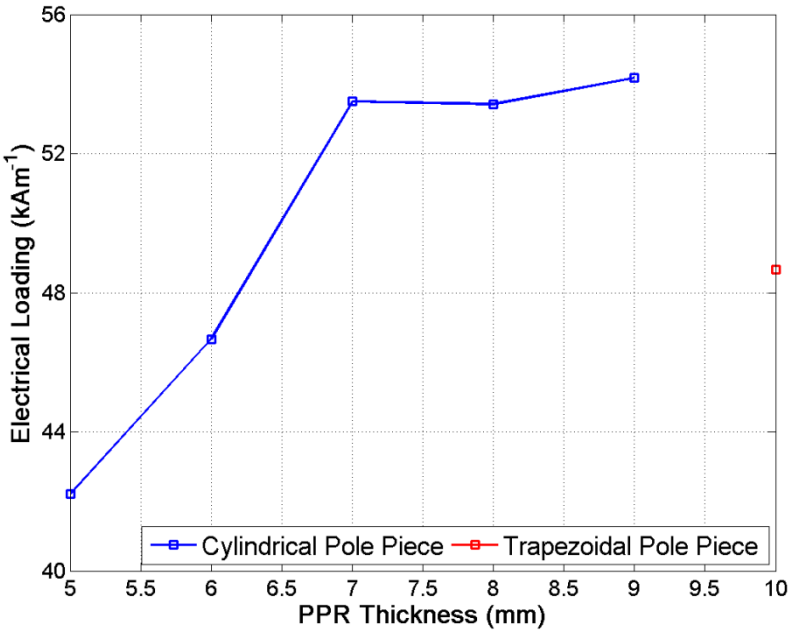

Figure 5.10 *Variation of electric loading with PP thickness in AFPDD with cylindrical PPs*

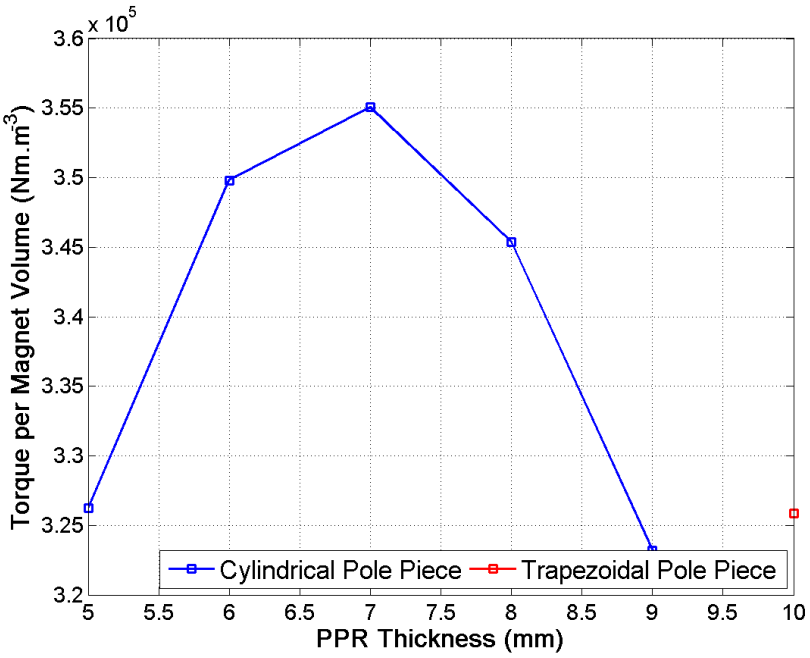

Figure 5.11 *Variation of T/MV with PP thickness in AFPDD with cylindrical PPs*

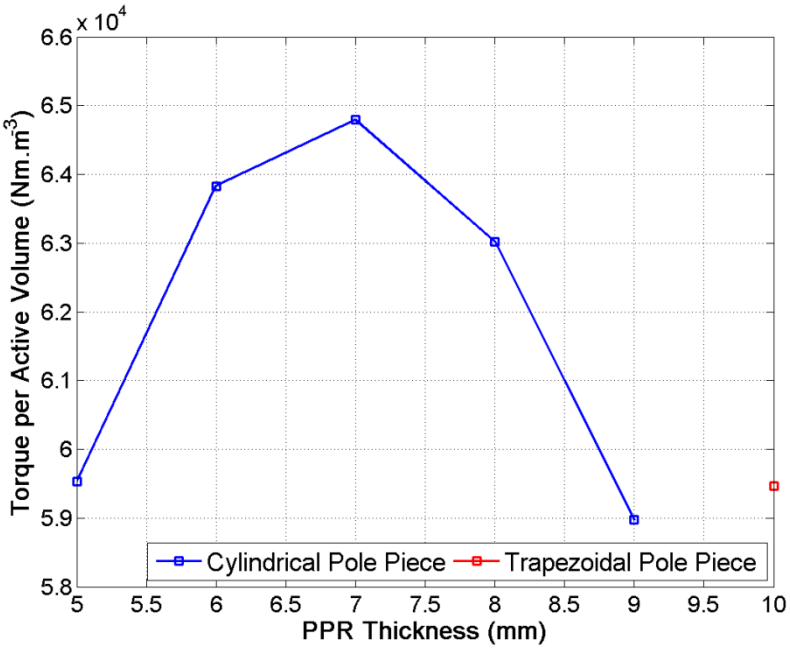

Figure 5.12 *Variation of T/AV with PP Thickness in AFPDD with cylindrical PPs*

5.1.3. Winding Calculations

Concentric pre-wound coils are chosen to simplify realisation of the winding. An accurate estimate of the winding length including end winding is required for

determining copper loss and power factor. A diagram of the concentric winding is shown in Figure 5.13 [5.10].

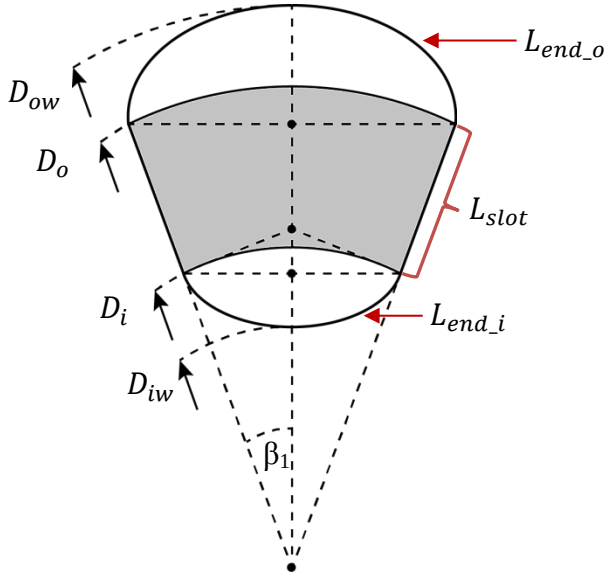

Figure 5.13 *Axial Coil Geometry for a concentric winding*

The inner and outer diameter of the tooth are D_i and D_o respectively and the half slot pitch is β_1. It is also important to note the maximum inner and outer diametric limits of the winding, D_{iw} and D_{ow} which are given by:

$$\beta_1 = \frac{\pi}{2Q_t} \tag{5.4}$$

$$D_{iw} = D_{\mathrm{i}}(1 - \sin(\beta_1)) \tag{5.5}$$

$$D_{ow} = D_{\mathrm{o}}(\sin(\beta_1) + \cos(\beta_1)) \tag{5.6}$$

where the number of stator slots is Q_t. The length of winding in the slot region L and the end winding lengths at the inner and outer diameter, L_{end_i} and L_{end_o} respectively are given by:

$$L_{end\_i} = \left(\frac{\pi}{2} - \beta_1\right) D_i \tan(\beta_1) \tag{5.7}$$

$$L_{end\_o} = \frac{\pi}{2} D_{\mathrm{o}} \sin(\beta_1) \tag{5.8}$$

$$L_{slot} = D_{\mathrm{o}} - D_{\mathrm{i}} \tag{5.9}$$

The total length of the concentric coil L_w is then used to calculate the resistance per coil R_c given by:

$$L_w = L_{end\_i} + L_{end\_o} + 2\, L_{slot} \tag{5.10}$$

$$\mathrm{R}_c = \frac{\rho_T L_w}{k_{pf} A_s} \tag{5.11}$$

where k_{pf} is the packing factor, A_s is the area of the slot and ρ_T the resistivity of the copper, which is adjusted to the operating temperature as:

$$\rho_T = \rho_{ref}(1 + \alpha_{cu}(T_{op} - T_{ref})) \tag{5.12}$$

where ρ_{ref} is the resistivity of copper at the reference temperature T_{ref} (usually 20ºC) and the temperature coefficient for the resistivity copper is α_{cu}. The number of turns per phase N is given by:

$$N = \frac{V_{DC}}{2} \omega_h \, K_e \tag{5.13}$$

where the selected DC link voltage is V_{DC}, the rated operating speed of the HSR ω_h and the back-EMF constant K_e.

5.1.4. Loss Mechanisms

Analysis of the loss mechanisms is important for both specifying components such as the winding and to estimate the temperature of the machine. The electromagnetic losses arise from hysteresis, eddy currents and copper losses.

The copper loss is given by:

$$P_{\mathrm{cu}} = 3I_{rms}^2 R_{ph} \tag{5.14}$$

where R_{ph} is the phase resistance and I_{rms} is the RMS current.

The loss within the SMC teeth, back iron and PPs is calculated using the finite element method and the iron loss model outlined in [5.11]. The eddy current and excess losses were considered negligible compared to the hysteresis loss due to the high resistivity of the SMC at 280μΩm [5.12]. For the Somaloy Prototyping Material (SPM) SMC, the hysteresis coefficient k_{h} and constant β were found to be 0.1279 and 1.875 respectively by curve fitting iron loss data supplied by the manufacturer. More recent work by the manufacturer resulted in the inclusion of an eddy current loss term in the core loss equation for SMC [5.13]. However, as this relies upon the body under investigation being of uniform cross section it is of limited use due to the complex geometry of the AFPDD. Therefore, the hysteresis loss P_{h} is then given by:

$$P_{\mathrm{hyst}} = k_h f B_m^{\beta} \tag{5.15}$$

where $B_m = B_{max} - B_{min}\,/2$ and B_{max} and B_{min} are the maximum and minimum flux densities reached in a hysteresis loop cycle. This expression assumes any offset on the value of B has no effect on the hysteresis loss. However, as the stator magnets impart an essentially dc field on the stator teeth in the AFPDD, this cannot be assumed

for the stator hysteresis loss, and as such a correction factor to account for the minor hysteresis loops is required, as given by [5.14]:

$$P_{\text{hyst}} = k_h f B_m^{\beta} \left(1 + \frac{0.65}{B_m} \sum_{i=1}^{N_l} \Delta B_i \right) \tag{5.16}$$

where N_l is the number of minor loops and ΔB_i is the magnitude of the flux density for the ith reversal. Although the correction factor was found empirically for laminated materials it was deemed sufficient as no such data could be found for SMC. Analysis of the hysteresis loss was implemented by finding the variation of flux density per element and then post processed using the correction factor. A summary of the hysteresis loss in the AFPDD operating at maximum power (PPR speed and output torque 1120rpm and 19.8Nm respectively) are given in Table 5.1.

Component	***Loss (W)***
Pole Piece Hysteresis Loss	10.16
Stator Hysteresis Loss	85.47

Table 5.1 *Hysteresis loss analysis (PPR speed = 1120rpm)*

Eddy currents present in the magnet material will further add to the electromagnetic losses. By dividing the magnets into a number of segments the length of the eddy current path can be reduced as shown in Figure 5.14. This results in an overall reduction of the magnet eddy current loss, found at the maximum power operating point, as shown in Figure 5.15. Three HSR segments were chosen and provided a 13% reduction in eddy current losses, reducing the eddy current loss from 13.7W to 11.94W. It was chosen to only segment the HSR magnets as the small physical size of the stator magnets being further divided would have resulted in a hard to construct component.

a)

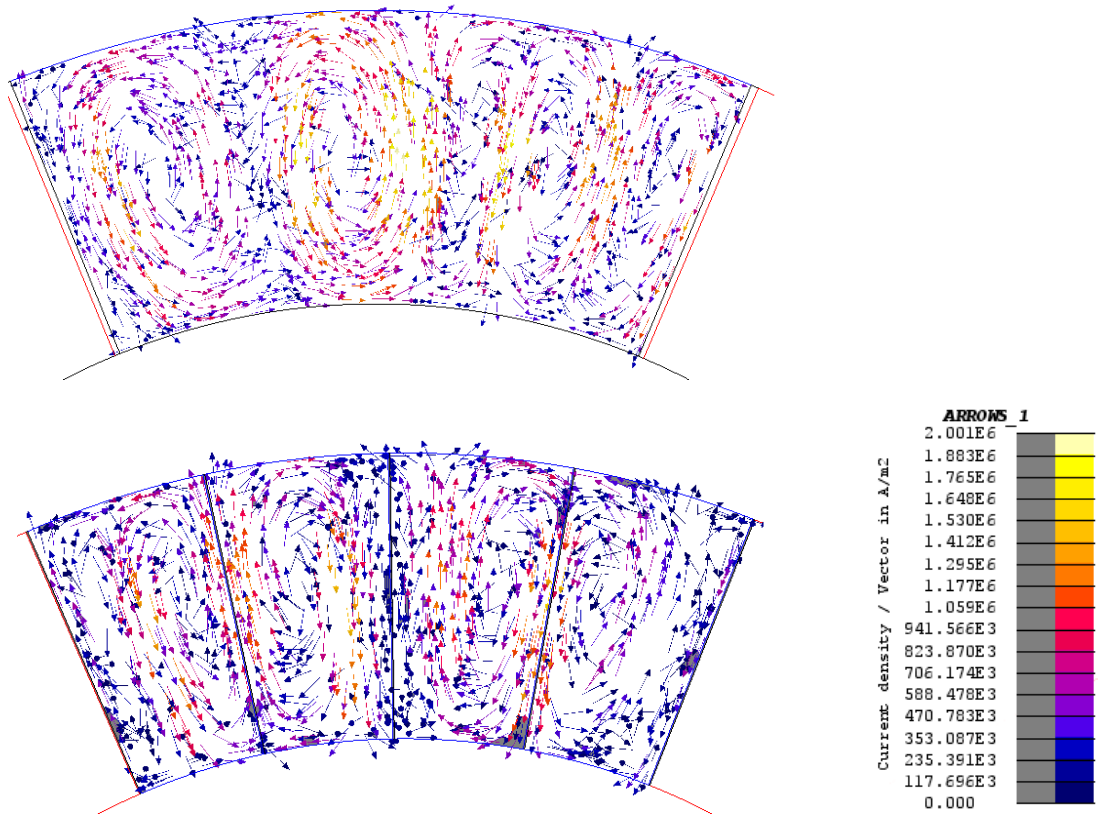

Figure 5.14 *HSR magnet eddy current plot a) Single segment per magnet pole b) Multiple segments per magnet pole*

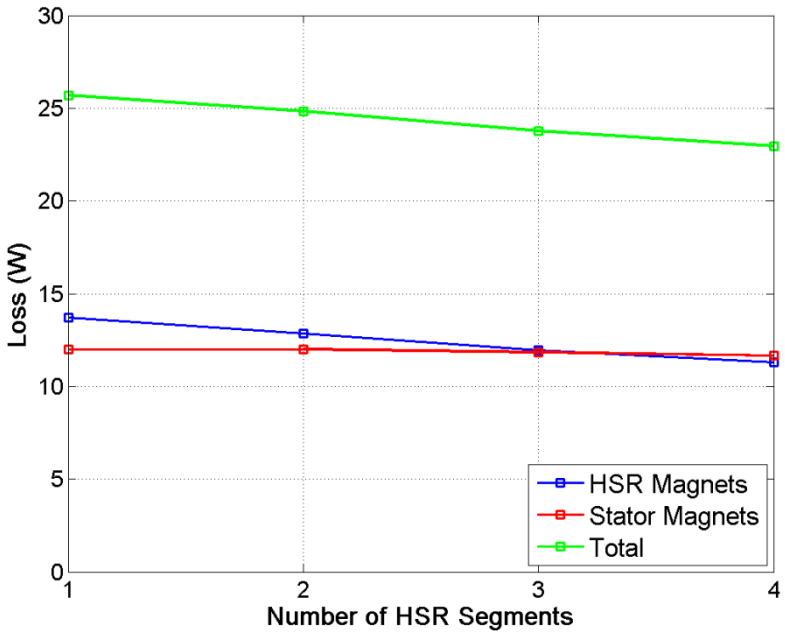

Figure 5.15 *Variation of magnet eddy current loss with HSR magnet segmentation (PPR speed = 1120rpm)*

5.1.5. Stator Tooth Design

The stator teeth and back iron were sized to allow for a working flux density of ~1.5T at the rated torque. Once the tooth tip had been sized a limit was placed on the slot axial length due to the maximum thickness of SMC blanks available. An optimal slot length can be found by investigating the inductance, power factor, losses and efficiency. The nominal rated torque in the following investigation is taken to be 80% of the gear pull out torque. The back-EMF constant K_e is given by:

$$K_e = \frac{\varepsilon}{\omega_h} \tag{5.17}$$

where ε is the back-EMF and ω_h is the speed of the HSR. The RMS phase current I_{rms} can be determined from:

$$I_{rms} = \frac{T_e}{\frac{3}{2}K_e} \tag{5.18}$$

where T_e is the rated torque. The power factor p_f is given by:

$$p_f = \cos\theta = \tan^{-1}\left(\frac{L_s I_{rms} p_h}{K_e}\right) \tag{5.19}$$

where the synchronous inductance $L_s = L_{AA} - M_{AB}$ is given by the self-inductance L_{AA} and the mutual inductance M_{AB} , p_h is the number of pole pairs on the HSR . The efficiency η is given by:

$$\eta = \frac{P_o}{P_o + P_{loss}} \tag{5.20}$$

where P_o is the output power and P_{loss} is the combined iron and copper losses.

The tooth pitch to slot pitch ratio, α_{TP} forced a compromise between magnetic and mechanical issues. A reduction in α_{TP} increases the opening between adjacent tooth tips, thus increasing power factor. Due to the requirement that the fixed magnet array would be bonded onto the stator teeth face, a value of $\alpha_{TP} > 0.9$ would give a larger surface to support the magnet. A final value of $\alpha_{TP} = 0.88$ is selected.

The limit imposed by the 20mm thickness of SMC blanks, resulted in a maximum allowable slot length of 13.8mm once the tooth tip had been sized to accommodate the magnetic flux without saturation. The variation of efficiency and loss with slot length are shown in Figure 5.16 and Figure 5.17 respectively. Due to further design of the HSR in Chapter 6 it was selected that the maximum operating speed of the HSR is 1120rpm, and as such the losses at this operating point are of particular interest. The rated torque is selected to be 19.8Nm.

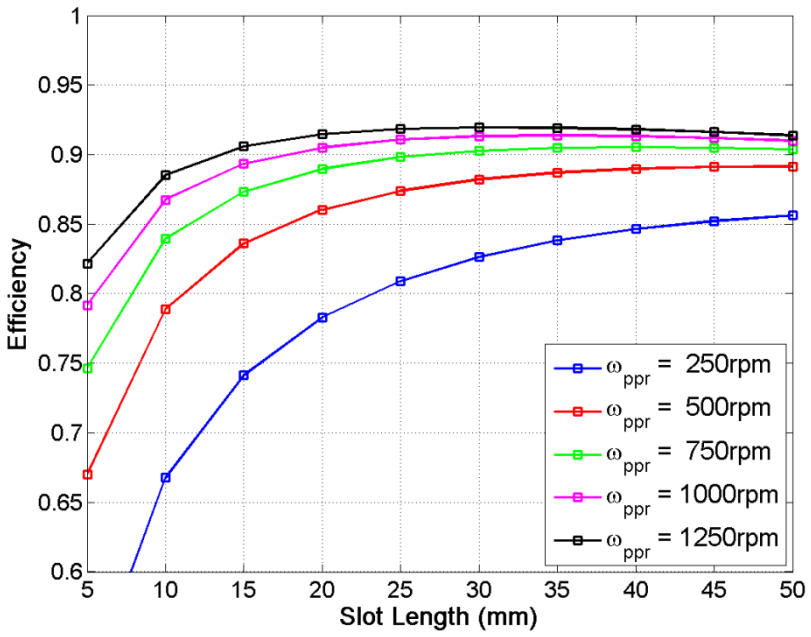

Figure 5.16 *Variation of efficiency with slot axial length at different PPR speeds*

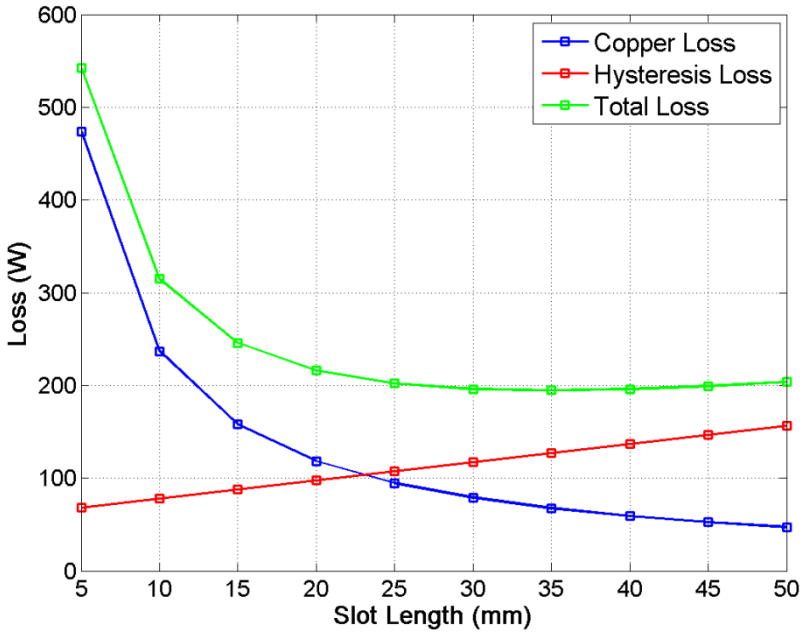

Figure 5.17 *Variation of loss with slot length (PPR speed=1120rpm, slot length = 13.8mm)*

The tooth body to slot pitch ratio, α_{TB} is an important factor in determining the maximum efficiency of the machine, as shown in Figure 5.18. Figure 5.19 also shows that the copper loss is dominant. $\alpha_{TB} = 0.4$ is selected as a trade-off between the efficiency and the area available for the mechanical attachment of the tooth body to stator back iron.

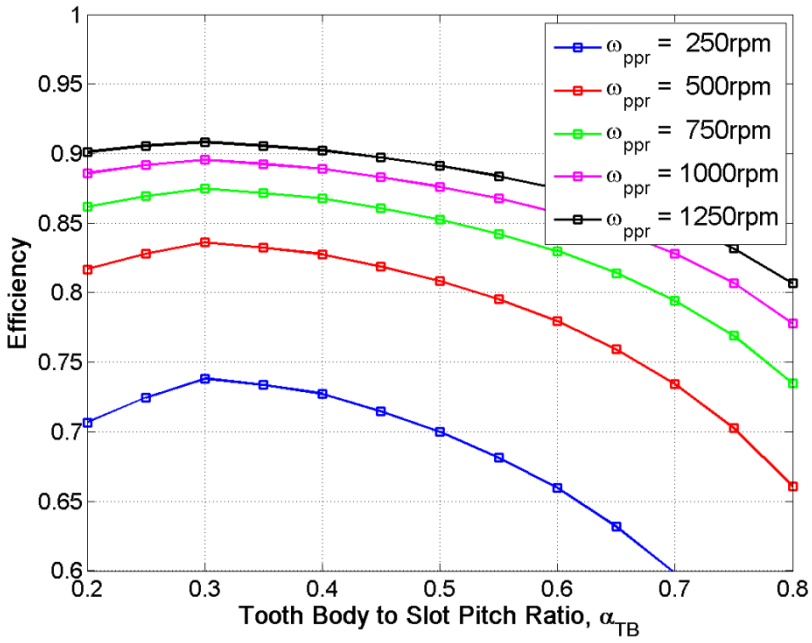

Figure 5.18 *Variation of efficiency with α_{TB} at different PPR speeds*

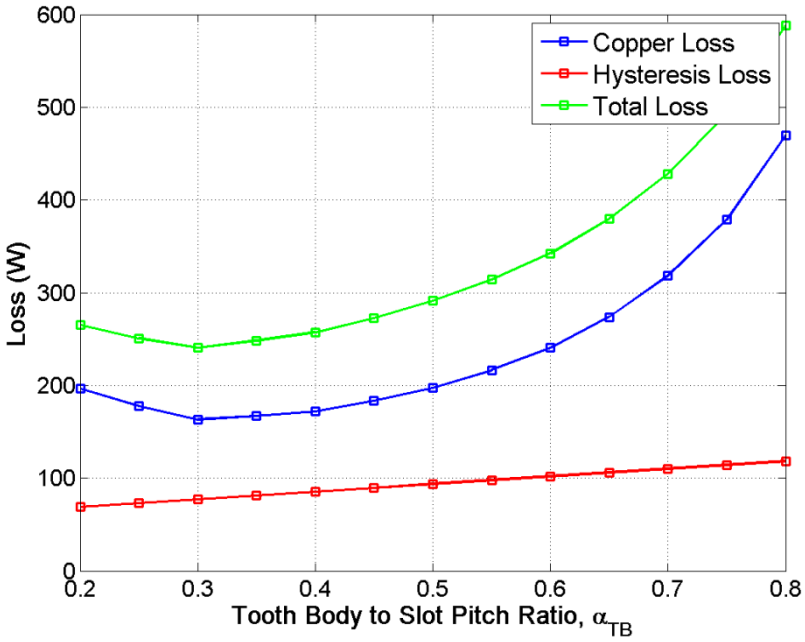

Figure 5.19 *Variation of loss with α_{TB} (PPR speed=1120rpm, slot length = 13.8mm)*

The efficiency map for the restricted slot length (13.8mm) and $\alpha_{TB} = 0.4$ is shown in Figure 5.20. A more optimal stator design with no slot length limitation is found with a

slot length of 50mm and $\alpha_{TB} = 0.2$, with the corresponding losses and efficiency shown in Figure 5.21 and Figure 5.22, respectively.

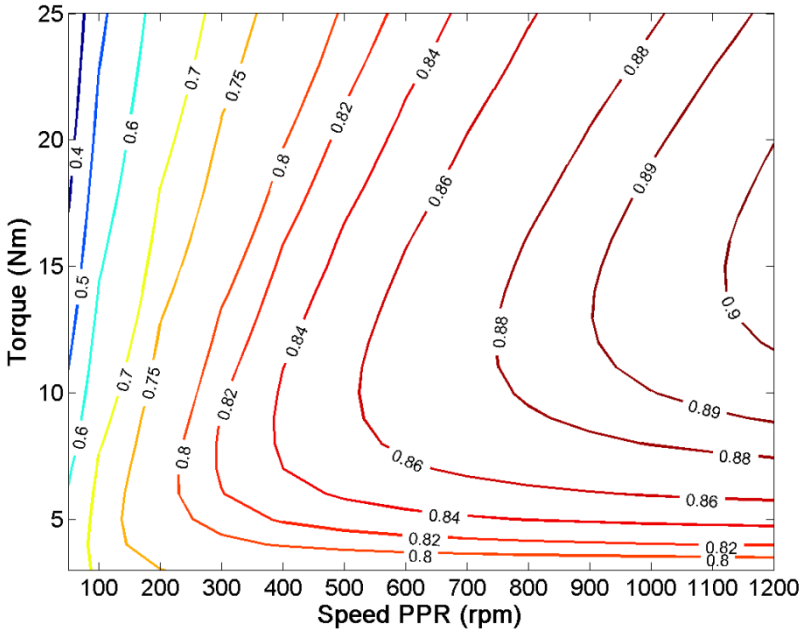

Figure 5.20 *Variation of efficiency with torque at different PPR speeds (Slot Length = 13.8mm)*

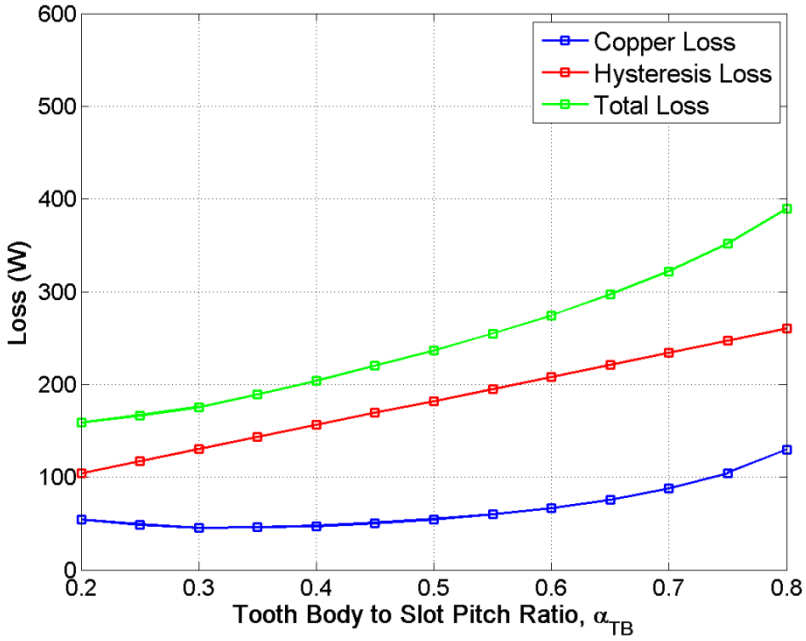

Figure 5.21 *Variation of loss with α_{TB} (PPR speed=1120rpm, slot length = 50mm)*

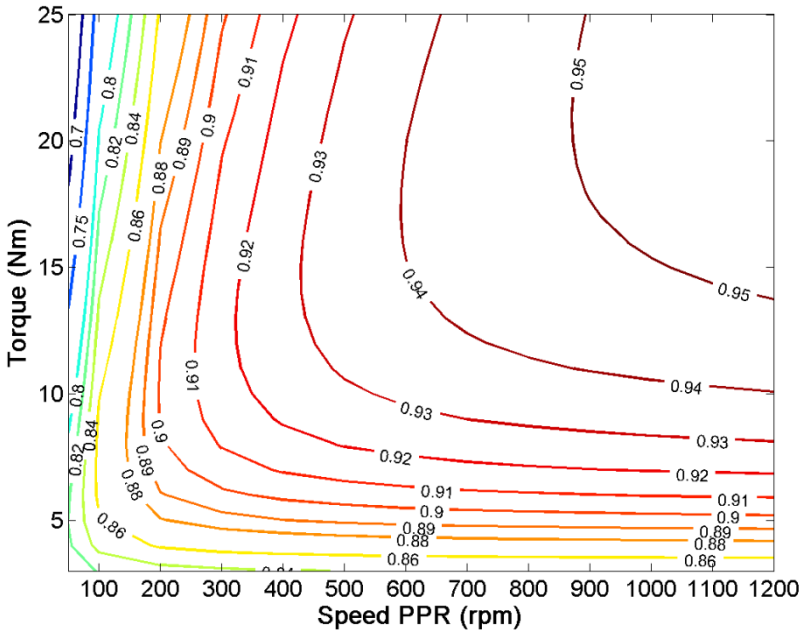

Figure 5.22 *Variation of efficiency with torque at different PPR speeds (Slot length = 50.0mm)*

5.2. Thermal Performance

The thermal aspects of the axial field AFPDD are an integral part of ensuring both the performance and longevity of the machine. The temperature should remain low enough to prevent demagnetisation of the magnets and also defines the materials used in the coil winding process.

An early example of thermal lumped parameter modelling for a radial TEFC (Totally Enclosed, Fan Cooled) can be seen in [5.15]. Mellor et al later developed a general cuboidal element thermal model and then an arc segment model ideal for modelling axial flux machines [5.16] [5.17]. Using the general arc segment model, examples achieved accuracies of <1% error when the ratio and arc angle criteria were met.

A 2D lumped parameter model for an axial flux machine was developed in [5.18]. Temperatures within 4% of the measured value were calculated by relating the earlier work of Mellor et al with experimentally derived heat transfer coefficients from [5.19].

Further attempts to understand the air flow between the rotating discs of axial machines using CFD (Computational Fluid Dynamics) are given in [5.20]. 2D axisymmetric models were used and showed good agreement (<5% error) between calculated and measured data. A particularly simplified model which uses only 8 elements is seen in [5.21]. An accuracy of ~10% was achieved and deemed sufficient for the model to be used as a design aid and tool for checking thermal performance.

The thermal analysis of an axial flux PM synchronous motor using Ansys is seen in [5.22]. This technique allowed the user to investigate temperatures in 3D and identify 'hot spots' within the model. Lumped parameter models have also been attempted in 3D such as in [5.23]. Variations on the amount of physical input data such as experimentally derived constants were considered and through fitting of model parameters accuracies of <10% error to measured data were attained.

The convection from a rotating shaft to ambient within a limited speed range ($v < 7.5$ ms^{-1}) is given in [5.24]. A good resource for contact resistances between materials is given in [5.25].

Initially the theory necessary to analyse the thermal aspects of the machine will be outlined in section 5.2.1. The lumped parameter model will then be constructed and temperatures of the machine calculated in section 5.2.2. The model will then be compared to FEA (Ansys) in section 5.2.3.

5.2.1. Theory

In Section 5.1 it was seen that the AFPDD power scales with the diameter cubed. In an enclosed machine with no water/oil cooling the surface of the case is the primary heat path to ambient via convection. As this surface area only scales with the diameter it is often the case that the performance of the machine becomes thermally limited. The thermal convection on a surface $\mathrm{R_{conv}}$ and the thermal conductance of a body $\mathrm{R_{cond}}$ are given by:

$$\mathrm{R_{conv}} = \frac{1}{hA} \tag{5.21}$$

$$\mathrm{R_{cond}} = \frac{l}{kA} \tag{5.22}$$

where h is the surface heat transfer coefficient, k is the thermal conductivity and A is the surface area of the body under convection or conduction.

The heat transfer coefficient in the air gap h_{gap} , caused by the movement of air due to the rotor rotation is given by:

$$h_{gap} = \frac{Nu\lambda_{air}}{g} \tag{5.23}$$

where g is the air gap thickness, λ_{air} is the thermal conductivity of air and Nu is the Nusselt number, which is treated as a convection constant given by:

$$\mathrm{Nu} = \begin{cases} 2, & if \quad Ta < 1700 \\ 0.128Ta^{0.367} & if \quad 1700 < Ta < 10^4 \\ 0.409Ta^{0.241} & if \quad 10^4 < Ta < 10^7 \end{cases} \tag{5.24}$$

where Ta is the appropriate Taylor number and corresponds to a deviation from static to laminar to turbulent air flow [5.18]:

$$\mathrm{Ta} = \mathrm{Re}^2 \frac{g}{r_o} \tag{5.25}$$

where r_o is outer radius of the rotor and Re is the Reynolds given by:

$$\mathrm{Re} = \frac{\omega_{rel}\, g}{\nu_\delta} \tag{5.26}$$

where ω_{rel} is the relative angular velocity between the convection surfaces (HSR-PPR or PPR-stator) and ν_δ is the kinematic viscosity of air. The convection constant from a rotating shaft h_s to ambient is given by [5.24]:

$$\mathrm{h}_s = 15.5(0.39\nu_{pp} + 1) \tag{5.27}$$

where ν_{pp} is the linear velocity of the PPR.

5.2.2. Lumped Parameter Model

Developing a lumped parameter model enables the thermal behaviour of the machine to be modelled more rapidly. In the case of an axial field machine an arc shaped lumped parameter block is most appropriate as shown in Figure 5.23(a). The implemented resistance network to model axial, radial and circumferential heat paths are shown in Figure 5.23(b).

The complete lumped parameter model implemented in Matlab Simulink is shown in Figure 5.24.

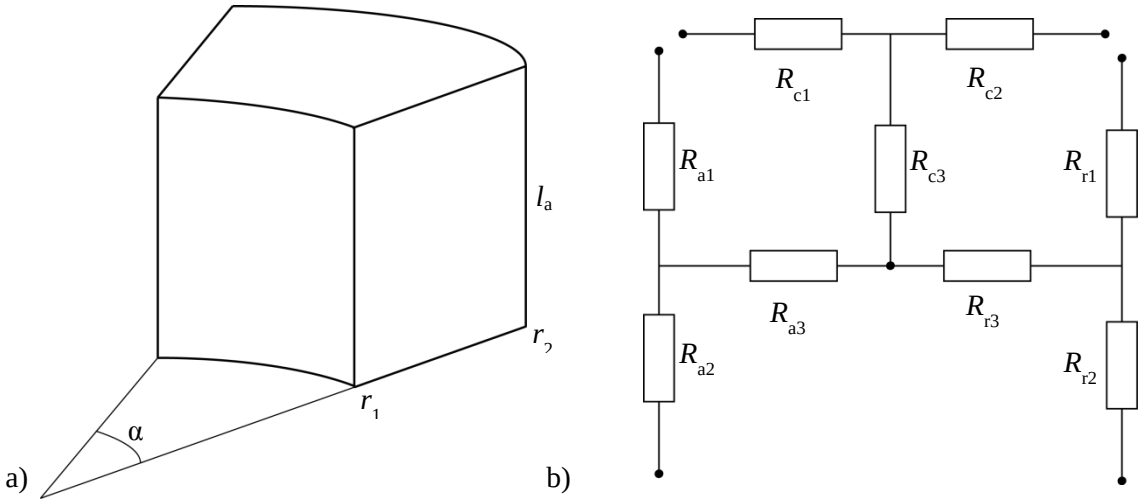

Figure 5.23 *Thermal lumped parameter a) General arc segment and b) Resistance network* [5.17]

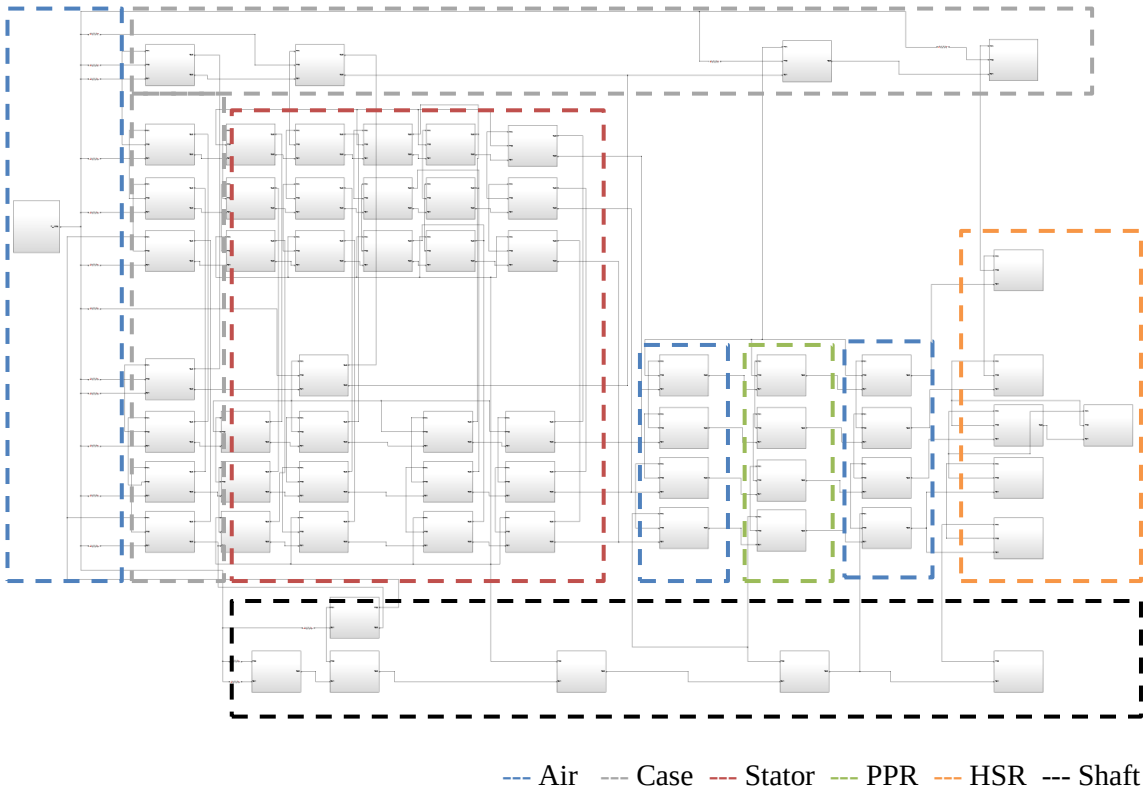

Figure 5.24 *Thermal lumped parameter implementation in Matlab Simulink*

Each element's thermal resistance in the 3D network is determined from the general arc segment model developed by Mellor et al [5.17]. The axial thermal resistances R_{a1} , R_{a2} , R_{a3} are given by:

$$R_{a1} = R_{a2} = \frac{180 L_{ap}}{\alpha_{as} \pi k_a (r_2^2 - r_1^2)} \tag{5.28}$$

$$R_{a3} = \frac{-60 L_{ap}}{\alpha_{as} \pi k_a (r_2^2 - r_1^2)} \tag{5.29}$$

where L_{ap} is the axial path length, α_{as} is the angle of the arc segment, r_1 and r_2 are the inner and outer radii of the arc segment and k_a is the axial thermal conductivity. Similarly the circumferential and radial thermal resistances are given by:

$$R_{c1} = R_{c2} = \frac{L_{cp}}{2 k_c L_a (r_2 - r_1)} \quad , \quad R_{c3} = \frac{-L_{cp}}{6 k_c L_a (r_2 - r_1)} \tag{5.30}$$

$$R_{r1} = \frac{90}{\alpha_{as} \pi k_r L_{ap}} \left[\frac{2 r_2^2 \, ln\left(\frac{r_2}{r_1}\right)}{r_2^2 - r_1^2} - 1 \right] \quad , \quad R_{r2} = \frac{90}{\alpha_{as} \pi k_r L_{ap}} \left[1 - \frac{2 r_1^2 \, ln\left(\frac{r_2}{r_1}\right)}{r_2^2 - r_1^2} \right] \tag{5.31}$$

$$R_{r3} = \frac{-45}{\alpha_{as} \pi k_r L_{ap} (r_2^2 - r_1^2)} \left[r_2^2 + r_1^2 - \frac{4 r_2^2 r_1^2 \, ln\left(\frac{r_2}{r_1}\right)}{r_2^2 - r_1^2} \right] \tag{5.32}$$

$$L_{cp} = \frac{\alpha_{as} \pi (r_1 + r_2)}{360} \tag{5.33}$$

where k_c and k_r are circumferential and radial thermal conductivities and L_{cp} is the average circumferential path length. Details of the thermal conductivities for the materials used in this model can be found in the Appendix. A block of the Matlab simulink implementation, including a negative resistance block and measurement of block temperature, is shown in Figure 5.25.

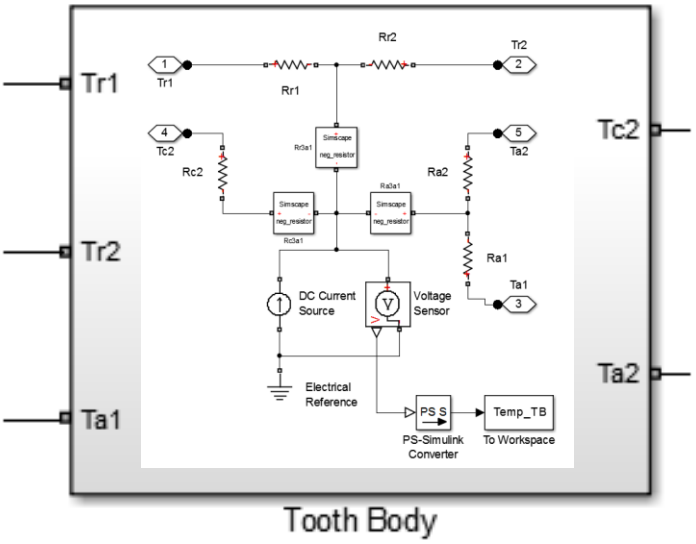

Figure 5.25 *Lumped parameter model Matlab Simulink model*

Although the machine is not geometrically symmetrical the period in which the geometry varies is significantly lower than the period in which the temperature variation within the machine occurs. As such symmetry can be used and only the angle occupied by a slot pitch is required for modelling. The symmetrical part is then comprised of several arc segments as shown in Figure 5.26.

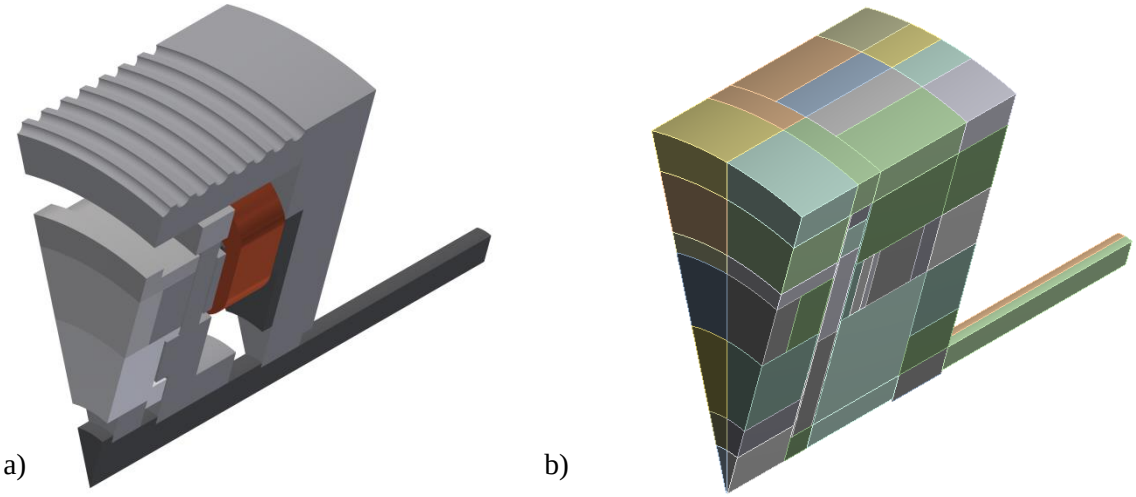

Figure 5.26 *Thermal symmetry in a) Geometric model and b) Ansys thermal model*

The general starting point is the ability of the case to dissipate heat. Using the power and calculated efficiency of the machine the power loss was determined. By specifying a maximum allowable temperature rise above ambient and knowing the case surface area the heat transfer coefficient of case was found to be $30W.m^{-2}.K$. This signifies that if the case is sufficiently finned it should be able to remove enough energy via convection to prevent the possibility of thermal runaway.

The lumped thermal model is used to predict the temperature when the AFPDD is operating at an output speed of 1120rpm (7000rpm on the HSR) and output power of 2.3kW. The variation of winding temperature with case convection constant is seen in Figure 5.27. A de-rating factor of the output torque and therefore resulting copper loss may be required to operate the machine at high power levels for long periods of time if the heat transfer coefficient of the case is lower than required. A de-rating factor of zero corresponds to the machine operating maximum power (PPR speed and torque 1120rpm and 19.8Nm respectively), whereas a de-rating factor of 0.5 is the machine operating at half of the maximum output power.

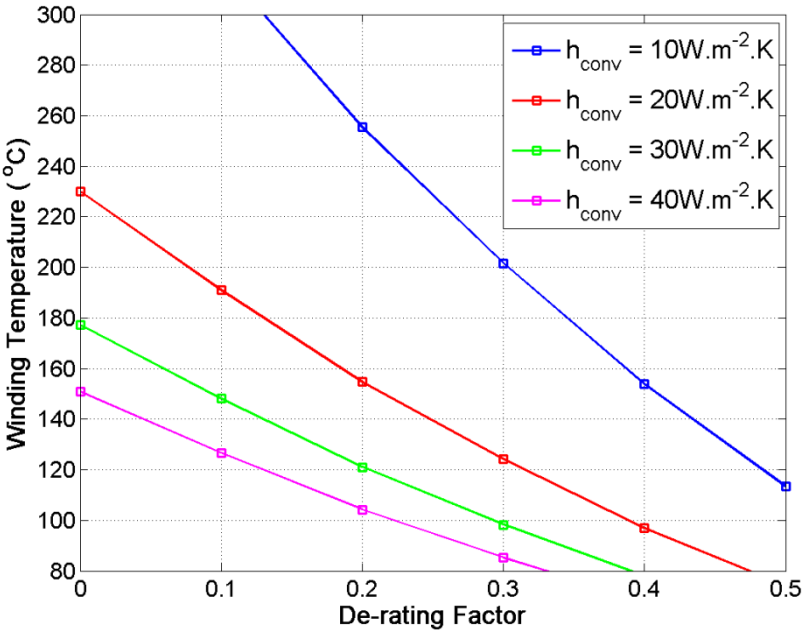

Figure 5.27 *Variation of winding temperature with De-rating Factor for case convection coefficient*

Achievable heat transfer coefficients for naturally cooled electrical machines from the case to air are typically range from the 10-40W.m^{-2}.K [5.17]. The addition of a finned outer case will increase the surface area by ~25% resulting in a further reduction of the winding temperature at a specific case convection coefficient.

5.2.3. AFPDD Thermal Performance

The thermal performance of the AFPDD at maximum power corresponds to the case in which the losses within the machine are at a maximum. A summary of the predicted losses within the AFPDD during that condition (PPR speed and output torque 1120rpm and 19.8Nm respectively) are summarised in Table 5.2.

Loss Mechanism	*Predicted Loss (W)*
HSR Bearing Loss	30.95
HSR Magnet Eddy Current Loss	11.94
Core Loss Pole Pieces	10.16
Stator Core Loss	85.47
Stator Copper Loss	83.38
Stator Bearing Loss	0.1
Stator Magnet Eddy Current Loss	11.83

Table 5.2 *Predicted losses in the components of the AFPDD*

By assuming the convection coefficient on the outer casing is $30W.m^{-2}.K$ with no de-rating factor the component temperatures from the FEA and LPM are given in Table 5.3.

	FEA	*LPM*
Component	***Av. (°C)***	***Av. (°C)***
Winding	150.7	152.9
Tooth Body	136.0	142.2
Stator Magnet	137.8	149.0
Back Iron	118.8	128.3
Pole Pieces	134.7	121.9
HSR Magnet	138.8	124.9
Case (Axial path)	113	123.0
Case (Radial path)	109.4	119.7

Table 5.3 *Stator component temperatures (Case heat transfer coefficient $30W.m^{-2}.K$)*

Figure 5.28 shows that at the maximum operating point the region with the highest temperature is the stator coils. Due to the coil temperature shown in Figure 5.29 being

less than 180ºC it will be suitable to specify the winding with Class H insulation. As the stator magnet temperature is ~135 ºC it will be necessary to use high temperature grades of magnet, such as N38EH. It is also interesting to note that the main heat path is conductive axially through the case to air, as shown in Figure 5.30.

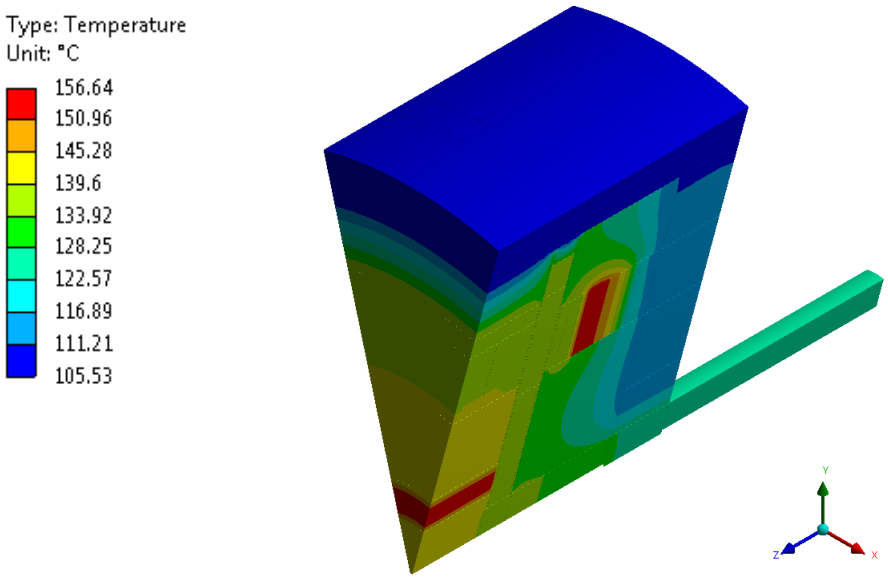

Figure 5.28 *AFPDD Temperatures (Case heat transfer coefficient 30W.m-^{2}.K)*

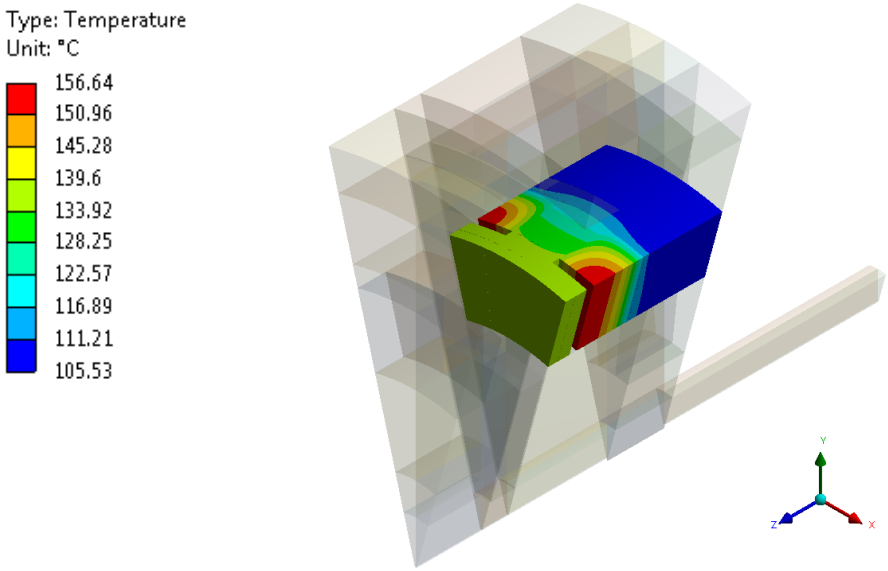

Figure 5.29 *Stator Temperatures (Case heat transfer coefficient 30W.m-^{2}.K)*

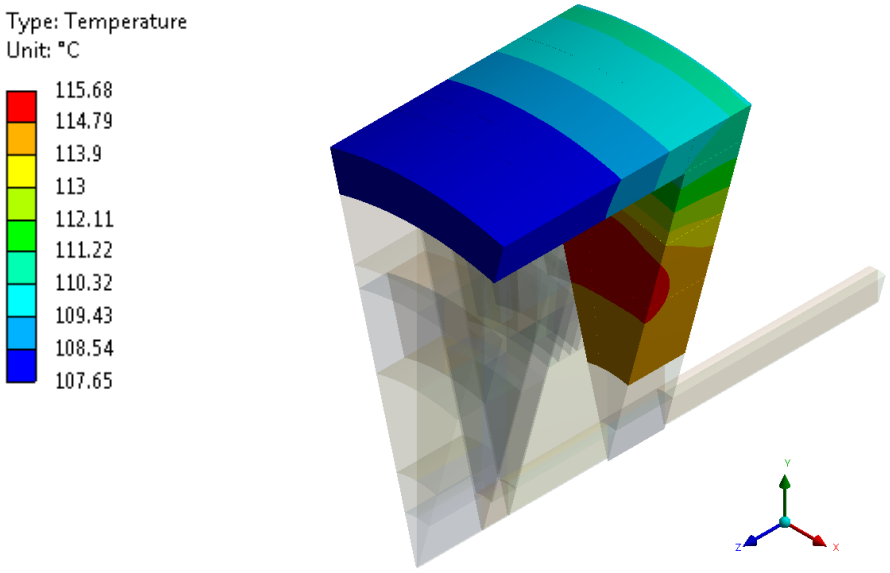

Figure 5.30 *Case Temperatures (Case heat transfer coefficient 30W.m-^{2}.K)*

5.3. Conclusions

The machine topology in which the ideal net forces on the HSR are zero is considered with the aim of significantly reducing the loading on the HSR bearings and to improve the robustness of the structure. In this study, it is shown that the AFPDD with cylindrical SMC PPs gives improved electromagnetic performance compared to trapezoidal PPs. An increase of ~8% output torque can be achieved by using cylindrical PPs when the maximum stress on the PP is constrained. The cylindrical PP also benefits from reduced mechanical stresses as discussed in Chapter 4. When designing the AFPDD it is seen that a compromise between MG output torque and fundamental flux density at the stator bore in order to limit the electric loading, must be sought. For this diameter of machine, selecting HSR and stationary array magnet thicknesses of 10mm and 2.5mm respectively represent a good compromise between pull-out torque and electrical loading.

The optimised stator design exhibited a predicted rated efficiency and power factor of 95% and 0.88, respectively. However, the limitations imposed by the available SMC

blanks limited the stator maximum predicted efficiency to ~90%. A slot length of 13.8mm and $\alpha_{TB} = 0.4$ were found to give the most optimal efficiency within the SMC limitations.

The winding and magnets temperatures were verified to ensure no performance degradation would occur during normal operation, and good agreement is shown between the lumped parameter model and 3D finite element analysis. The thermal analysis showed the main heat path of the AFPDD is an axial conduction from the stator to the case then convection to ambient air. Temperatures within the AFPDD could be limited to 150ºC given a case heat transfer coefficient of 30W.m^{-2}.K.

Chapter 6 will consider the building and testing of the aforementioned cylindrical PP AFPDD design. Images from the CAD models and working drawings produced to realise the AFPDD are contained within the Appendix.

5.4. References

[5.1] K. Atallah, J. Rens, S. Mezani, and D. Howe, "A Novel 'Pseudo ' Direct-Drive Brushless Permanent Magnet Machine," *IEEE Trans. Magn.*, vol. 44, no. 11, pp. 4349–4352, 2008.

[5.2] D. J. Evans and Z. Q. Zhu, "Optimal torque matching of a magnetic gear within a permanent magnet machine," *IEEE Int. Electr. Mach. Drives Conf.*, pp. 995–1000, 2011.

[5.3] W. N. Fu and S. L. Ho, "A novel axial-flux electric machine for in-wheel gearless drive in plug-in hybrid electric vehicles," in *Digests of the 2010 14th Biennial IEEE Conference on Electromagnetic Field Computation, CEFC 2010*, 2010, no. April 2008, p. 7062.

[5.4] S. L. Ho, S. Niu, and W. N. Fu, "Design and analysis of a novel axial-flux electric machine," *IEEE Trans. Magn.*, vol. 47, no. 10, pp. 4368–4371, 2011.

[5.5] N. Niguchi, K. Hirata, A. Zaini, and S. Nagai, "Proposal of an Axial-Type Magnetic-Geared Motor," in *International Conference on Electrical Machines (ICEM)*, 2012, pp. 738–743.

[5.6] C. Tong, Z. Song, P. Zheng, J. Bai, and Q. Zhao, "Research on Electromagnetic Performance of an Axial Magnetic-Field-Modulated Brushless Double-Rotor Machine for Hybrid Electric Vehicles," in *17th International Conference on Electrical Machines and Systems (ICEMS)*, 2014, pp. 2896–2902.

[5.7] M. Johnson, M. C. Gardner, and H. A. Toliyat, "Design and Analysis of an Axial Flux Magnetically Geared Generator," in *IEEE Energy Conversion Congress and Exposition (ECCE)*, 2015, pp. 6511–6518.

[5.8] R.-J. Wang and S. Gerber, "Design and Evaluation of a Disc-Type Magnetically Geared PM Wind Generator," in *4th International Conference on Power Engineering, Energy and Electrical Drives*, 2015, pp. 1259–1264.

[5.9] D. J. Patterson, J. L. Colton, B. Mularcik, B. J. Kennedy, S. Camilleri, and R. Rohoza, "A comparison of radial and axial flux structures in electrical machines," *2009 IEEE Int. Electr. Mach. Drives Conf.*, pp. 1029–1035, May 2009.

[5.10] A. Cavagnino, M. Lazzari, F. Profumo, and A. Tenconi, "A comparison between the axial flux and the radial flux structures for PM synchronous motors," *IEEE Trans. Ind. Appl.*, vol. 38, no. 6, pp. 1517–1524, 2002.

[5.11] P. A. Hargreaves, B. C. Mecrow, and R. Hall, "Calculation of iron loss in electrical generators using finite-element analysis," *IEEE Trans. Ind. Appl.*, vol. 48, no. 5, pp. 1460–1466, 2012.

[5.12] Hoganas AB Ltd., "Somaloy Prototyping Material (SPM) 2015 Datasheet," 2015.

[5.13] Hoganas AB Ltd., "Somaloy Prototyping Material (SPM) 2016 Datasheet," 2016.

[5.14] J. D. Lavers, P. P. Biringer, and H. Hollitscher, "A simple method of estimating

the minor loop hysteresis loss in thin laminations," *IEEE Trans. Magn.*, vol. 14, no. 5, pp. 386–388, 1978.

[5.15] P. H. Mellor, D. Roberts, and D. R. Turner, "Lumped parameter thermal model for electrical machines of TEFC design," *IEE Proc. B Electr. Power Appl.*, vol. 138, no. 5, p. 205, 1991.

[5.16] R. Wrobel and P. H. Mellor, "A general cuboidal element for three-dimensional thermal modelling," *IEEE Trans. Magn.*, vol. 46, no. 8, pp. 3197–3200, 2010.

[5.17] N. Simpson, R. Wrobel, and P. H. Mellor, "A general arc-segment element for three-dimensional thermal modeling," *IEEE Trans. Magn.*, vol. 50, no. 2, pp. 2–5, 2014.

[5.18] N. Rostami, M. R. Feyzi, J. Pyrhonen, A. Parviainen, and M. Niemela, "Lumped-Parameter Thermal Model for Axial Flux Permanent Magnet Machines," *IEEE Trans. Magn.*, vol. 49, no. 3, pp. 1178–1184, 2013.

[5.19] K. M. Becker and J. Kaye, "Measurements of Diabatic Flow in an Annulus With an Inner Rotating Cylinder," *J. Heat Transf.*, vol. 84, pp. 97–105, 1962.

[5.20] F. Marignetti and V. D. Colli, "Thermal Analysis of an Axial Flux Permanent-Magnet Synchronous Machine," *IEEE Trans. Magn.*, vol. 45, no. 7, pp. 2970–2975, 2009.

[5.21] A. Di Gerlando, G. M. Foglia, M. F. Iacchetti, and R. Perini, "Thermal modeling for the design and check of an axial flux PM motor," in *Proceedings - 2014 International Conference on Electrical Machines, ICEM 2014*, 2014, pp. 1441–1447.

[5.22] J. Shazly, S. Wahsh, and A. Yassin, "Thermal Analysis of Axial Flux Permanent Magnet Synchronous Motor using 3D Finite Elements," *Int. J. Therm. Technol.*, vol. 4, no. 4, pp. 313–319, 2014.

[5.23] O. Wallscheid and J. Bocker, "Design and identification of a lumped-parameter thermal network for permanent magnet synchronous motors based on heat transfer theory and particle swarm optimisation," in *17th European Conference on Power Electronics and Applications (EPE'15 ECCE-Europe)*, 2015, pp. 1–10.

[5.24] G. Henneberger, K. Ben Yahia, and M. Schmitz, "Calculation And Identification Of A Thermal Equivalent Circuit Of A Water Cooled Induction Motor For Electric Vehicle Applications," in *Seventh International Conference on Electrical Machines and Drives*, 1995, no. 412, pp. 6–10.

[5.25] D. Staton, A. Boglietti, and A. Cavagnino, "Solving the more difficult aspects of electric motor thermal analysis in small and medium size industrial induction motors," *IEEE Trans. Energy Convers.*, vol. 20, no. 3, pp. 620–628, 2005.

Chapter 6

Manufacture and Testing of an Axial Field Pseudo Direct Drive

There are limited previous instances in which axial magnetic gears and magnetically geared machines have been realised as prototypes. An example of a mechanically coupled, single sided axial magnetically geared machine was constructed by M. Johnson in [6.1]. A prototype axial magnetic gear was also developed by S. Mezani et al in [6.2].

As such the construction of such machines poses several key challenges. The winding, stator teeth and stationary magnet array require development to minimise the associated assembly issues relating to the stator of an axial field PDD (AFPDD). Further to this the design includes a complex shaft and bearing arrangement which requires consideration.

In Section 6.1-6.5 the design and manufacture of the AFPDD are considered. Testing of the completed prototype is then presented in Section 6.6. Figure 6.1 shows the cross section of the manufactured AFPDD with Figure 6.2 indicating a breakdown of the sub-assemblies to an individual component level.

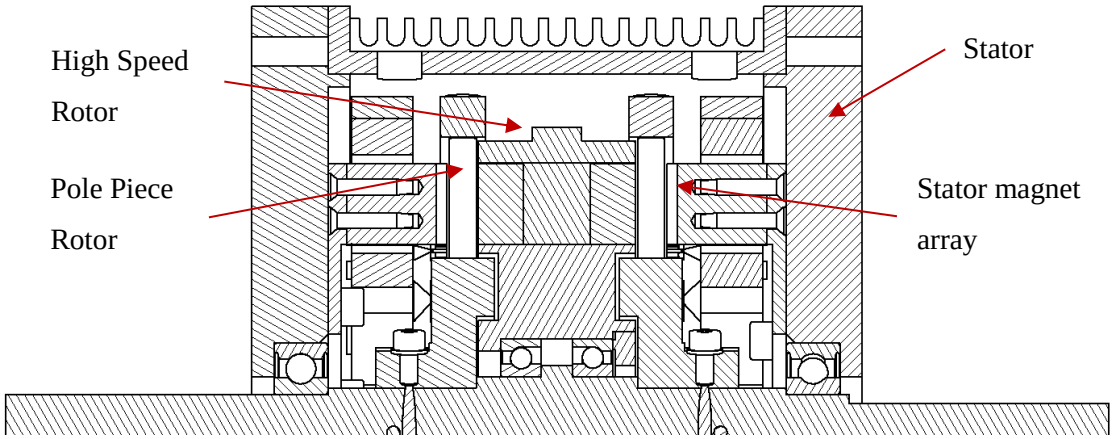

Figure 6.1 *Cross section of an AFPDD*

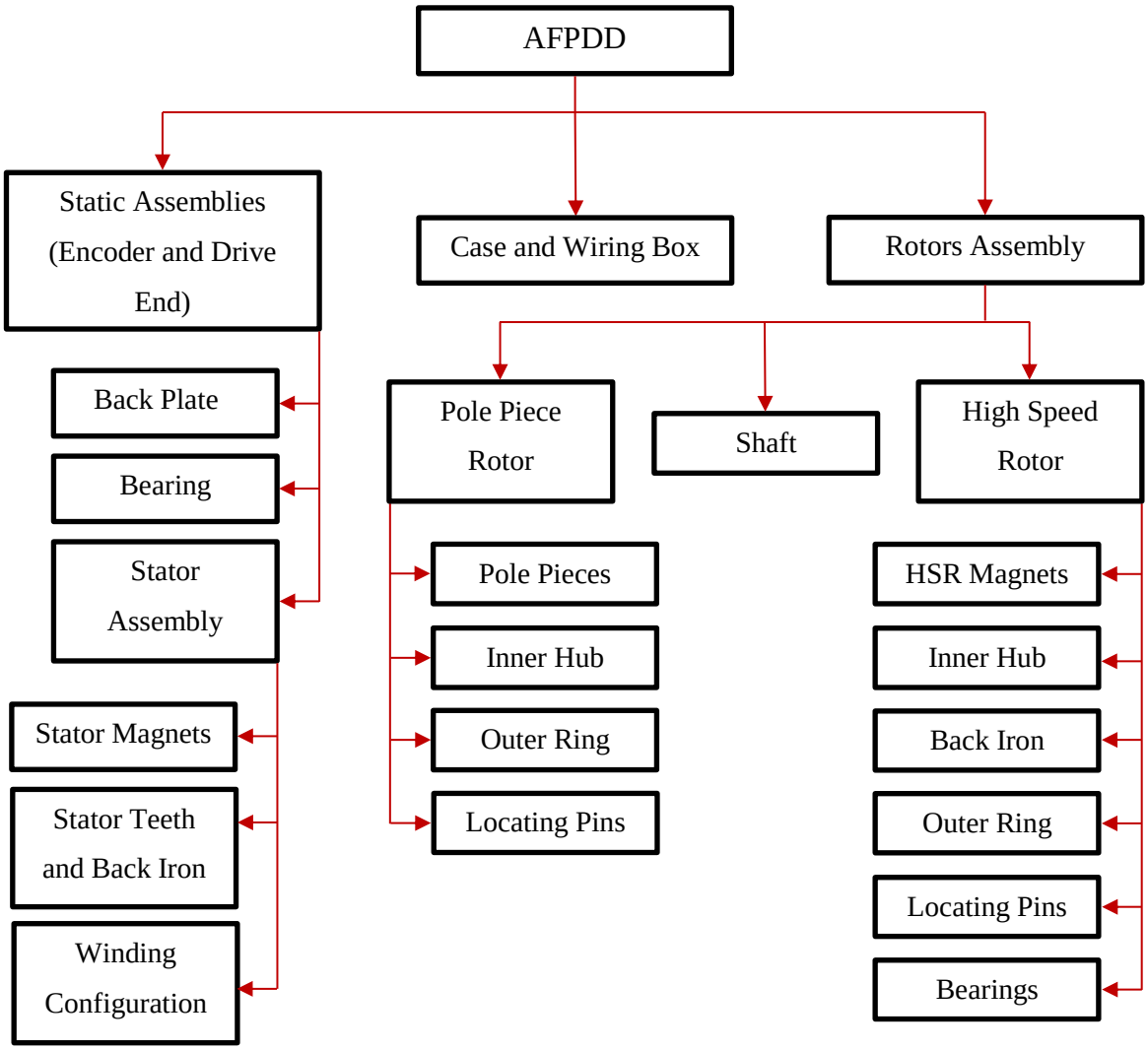

Figure 6.2 *Component structure*

6.1. Stator Assembly

A number of key stator design aspects were considered for the chosen AFPDD configuration. SMC was selected for the stator back iron and teeth as the SMC offered the most appropriate option to prevent high eddy current losses. Tape wound, punched slot laminated stators for AF machines exist but due to the nature of producing a single prototype would have been prohibitively expensive [6.3]. The SMC also enabled complex 3D shapes to be produced. This was particularly important to facilitate simple positioning of the stator magnets, predominantly those between stator teeth, as the robustness of the magnet array is critical to the machine operation. The manufacture was further eased by separating the tooth and back iron SMC components which permitted the use of pre-wound coils, as shown in Figure 6.3.

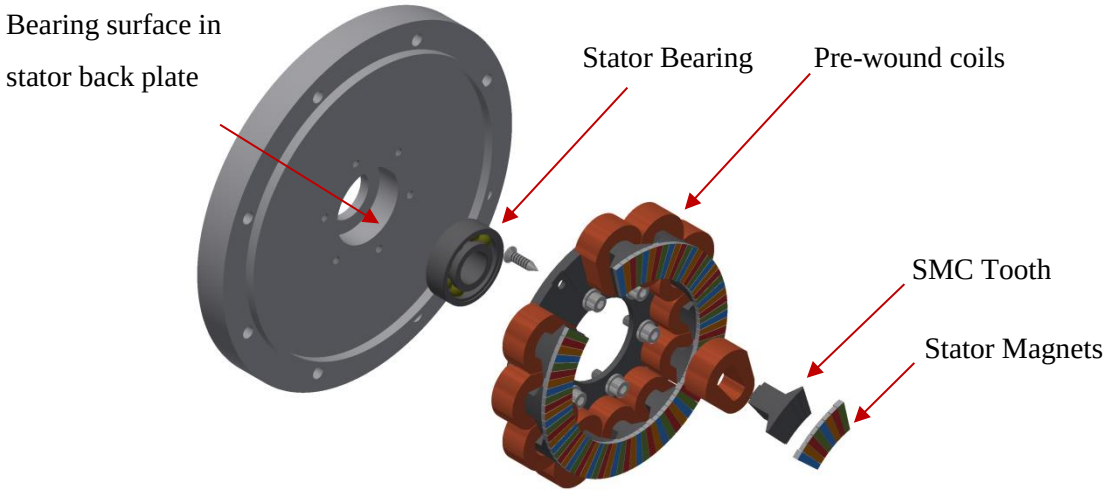

Figure 6.3 *Stator assembly*

6.1.1. Stationary Magnet Array

A significant challenge with the stationary magnet array are those magnets situated between the stator teeth. This is due to the limited bond area when only the surfaces of the teeth are used for location. One option is to entirely remove those magnets but in

this case would result in ~14% reduction in gear pull-out torque. Alternatively, the tooth pitch to slot pitch ratio could be increased to increase bond area of the magnet. However, this is detrimental to the power factor of the machine. Figure 6.4 shows a larger tooth-pitch to slot-pitch ratio is used for the tooth tip which supports the magnet (A). A lower tooth-pitch to slot-pitch ratio is then selected for the tooth tip edges closest to the airgap (B). This enabled the magnet adhesion area to be increased without negatively affecting the power factor of the machine.

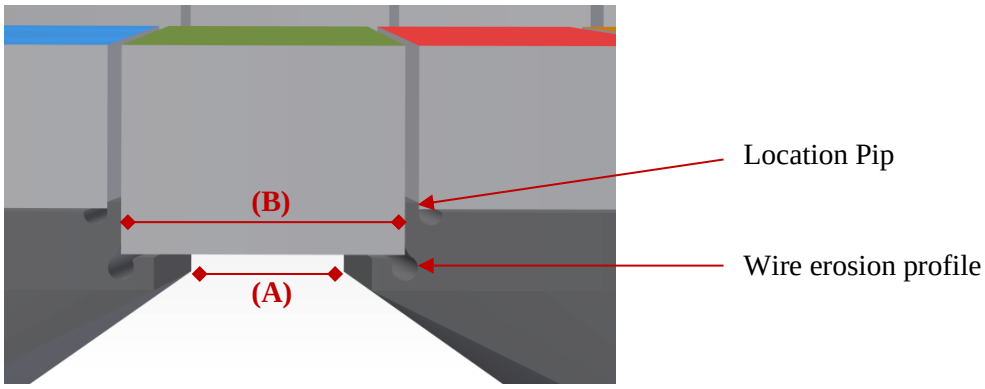

Figure 6.4 *Stator magnet retention*

6.1.2. Accommodating Pre-wound Coils

The coil winding of the machine was simplified by choosing to use separate teeth and back iron components and thus pre-wound coils. These coils can be wound on a bobbin and are an ideal candidate for mass manufacture as the process can be easily automated. However, separating the two SMC components of the stator presents a question surrounding the method of assembling the two components. SMC is conventionally formed to suit a specific shape and as such methods of joining two SMC components are not commonly known. It is also important to minimise any air gaps between the two components. This problem is further elevated as the construction must be able to withstand the forces subject to the stator teeth. FEA was used to establish an estimate of the force per tooth of approximately 580N. A summary of tested assembly methods is

given in Table 6.1, which indicated that only the self-tapping screw with adhesive had sufficient strength to prevent movement of the teeth. It was decided that two screws per tooth would provide sufficient joining strength and also aid in good location of the teeth. Furthermore, the holes in the SMC were pre-tapped to prevent excessive force during assembly from rupturing the SMC.

Assembly Type	***Failure Force (N)***	***Failure Type/ Limitation***
M6 Metal Bolt with Threaded hole	569	Failure of threaded hole. Thin wall thickness causes rupture of SMC
Plastic Rawl Plug with M6 Metal Bolt	232	Insufficient force exerted on the hole causing complete separation of insert and test piece
8mm Jack Nut with M4 bolt	151	
8mm Neoprene Nut with M4 bolt	125	
3.2mm Pop rivet	98	
4mm Pop rivet	-	Pressure from Pop rivet caused rupturing of SMC
5mm screw (self-tapping)	370	Screw becoming loose and effectively unscrewed from test piece
5mm screw with adhesive (self-tapping) (Loctite 648/7649)	>1275	Maximum force available used with no failure

Table 6.1 *Stator tooth assembly method*

Pressed SMC stator teeth would have been preferable due to the possibility of increased magnetic and mechanical performance of the material. Furthermore, good dimensional accuracy and surface finish of the parts can be achieved without the need for further processing. However, due to the low quantity order of this prototype, conventional machining techniques such as milling and wire erosion have been used as a cost effective alternative. It has been shown that conventional machining of SMC increases the iron loss of the material [6.4]. Conventionally the sides of the stator teeth would be tapered from inner to outer diameter. This could be problematic to the assembly of stator tooth and stator back iron if tooth is oversized or slot is undersized at any point. The resulting misalignment would have a significant effect on both the axial airgap and

space between teeth in which a magnet of the stationary magnet array is located. To overcome this, the straight sided location feature shown in Figure 6.5 was added to ease the manufacture and achieve a tight fit between the assembled components.

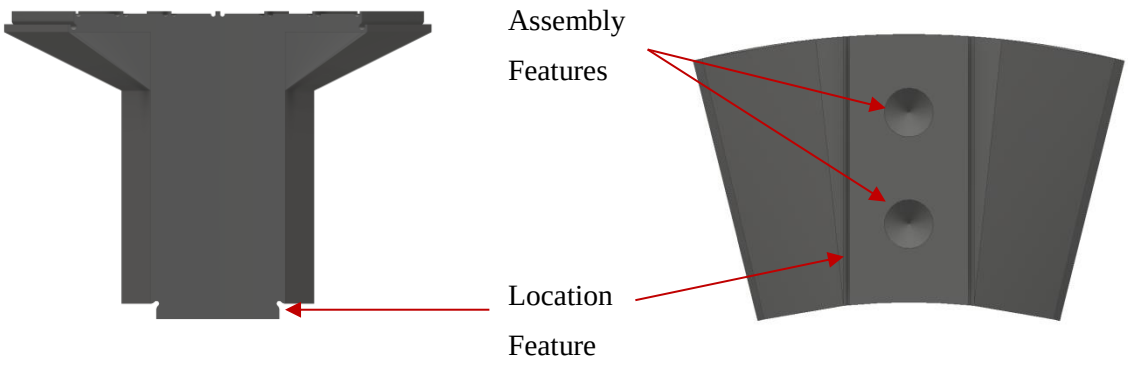

Figure 6.5 *Stator tooth assembly features*

6.1.3. Stator Prototype

Three key steps had to be successfully realised to ensure the magnetic, electrical and mechanical performance of the device. Firstly the windings, including thermometry, were assembled with the SMC teeth and back iron. The stationary magnet array was then bonded to the surface of the SMC teeth. Finally the entire structure was encapsulated in epoxy for increased mechanical and thermal performance.

Pre-formed coils were produced using winding tooling shown in Figure 6.6(a) and (b). Both the size and resistance of the coils were measured prior to assembly to ease manufacture and realise the correct electrical characteristics. Figure 6.6(c) shows a cross section of the copper with a packing factor of ~0.53 achieved. The coils were then assembled with the stator teeth and stator back iron, with the phase interconnects made as shown in Figure 6.6(d).

a) 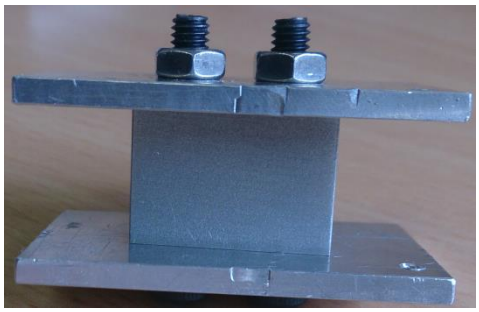 b) 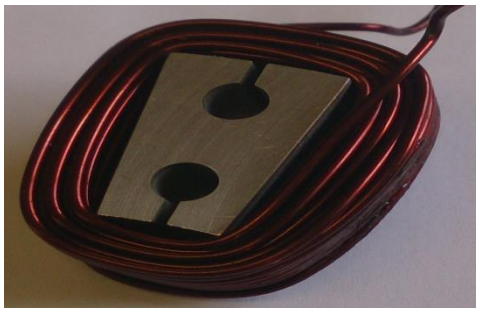

c)  d) 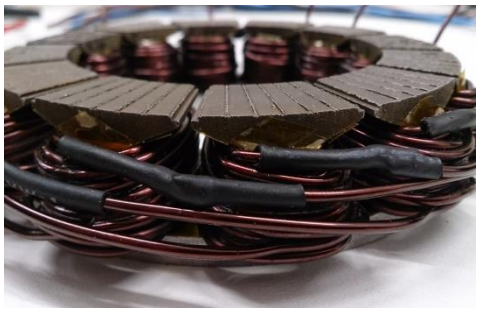

Figure 6.6 *Winding a) Tooling b) Wound coil c) Coil cross section d) Stator prior to potting*

A key concern prior to bonding the stator magnet array was the overall axial length of the teeth-coil-back iron assembly. Any increase in axial length would reduce the physical airgap between the stator and the PPs, possibly leading to collision between those components. Meanwhile a smaller than specified axial length would decrease the magnetic performance of the AFPDD.

To ensure the device resembled the specified dimensions as closely as possible the stators were measured using a Mitutoyo LH-600 Linear Height Gauge. By removing excessive axial length variations the axial height of the components was brought within tolerance as shown in Figure 6.7.

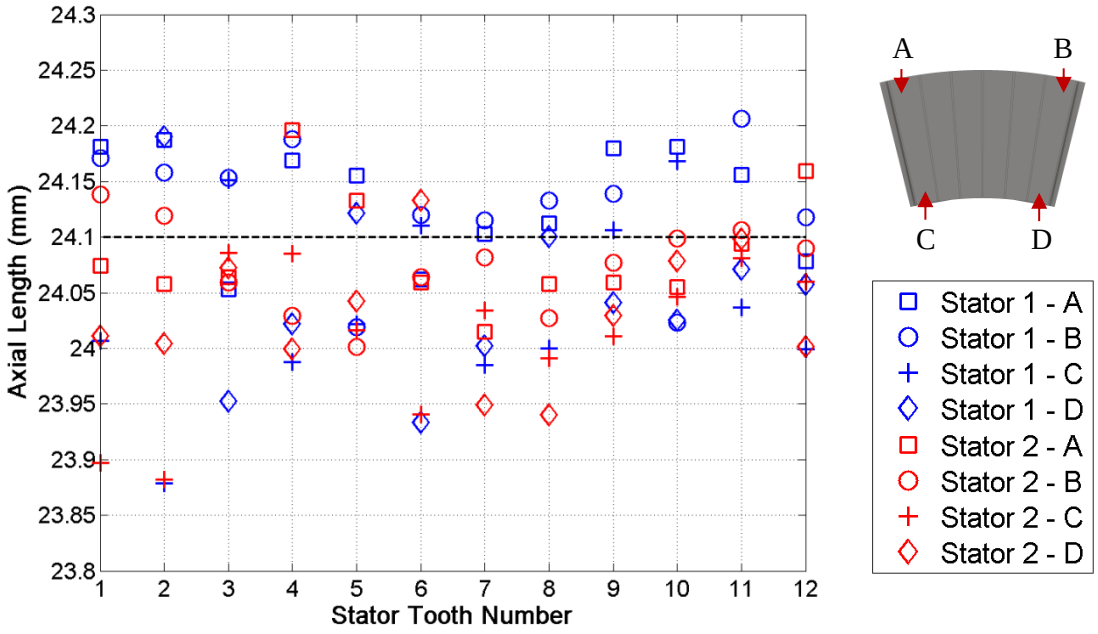

Figure 6.7 *Variation of axial length per stator tooth*

To position the magnets tooling was used alongside the designed features in the face of the SMC to accurately locate each magnet as shown in Figure 6.8(a). The use of a location pip, as seen in Figure 6.8(b), was advantageous to correctly position both the magnets on the surface of the stator teeth and the magnets which bridge two stator teeth. The completed array along with visualisation of the magnetic field using green viewing paper can be seen in Figure 6.8(c) and (d) respectively.

a) 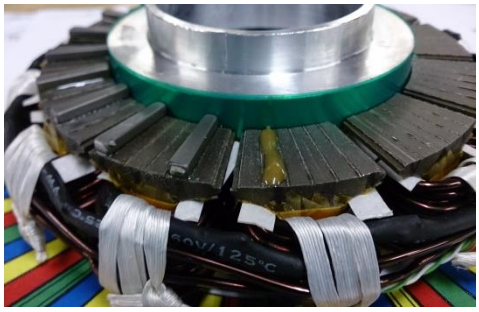 b) 

c) 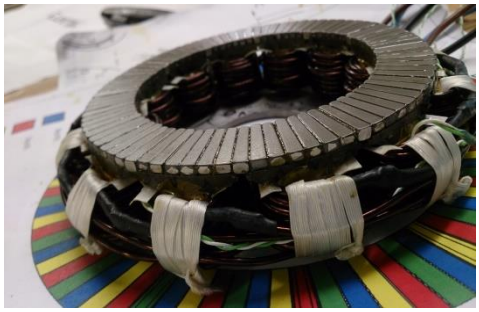 d) 

Figure 6.8 *Stator array a) During bonding b) Bridge magnet c) Complete array d) Magnetisation pattern*

The final stage of the construction of each stator was the encapsulation phase. Prior to this K-type thermocouples were fitted to each stator at the stator magnets, tooth body and end winding.

The low mechanical strength of the SMC made the encapsulation mould particularly challenging. The use of silicon grease and PTFE tape were essential to ensure low stresses were applied to the SMC when releasing the mould. The potting tooling, shown in Figure 6.9(a), featured a chamfer and O-rings to correctly seal the mould. The inner tooling (yellow) and outer tooling (green) are dimensioned to ensure the final dimensions of the stator epoxy cannot conflict with the PPR and the bearing surfaces remain clean. The epoxy chosen was a Duralco 4538 (Formulation A) as it offers a ‘stress free’ potting process, due to the material’s flexible nature, but cures to a rigid material with a tensile strength similar to that of SMC.

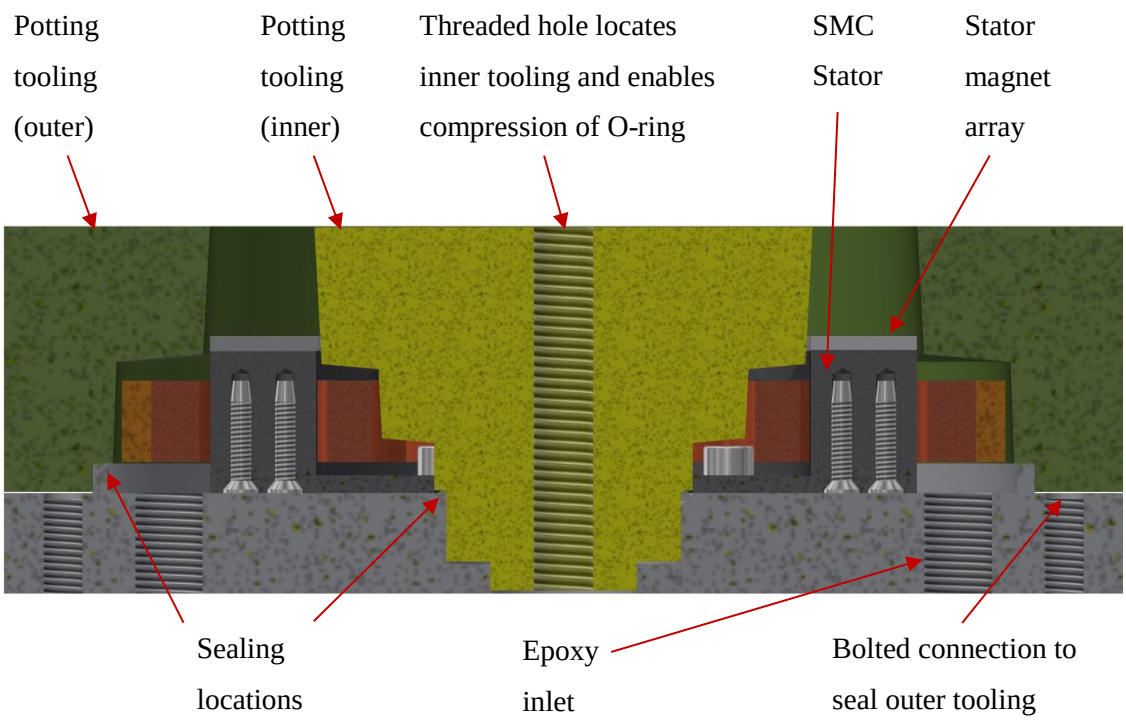

(a)

(b)

Figure 6.9 *Stator a) Mould CAD model b) Encapsulated stator*

6.2. Rotors Assembly

The rotor assembly consists of the shaft, HSR, bearings and the PPR. The layout of the two rotor assembly is shown in Figure 6.10. Further details regarding the HSR and PPR are provided in Section 6.3 and 6.4.

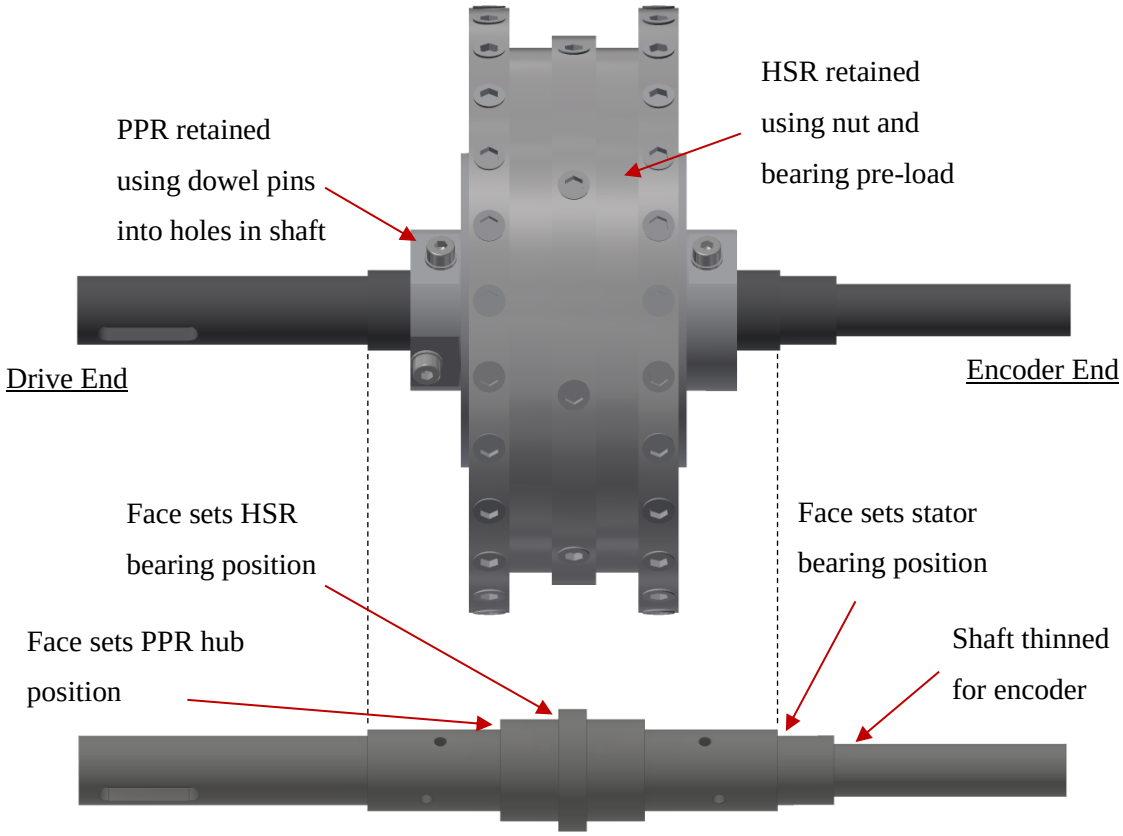

Figure 6.10 *Two rotor assembly*

The shaft was sized to both withstand the required output torsion and the static shaft deflection due to the mass of the HSR and PPR. The points of contact with the stator bearing were given zero displacement and the properties of EN-8 steel used. The forces resulting from the mass of the HSR and PPR are then applied to the shaft and the resulting deformation and stress distribution shown in Figure 6.11 and Figure 6.12. Using Ansys a deformation of 98µm and von-Mises stress of 0.5MPa were found.

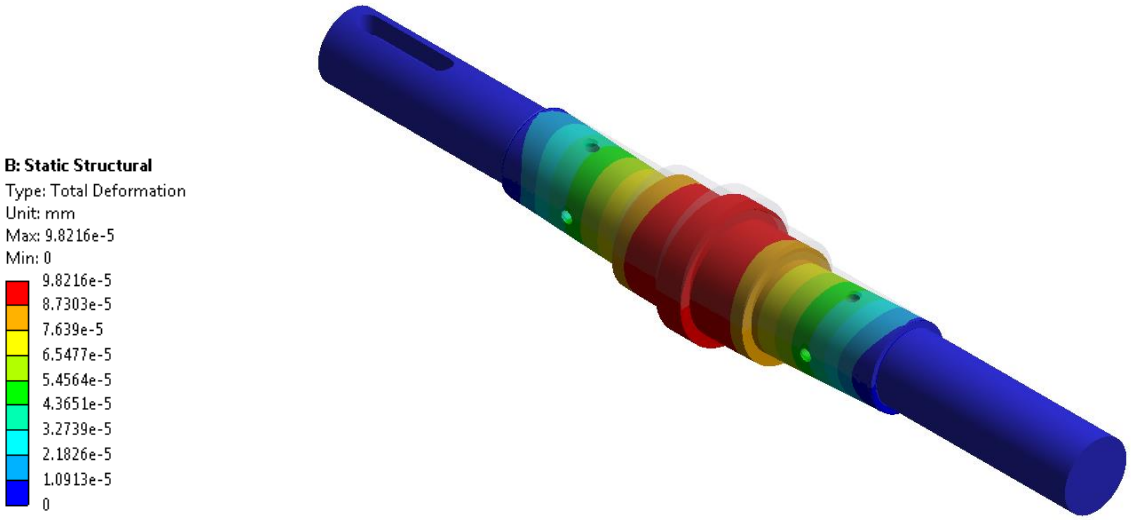

Figure 6.11 *Shaft bending deformation*

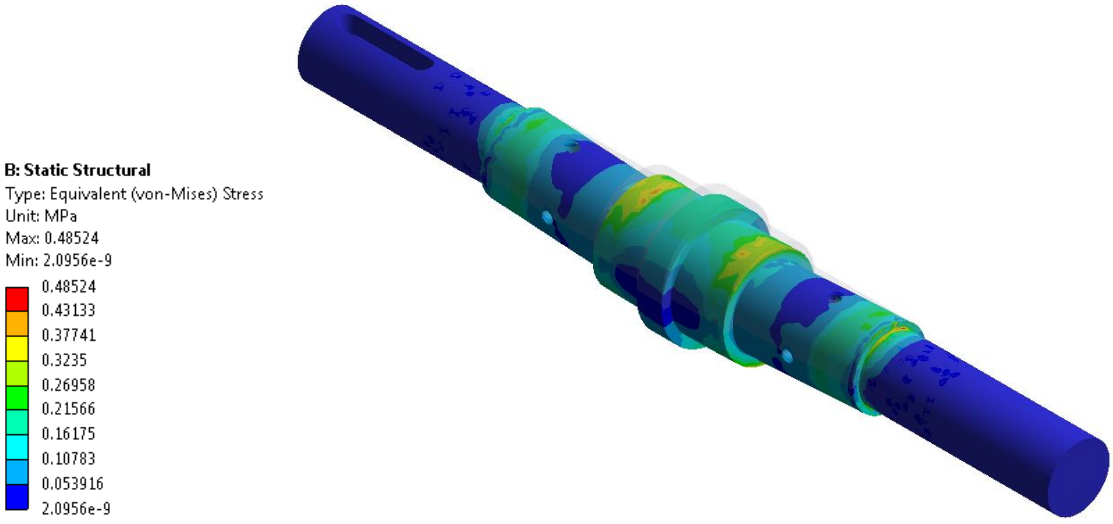

Figure 6.12 *Shaft bending von-Mises stress*

6.3. High Speed Rotor

6.3.1. HSR Bearing Arrangement

The HSR axial force is ideally zero due to the symmetry of the topology chosen. Due to manufacturing imperfections this may not be the case and the HSR may undergo axial loading. The resulting moment would cause a tilting of the HSR and a closing of the airgap, possibly causing contact between the HSR and PPR. The tilting, represented in

Figure 6.13(b) by an angle θ_t, can be mitigated by using a stiff shaft, rigid bearings and also by maximising the distance between the bearing centres.

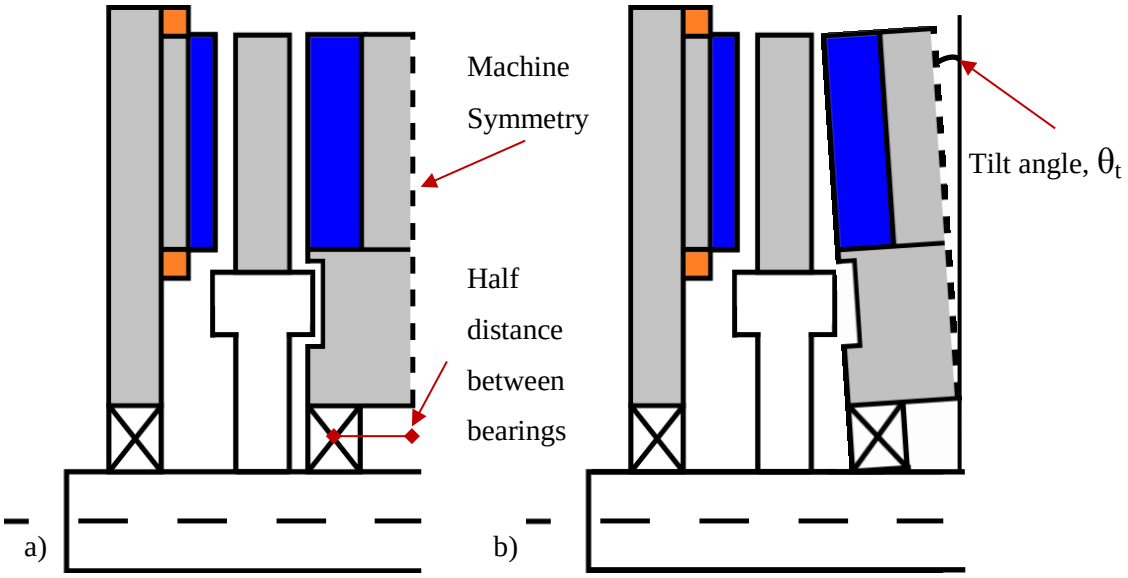

Figure 6.13 *HSR a) No axial loading and b) With axial loading*

The bearings chosen must therefore be able to accommodate both radial and axial loads. As a high stiffness is required to reduce the effect of any tilting, high precision angular contact ball bearings were chosen. The equivalent load on the bearings P can be calculated by:

$$P = XF_r + YF_a \tag{6.1}$$

where F_r is the radial load, F_a is the axial load and X and Y are the radial and axial load factors which are determined from the data sheet of the selected bearings [6.5]. Using the bearing load P, a basic load rating C can be calculated by:

$$C = \frac{f_h P}{f_n} \tag{6.2}$$

where f_h is the fatigue life factor and f_n is the speed factor. Both f_h and f_n are determined from manufacturer's empirical data using a known operating speed and

required bearing life. A de-rated bearing rating lifetime L_{10} can be defined as the lifetime at which a bearing under normal operating conditions (free from shock loading, under 125ºC and correctly lubricated) and has a 90% statistical reliability of reaching the required bearing life and is given by:

$$L_{10} = \left(\frac{C}{P}\right)^3 \tag{6.3}$$

The friction between the bearing balls, seals, the inner race and outer race results in energy loss. This bearing loss due to friction N_{R} can be estimated from the following formula alongside additional information from the manufacturer's website [6.5]:

$$N_{\mathrm{R}} = 1.05 \times 10^{-4}.M.\omega_b \tag{6.4}$$

where M is the total frictional moment of the bearing (N.mm) and ω_b is the relative speed between the bearing inner and outer races (r/min). The total frictional moment is comprised of the rolling friction, sliding friction, friction arising from seals and any additional drag losses.

The shaft is supported by two bearings in the outer case. In turn bearings on the shaft support the freely rotating HSR. To accurately position both the HSR bearings and the PPR, the steps in the shaft shown in Figure 6.14 have been used to locate the components.

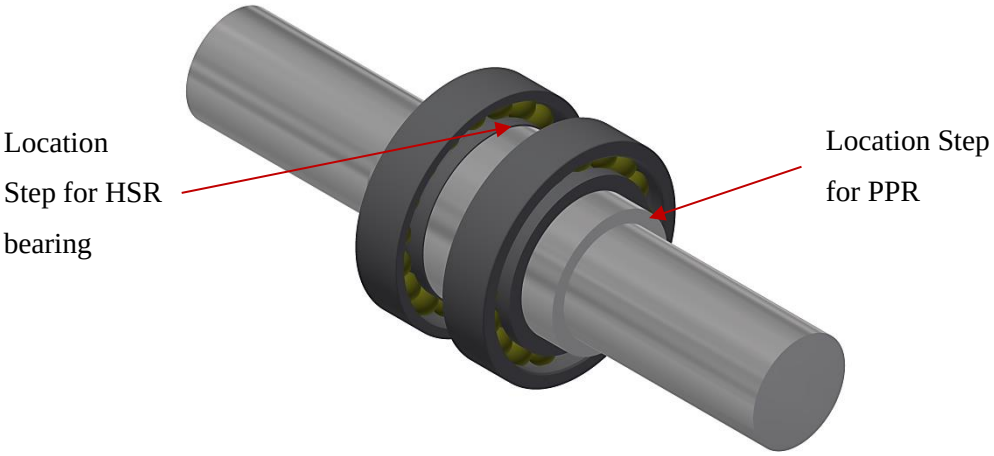

Figure 6.14 *Shaft and HSR bearing arrangement*

To improve the ability of the HSR to resist axial forces the bearing arrangement outlined in Figure 6.15 is realised. The sub-assembly comprises of the HSR, HSR bearings, shaft and locking nut. The distance between bearing centres is fixed by the location features on the shaft, with the locking nut providing the necessary axial force to prevent axial movement of the HSR. This arrangement also benefits by transferring the axial pre-load through the two bearings from a single side which helps to centrally locate the HSR on the shaft.

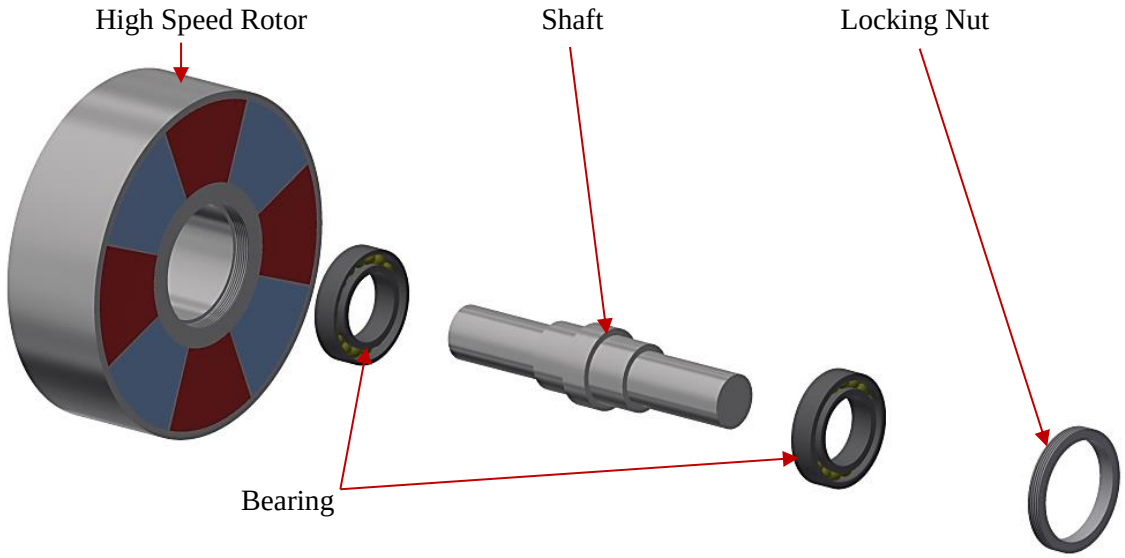

Figure 6.15 *HSR bearing pre-loading arrangement*

An estimate of the required tightening torque M_t required to preload the bearing using a precision lock nut is given by [6.5]:

$$M_t = K\left(F_s + \left(N_{cp}F_f\right) + G_{A,B,C,D}\right) \tag{6.5}$$

where K is the calculation factor dependent on the thread, F_s is the minimum axial clamping force, N_{cp} is the number of bearings in the same orientation as the bearing in contact with the locking nut, F_f is the axial fitting force and $G_{A,B,C,D}$ is the pre-set bearing preload prior to mounting. The required tightening torque was 13.51Nm. As a conventional torque wrench cannot be used a specific pin spanner was designed to tighten the nut. Using this spanner alongside a digital scale, with the known pivot radius equates to a required reading of 10.8kg to achieve the correct tightening torque.

6.3.2. HSR Outer Ring Design

One advantage of the AFPDD is the ability to remove a significant part of the magnet retention structure from within the active magnetic field path. An outer ring for the HSR was designed to withstand the centrifugal force F_c on the magnets trying to escape retention during motion and is given by:

$$F_{\mathrm{c}} = m_m r_m {\omega_h}^2 \tag{6.6}$$

where m_m is the magnet mass, r_m is the mean radius of the outer ring and ω_h is the HSR speed. The resultant radial pressure P_r exerted on the outer ring is given by:

$$P_{\mathrm{r}} = \frac{F_c}{2r_m l_r} \tag{6.7}$$

where l_r is the length of the axial outer ring. The mechanical limit set by the maximum permissible hoop stress, σ_h of the material given by:

$$\sigma_{\mathrm{h}} = \frac{F_h}{2t_r l_r} \tag{6.8}$$

where t_r is the radial wall thickness of the outer ring and F_h is the force on the hoop. By equating F_c and F_h the hoop stress σ_{h} is given by:

$$\sigma_{\mathrm{h}} = \frac{P_r r_m}{t_r} \tag{6.9}$$

The variation of hoop stress with HSR speed is shown in Figure 6.16. At the rated speed of 7000rpm an outer ring with $t_r = 5mm$ provides magnet retention whilst maintaining a safety factor of ~2 for the outer ring material.

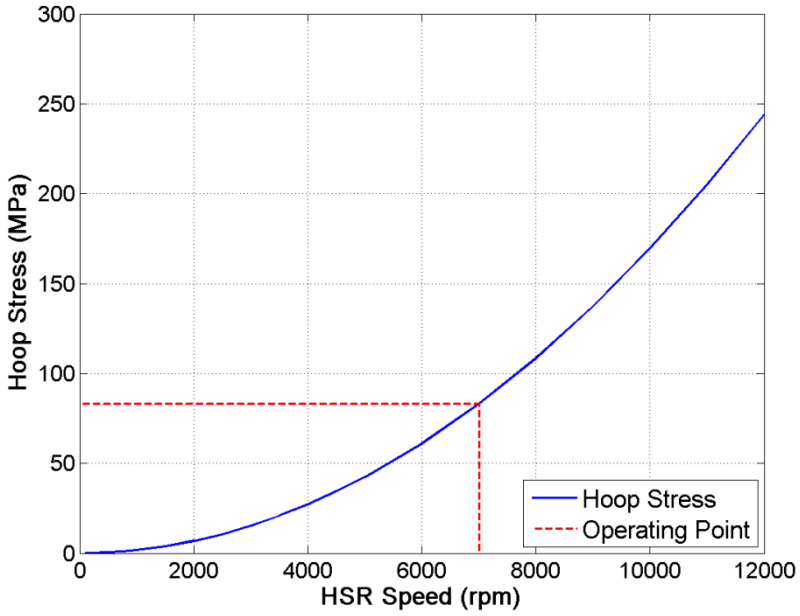

Figure 6.16 *Variation of hoop stress with HSR speed*

6.3.3. HSR Prototype

When produced the high-speed rotor showed a 0.7mm run-out on the surface of the disc meaning the rotor axial surface and shaft were not perpendicular. The likely cause of this is due to the misalignment of the HSR components and the difficulties associated with assembling pre-magnetised parts. This meant the face had to be trued-up to parallel

by removing a small proportion of magnet material. To achieve the specified airgap the HSR had to be recentralised on the shaft by spacing the PPR appropriately. Once assembled the high-speed rotor was statically balanced on the shaft in accordance with ISO 1940-1. Figure 6.17(a) and (b) show the HSR back iron and hub components. A test assembly of the HSR without magnets is shown in Figure 6.17(c) with the fully assembled HSR shown in Figure 6.17(d).

a) 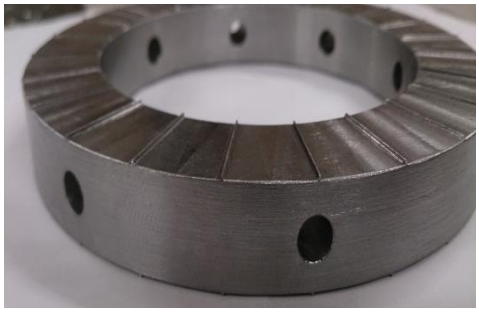 b) 

c) 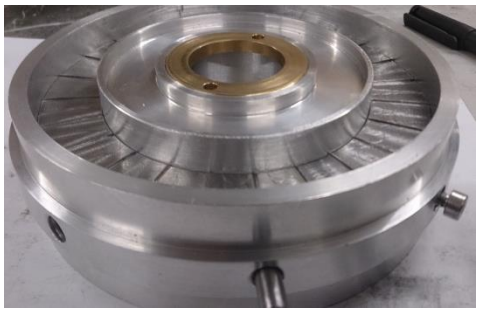 d) 

Figure 6.17 *HSR a) Back iron b) Hub on shaft c) Pre-magnet bonding d) Completed HSR*

6.4. Pole Piece Rotor

As discussed in Chapter 5 a cylindrical PP was chosen for its ability to give a high output torque whilst being subjected to lower axial force. An outer ring will also be used to retain the pole pieces with the final structure shown in Figure 6.18.

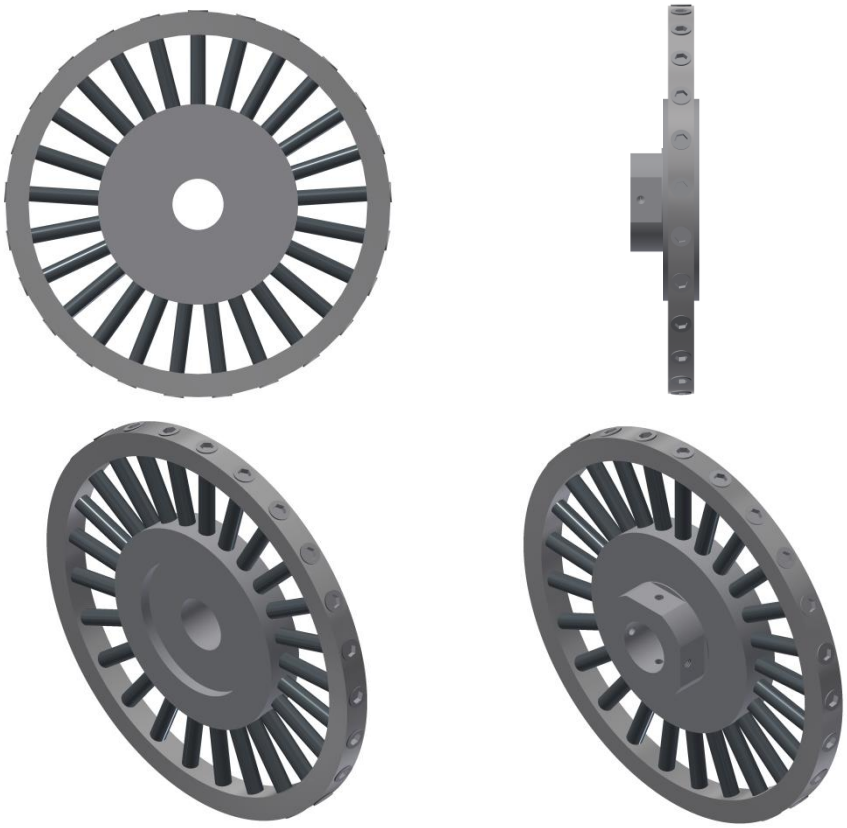

Figure 6.18 *PPR structure with cylindrical PPs*

6.4.1. PPR Construction

To ensure the forces on the PPs are minimised insertion into the PPR structure occurs after assembly of the machine. The PPR structure is constructed by first placing non-magnetic pins between the PPR hub and the PPR outer ring. These are partially threaded and secure the concentricity of the two parts, allowing a PP to be inserted from a slot in the case. A socket set screw is inserted to retain the PP, with the non-magnetic pins removed allowing the remaining PPs to be inserted.

To achieve the small air gap required and also allow sufficient material to support the PP it was necessary that a section of the inner hub of the PPR run within the inner hub of the HSR. These features can be seen in Figure 6.19. Due to manufacturing difficulties the PPR Hub pin and retaining shoulder bolt were replaced with a socket set grub screw to provide the clamping force required between the PPR and the shaft.

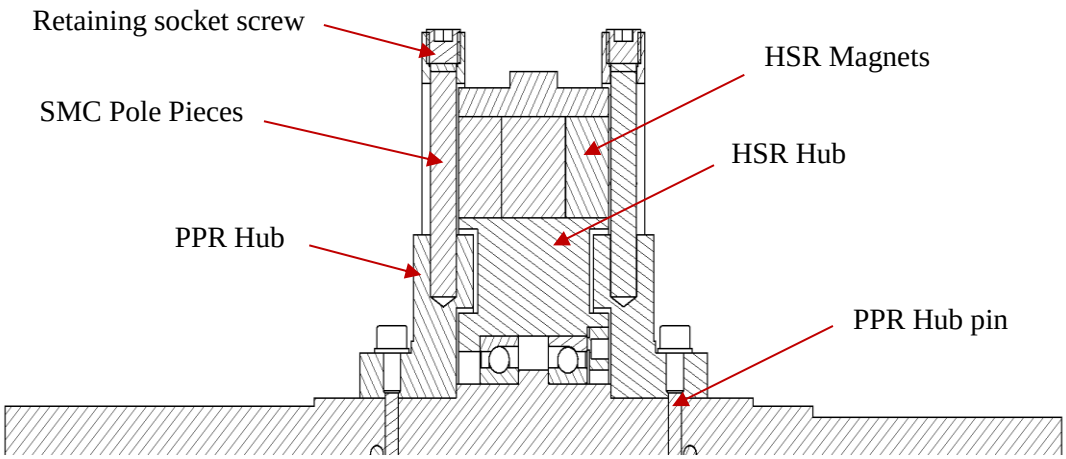

Figure 6.19 *'Inter-locking' HSR and PPR*

6.4.2. PPR Prototype

The PPR prototype hub and outer ring with the temporary non-magnet pins are shown in Figure 6.20(a) and (b). Figure 6.20(c) shows a trial PP insertion and the completed PPR within the AFPDD is shown in Figure 6.20(d).

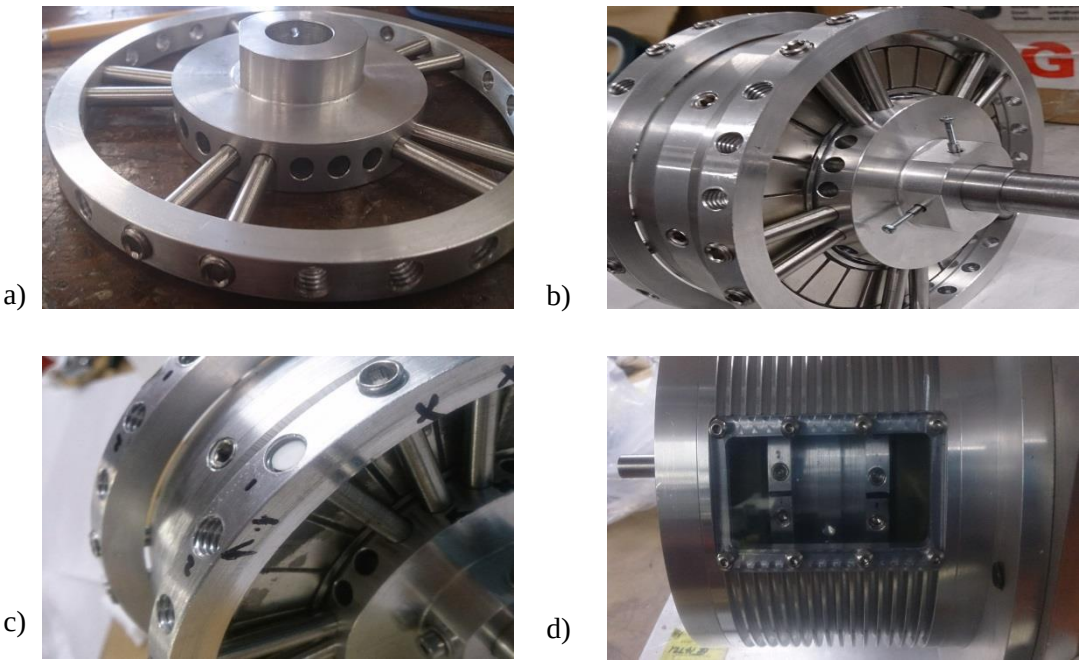

Figure 6.20 *PPR a) Pre-assembly b) Assembled with HSR c) PP insertion d) Completed PPR*

6.5. Casing

The case required several features unique to the AFPDD. Figure 6.21(a) show a 'window' into the case with a separate cover to allow for the PPs to be inserted after the rotor assembly was mounted in the case. As with many conventional electrical machines the outer diameter of the case was finned to improve the thermal performance of the machine. Figure 6.21(b) shows outlets for the stator phase windings, which were later removed as the phase winding was taken radially outward from the stator back plates.

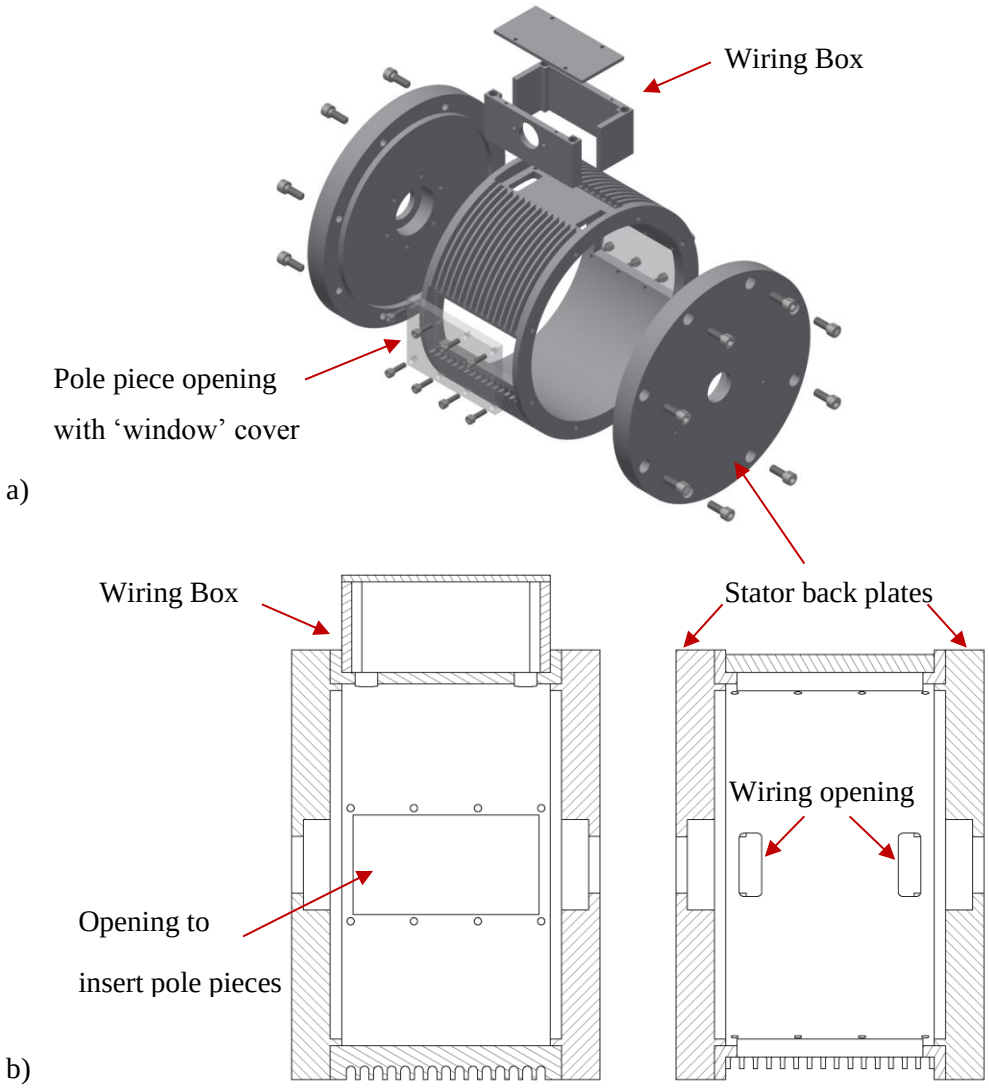

Figure 6.21 *Case design a) 3D view and b) Cross section view*

6.5.1. Case Prototype

The final wiring box of the case produced increased in size from the initial design to accommodate the number of wiring connections to be made. Figure 6.22(a) shows a black shrouded wiring bundle from each stator, which contains the phase and thermocouple wires. After the interconnections are made the AFPDD 3-phase output connector and thermocouples exit the wiring box are shown in Figure 6.22(b).

a) 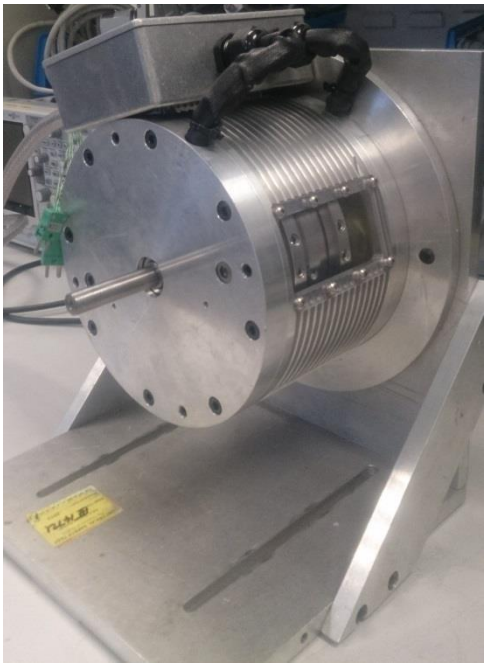 b) 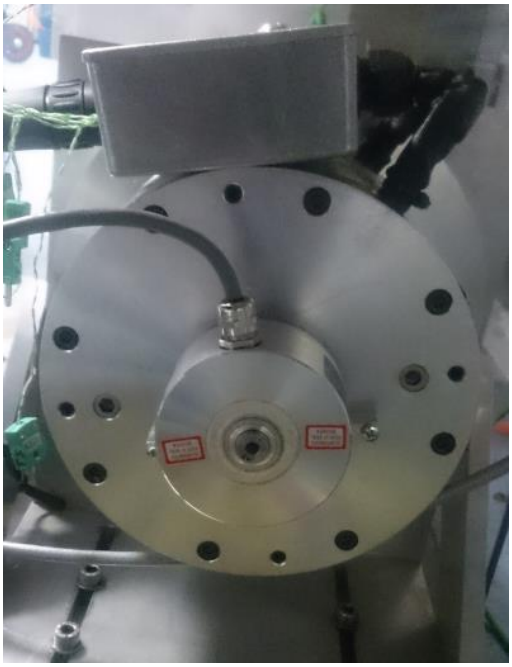

Figure 6.22 *AFPDD a) Case and mounting bracket b) Encoder and wiring output*

6.6. Testing

In order to verify previous analysis of the AFPDD it is necessary to test the prototype machine. This is complicated by the mechanical arrangement as there is no direct access to the HSR via a shaft. Therefore, both static and on-load tests were conducted to verify key parameters such as the pull-out torque and motor back EMF constant. Parameters of the prototype AFPDD are given in Table 6.2

Quantity	***Value***
Pole pairs on HSR, p_h	4
Pole pieces, n_s	25
Pole pairs on stator	21
Gear Ratio, G_r	6.25
Axial thickness of HSR PMs	10mm
Axial thickness of PPs	6mm
Axial thickness of stator PMs	2.5mm
Outer Diameter	120mm
Remanence of PMs	1.25T
Relative recoil permeability	1.05
Slot Packing Factor	0.53
Magnet Mass (HSR / Stator)	1.081kg (0.865kg/0.216kg)
Copper Mass	0.955kg
Mass of stator SMC	1.339kg
Mass of Pole Piece SMC	0.190kg
Total Active Mass	3.565kg
Total Mass	10.50 kg
Rated Torque	19.8Nm
Pull-out Torque	24.5Nm

Table 6.2 *Summary of AFPDD parameters*

6.6.1. AFPDD Pull-out Torque

The magnetic gear pull-out torque was measured to be 24.5Nm, compared to the predicted value 25.2Nm, a 3% reduction. However, as approximately 3-5% of the magnet material on each stator was removed to bring the stators within the required flatness tolerance a small reduction in pull-out torque was to be expected.

6.6.2. AFPDD Electrical Parameters

The measured values of resistance and inductance per stator and for the complete machine, as measured with a Hioki 3522 LCR meter, are given in Table 6.3.

Stator 1	***A***	***B***	***C***	***Predicted***
Resistance (mΩ)	58.9	62.2	60.0	60.5
Inductance (μH)	272.8	254.5	248.0	255.1
Stator 2	***A***	***B***	***C***	
Resistance (mΩ)	60.5	58.6	61.2	60.5
Inductance (μH)	241.3	244.2	243.2	255.1
Phase Resistance (mΩ)	119.4	120.8	121.2	121
Phase Inductance (μH)	514.1	498.7	491.2	510.2

Table 6.3 *AFPDD electrical parameters*

6.6.3. AFPDD Static Testing

To measure the electromagnetic coupling between the winding and the HSR, a static torque test was conducted with the test setup shown in Figure 6.23. By rotating the stator on a lathe chuck and fixing the position of the HSR the relative angle between the stator and HSR was varied. The torque reaction was then measured using a lever of known length and precision weight scales. Access to the HSR is restricted by the size of the window in the case and as such the results shown in Figure 6.24 are taken over a limited angular rotation.

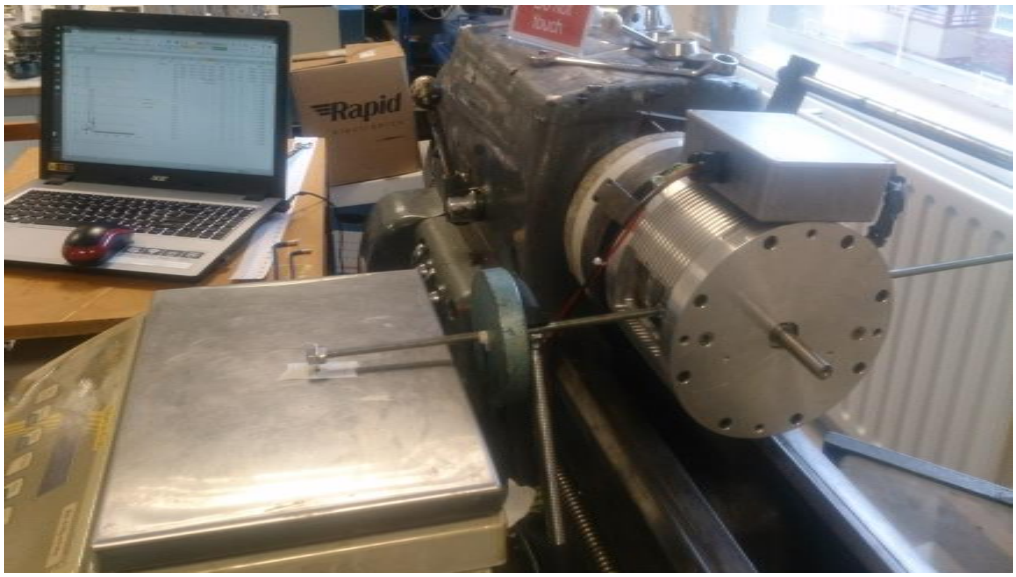

Figure 6.23 *Static torque test setup*

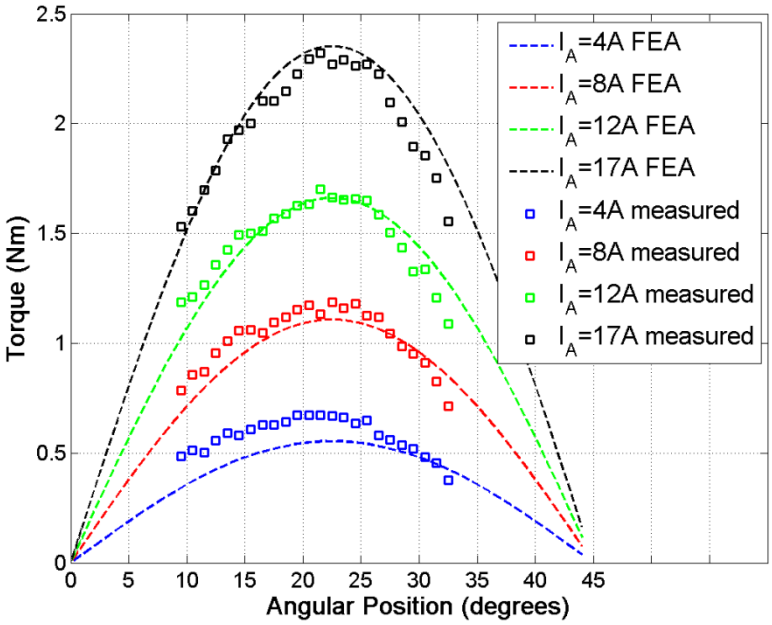

Figure 6.24 *Variation of torque with HSR angular position*

6.6.4. AFPDD No Load Testing

The first measurement conducted under no load conditions was the back EMF of the AFPDD. The results of this test are shown in Figure 6.25, with only a single phase shown for clarity.

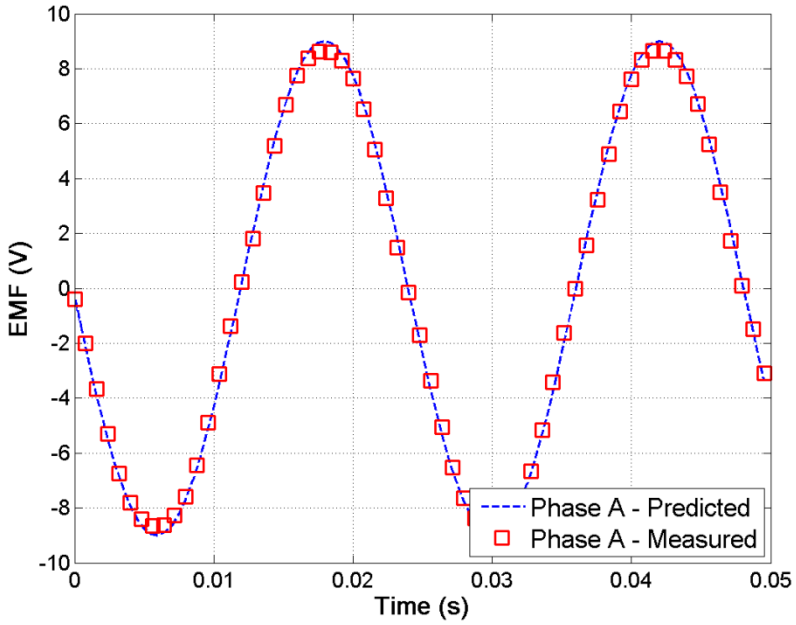

Figure 6.25 *Variation of EMF with time*

During the AFPDD no load EMF test one PPR became loose due to a lack of connection between the grub screws in the PPRs and shaft. As this connection is the main load path in which torque is transmitted to the shaft the machine required opening to correct the problem. Once reassembled it was found that one stator had a reduced voltage output as shown in Figure 6.26, likely due to an enlarged air gap at that side of the machine. However, due to the corrective action taken to secure the PPR to the shaft, including the use of adhesives, it was no longer possible to separate the components to adjust the air gap. As such the three phase back EMF shown in Figure 6.27 was attained using the experimental setup shown in Figure 6.28 after the AFPDD was reassembled with an enlarged air gap. This resulted in the back-EMF constant, and thus torque constant, being reduced to 0.027V.s.rad^{-1} from the designed value of 0.35 V.s.rad^{-1}. Further evidence of this was seen in the reduction of the AFPDD pull-out torque from 24.5Nm to 19.6Nm, a 20% reduction.

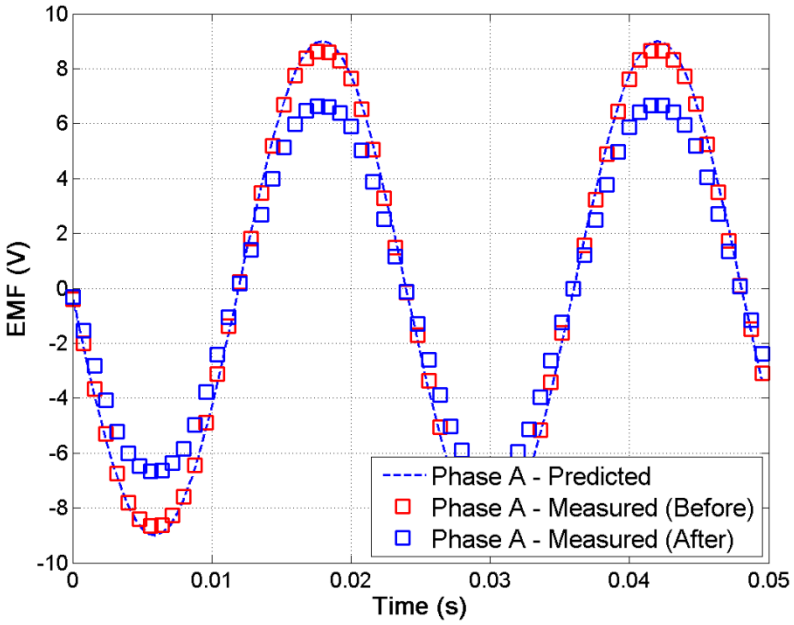

Figure 6.26 *Variation of EMF with time (before and after reassembly)*

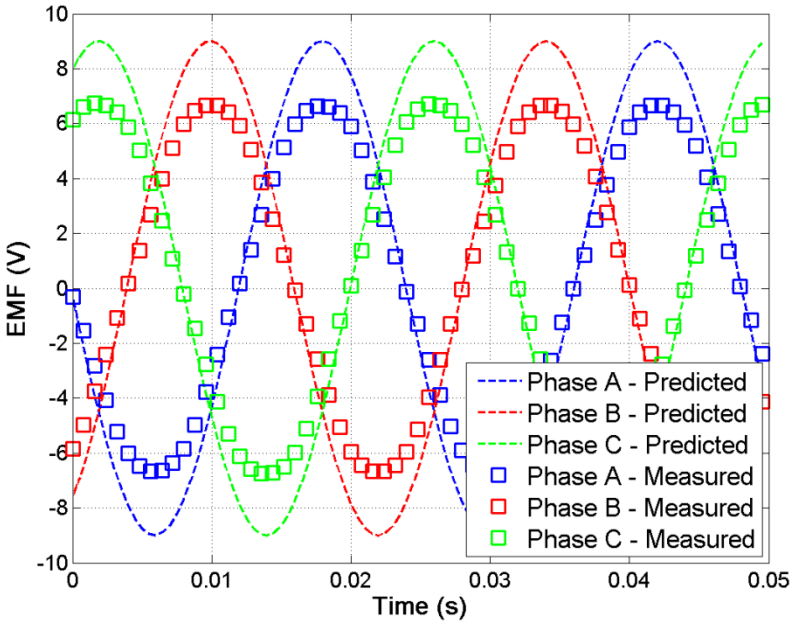

Figure 6.27 *Variation of EMF with time (after reassembly)*

a)

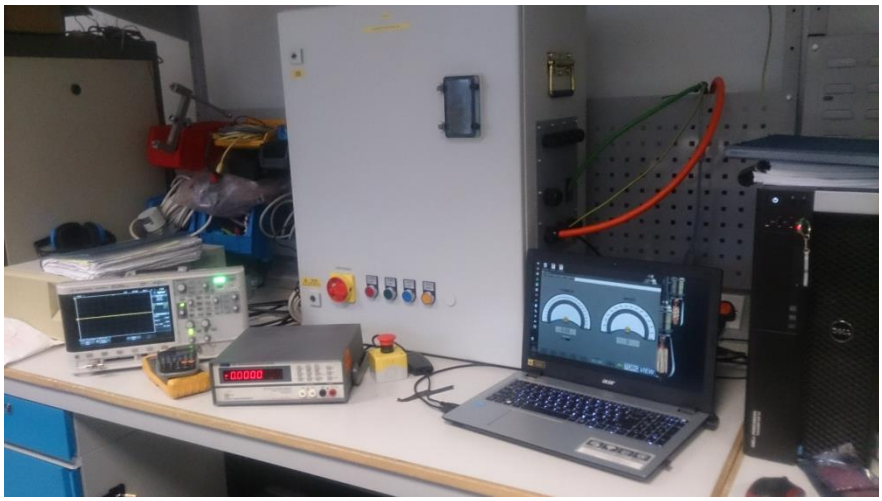

b)

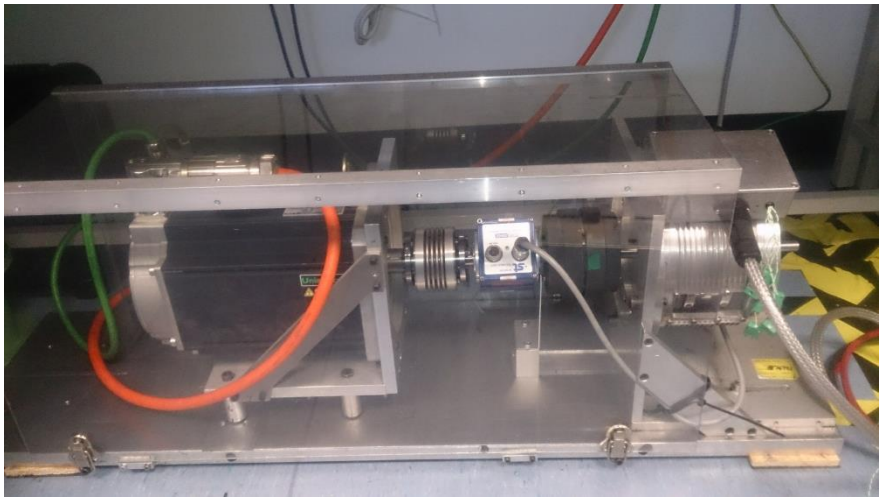

Figure 6.28 *Test setup a) Drive cabinet b Drive machine coupled to AFPDD*

Furthermore it became evident that excessive torque, shown in Figure 6.29, was necessary to cause rotation and resulted in excessive losses within the device under no load conditions. These are mainly attributed to losses in PPR and HSR supporting structures and are indicated by the increase in temperature of both HSR and PPR components relative to the stators, as shown in Figure 6.30.

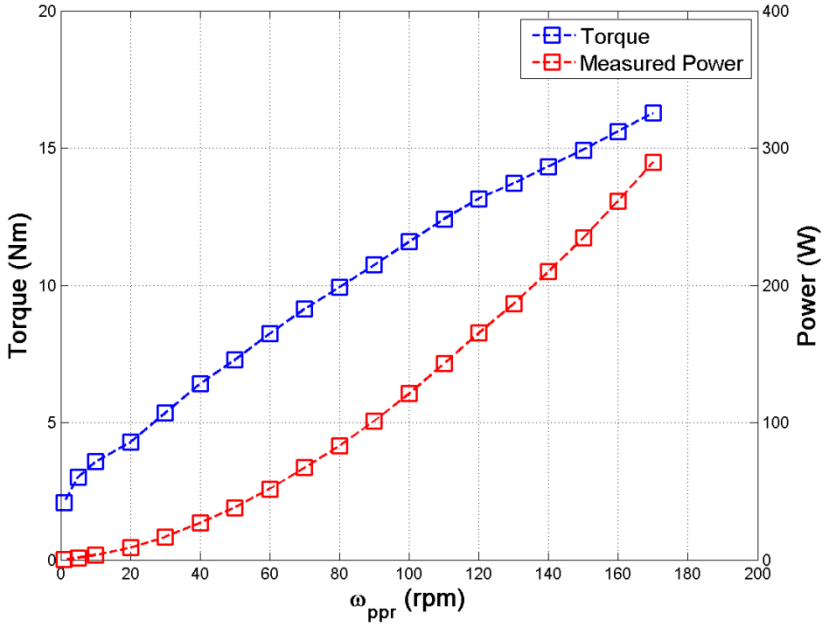

Figure 6.29 *Variation of torque and power with PPR speed (No load condition)*

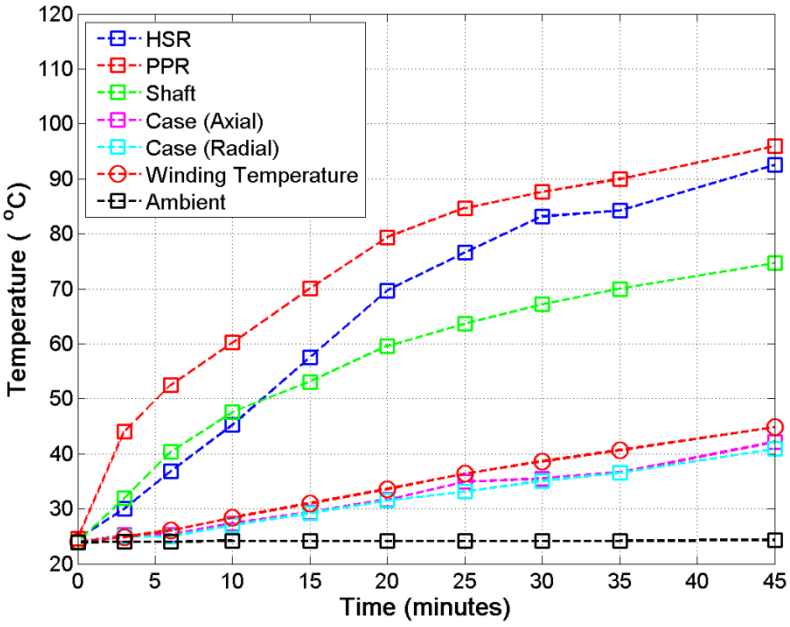

Figure 6.30 *Variation of temperature with time*

To investigate the cause of significant temperature rise within the PPR it was necessary to model the supporting structures. The model complexity required these components to be excluded from previous electromagnetic analyses. However, due to the use of a

different software package (Opera 3d) it was possible to analyse the supporting structures. Furthermore, the loss density of components modelled in the FEA had to be scaled by volume to that of the prototype parts, due to their complex shape and the need for a uniform profile in the air gap of the FEA model, as shown in Figure 6.31. It was found that the highest loss density could be attributed to the PPR hub, due to the eddy currents formed within the aluminium structure.

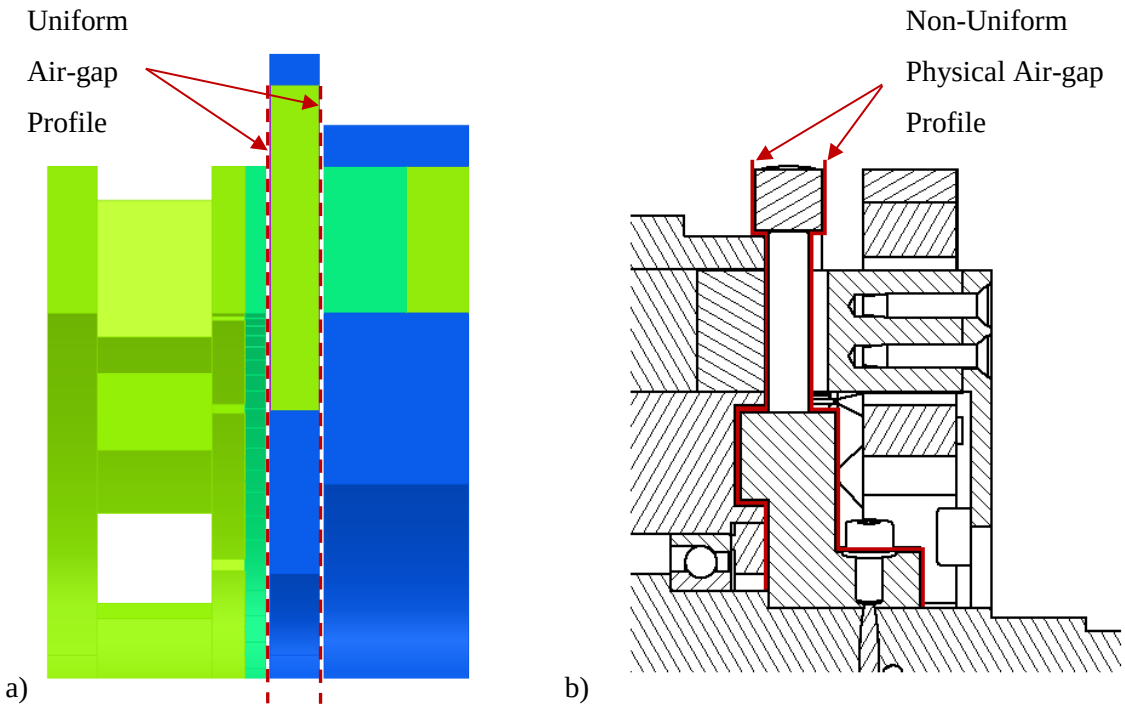

Figure 6.31 *Air gap in a) FEA model and b) Manufactured prototype*

The frictional moment of the bearings could be isolated at low speeds, where the effect of the eddy current losses is negligible. As such, a linear scaling of the bearing loss with speed can be predicted and incorporated into a total predicted loss. This shows good agreement with the measured no load input power, the power loss due bearing loss and eddy current losses, as seen in Figure 6.32. Aluminium was chosen for the PPR support structures due to its low cost and manufacturability. However, as the eddy current is the dominant loss mechanism this material choice is not appropriate for use in future

components of this nature. A more suitable material which still retains good manufacturability is stainless steel and would significantly reduce the loss within this component. The eddy currents in an aluminium and stainless steel PPR with the PPs removed for clarity are shown in Figure 6.33(a) and Figure 6.33 (b) respectively. Furthermore, steps could be taken to interrupt the eddy current path via slitting. Alternatively, a glass fibre composite structure would not suffer from such losses, but is inherently more difficult to manufacture.

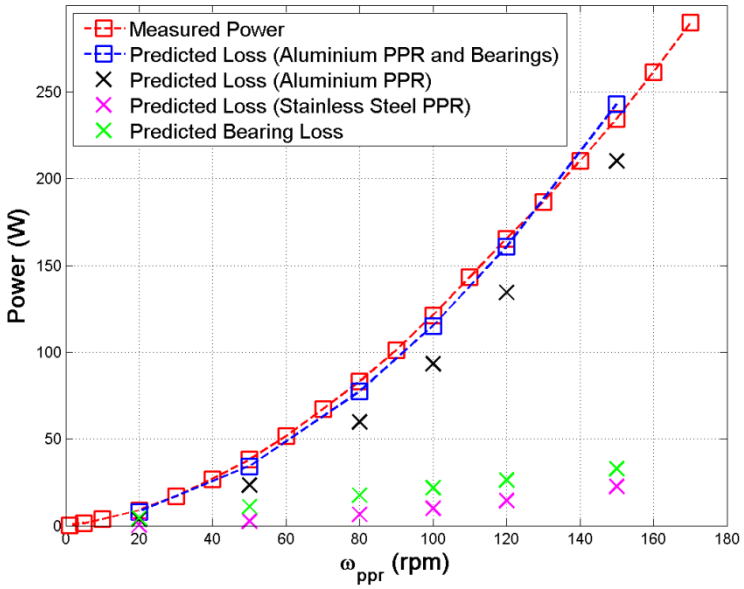

Figure 6.32 *Variation of loss with PPR speed (No load condition)*

a)

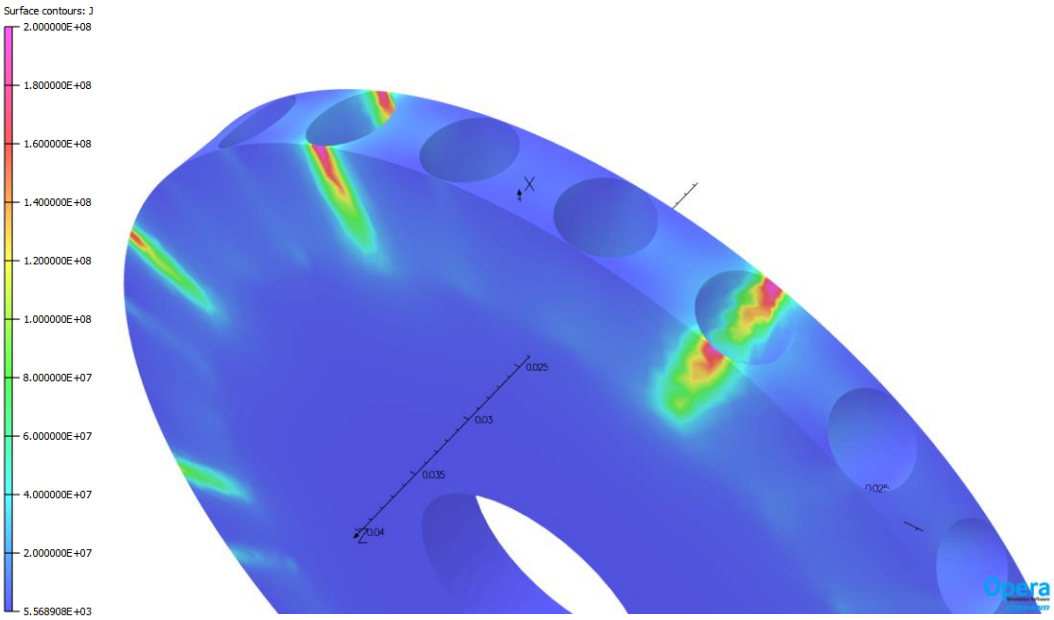

b)

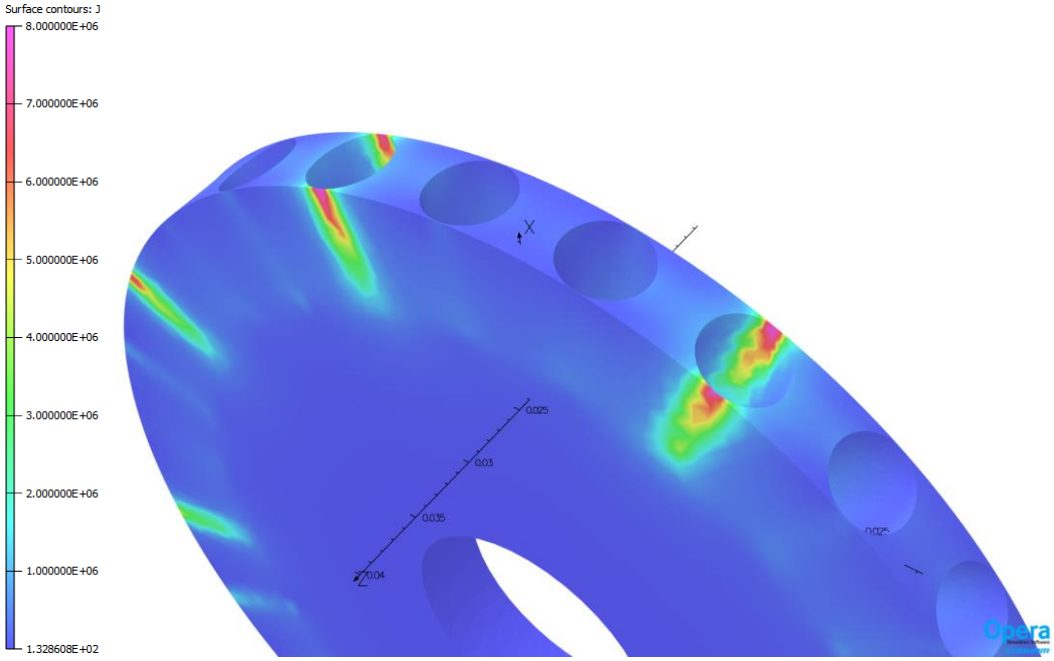

Figure 6.33 *Eddy currents in a) Aluminium PPR hub and b) Stainless steel PPR hub*

6.6.5. AFPDD On Load Testing

Conventionally electrical machines are often driven on a dynamometer against a load machine to test the on load performance. By actively controlling the current magnitude and phasing angles the torque-speed characteristics can be determined. However, this requires accurate position sensing or sensorless control. Due to the arrangement of the dual rotors within the chosen AFPDD topology, access to the HSR for position sensing

was not possible. Furthermore, sensorless control was not possible with the available industrial drive units. It is also possible to infer the HSR position from the PPR position as shown in [6.6] [6.7]. However, development of such control algorithms and associated power electronics were beyond the scope of this thesis. As such a passive system layout was chosen, in which the AFPDD is mechanically driven via a conventional PM motor and industrial drive unit. The AFPDD is electrically connected via a three phase rectifier to a variable resistor bank, enabling variation of the AFPDD load.

To model torque-speed characteristics the AFPDD parameters were used alongside the Matlab model, shown in Figure 6.34, to simulate the behaviour of the AFPDD under on-load conditions. The speed-torque characteristic shown in Figure 6.35 was attained by removing the influence of the no load losses found in the aluminium PPR hub and shows good agreement can be seen between the predicted and measured values. It worth noting that maximum power which could be measured was limited by the torque required to overcome the no load losses. Beyond this limit, the torque applied to the AFPDD was beyond the designed pull-out torque and as such the AFPDD pole-slips.

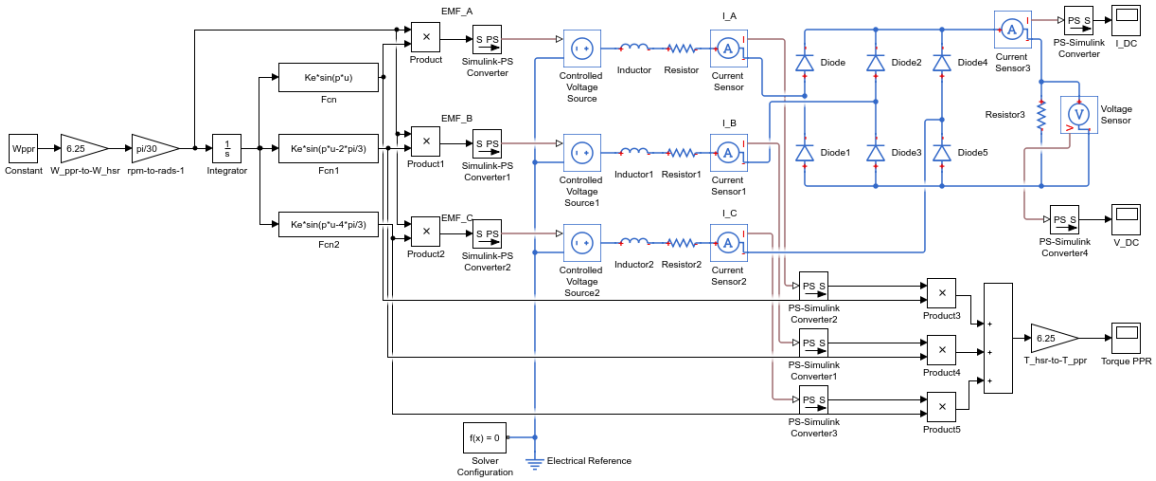

Figure 6.34 *On load Matlab model*

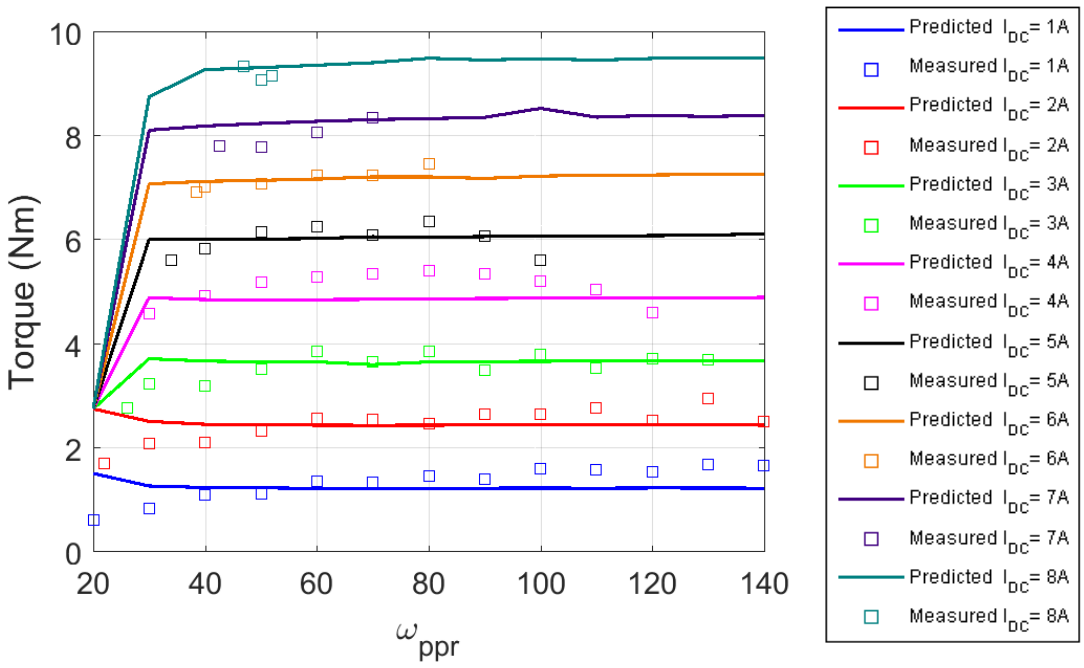

Figure 6.35 *Variation of torque with PPR speed (On load)*

6.6.6. AFPDD Torque Overload Testing

The inherent torque overload behaviour of the AFPDD was also tested as shown in Figure 6.36. This was done by applying a load beyond the pull-out torque of the magnetic gear. Region A shows the AFPDD during normal operation, with Region B showing the pole slipping behaviour when the applied torque is beyond the pull-out torque value of the AFPDD. Region C shows the AFPDD returning to normal operation after the applied torque is returned below the pull-out torque value.

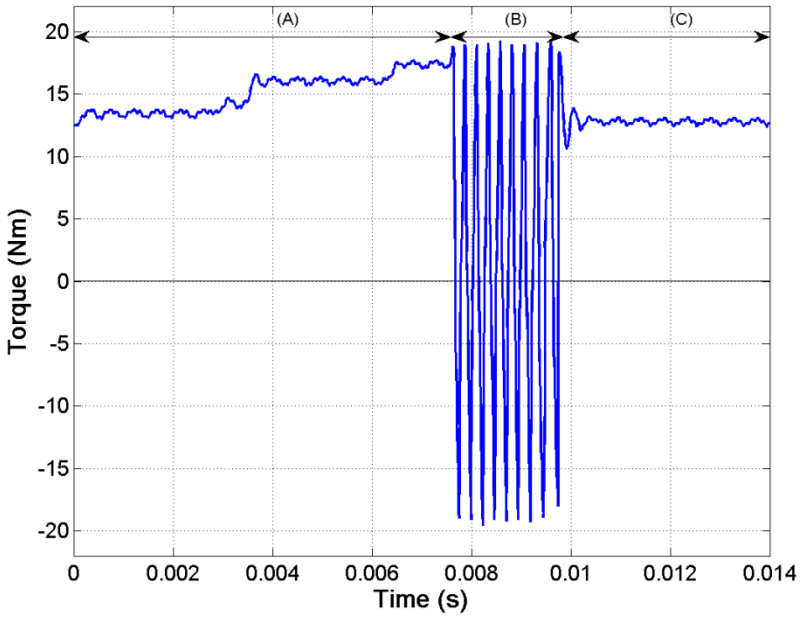

Figure 6.36 *Variation of torque with time (AFPDD MG pull-out)*

6.7. Conclusions

Prototyping the AFPDD presented several significant challenges. Novel methods for assembling SMC components to ease manufacture were tested and successfully realised in the dual stator AFPDD. Although the resulting torque density of the machine was impacted due to the sizing constraints imposed by the available SMC, the prototype AFPDD realised a torque per active volume of 5.55Nm/kg.

The AFPDD was tested under pull-out conditions, and withstood repeated pole slipping without mechanical damage to the PPs or surrounding structures. As such the dual rotor assembly verified previous predictions regarding the applicability of cylindrical PPs with no circumferential support. Furthermore the prototype AFPDD pull-out torque of 24.5Nm was within 3% of the predicted value.

Due to the structure which supports the PP, excessive eddy current losses were found in the device. This effect could be reduced or eliminated by designing the PPR supporting

structure and materials. However, due to the complexity and expense of producing new components, likely to be made from non-magnetic stainless steel or fibre glass, this is beyond the scope this PhD.

Good agreement was found between the AFPDD prototype and the FEA analyses performed in previous work. The torque per amp characteristic was verified during static testing. Due to an error during reassembly of the machine for the rotational testing phase, the subsequent performance of the machine was reduced. However, when accounting for these changes from the original design, the torque-speed characteristic agreed well with FEA and Matlab model.

6.8. References

[6.1] M. Johnson, M. C. Gardner, and H. A. Toliyat, "Design and Analysis of an Axial Flux Magnetically Geared Generator," in *IEEE Energy Conversion Congress and Exposition (ECCE)*, 2015, pp. 6511–6518.

[6.2] S. Mezani, K. Atallah, and D. Howe, "A high-performance axial-field magnetic gear," *J. Appl. Phys.*, vol. 99, no. 8, p. 08R303, 2006.

[6.3] M. Aydin, S. Huang, and T. a Lipo, "Axial flux permanent magnet disc machines: a review," *Conf. Rec. SPEEDAM*, pp. 61–71, 2004.

[6.4] T. Iwawaki, M. Inamori, and M. Morimoto, "Variation of iron loss by manufacturing method of SMC motor core," in *International Conference on Electrical Machines and Systems (ICEMS)*, 2013, vol. 2, pp. 2040–2043.

[6.5] SKF, *Super-precision bearings*. 2013.

[6.6] M. Bouheraoua, J. Wang, and K. Atallah, "Observer Based State Feedback Controller Design for Pseudo Direct Drive using Genetic Algorithm," in *6th IET International Conference on Power Electronics, Machines and Drives (PEMD)*, 2012, pp. 1–6.

[6.7] M. Bouheraoua, J. Wang, and K. Atallah, "Speed control for a Pseudo Direct Drive permanent magnet machine with one position sensor on low-speed rotor," *2013 Int. Electr. Mach. Drives Conf.*, pp. 986–992, May 2013.

Chapter 7 Conclusions

Methods for improving the current magnetically geared electrical machine technology toward mass manufacture are presented and applied to both radial and axial field machines.

In order to investigate the use of alternative windings to ease the manufacture of radial field PDD machines, a comparison was made to an existing concentric wound PDD. It was shown that PDDs with alternative windings can be realised, albeit with reduced torque density of ~30%. Nevertheless, shear stresses in excess of 70kPa could still be achieved under natural air cooling conditions. Special attention was given to the forces exhibited by a pole-piece, and it was shown that both the average and dynamic forces are affected by the load condition. Futhermore, both the PP and PPR forces were seen to increase when adopting the proposed topology. Interesting future research could be conducted to prototype PDDs with alternative windings.

The use of 3D FEA has been employed to optimise of key parameters of an AMG. The reduction of the air gap was explored to improve torque transmission, with 0.5mm found to be feasible in small scale prototypes. Furthermore, the resultant magnetic force, which the PPs are subjected to, increases significantly for smaller airgaps, and is limited by the mechanical strength of the PP material. Diminishing returns are seen when reducing the inner-diameter to outer-diameter ratio, λ below 0.5. Increasing λ above 0.5 reduces the torque, shear stress and force per PP but increases torque per magnet volume. As such λ of 0.7 was chosen as an effective compromise between torque output, force on the PP and magnet volume.

The PP in the AMG is required to perform magnetically and mechanically, by both modulating the field in a low loss manner and withstand the magnetic forces it is subjected to. A preferable solution to the magnetic challenge is to use SMC PPs, due to their isotropic properties and their ability to accommodate the 3D nature of the flux. As such the PP shape was investigated in structures which are simple to construct and have no supporting material in the active region. It was also shown that using a trapezoidal PP requires an increase in axial thickness beyond the optimal electromagnetic sizing to reduce stress in the SMC to an acceptable level. A cylindrical PP provides a more optimal solution in terms of reducing stress in the PP and transmitted torque capability. The shape further benefits as no torque about its own axis exists and both PP and PPR hub manufacture are significantly simplified. It is interesting to note that the use of cylindrical PPs seems more suited to AMGs than CMGs.

An AFPDD machine topology with two stators, two PPRs and a single HSR, was considered with the aim of significantly reducing the loading on the HSR bearings and to improve the robustness of the structure. As in the AMG, it is shown that the AFPDD with cylindrical SMC PPs gives improved electromagnetic performance compared to trapezoidal PPs. When designing the AFPDD it is seen that a compromise between MG output torque and fundamental flux density at the stator bore in order to limit the electric loading, must be sought. The optimised AFPDD stator design exhibited predicted rated efficiency and power factor of 95% and 0.88, respectively. However, the limitations imposed by the available SMC blanks limited slot depth to ~14mm and as such limited the stator predicted maximum efficiency to ~90%.

Thermal analysis of the AFPDD was employed to ensure no performance degradation would occur during normal operation. Good agreement was shown between the lumped

parameter and 3D finite element analysis. Furthermore, the thermal analysis informed the specification of winding and magnets materials.

A prototype was designed and manufactured to investigate the performance of the AFPDD and presented several significant challenges. To enable production of the AFPDD a full CAD model including working drawings was developed. Novel methods were tested for assembling SMC components to ease manufacture, with a combination of mechanical fastening and adhesive found to be most favourable. The dual rotor assembly verified previous predictions regarding the applicability of cylindrical PPs with no circumferential support. The pull-out torque of the prototype was found to be 24.5Nm and within 3% of the predicted value of 25.2Nm. No-load tests on the AFPDD have shown that a significant loss component, not initially considered in the analysis, exists. However, following further analysis, it is shown that due to leakage flux, significant eddy currents are induced in the aluminium structure which supports the PPs. It is also shown that by adopting a higher electrical resistivity non-magnetic stainless steel, these losses can be significantly reduced. Nevertheless, good agreement exists between measured and predicted EMF and pull-out torque.

Although a prototype was manufactured, its performance over the intended operating range could not be fully demonstrated due to the no-load loss characteristic. As such future work to fully realise the AFPDD concept could include extensive analysis of structures with the aim of reducing this effect. Operation of this AFPDD topology under motoring conditions using sensorless control could be investigated as an appealing method of utilising the robust structure of the AFPDD.

The scalability of SMC PPs within larger AMGs and AFPDDs would be of potential interest. An alternative to the SMC stator core material is tape wound laminations,

which although not appropriate to prototype machines, could be attractive to future designs of larger AFPDDs. Furthermore, the manufacture of larger AFPDDs could also benefit from research regarding the arrangement in which multiple AFPDD modules are arranged along a shaft to form a single machine. This could be conducted via the formation of analytical expressions or using FEA studies.

In summary, though challenges remain with the implementation of the novel AFPDD structure, it showed significant potential as a robust, simple to manufacture magnetically geared electrical machine. Both the radial and axial topologies of the PDD investigated were adapted to exhibit the required attributes of a magnetically geared electrical machine suitable for mass manufacture.

Appendix

Appendix I. Material Properties

The material properties, were appropriate, are given at 20°C.

Material	***Property***	***Value***	***Units***
Magnetic Material – N38EH	Remanence	1.25	T
	Relative recoil permeability	1.05	
	Resistivity	180	μΩ.cm
	Density	7500	$kg.m^{-3}$
	Isotropic Thermal Conductivity	9	W / m k
Soft Magnetic Composite (SPM)	Resistivity	280	μΩ.m
	Density	7450	$kg.m^{-3}$
	Tensile Rupture Strength (TRS)	80	MPa
	Relative Permeability	Non-linear (See Figure 1.4)	
	Isotropic Thermal Conductivity	25	W / m k
Low Carbon Steel (M270-35A)	Resistivity	52	μΩ.cm
	Density	7800	$kg.m^{-3}$
	Relative Permeability	Non-linear (See Figure 1.4)	
	Thermal Conductivity	50	W / m k
Aluminium	Resistivity	2.8	μΩ.cm
	Density	2800	$kg.m^{-3}$
	Relative Permeability	1.000022	
	Isotropic Thermal Conductivity	140	W / m k
Stainless Steel (Type 316)	Resistivity	74	μΩ.cm
	Density	8000	$kg.m^{-3}$
	Relative Permeability	1.008	
Copper	Resistivity	1.68	μΩ.cm
	Temperature Coefficient of Resistivity	0.0039	
	Density	8940	$kg.m^{-3}$
	Orthotropic Thermal Conductivity	200,2,2	W / m k

Appendix II. Manufacturing Drawings

The manufacturing drawings for each part used in the production of the AFPDD prototype are contained within the following sections:

Section	***Part***
Appendix I	AFPDD Cross Section
Appendix II. HSR	HSR_Magnet
	HSR_Nut
	HSR_Nut_Tooling
	HSR_Dowel
	HSR_Rotor_Inner
	HSR_Rotor_Outer
	HSR_ Outer_Band
	Shaft
	HSR_with_shaft_and_cap
Appendix III. PPR	PPR_Pole
	PPR_Blank_Pin
	PPR_Hub
	PPR_Outer_Band
	PPR_Stud
	PPR_Assembly
Appendix IV. Stator	ST_Magnet_NS
	ST_Magnet_NS_Thick
	ST_Magnet_EW
	ST_Magnet_EW_Thick
	ST_Tooth_Trap_New
	ST_BI
	ST_Back_Plate_EE
	ST_Back_Plate_NEE
	ST_Stator_Assembly_with_ST_Magnets
Appendix V. Tooling	Winding_Tooling_1
	Winding_Tooling_2
	Winding_Tooling_3
	Assembly_Winding_Tooling
	Epox_Central_Tooling
	Epox_Outer_Tooling
	Mould_Assembly_Cross_Section

Appendix II-A. AFPDD Cross Section

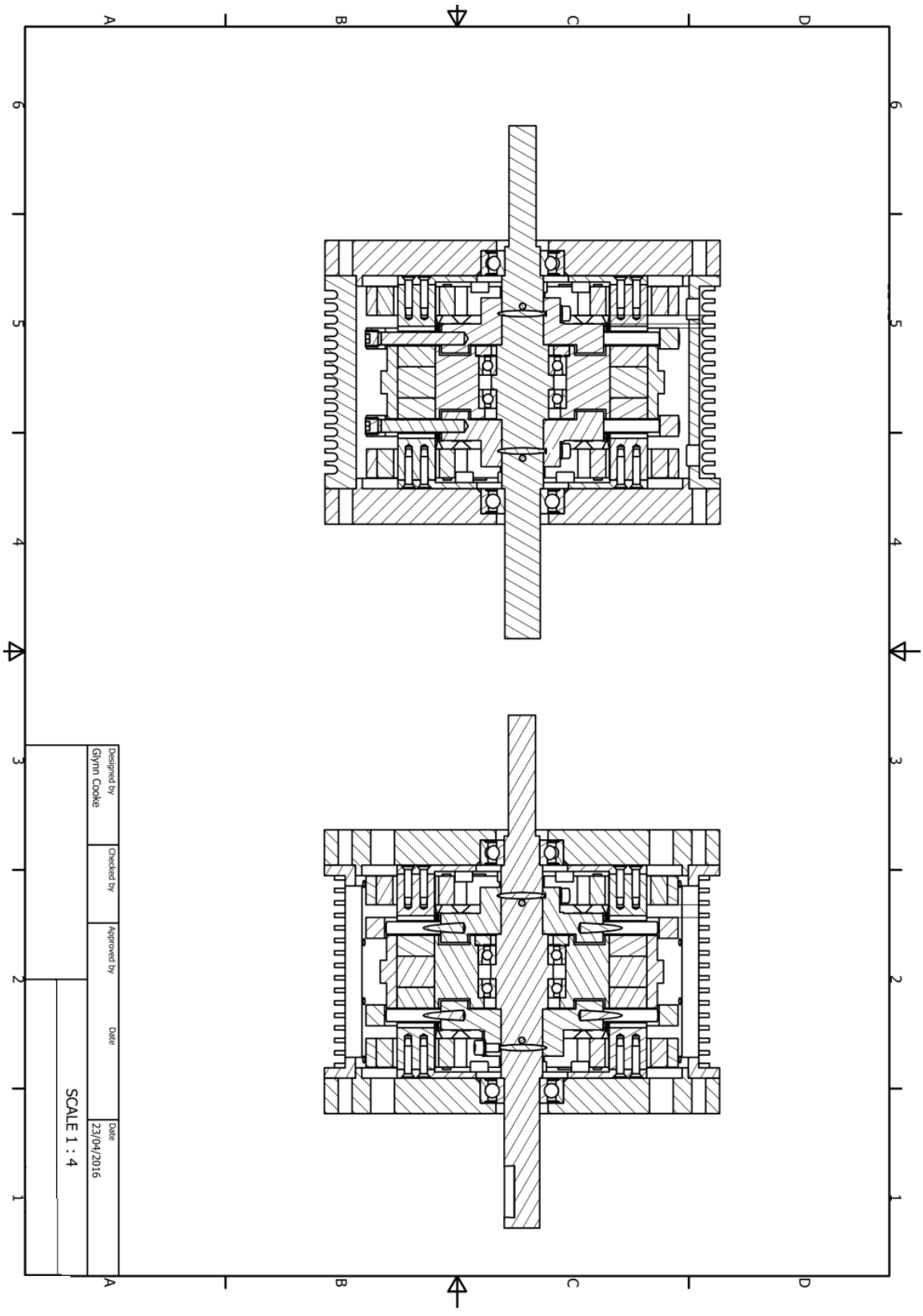

Appendix II-B. HSR

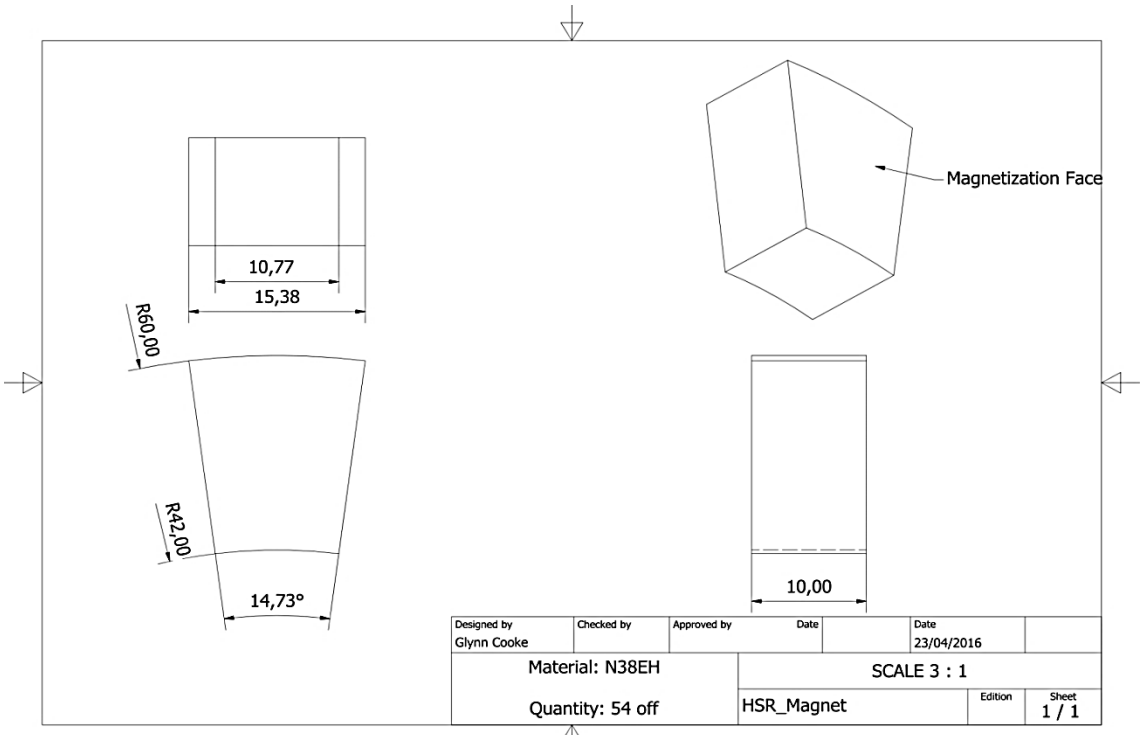

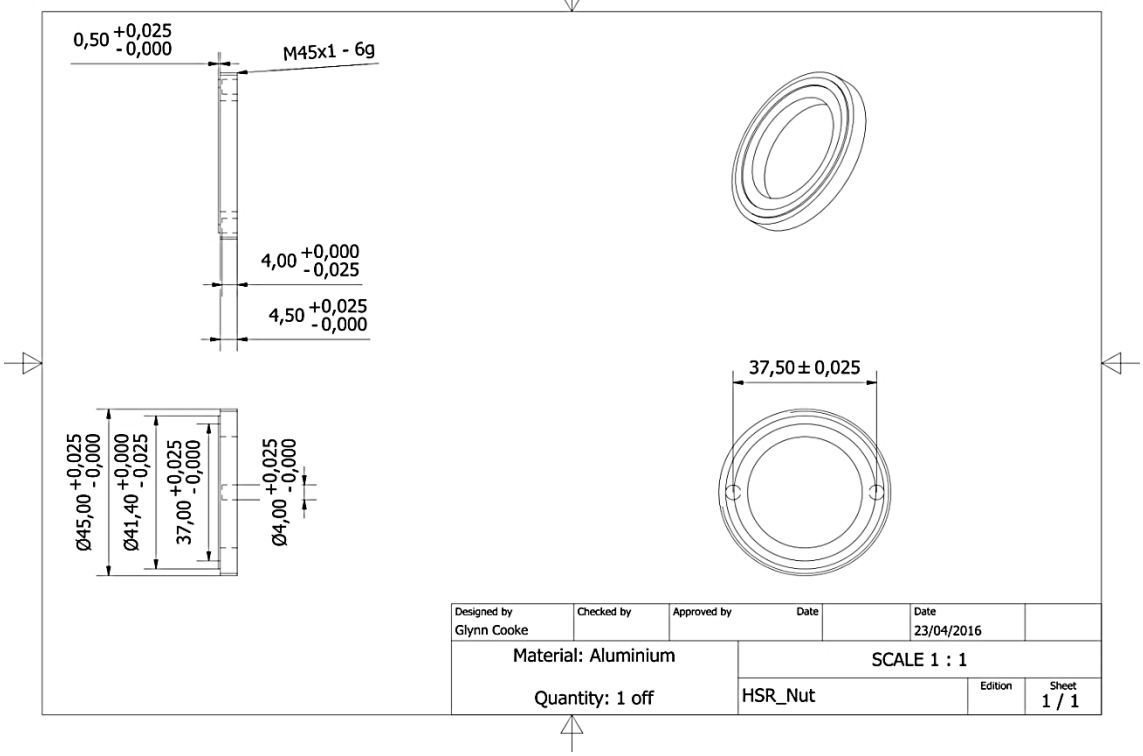

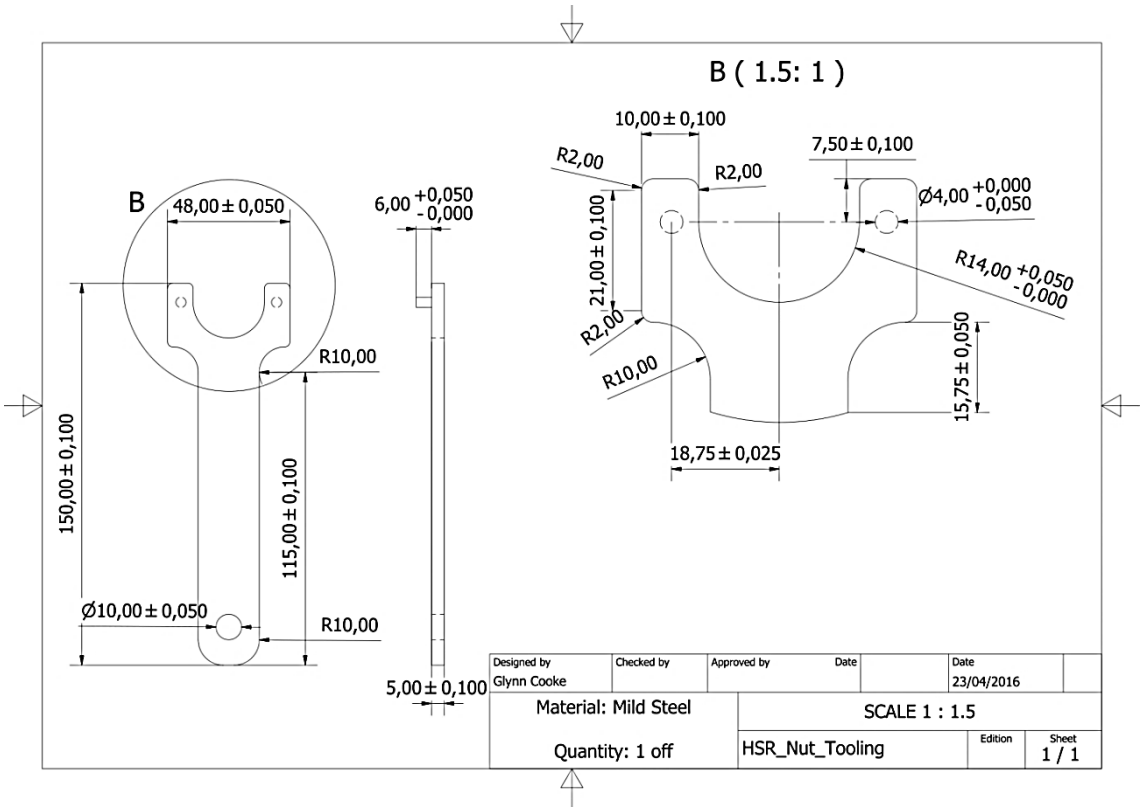
B (1.5: 1)
B
48,00 ± 0,050
6,00 +0,050 -0,000
R10,00
150,00 ± 0,100
115,00 ± 0,100
Ø10,00 ± 0,050
R10,00
5,00 ± 0,100
10,00 ± 0,100
R2,00
R2,00
7,50 ± 0,100
Ø4,00 +0,000 -0,050
21,00 ± 0,100
R14,00 +0,050 -0,000
R2,00
R10,00
15,75 ± 0,050
18,75 ± 0,025
Designed by
Glynn Cooke
Checked by
Approved by
Date
Date
23/04/2016
Material: Mild Steel
Quantity: 1 off
SCALE 1 : 1.5
HSR_Nut_Tooling
Edition
Sheet
1 / 1

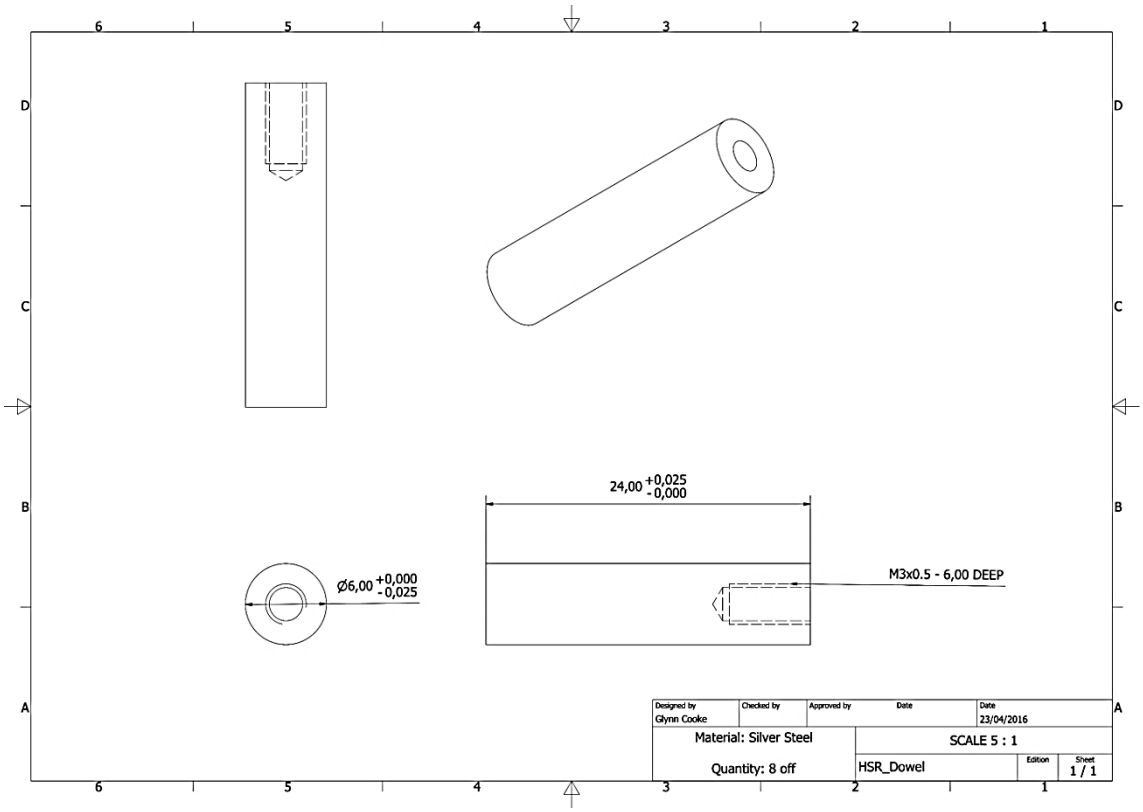
24,00 +0,025 -0,000
Ø6,00 +0,000 -0,025
M3x0.5 - 6,00 DEEP
Designed by
Glynn Cooke
Checked by
Approved by
Date
Date
23/04/2016
Material: Silver Steel
Quantity: 8 off
SCALE 5 : 1
HSR_Dowel
Edition
Sheet
1 / 1

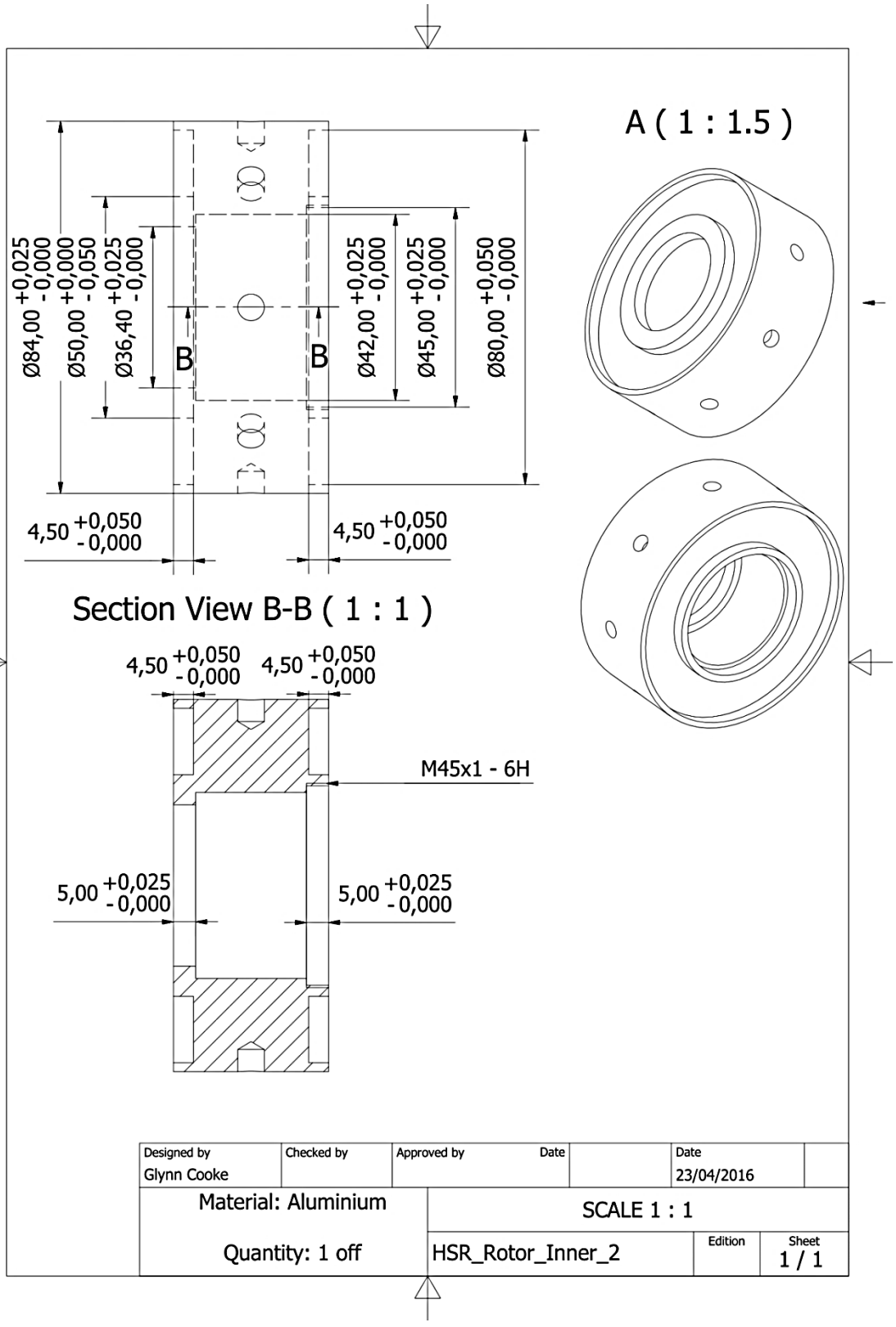
A (1 : 1.5)
Ø84,00 +0,025 -0,000
Ø50,00 +0,000 -0,050
Ø36,40 +0,025 -0,000
Ø42,00 +0,025 -0,000
Ø45,00 +0,025 -0,000
Ø80,00 +0,050 -0,000
B
B
4,50 +0,050 -0,000
4,50 +0,050 -0,000
Section View B-B (1 : 1)
4,50 +0,050 -0,000
4,50 +0,050 -0,000
M45x1 - 6H
5,00 +0,025 -0,000
5,00 +0,025 -0,000
Designed by
Glynn Cooke
Checked by
Approved by
Date
Date
23/04/2016
Material: Aluminium
Quantity: 1 off
SCALE 1 : 1
HSR_Rotor_Inner_2
Edition
Sheet
1 / 1

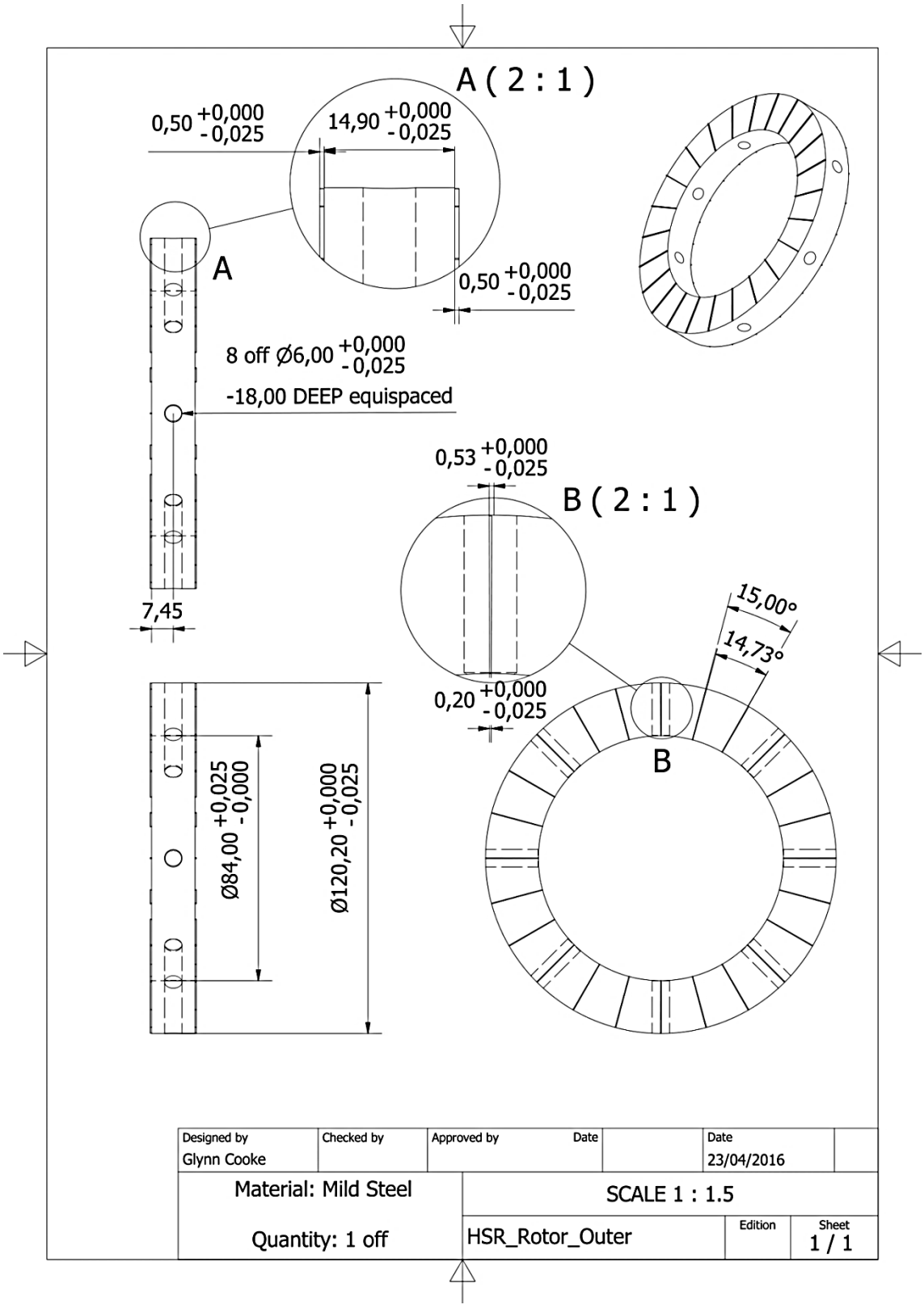
A (2 : 1)
0,50 +0,000 -0,025
14,90 +0,000 -0,025
A
0,50 +0,000 -0,025
8 off Ø6,00 +0,000 -0,025
-18,00 DEEP equispaced
7,45
0,53 +0,000 -0,025
B (2 : 1)
15,00°
14,73°
0,20 +0,000 -0,025
B
Ø84,00 +0,025 -0,000
Ø120,20 +0,000 -0,025
Designed by
Glynn Cooke
Checked by
Approved by
Date
Date
23/04/2016
Material: Mild Steel
Quantity: 1 off
SCALE 1 : 1.5
HSR_Rotor_Outer
Edition
Sheet
1 / 1

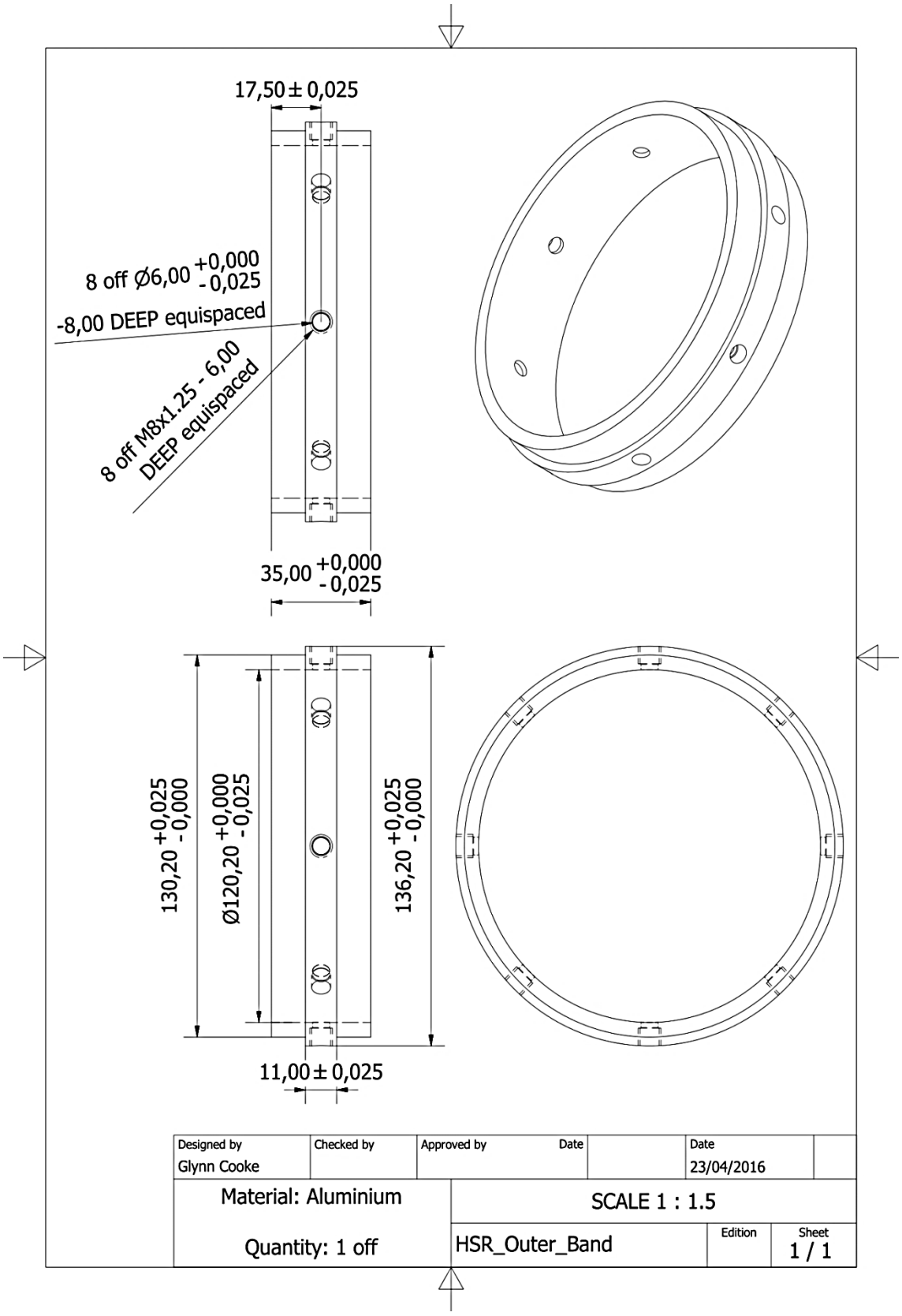
17,50 ± 0,025
8 off Ø6,00 +0,000 -0,025
-8,00 DEEP equispaced
8 off M8x1.25 - 6,00 DEEP equispaced
35,00 +0,000 -0,025
130,20 +0,025 -0,000
Ø120,20 +0,000 -0,025
136,20 +0,025 -0,000
11,00 ± 0,025
Designed by
Glynn Cooke
Checked by
Approved by
Date
Date
23/04/2016
Material: Aluminium
Quantity: 1 off
SCALE 1 : 1.5
HSR_Outer_Band
Edition
Sheet
1 / 1

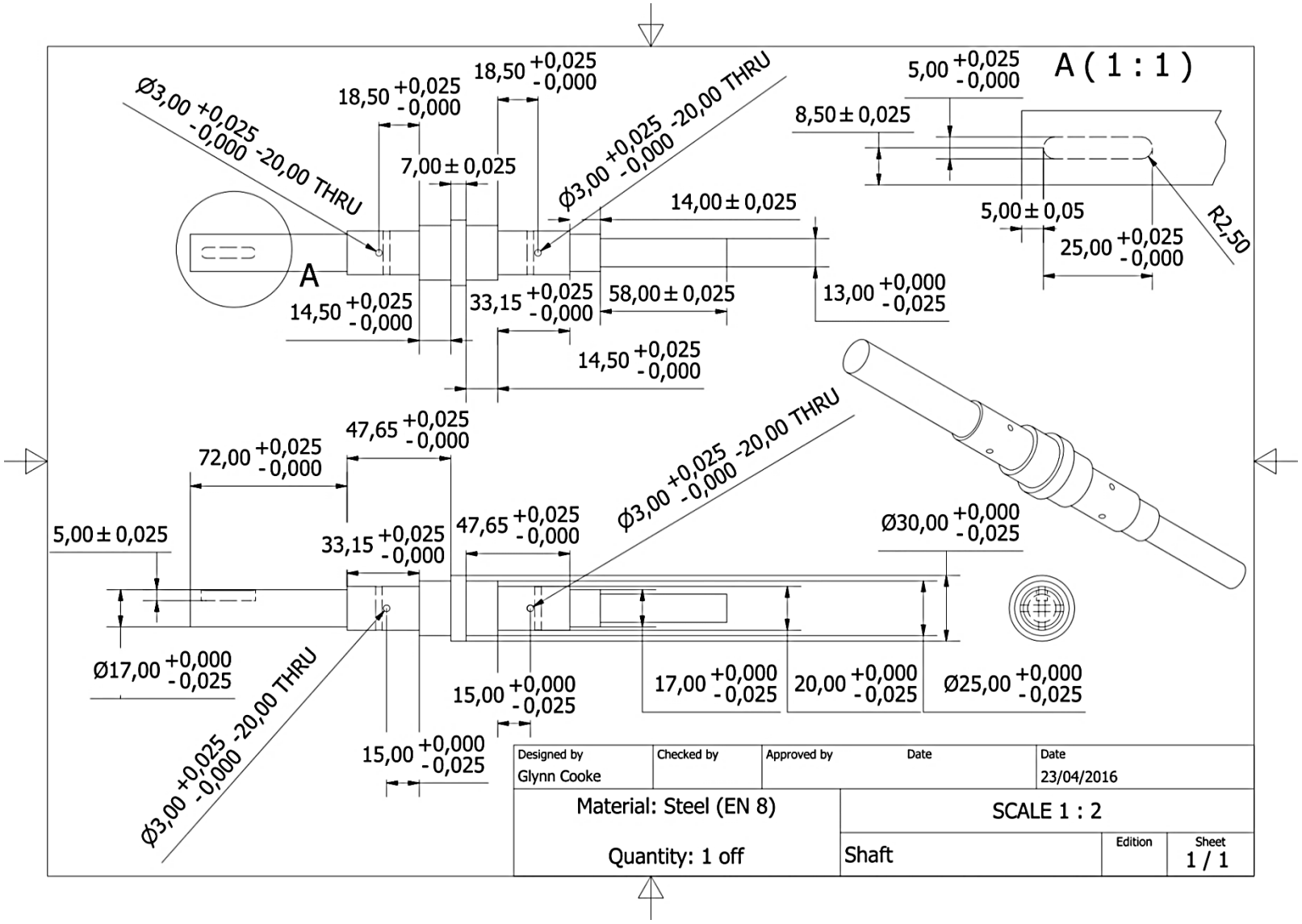
Ø3,00 +0,025 -0,000 -20,00 THRU
18,50 +0,025 -0,000
18,50 +0,025 -0,000
7,00 ± 0,025
Ø3,00 +0,025 -0,000 -20,00 THRU
14,00 ± 0,025
A
14,50 +0,025 -0,000
33,15 +0,025 -0,000
58,00 ± 0,025
13,00 +0,000 -0,025
14,50 +0,025 -0,000
5,00 +0,025 -0,000
A (1 : 1)
8,50 ± 0,025
5,00 ± 0,05
25,00 +0,025 -0,000
R2,50
47,65 +0,025 -0,000
72,00 +0,025 -0,000
Ø3,00 +0,025 -0,000 -20,00 THRU
5,00 ± 0,025
33,15 +0,025 -0,000
47,65 +0,025 -0,000
Ø30,00 +0,000 -0,025
Ø17,00 +0,000 -0,025
15,00 +0,000 -0,025
17,00 +0,000 -0,025
20,00 +0,000 -0,025
Ø25,00 +0,000 -0,025
Ø3,00 +0,025 -0,000 -20,00 THRU
15,00 +0,000 -0,025
Designed by
Glynn Cooke
Checked by
Approved by
Date
Date
23/04/2016
Material: Steel (EN 8)
Quantity: 1 off
SCALE 1 : 2
Shaft
Edition
Sheet
1 / 1

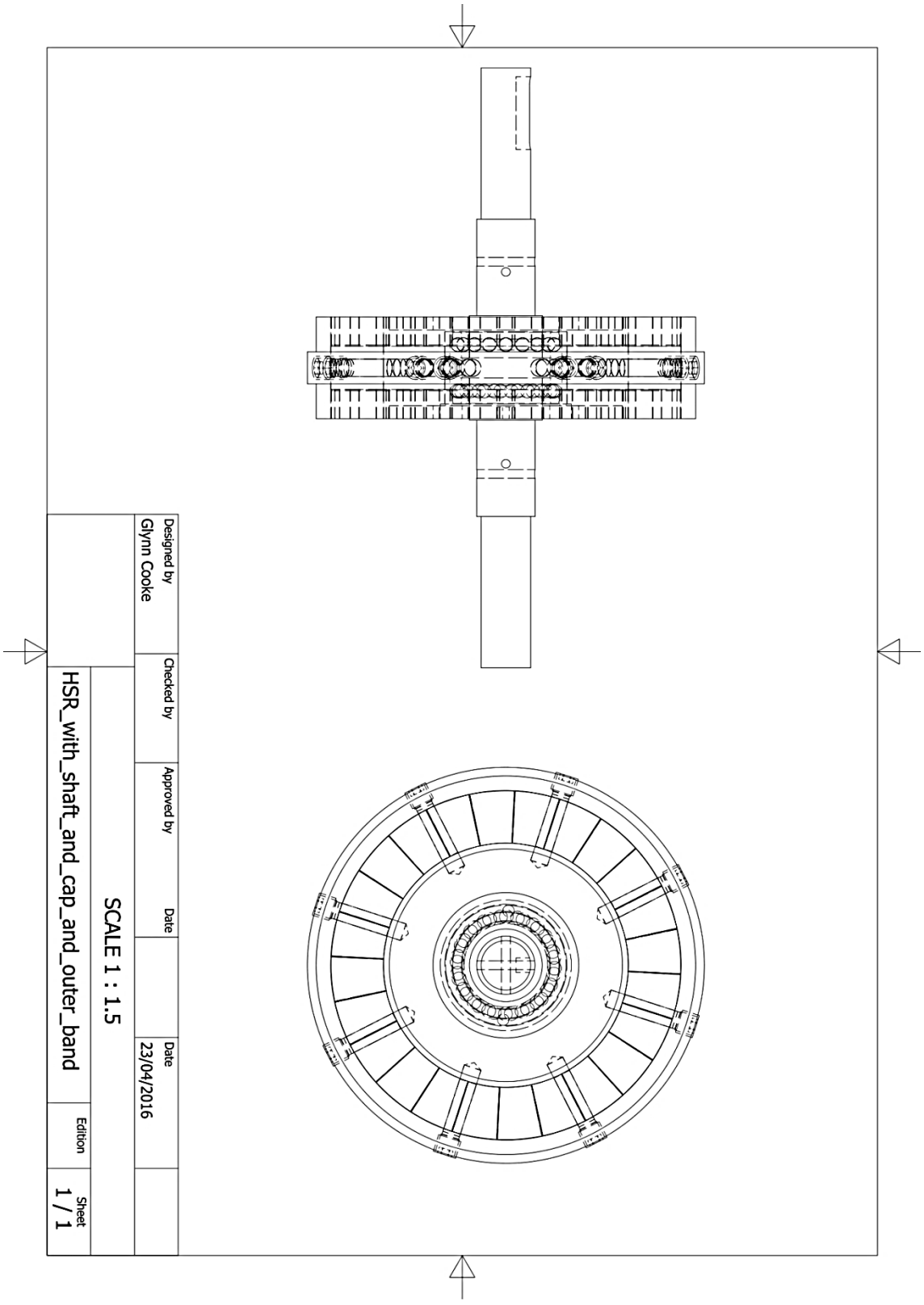
Designed by
Glynn Cooke
Checked by
Approved by
Date
Date
23/04/2016
SCALE 1 : 1.5
HSR_with_shaft_and_cap_and_outer_band
Edition
Sheet
1 / 1

Appendix II-C. PPR

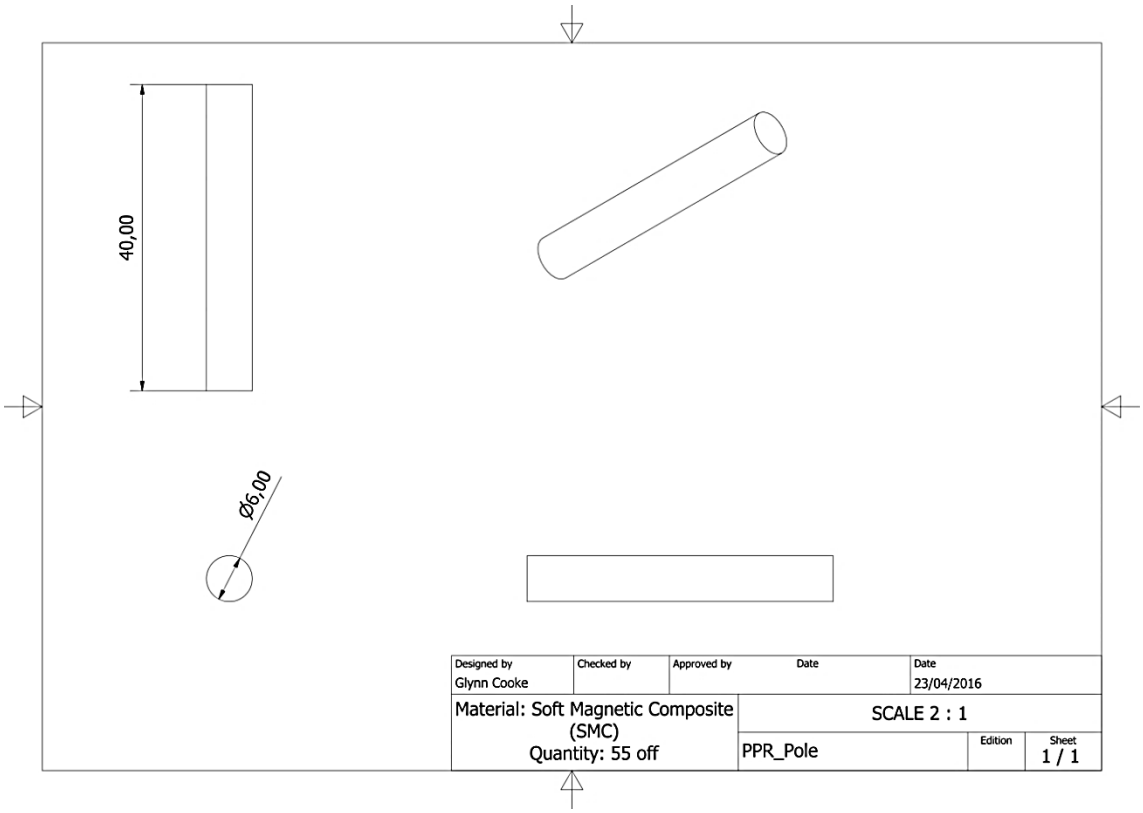

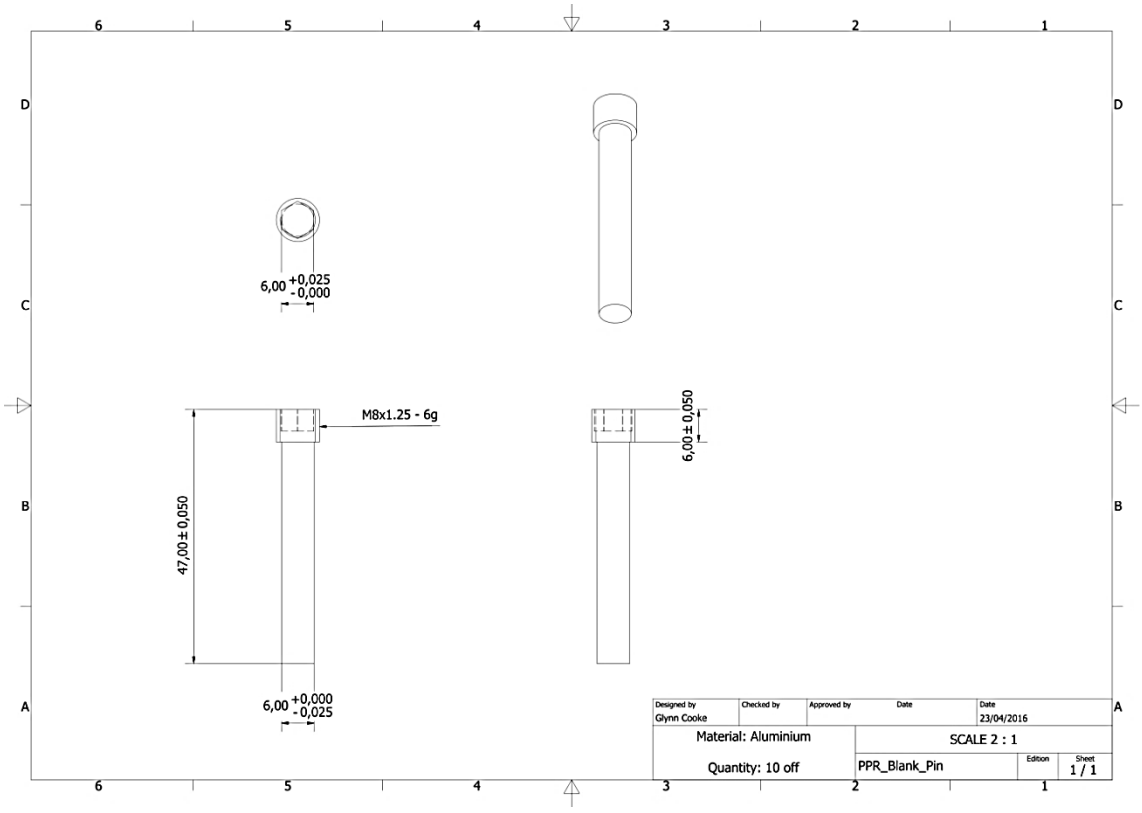

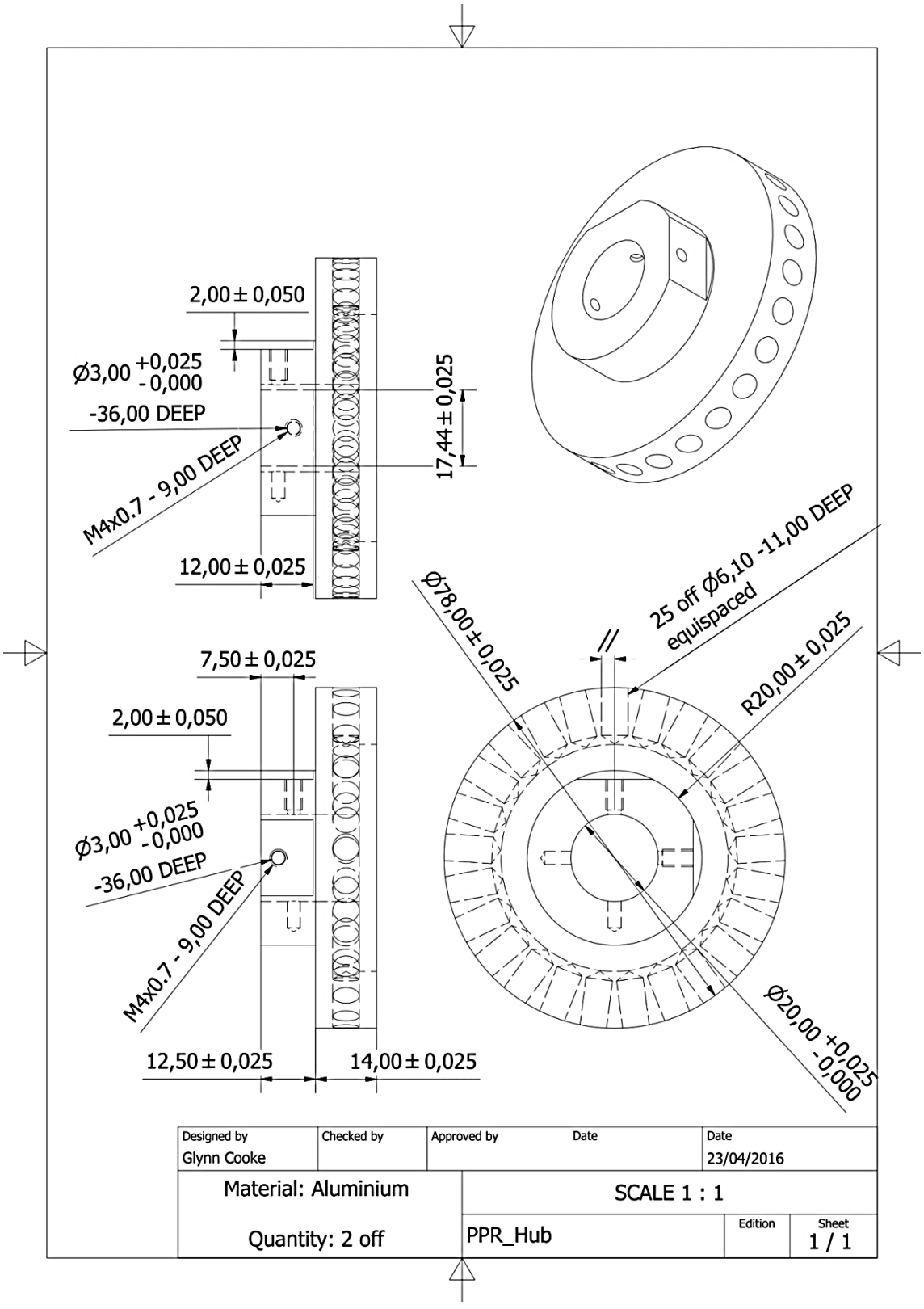
2,00 ± 0,050
Ø3,00 +0,025 -0,000
-36,00 DEEP
M4x0.7 - 9,00 DEEP
17,44 ± 0,025
12,00 ± 0,025
7,50 ± 0,025
2,00 ± 0,050
Ø3,00 +0,025 -0,000
-36,00 DEEP
M4x0.7 - 9,00 DEEP
12,50 ± 0,025
14,00 ± 0,025
Ø78,00 ± 0,025
25 off Ø6,10 -11,00 DEEP equispaced
R20,00 ± 0,025
Ø20,00 +0,025 -0,000
Designed by
Glynn Cooke
Checked by
Approved by
Date
Date
23/04/2016
Material: Aluminium
Quantity: 2 off
SCALE 1 : 1
PPR_Hub
Edition
Sheet
1 / 1

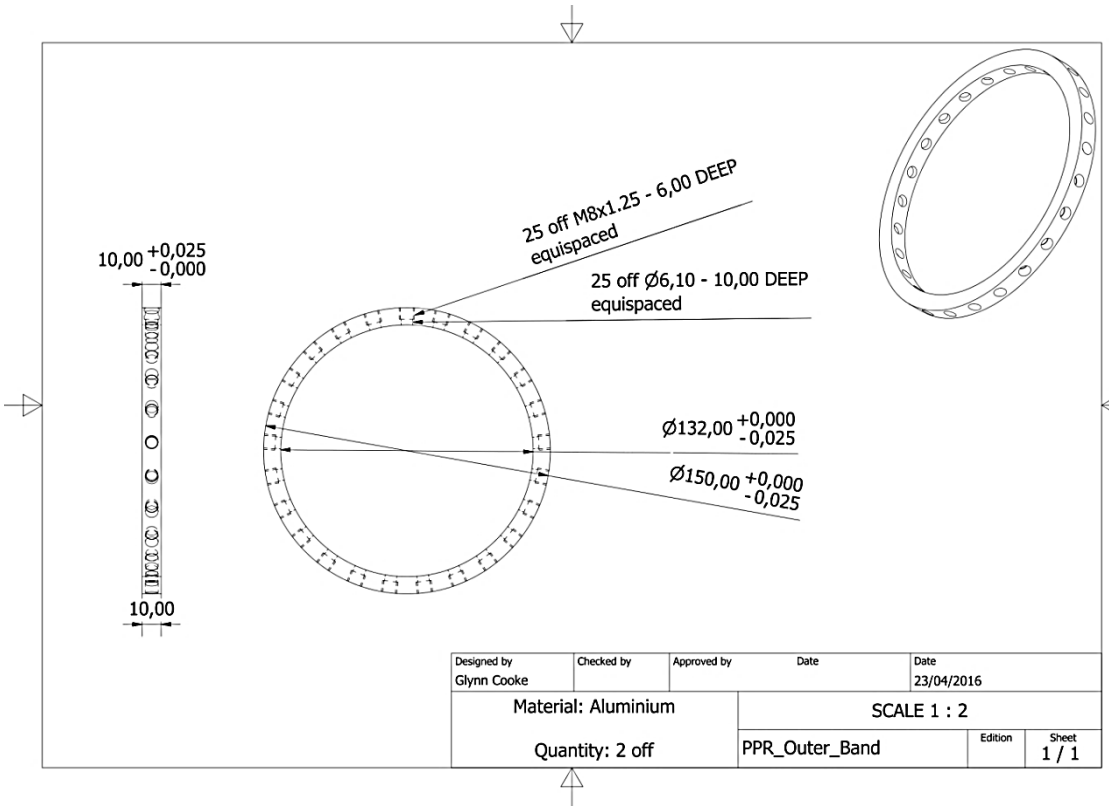
10,00 +0,025
-0,000
10,00
25 off M8x1.25 - 6,00 DEEP
equispaced
25 off Ø6,10 - 10,00 DEEP
equispaced
Ø132,00 +0,000
-0,025
Ø150,00 +0,000
-0,025
Designed by
Glynn Cooke
Checked by
Approved by
Date
Date
23/04/2016
Material: Aluminium
Quantity: 2 off
SCALE 1 : 2
PPR_Outer_Band
Edition
Sheet
1 / 1

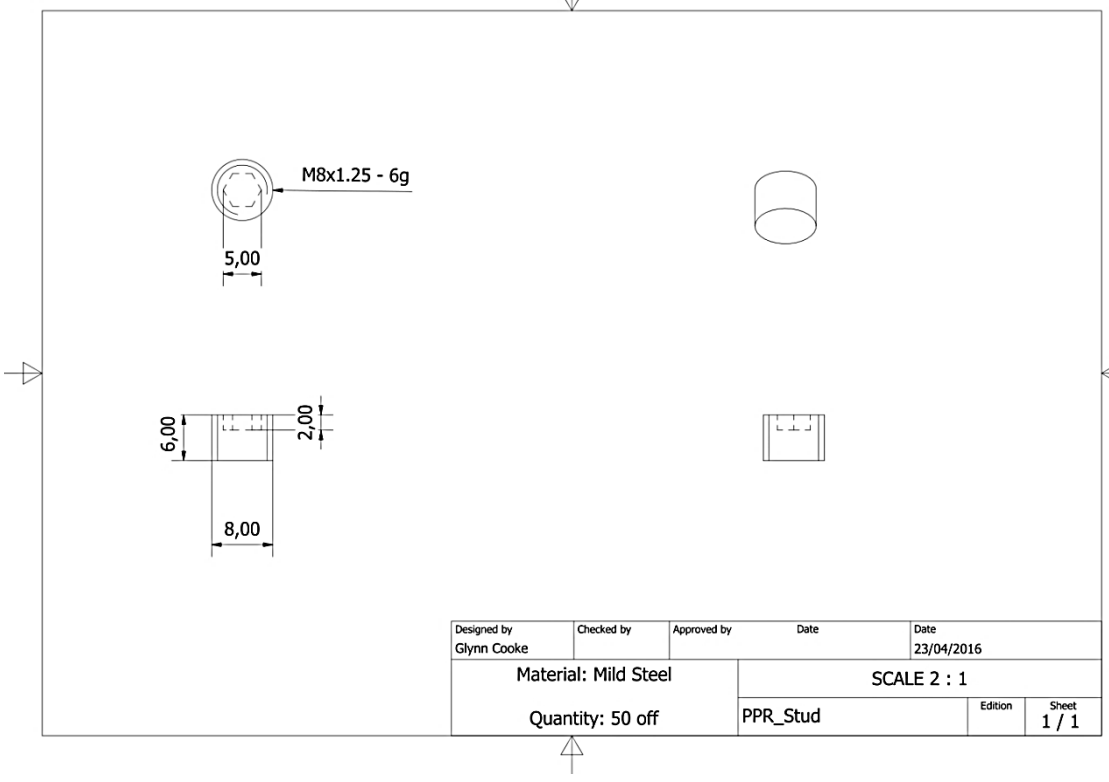
M8x1.25 - 6g
5,00
6,00
2,00
8,00
Designed by
Glynn Cooke
Checked by
Approved by
Date
Date
23/04/2016
Material: Mild Steel
Quantity: 50 off
SCALE 2 : 1
PPR_Stud
Edition
Sheet
1 / 1

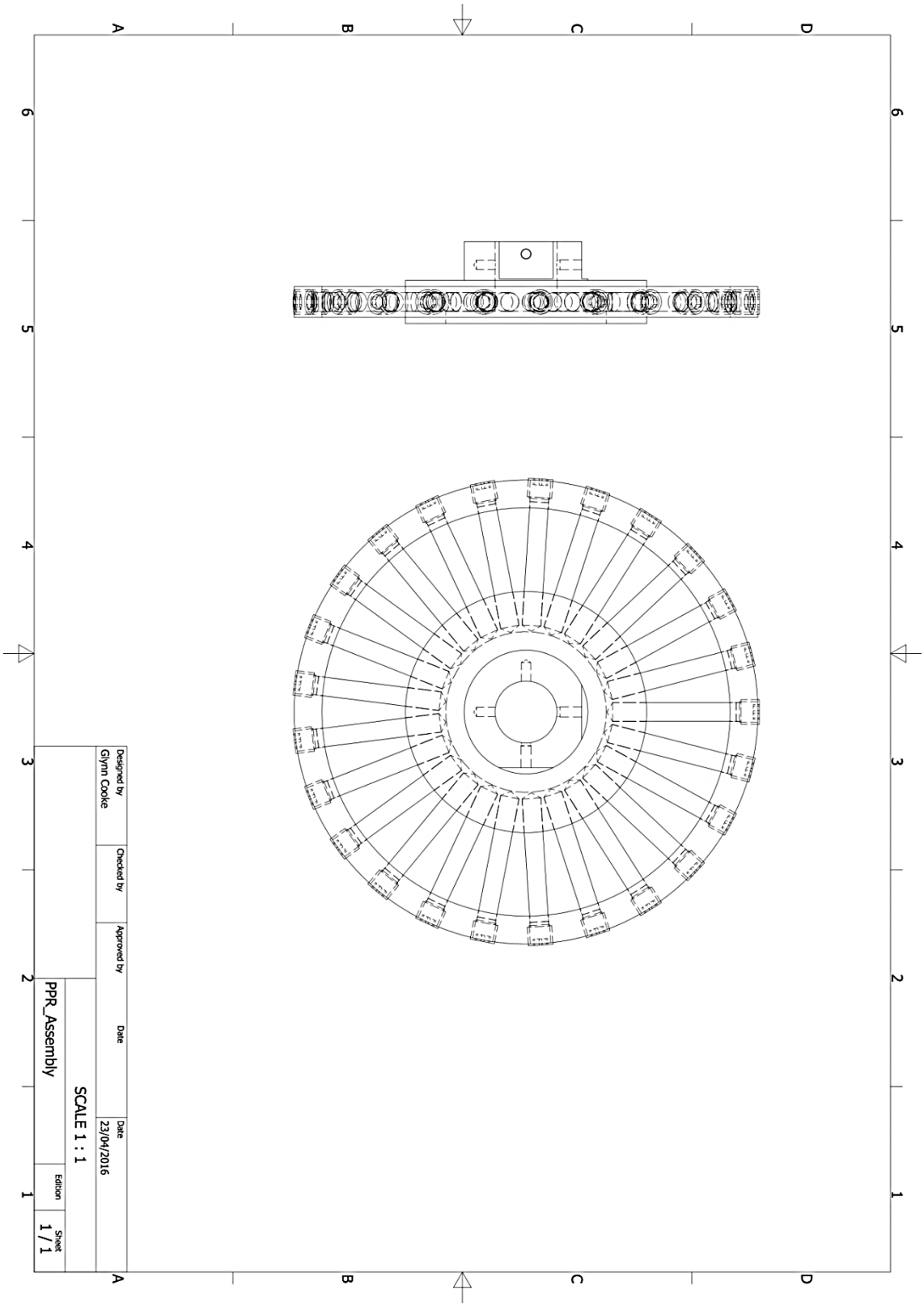
A
B
C
D
1
2
3
4
5
6
Designed by
Glynn Cooke
Checked by
Approved by
Date
Date
23/04/2016
PPR_Assembly
SCALE 1 : 1
Edition
Sheet
1 / 1

Appendix II-D. Stator

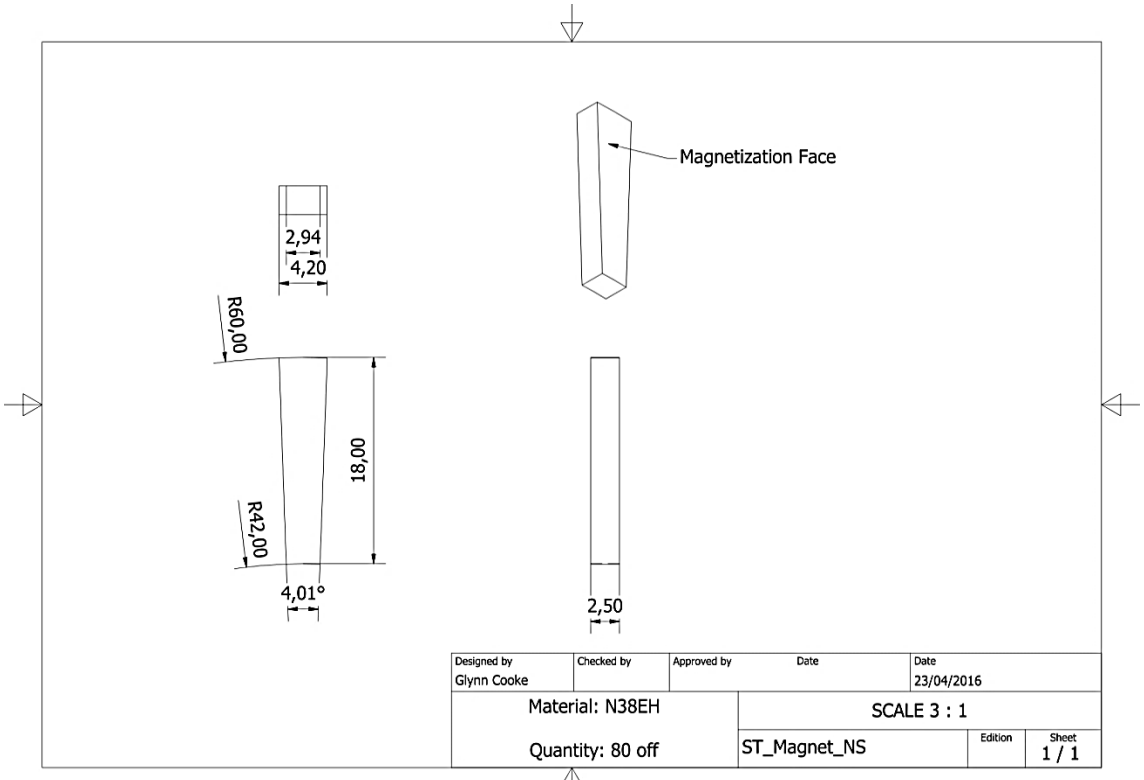

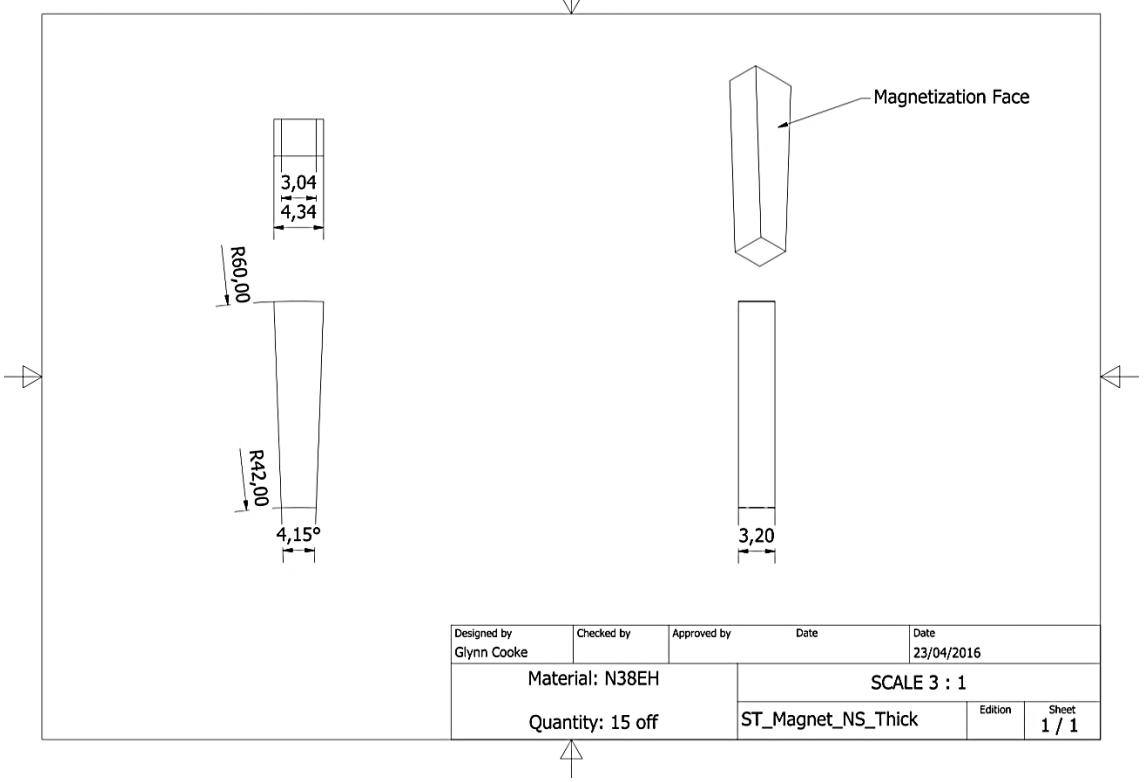

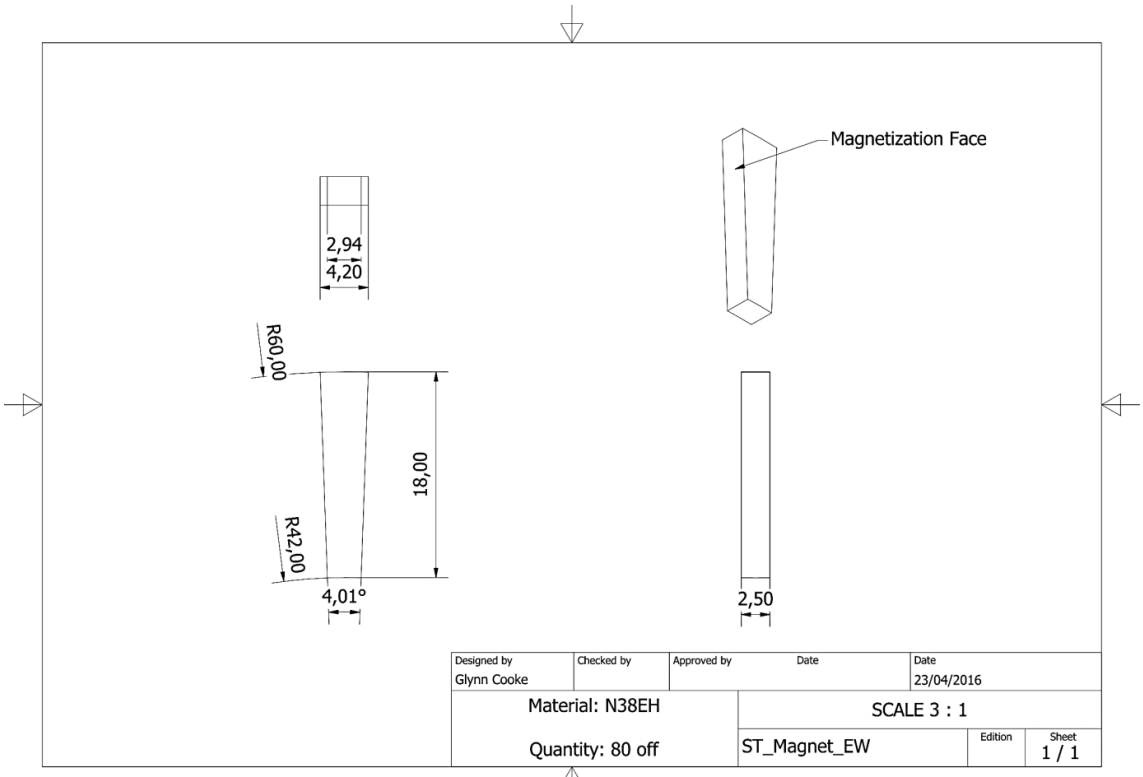
Magnetization Face
2,94
4,20
R60,00
18,00
R42,00
4,01°
2,50
Designed by
Glynn Cooke
Checked by
Approved by
Date
Date
23/04/2016
Material: N38EH
Quantity: 80 off
SCALE 3 : 1
ST_Magnet_EW
Edition
Sheet
1 / 1

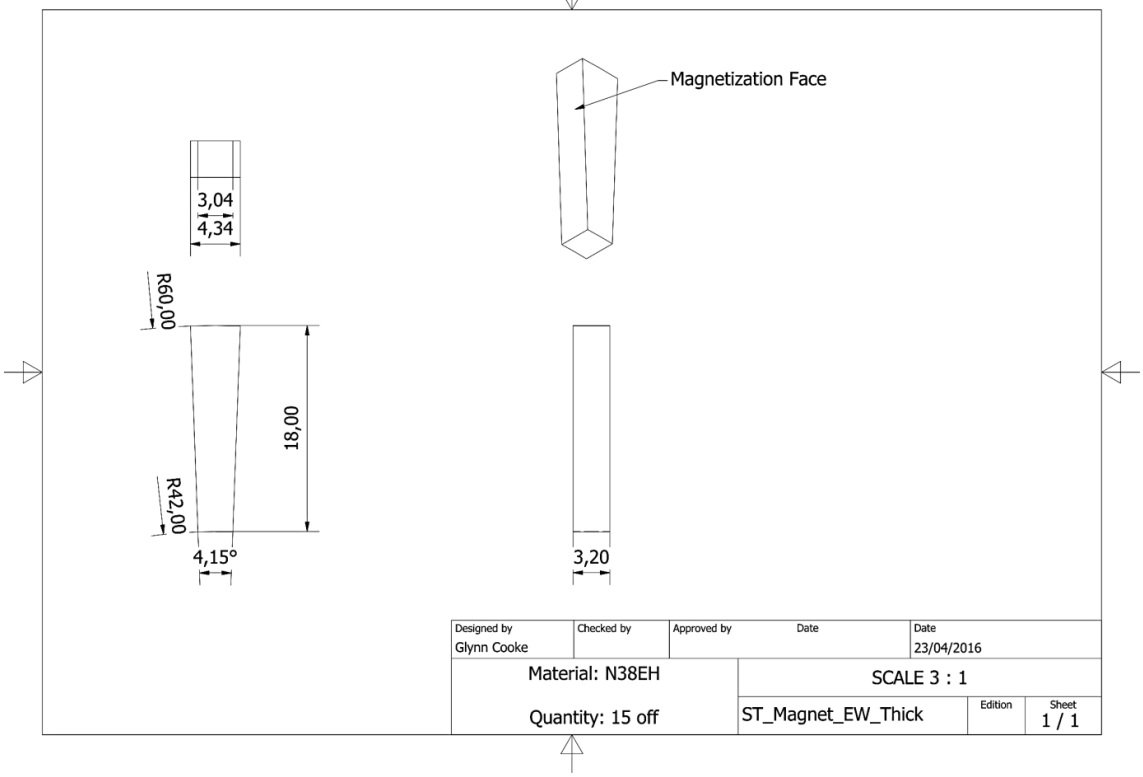
Magnetization Face
3,04
4,34
R60,00
18,00
R42,00
4,15°
3,20
Designed by
Glynn Cooke
Checked by
Approved by
Date
Date
23/04/2016
Material: N38EH
Quantity: 15 off
SCALE 3 : 1
ST_Magnet_EW_Thick
Edition
Sheet
1 / 1

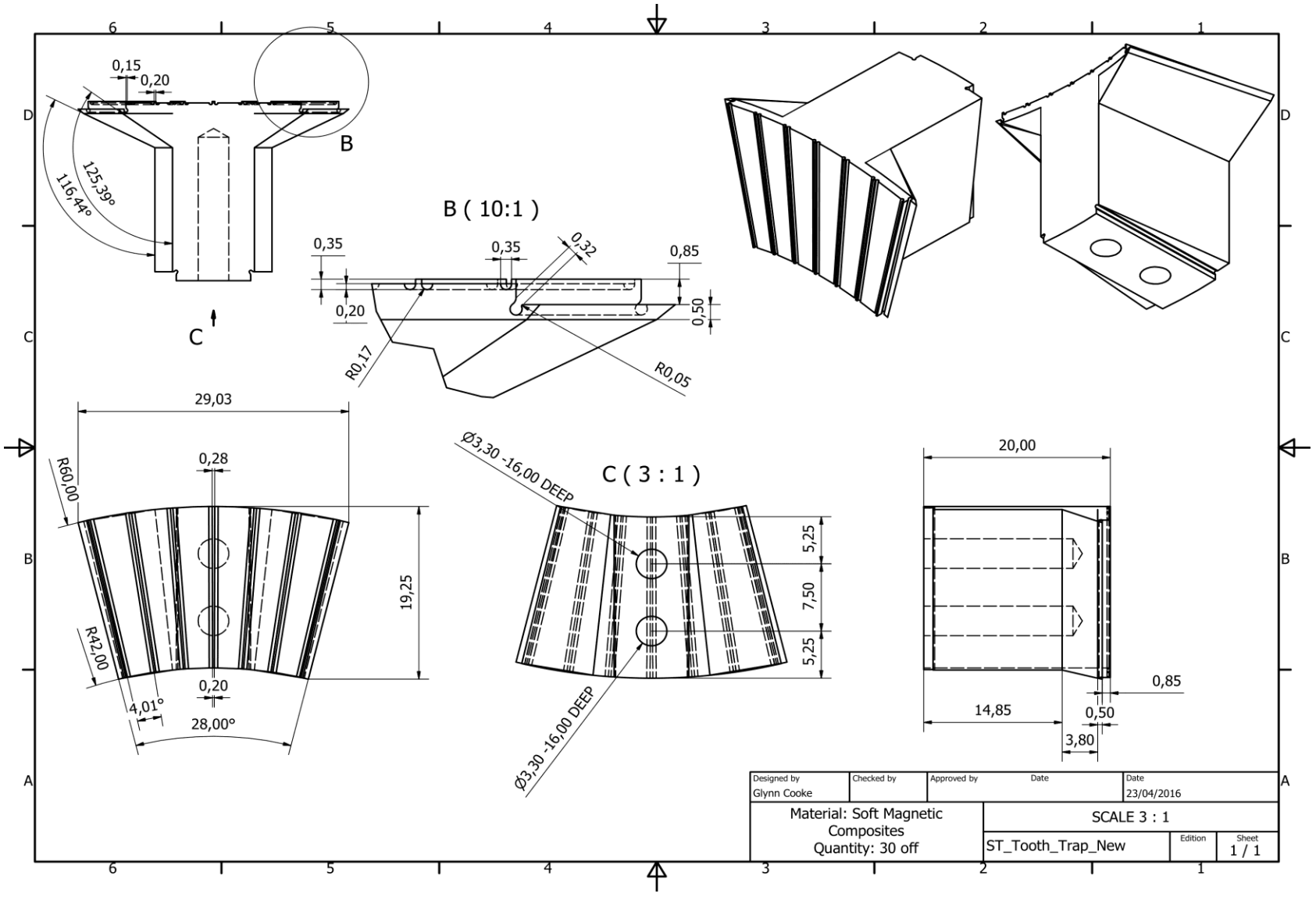
0,15
0,20
125,39°
116,44°
B
B (10:1)
0,35
0,35
0,32
0,85
0,20
0,50
R0,17
R0,05
C
C (3 : 1)
29,03
0,28
R60,00
19,25
R42,00
0,20
4,01°
28,00°
Ø3,30 -16,00 DEEP
5,25
7,50
5,25
Ø3,30 -16,00 DEEP
20,00
0,85
14,85
0,50
3,80
Designed by
Glynn Cooke
Checked by
Approved by
Date
Date
23/04/2016
Material: Soft Magnetic Composites
Quantity: 30 off
SCALE 3 : 1
ST_Tooth_Trap_New
Edition
Sheet
1 / 1

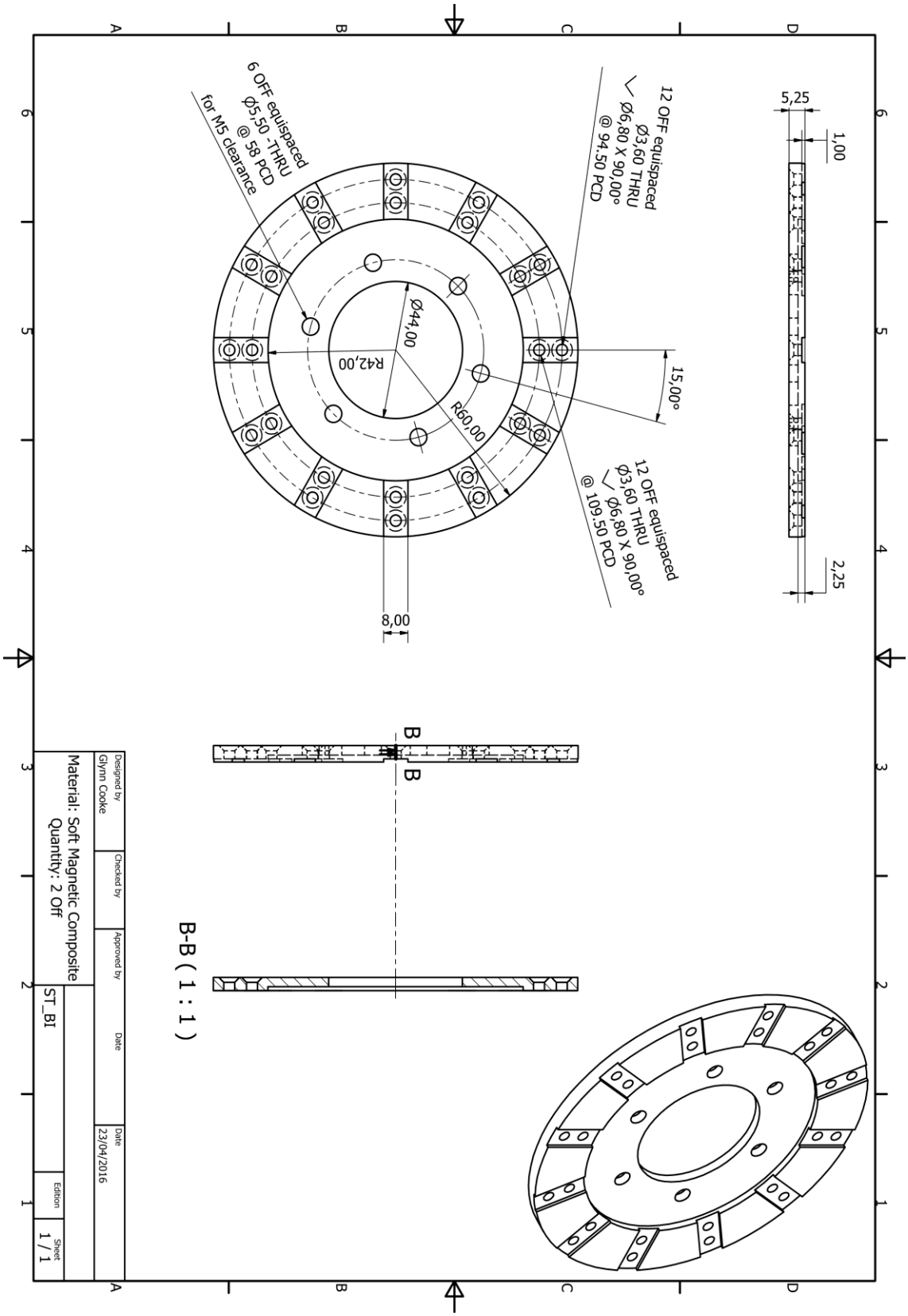
5,25
1,00
2,25
12 OFF equispaced
Ø3,60 THRU
Ø6,80 X 90,00°
@ 94,50 PCD
6 OFF equispaced
Ø5,50 -THRU
@ 58 PCD
for M5 clearance
Ø44,00
R42,00
R60,00
15,00°
12 OFF equispaced
Ø3,60 THRU
Ø6,80 X 90,00°
@ 109,50 PCD
8,00
B
B
B-B (1 : 1)
Designed by
Glynn Cooke
Checked by
Approved by
Date
Date
23/04/2016
Material: Soft Magnetic Composite
Quantity: 2 Off
ST_BI
Edition
Sheet
1 / 1

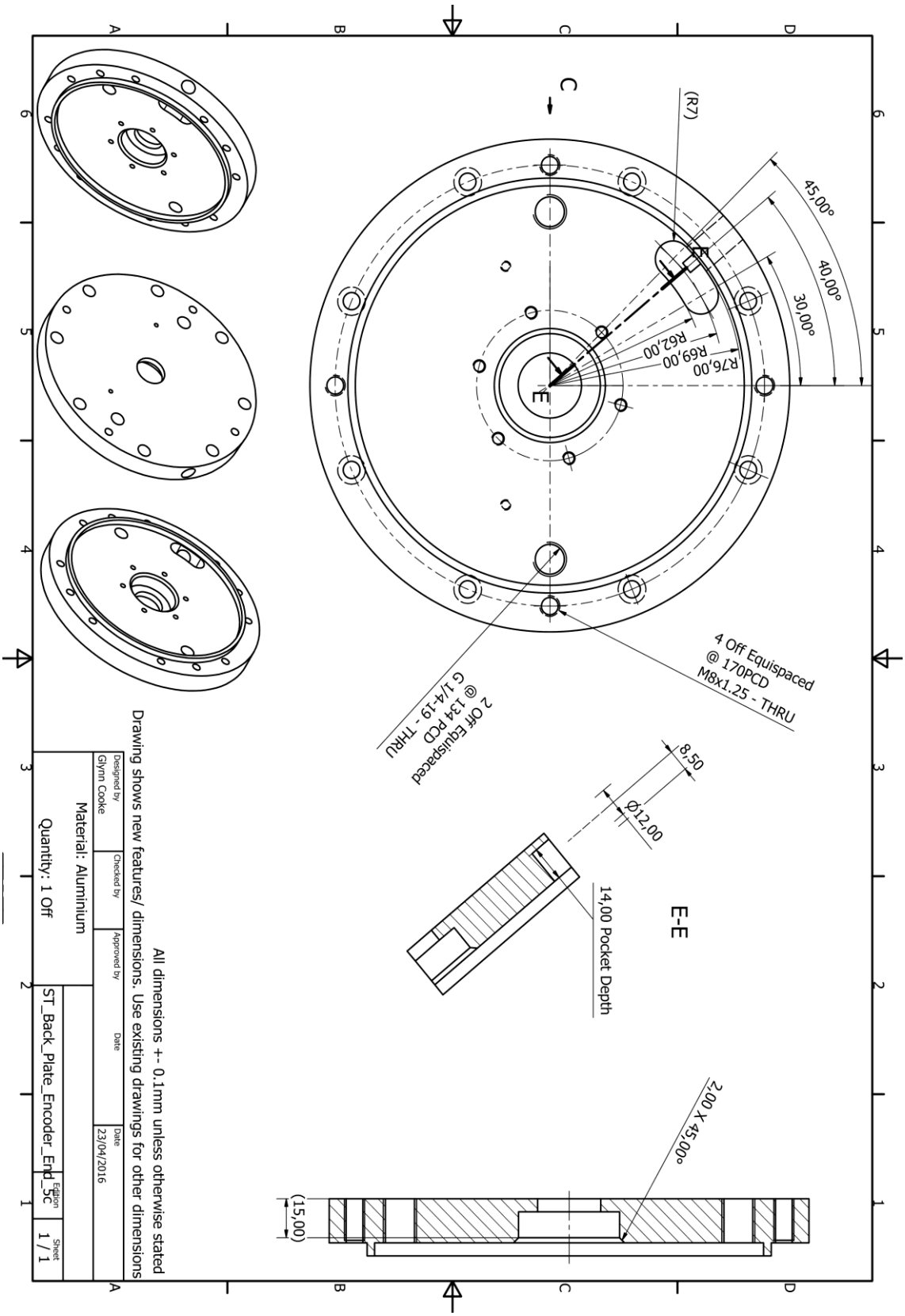
C
(R7)
45,00°
40,00°
30,00°
R76,00
R69,00
R62,00
E
4 Off Equispaced
@ 170PCD
M8x1,25 - THRU
2 Off Equispaced
@ 134 PCD
G 1/4-19 - THRU
8,50
Ø12,00
14,00 Pocket Depth
E-E
2,00 X 45,00°
(15,00)
All dimensions +- 0.1mm unless otherwise stated
Drawing shows new features/ dimensions. Use existing drawings for other dimensions
Designed by
Glynn Cooke
Checked by
Approved by
Date
23/04/2016
Material: Aluminium
Quantity: 1 Off
ST_Back_Plate_Encoder_End_5C
Edition
Sheet
1 / 1

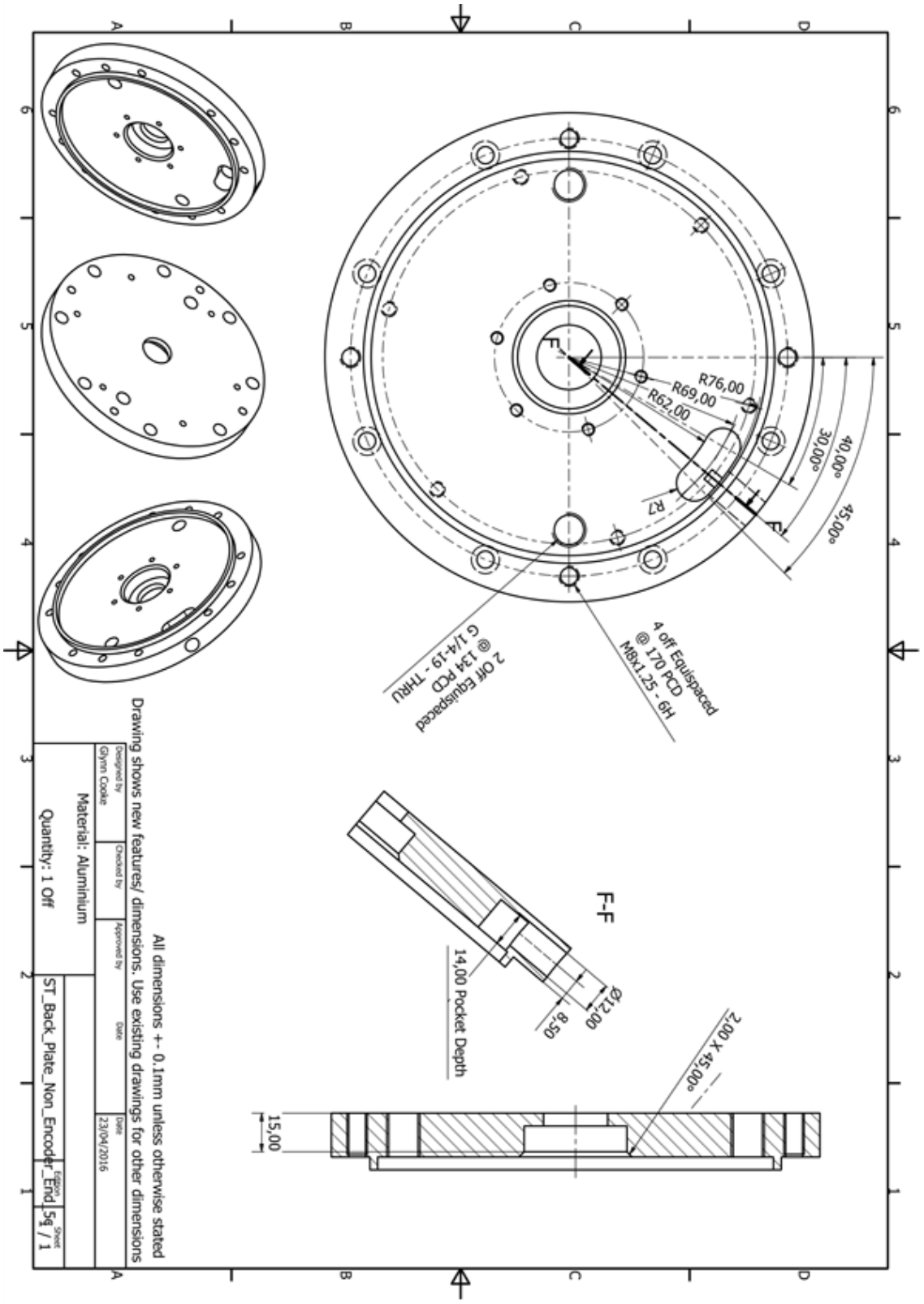
R76,00
R69,00
R62,00
R7
45,00°
40,00°
30,00°
4 off Equispaced
@ 170 PCD
M8x1.25 - 6H
2 Off Equispaced
@ 134 PCD
G 1/4-19 - THRU
F-F
14,00 Pocket Depth
Ø12,00
8,50
2,00 X 45,00°
15,00
All dimensions +- 0.1mm unless otherwise stated
Drawing shows new features/ dimensions. Use existing drawings for other dimensions
Designed by
Glynn Cooke
Checked by
Approved by
Date
23/04/2016
Material: Aluminium
Quantity: 1 Off
ST_Back_Plate_Non_Encoder_End
Sheet
Sq / 1

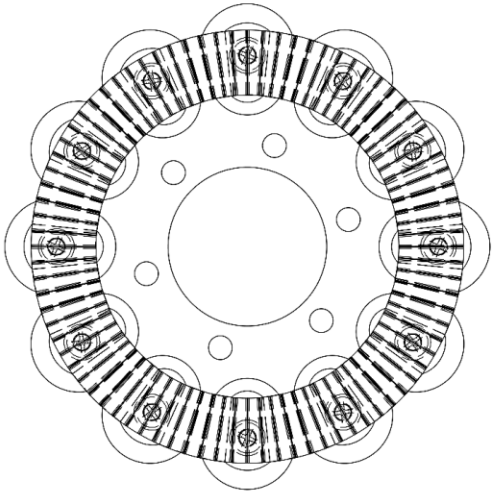

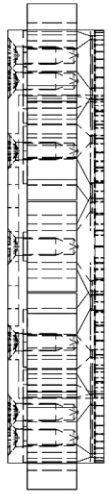

Designed by	Checked by	Approved by	Date	Date
Glynn Cooke				23/04/2016

SCALE 1 : 1.5

ST_Stator_Assembly_with_ST_Mag_3	Edition	Sheet
		1 / 1

Appendix II-E. Tooling

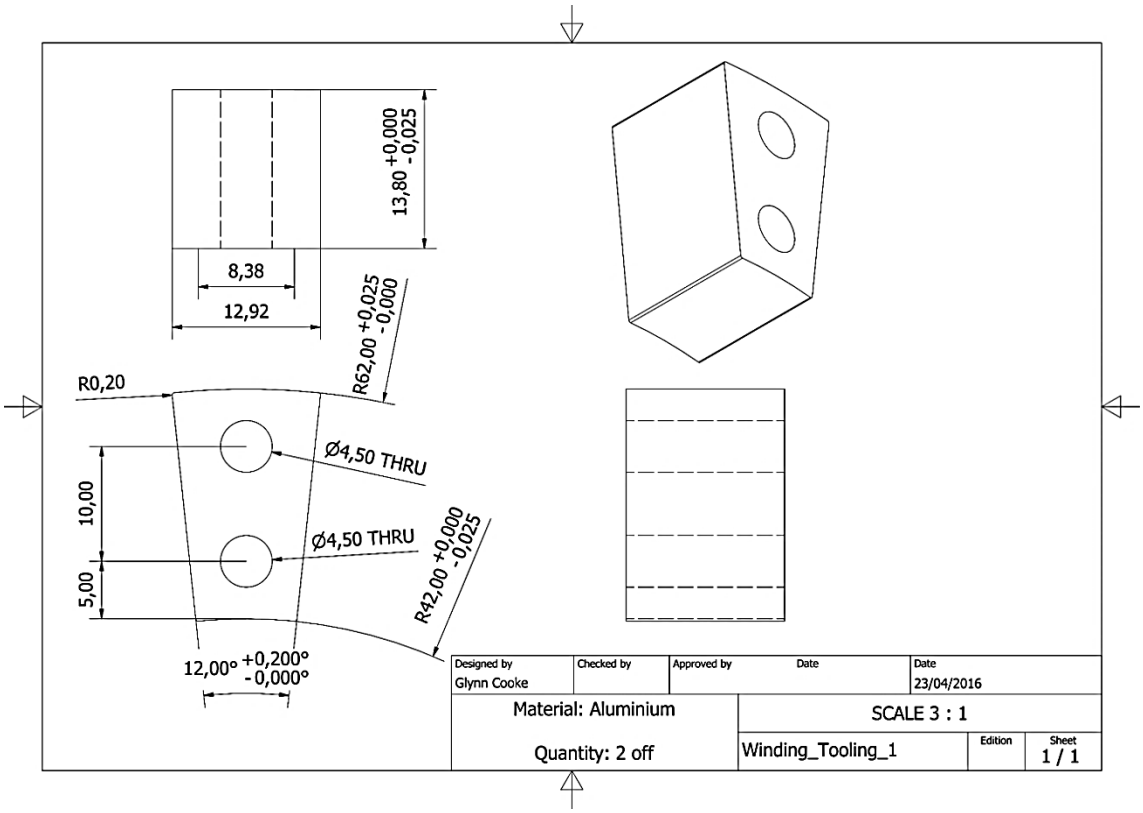

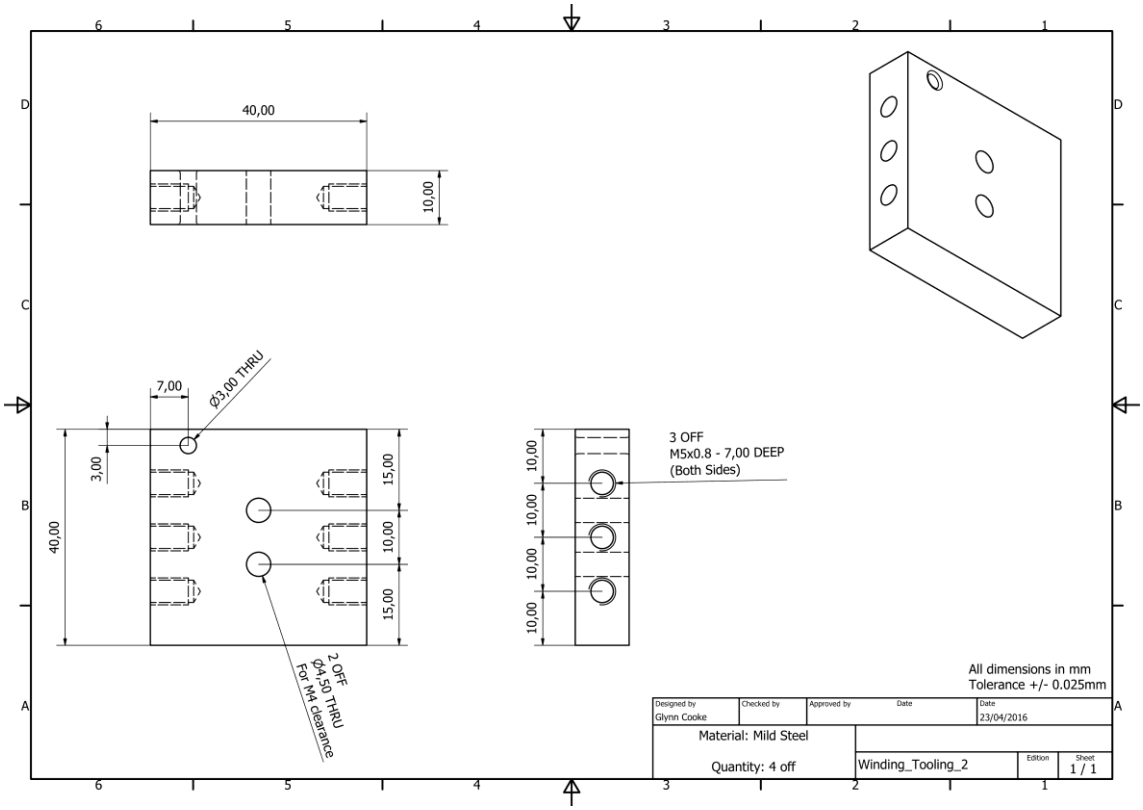

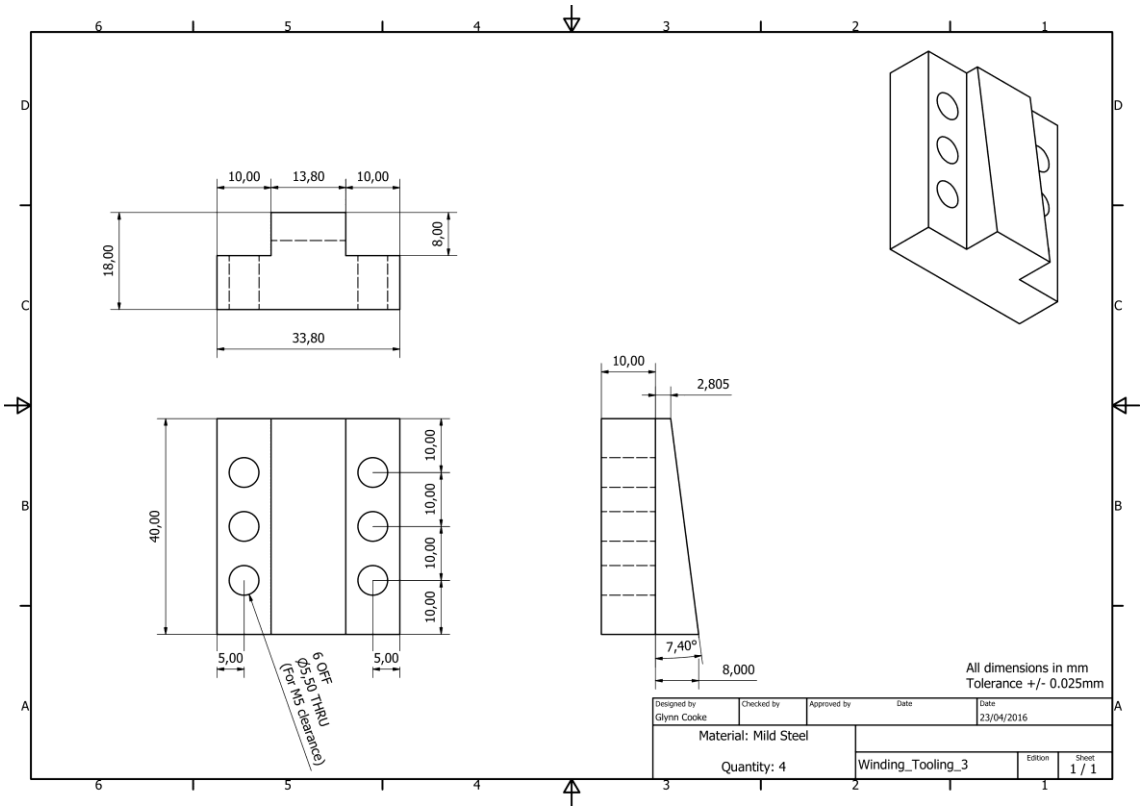
10,00
13,80
10,00
8,00
18,00
33,80
10,00
2,805
40,00
10,00
10,00
10,00
10,00
5,00
5,00
6 OFF
Ø5.50 THRU
(For M5 clearance)
7,40°
8,000
All dimensions in mm
Tolerance +/- 0.025mm
Designed by
Glynn Cooke
Checked by
Approved by
Date
Date
23/04/2016
Material: Mild Steel
Quantity: 4
Winding_Tooling_3
Edition
Sheet
1 / 1

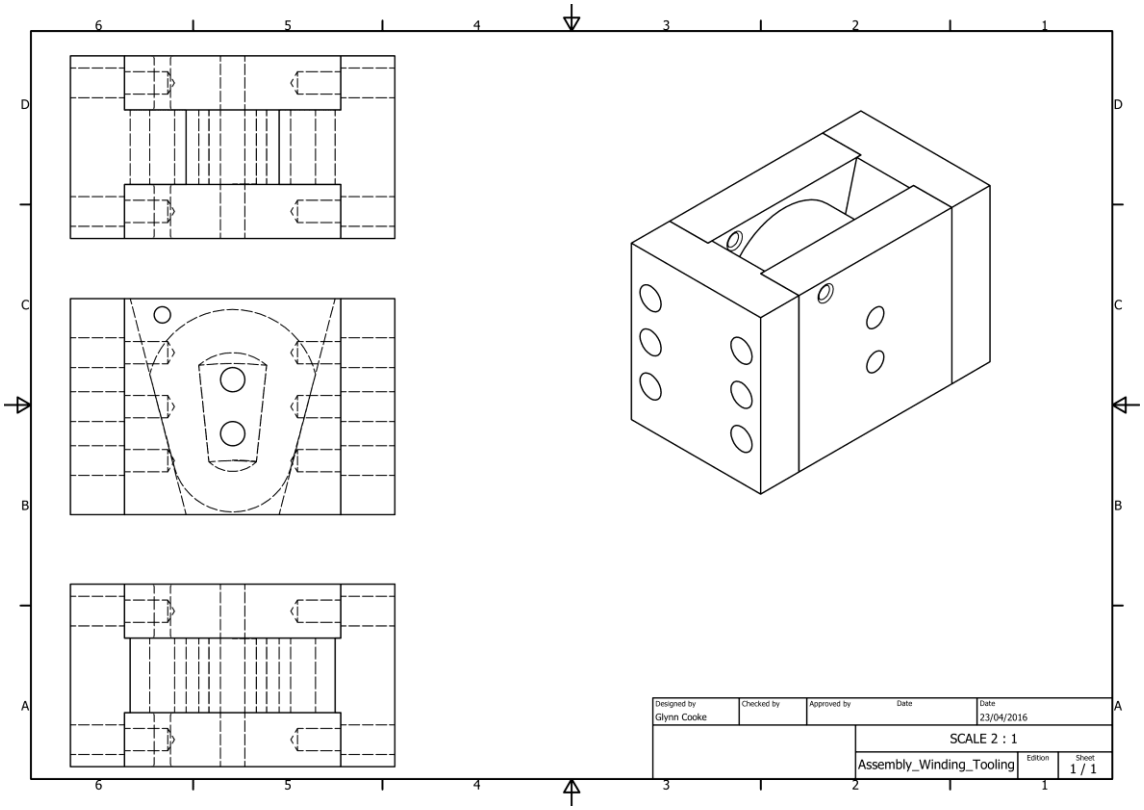
Designed by
Glynn Cooke
Checked by
Approved by
Date
Date
23/04/2016
SCALE 2 : 1
Assembly_Winding_Tooling
Edition
Sheet
1 / 1

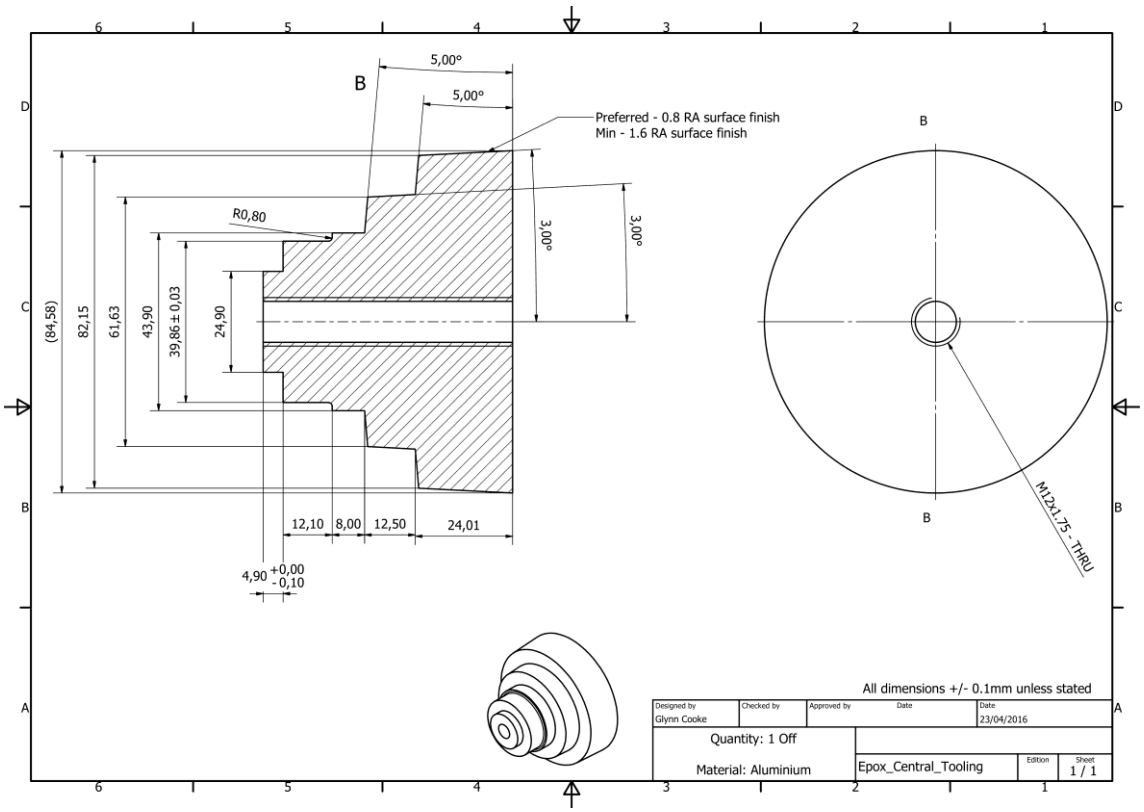
5,00°
5,00°
B
Preferred - 0.8 RA surface finish
Min - 1.6 RA surface finish
R0,80
3,00°
3,00°
(84,58)
82,15
61,63
43,90
39,86 ± 0,03
24,90
12,10
8,00
12,50
24,01
4,90 +0,00 -0,10
B
B
M12x1,75 - THRU
All dimensions +/- 0.1mm unless stated
Designed by
Glynn Cooke
Checked by
Approved by
Date
Date
23/04/2016
Quantity: 1 Off
Material: Aluminium
Epox_Central_Tooling
Edition
Sheet
1 / 1

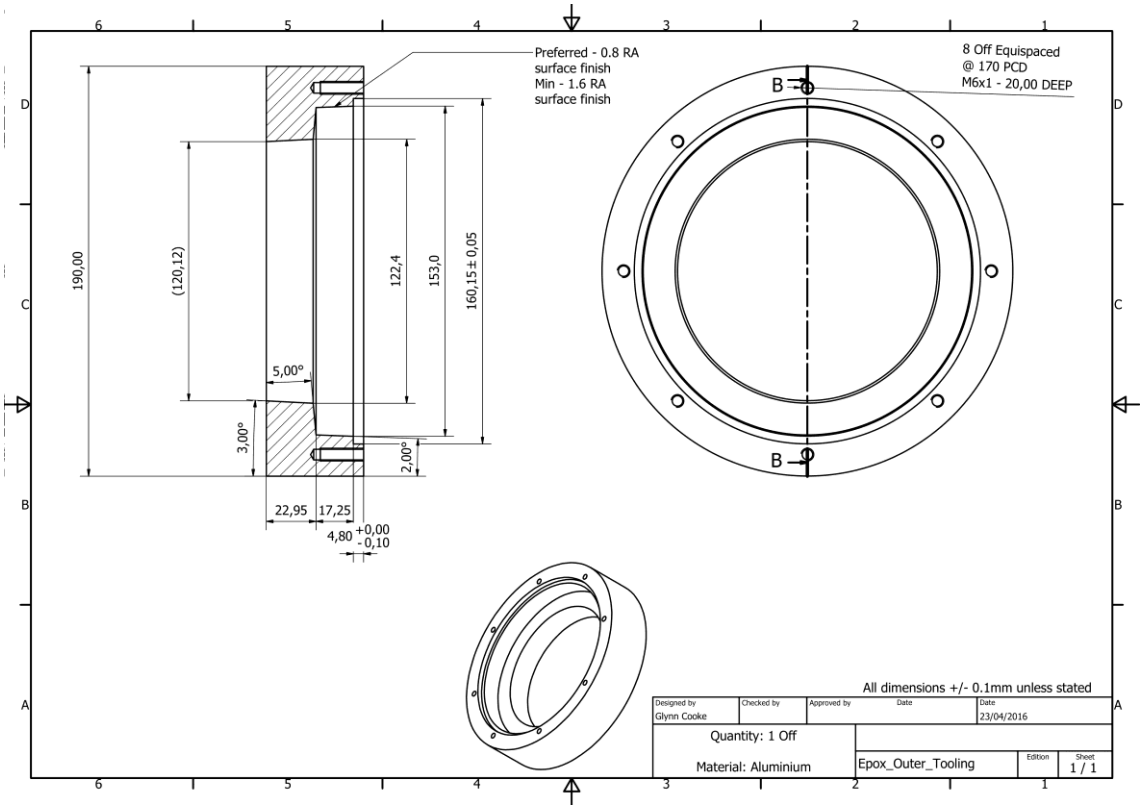
Preferred - 0.8 RA
surface finish
Min - 1.6 RA
surface finish
8 Off Equispaced
@ 170 PCD
M6x1 - 20,00 DEEP
B
B
190,00
(120,12)
122,4
153,0
160,15 ± 0,05
5,00°
3,00°
2,00°
22,95
17,25
4,80 +0,00 -0,10
All dimensions +/- 0.1mm unless stated
Designed by
Glynn Cooke
Checked by
Approved by
Date
Date
23/04/2016
Quantity: 1 Off
Material: Aluminium
Epox_Outer_Tooling
Edition
Sheet
1 / 1

B-B (1 : 1)

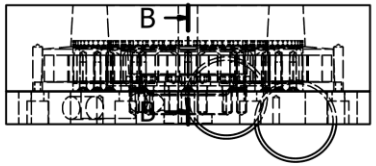

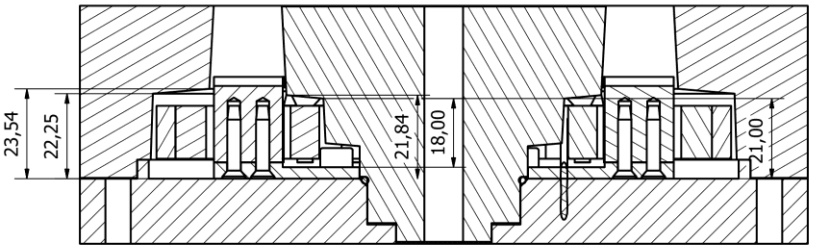

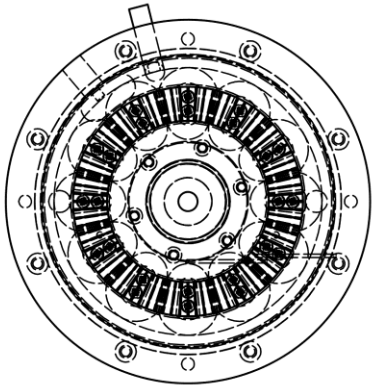

Designed by	Checked by	Approved by	Date	Date
Glynn Cooke				23/04/2016

SCALE 1 : 2